R. & M. No. 3721

MINISTRY OF DEFENCE (PROCUREMENT EXECUTIVE)

AERONAUTICAL RESEARCH COUNCIL
REPORTS AND MEMORANDA

The Lift and Stalling Characteristics of a 35 deg. Swept Back Wing Designed to have Identical Chordwise Pressure Distributions at all Spanwise Stations when near Maximum Lift

By D. S. Woodward and D. E. Lean
Aerodynamics Dept., R.A.E., Farnborough

LONDON: HER MAJESTY'S STATIONERY OFFICE
1973
PRICE £4·80 NET

The Lift and Stalling Characteristics of a 35 deg. Swept Back Wing Designed to have Identical Chordwise Pressure Distributions at all Spanwise Stations when near Maximum Lift

By D. S. WOODWARD and D. E. LEAN

Aerodynamics Dept., R.A.E., Farnborough

Reports and Memoranda No. 3721*

March, 1971

Summary

A 35 deg. swept back wing of aspect ratio 7 has been designed so that, according to the R.A.E. Standard Method, the planform gives a constant spanwise C_L distribution, whilst the camber and twist distributions, coupled with local thickness modifications, combine to provide identical chordwise pressure distributions at all spanwise stations at an overall C_L of 0·8. At mid-semi span the aerofoil section normal to the mean sweep line was a 12·2 per cent thick R.A.E. 100, and the design C_L was chosen to be close to the maximum values obtained experimentally for this section. Overall forces, flow visualization, and detailed pressure plotting tests were conducted on this model at three Reynolds numbers.

The pressure plotting results showed that the theoretical loading was quite closely attained except close to the leading edge near the root and out towards the tip. Very high peak suctions were observed near the leading edge within the inboard 10 per cent of the span, and these tended to dominate the stall behaviour of the wing. Nevertheless, it was possible to identify swept wing versions of the various classifications of two-dimensional stall pattern, and a good correlation was obtained between the sectional $C_{L\max}$ figures attained in two-dimensional flow and in the mid-semi span region.

---

* Replaces R.A.E. Technical Report 71050-A.R.C. 33 417

LIST OF CONTENTS

1. Introduction

It is well known that, as the sweep of wings is increased, there is a general tendency for the maximum lift to decrease and for the pitching moment at the stall to change in the nose-up direction.

Whilst the problem of providing increased $C_{L_{\max}}$ has been overcome largely by the application of existing sectional concepts and the flow below the stall is broadly understood, the problem of providing acceptable handling characteristics has had to be solved separately on each aircraft by a process of *ad hoc* development, and the flow at and beyond the stall is not well understood. Primarily this is because these flows involve extensive interactions between the separated flow regions and the main stream, and these are not easily amenable to mathematical analysis and tend to be sensitive to changes in Reynolds number.

Therefore the first objective of the tests described here was to provide increased understanding of some of the factors governing the behaviour of swept wings at, and beyond, the stall. Although there are many parameters that are possibly relevant, the argument put forward in Section 2 suggests the spanwise, and chordwise, loadings are amongst the most important. In order to explore the effects of varying these loadings, the R.A.E. Standard Method[1-5] has been used to design a wing to have a particular loading, close to the estimated value of $C_{L_{\max}}$, which is unlike that usually obtained on a conventional tapered planform. On this wing detailed measurements of the surface pressure distribution have been made, up to, and beyond the stall, so that the origin and development of the stall can be traced and related to the pre-stall load distribution.

A second objective now emerges, since, by comparing measured loadings with those for which the wing was designed, some assessment can be made of the limitations of the R.A.E. Standard Method when used outside the bounds of the twin assumptions of small camber and low C_L.

Since the design loading chosen approximated to an infinite sheared wing over much of the span, the experiment offered a good chance to compare the measured $C_{L_{\max}}$ and stalling behaviour of sections near the middle of the semi-span with results obtained from a two-dimensional test of the same section[12]. This comparison became the third objective of the tests and the aerofoil section was specially selected with this objective in mind.

In order to assist the reader who may be interested in only part of this Report the sections most relevant to each of these three objectives have been listed below.

(a) The overall stall pattern.
Section 2 outlines present concepts of the stall of simple swept wings.
Section 4 describes the overall force measurements and surface flow patterns.
Section 5.3 describes the variation of local lift coefficient across the span up to and beyond the stall.
Section 5.5 describes the overall pressure distributions over the wing.
Section 7 describes what, in our view, are the processes involved in the stall of this wing.

(b) Comparison of the measured loadings with the design loading.
Section 3.3 describes the planform design.
Section 3.5 describes the design of the spanwise variation of aerofoil section.
Section 5 presents the results from the surface pressure measurements.

(c) Comparison of $C_{L_{\max}}$ and stall pattern in two-dimensional and three-dimensional flow.
Section 5.6 compares the chordwise pressure distributions at three spanwise stations.
Section 6 compares the $C_L - \alpha$ and $C_M - C_L$ relations obtained in a two-dimensional test[12] with those obtained from sections near mid-semi span.

It will be shown that the design loading was attained on the wing except in a region close to the leading edge near the root (and possibly near the tip as well). Nevertheless, this discrepancy was sufficient to produce a premature stall at the root unless transition was artificially stimulated by a short length of wire. Despite the fact that the stall originated near the root, the wing still displayed a fairly strong nose-up pitch at the stall, and the results from the pressure plotting show the reason for this clearly. The comparison of the loadings and stall patterns between sections near mid-semi span and the same section in two-dimensional flow in general showed a surprisingly good correspondence.

2. Qualitative Description of the Stall of Simple Swept Wings

We will define a 'simple' swept wing as being an untwisted wing of straight tapered planform having no spanwise variation of aerofoil section, the aerofoil section being restricted to having small camber. When considering the stalling behaviour of such a wing we can confine our attention to the incidence loading since this will be the dominant term in the pressure distributions near maximum lift.

Küchemann[2] has shown that a simple swept wing of high aspect ratio ($A > 3$) can be considered as being divided into three spanwise regions as shown in Fig. 1. The three regions have the following basic characteristics.

Region (2) *sheared wing region.* The chordwise loading due to incidence on a thin wing in this region has the same shape as in two-dimensional flow, namely $[(1-x)/x]^{\frac{1}{2}}$, but the local lift curve slope, $\partial C_L/\partial \alpha_e$, is reduced from 2π to $2\pi \cos \phi$.

Region (1) *root region.* The chordwise loading due to incidence on a thin wing in this region changes continuously across it, and may be closely represented by the kernel $[(1-x)/x]^n$ where n varies from 1/2 at the junction with region (2) to $\frac{1}{2}\{1 - \phi/(\pi/2)\}$ at the root. As a consequence of this, the local sectional lift curve slope $\partial C_L/\partial \alpha_e$ also varies across this region, reducing from $2\pi \cos \phi$ at the junction with region (2) to $2\pi[1 - \phi/(\pi/2)]$ at the root and being generally expressable as $(4\pi n \cos \phi)/(\sin \pi n)$. To produce this chordwise loading shape on a two-dimensional aerofoil it would be necessary to add positive camber, so the sections within region (1) can be loosely thought of as existing in a negatively cambered airflow, the shape of which depends upon the spanwise position within the region and the magnitude upon the effective wing incidence, or lift coefficient.

Region (3) *tip region.* If we consider a swept back wing with an uncambered thickness distribution at zero lift, then the streamlines close to the surface in the vicinity of mid-semi span will be curved in plan view. As the centre is approached this curvature will decrease and must become zero in the plane $y/s = 0$, and this will affect the velocity distribution on the surface near the root. In a similar way, the curvature will decrease as the tip is approached and will become zero at some unknown distance outboard of the tip. Nevertheless, experience has shown that it is an acceptable approximation to assume that the curvature becomes zero at the tip, and thus that the form of the surface velocity distribution is the same as if the wing were reflected in the plane of the tip.

In the lifting case, this argument still holds good within the centre region (and explains the changing loadings described above) but it is much harder to accept within the tip region. Nevertheless, experience[2] indicates that in this case too, an acceptable approximation is to assume that the wing is reflected in the plane of the tip.

It follows, then, that the chordwise loading may still be represented by the kernel $[(1-x)/x]^n$ but that n will now vary from 1/2 at the junction with region (2) to a value of $\frac{1}{2}\{1 + \phi/(\pi/2)\}$ at the tip itself, and that, consequently, the local sectional lift curve slope $\partial C_L/\partial \alpha_e$ increases through this region from $2\pi \cos \phi$ at the junction with region (2) to $2\pi\{1 + \phi/(\pi/2)\}$ at the tip, the general form $(4\pi n \cos \phi)/(\sin \pi n)$ still being applicable at other points. In contrast to the root region, the sections within this region can now be loosely thought of as existing in a positively cambered airflow thus inducing loadings which would correspond to a negative camber on a two-dimensional aerofoil.

The most immediately obvious effect of the centre and tip regions is on the spanwise distribution of local lift coefficient, which changes relative to the unswept case as sketched in Fig. 2. On the basis of this change alone, it might be expected that the origin of the stall will move outboard as the sweep is increased. However, the shape of the chordwise loadings within the centre and tip regions described above further accentuates this trend, since, if we think of these loadings as occurring on a two-dimensional section, the sections within the tip region would have a tendency towards a leading-edge, or even a thin-aerofoil stall pattern[7,8] compared with the sections in the sheared wing region(2), and a corresponding tendency towards lower values of $C_{L_{\max}}$; conversely, the sections in the centre region (1) will have a tendency towards a trailing-edge stall pattern and therefore will be likely to attain higher values of $C_{L_{\max}}$ than the sections in the sheared wing region. Furthermore, previous experiments have shown[9] that the boundary-layer thickness at the trailing edge near the root is small, rises rapidly with distance from the root in region (1), holds a nearly constant level through region (2), and possibly rises slightly again in region (3). When all these features are combined, it is clear that the stall almost inevitably originates out near the tip, whilst the flow near the wing root will remain attached to a much higher incidence. Due to the sweep, the changes in the spanwise lift distribution as the stall progresses, show themselves as changes in pitching moment, so that the initial stall outboard produces the familiar nose-up change in pitching moment. This change is continued and reinforced, as the stall spreads inboard, by the attached flow near the root.

Of course, the situation of an actual aircraft wing is much more complex than that described above, Nevertheless the trends with increasing incidence must still be the same, and it is very often found that they are still strong enough to dominate the stall pattern, particularly at low Reynolds numbers[10].

3. Design of the Wind-Tunnel Model

3.1. General Considerations

In Section 2 we were able to demonstrate a broad understanding of the stall of swept wings. It therefore seems sensible to start an investigation of swept wing stalling from this point, rather than immediately becoming embroiled in the complexities of multiple aerofoils and spanwise discontinuities. Further, within the simple arguments used, the undesirable tendency to pitch nose-up at the stall could be traced to the combined effects of the spanwise distribution of local lift coefficient and of the spanwise variation in chordwise loading which are produced by the influences of the root and tip. Thus, according to our simple arguments, if our simple swept wing were to be re-designed (using twist, camber, and planform shaping) so that all these spanwise variations were eliminated, then the whole wing should stall simultaneously and little pitching moment change should result.

Clearly this is unlikely to happen. Partly because there must be other factors of importance which our simple arguments have ignored, and partly because it is unlikely that we shall achieve precisely the loading we require, since we do not have a complete design method for calculating the shape of a swept, thick, non-planar wing to support a given loading in a viscous fluid. Nevertheless the use of existing design methods should result in a wing whose actual loading is sufficiently different from that of a tapered wing of constant-section to indicate how much the stalling behaviour depends on the pre-stall loading.

Since there is little chance of developing a new theory which does not rest on the twin simplifying assumptions of small C_L and small camber which underlie the present design methods, it is clearly of interest to know what errors are involved when these methods are applied to cases where these assumptions are no longer valid. In the past, it has often been found that the errors are acceptable (e.g. flap induced lift increments from thin-aerofoil theory[6]); in the present case, comparison between the theoretical and experimental loadings should show the likely magnitude of these errors, although the influence of the boundary layer on the experimental loadings must not be forgotten.

At this stage in the investigation one of our main aims must be to understand the processes involved in the stalling behaviour, and therefore it would clearly be valuable to be able to distinguish various categories of stall, in a similar way to the well-known[11] three types of stall in two-dimensional flow. Since the loadings on this wing will be almost constant across the span at the stall, this experiment offers a good chance to discover if the two-dimensional stall behaviour is reproduced in any recognisable form in the swept case, and the basic section of this wing was chosen with this aim in view.

Having discussed the design and aims of the model in general terms let us now consider its geometry in more detail.

3.2. Geometric Parameters

An aspect ratio of 7 and a sweep-back angle of 35 degrees were chosen as being reasonably representative of existing and proposed swept-wing transport-designs. As the tests were to be carried out in the No. 2 $11\frac{1}{2}$ ft × $8\frac{1}{2}$ ft tunnel a span of 7 ft (2·135 m) and a standard mean chord of 1 ft (0·305 m) were chosen as being suitable.

3.3. Planform

Since we know that both the shape of the chordwise loadings due to incidence, and the effective lift curve slope, vary across the span, it will be clear that the design condition can be realised at one incidence only, and at all other incidences it will be necessary to accept a degree of non-uniformity. Although, in principle, our design condition can be achieved on a wing of any planform shape by the addition of suitable amounts of twist and camber, the degree of non-uniformity at off-design conditions can be minimised by securing a constant spanwise C_{L_L} distribution by means of suitable planform shaping, as described by Brebner[3]. The additional geometric complexity thus introduced was thought to be worth while because of the greater aerodynamic simplicity. As a demonstration of the overall influence of the centre and tip effects it is interesting to note that, on a straight wing, the planforms for elliptic loading and for a constant spanwise C_{L_L} distribution are identical, but, as the sweep increases, these two diverge increasingly as shown in Fig. 3. It will be seen that for elliptic loading, the root chord increases, and the tip decreases, relative to an elliptic chord distribution, whilst the converse is true on the planform which gives a constant spanwise C_{L_L} distribution, thus leading to the characteristic inverse taper near the root. The planform for this wing, which is shown in Fig. 6, was generated by a digital computer program using an iterative method similar to that employed by Brebner[3], but employing some additional features within the iterative loop which gave a closer control of the aspect ratio of the final planform.

3.4. Choice of Basic Aerofoil Section and the Design C_L

As described above, the basic wing section (i.e. that at the mid-semi span) was chosen, in an attempt to discover whether the typical changes of stall pattern observed on two-dimensional aerofoils[7,11] occurred in any recognisable form on a swept wing. All the evidence suggests that the large extent of separated flow (long bubble) that exists on a section which experiences a thin-aerofoil stall in two-dimensional flow, is significantly affected by the addition of sweep and is usually transformed from a quasi-closed cell into a vortex. Even if this were not so, the long bubble is such a large perturbation on the flow that it becomes pointless to compare the experimental results with any aerofoil or wing theory that assumes an attached flow. For these reasons it was felt unlikely that it would be profitable to explore the boundary between thin-aerofoil and leading-edge stall; furthermore it is unlikely that a thin aerofoil stall will occur on a typical swept-wing transport-aircraft even at tunnel Reynolds numbers. Clearly then, it is the boundary between the leading-edge, and the trailing-edge, stall patterns which is the obvious one to attempt to explore on this model.

Since the usable speed range of the tunnel for this type of test is from approximately 300 ft/sec to 80 ft/sec (91·4 to 24·4 m/sec) (limited at high speed by the need to avoid strong compressibility effects at high lift, and at low speed by the accuracy attainable in reading pressures on an inclined multi-tube manometer) a section was required which would experience the required change in stall behaviour somewhere in the range 140–160 ft/sec (42·8 to 48·8 m/sec). In terms of Reynolds number based on a 1 ft standard mean chord this range becomes

$$0{\cdot}90 \times 10^6 < R_{\bar{c}} < 1{\cdot}0 \times 10^6 .$$

The details of how it was decided that a 10 per cent t/c R.A.E. 100 section along wind would be likely to satisfy this requirement, and the subsequent experimental confirmation of this behaviour, have already been given in Ref. 12, so it is not necessary to repeat this here, save to say that the selection was based upon the Owen and Klanfer[13] criterion of short bubble bursting, used in conjunction with the boundary-layer calculations reported by Curle and Skan[14] on some R.A.E. sections. However in the interests of clarity, it is probably worth reproducing the definitions of, and the relations between, the sheared-wing and yawed-wing section-geometries which were used in Ref. 12, and these are shown in Fig. 4. In common with the earlier report it will be assumed, at least initially, that two-dimensional and yawed-wing conditions are essentially the same and this defines the transformations from sectional coefficients on the swept wing to those in two-dimensional flow.

Having chosen the basic wing section, but prior to evaluating its lifting and stall performance, the problem had to be faced of specifying the overall C_L for which the twist and camber distributions would be designed. Clearly this is a problem of some delicacy, since, if the value chosen was too high, then there was a distinct risk that significant flow separations would arise before the design C_L could be reached (as was the case in a similar previous experiment conducted by Brebner[15]) thus invalidating the experiment; whereas if it was chosen too low, then the basic spanwise variations of the chordwise pressure distributions would once again be in evidence by the time the stall was reached.

Within the small Reynolds number range in which the leading-edge stall pattern gives way to the trailing-edge pattern (on this aerofoil $0{\cdot}91 \times 10^6 < R_{\bar{c}} < 1{\cdot}0 \times 10^6$ as mentioned above) the boundary layer calculations of Curle and Skan[14] suggest that the $C_{L_{\max}}$ of the basic section is approximately 1·10; on the swept wing this gives a sectional $C_{L_{\max}}$ of approximately 0·75 using the relations of Fig. 4. Since previous evidence[35] on similar sections showed that $C_{L_{\max}}$ could confidently be expected to rise steadily with Reynolds number even in the trailing-edge stall regime, $C_L = 0{\cdot}8$ was chosen as the design value from which to calculate the twist and camber distributions.

Now that the two-dimensional behaviour of the basic section is available[12], it is interesting at this point to see what kind of behaviour might be expected on the swept wing assuming the correspondence between the two-dimensional and the yawed wing conditions. Using the relations shown in Fig. 4 it will be seen that $C_{L_L} = 0{\cdot}8$ corresponds to a sectional

$$\hat{C}_{L_L} = 0{\cdot}80 \sec^2\phi = 1{\cdot}19,$$

and comparing this with the measured $C_{L_{\max}}$ characteristics of the section shown in Fig. 5, suggests that the wing will begin to stall before the design C_L can be attained for values of R_y less than about $0{\cdot}92 \times 10^6$, i.e. $R_{\bar{c}} < 1{\cdot}37 \times 10^6$ or below a test velocity of 220 ft/sec (67 m/sec), based on the standard mean chord of 1 ft. It can thus be seen that the chosen value of the design C_L sits nicely in the middle of the range of $C_{L_{\max}}$ of the basic section: at tunnel speeds above about 220 ft/sec (67 m/sec) the stall should occur at a C_L above the design value, so that the intrinsic spanwise variation of chordwise pressure distribution will be slightly in evidence once more and there should be a general tendency towards a trailing-edge stall pattern; at tunnel speeds below about 220 ft/sec (67 m/sec) the stall should occur at a C_L somewhat below the design value so that the highest suction peaks should occur towards the root and there should be a general tendency towards a leading-edge stall pattern.

3.5. Camber and Twist Distribution and Thickness Modification

The spanwise distributions of camber and twist are shown in Fig. 6. They were determined from the relations given by Brebner[4] using the hyperbolic form of the interpolation function λ as given by

$$\lambda = \sqrt{1 + \left(2\pi\frac{\tan\phi}{\phi}y\right)^2} - 2\pi\frac{\tan\phi}{\phi}y,$$

the camber line shape being that denoted by $m = 0{\cdot}5$ in Brebner's[4] notation.

Some difficulty was experienced in 'cladding' the camber line with the thickness distribution. Initially, an attempt was made to follow N.A.C.A. practice and add the thickness normal to the camber line, but this method produced upper surface profiles near the root which doubled back and crossed-over themselves close to the leading edge, because of the rapid variation of camber line slope in that region. Finally, therefore, it was decided to add the thickness normal to the chord line after the latter had been twisted. This unfortunately leads to profiles with rather small nose radii near the root, again due to the high slope of the camber line in this area, and this may partially account for the behaviour of the flow on this wing.

This difficulty is, of course, caused by the large camber needed to achieve the design loading, coupled with the high curvature of the camber line near the leading edge. In more usual cases where aerofoils are built up by the superposition of a thickness form upon a camber line, these are both smaller and no difficulty is apparent. For the present extreme case, a suitable way to carry out the 'cladding' procedure has not yet been devised.

The camber and twist variations across the span are designed to counteract the centre and tip effects on the loadings due to incidence; there is also a centre and tip effect on the pressure distribution due to the thickness form of the section, although its spanwise extent is less than in the case of the incidence loadings. This effect can also be counteracted by a modification to the thickness shape of the section as described by Weber[5]. The required modification was calculated for this wing and basic section, by generating the matrix coefficients $[S_{\mu\nu}{}^{(20)}]$ and $[S_{\mu\nu}{}^{(21)}]$ for 35 degrees sweep and using these in an iterative cycle, as suggested by Weber, to generate a root thickness form which had as near as possible the required velocity distribution whilst still remaining a singly closed contour. The difference between this root section and the basic thickness form was then faded out spanwise from the root and tip according to the interpolation functions $K_2{}^1$. Computer programs were developed to perform these calculations.

Three typical sections of the wing obtained in this way are shown in Fig. 7.

Front and rear views of the model mounted in the tunnel are shown in Figs. 8 and 9. A detailed description of the construction of the model and the experimental method including the data reduction is given in Appendix I.

4. Balance Measurements and Flow Visualization

It was originally intended to test this wing at 80, 160 and 320 ft/sec (24·4, 48·8, 97·6 m/sec) well into the post-stall regime. Unfortunately during a preliminary series of balance measurements at 320 ft/sec (97·6 m/sec) the wing developed a large amplitude pitching oscillation at 18 degrees incidence, which was sufficient to severely strain the sting mounting. After this had been repaired it was felt prudent to reduce the top tunnel speed to 280 ft/sec (85·4 m/sec) and to fit an oil damping bath as described in Appendix I; it also seemed sensible to restrict the maximum incidence at this speed to below 15 degrees (except for one occasion when measuring only overall loads) because of the severe buffeting that was experienced above the stall. Therefore the complete development of the flow in the post-stall regime has been investigated only at the two lowest Reynolds numbers.

Figure 12 shows the overall lifting performance of the wing with no transition fixing. It is clear that substantial areas of flow separation are occurring well before the design C_L, and that the onset of these separations is fairly sensitive to changes in tunnel speed. The maximum local Mach number measured on the wing in this configuration is around 0·75, and the two-dimensional tests of the basic aerofoil section[12] suggested little dependence on Mach number over this range of velocity and C_L, so that it seems likely that Reynolds number is primarily responsible for the variations shown in Fig. 12.

Exploratory flow visualization, using tufts, indicated that the initial separation did not occur until α exceeded 5 degrees and was restricted to an area near the leading edge close to the root. The subsequent development of this separated region with increasing incidence appeared to be similar to that observed by Brebner[15] on a similar model of higher sweep. Working on the hypothesis that this initial separation could be thought of as a local area of thin-aerofoil stall occurring on a swept leading edge, an attempt was made to reduce the extent and growth of the long bubble by fixing transition close to the leading edge in the vicinity of the root by means of a wire running spanwise. Figure 13 shows that the addition of the wire enabled the design C_L to be reached at both the higher Reynolds numbers before any significant areas of flow separation occurred. The flow visualization pictures (Figs. 19–26) further show that the size and rate of growth of the bubble were both reduced.

No systematic attempt was made to optimise the size and spanwise extent of the wire at each of the test Reynolds numbers; a rough optimum was found at the lowest Reynolds number and this configuration was then used at the higher Reynolds numbers as well. The final configuration is shown in relation to the wing leading edge in Fig. 18. The wire used was 26 gauge (0·018 in., 0·46 mm, diameter, 0·15 per cent $\bar{c}$) and extended 4·20 in. (10·68 cm) spanwise to $y/s = 0{\cdot}10$; 34 gauge (0·010 in., 0·25 mm diameter) wire was also tried but found to be inadequate at 80 ft/sec (24·4 m/sec), although little difference between the two cases could be detected at 160 ft/sec (48·8 m/sec). The effectiveness of the wire decreased as its spanwise extent was reduced, but further lengthening did not produce any improvement. If we assume that the velocity across the wire is equal to free stream speed (i.e. $C_p = 0$), and it can be seen from the pressure plotting results that this is a reasonable approximation, then the minimum wire-Reynolds number that was found to be effective is $R_w = 850$ in both cases. This value is only slightly higher than that usually suggested for fixing transition in mild pressure gradients, which can easily be explained in terms of the local, extremely thin, boundary layer and highly-accelerating pressure gradient. At 160 ft/sec and 280 ft/sec

(48·8 m/sec and 85·4 m/sec) the values of the wire Reynolds number in the configuration used were 1700 and 3000 respectively.

Unlike most occasions where transition is fixed on a wind-tunnel model, the flow in the wire-on case here should not be viewed as being more representative of full-scale Reynolds number than the wire-off case; this would clearly be unreasonable in view of the limited spanwise extent of the wire. In this case, the sole purpose of the wire is to delay the onset of the root separation and to reduce its size so that it no longer dominates the stall pattern.

The flow development on the wing, with and without the wire, can be traced from the flow visualization pictures of Figs. 19–26. Beginning with the wire-off case at 80 ft/sec shown in Fig. 19, it can be seen that, at low incidence, $\alpha = 3{\cdot}6$ degrees, transition occurs at around 25 to 30 per cent chord over the outer 80 per cent of the wing, but moves rapidly forward to the leading edge further inboard. This behaviour is to be expected in view of the adverse gradients which must exist behind the suction peaks generated by the negative camber on the sections in the root region. The effect of the wire at low incidences can be seen by comparing the top pictures of Figs. 19 and 20. From 40 per cent semi span outboard, the transition positions are virtually unaltered, but inboard of this the transition position is moved forward by the presence of the wire, although naturally little difference can be seen over the inboard 12 to 13 per cent where it was originally close to the leading edge. In these top pictures ($\alpha = 3{\cdot}6$ degrees) there is little evidence of flow separation near the root, with or without the wire, but by $\alpha = 6{\cdot}5$ degrees a local separation near the leading edge can be seen extending over the inner 10 per cent of the semi span and up to a maximum of about 20 per cent chord. With increase of incidence on the clean wing this separated region grows both spanwise and chordwise, showing flow patterns more and more reminiscent of those produced by vortices above slender wings, until by $\alpha = 10{\cdot}20$ degrees on Fig. 21 a clear vortex pattern is obtained, with, however, a distinct amount of attached flow existing outboard. Further increase of incidence to $\alpha = 11{\cdot}70$ degrees, results in detachment of the flow over the whole of the wing surface, a vortex springing from near the apex and crossing the trailing edge of the wing at about 70 per cent semi span, leaving a large dead-air region. As the post-stall regime is penetrated deeply to $\alpha = 17{\cdot}9$ degrees, the sweep of the vortex increases so that the vortex crosses the trailing edge of the wing inboard of mid-semi span, resulting in an enlargement of the 'dead-air' region of the wing. The somewhat peculiar looking 'channelled' separation lines that run at an angle across the wing at the highest incidences are probably secondary separation lines, representing separation of the re-attached flow under the vortex.

If we compare this flow development with increasing incidence with that shown in Figs. 20 and 22 where the wing is fitted with the wire, it can be seen that, at all incidences below about 10 degrees, the addition of the wire produces a significant reduction in the chordwise and spanwise extent of the separated region near the root, so that, for instance, the size of the separated region at $\alpha = 10{\cdot}20$ degrees with the wire on, is roughly comparable to that at $\alpha = 6{\cdot}5$ degrees without the wire. Above this incidence simple comparison between the wire-on and wire-off cases is no longer possible until deep into the post-stall regime, where, from the last photographs in each of Figs. 21 and 22, the flows in the two cases are evidently very similar.

In the wire-off case all the flow pictures up to and including that for $\alpha = 10{\cdot}20$ degrees, show the inboard separated region as being terminated outboard by a region of completely attached flow which shows no sign of an incipient stall. Because of this, it is reasonable to postulate that the stall pattern of this wing at $R_{\bar{c}} = 0{\cdot}51 \times 10^6$ wire-off, is very largely determined by the characteristics of the root separation and has little or nothing to do with the stalling characteristics of the sections outboard of, say, 20 per cent semi span. Therefore, when a different type of flow pattern occurs, as at $\alpha = 10{\cdot}90$ degrees in Fig. 22, where the pattern over the outer 60 per cent of the semi span suggests the onset of a trailing-edge stall, it is also plausible to suggest that this change is due to the appearance of the basic stalling characteristics of the sections in that region of the wing. The plausibility of this concept is heightened if it can be accepted that the 'streak' which springs from the outer end of the root separation at $\alpha = 10{\cdot}20$ degrees in Fig. 22, marks the outer edge of the flow which is immediately affected by the existence of the root separation. Nevertheless we should still remember that this apparent onset of a trailing-edge stall pattern outboard may have its origins in the root separation, particularly as it appears to be associated with a reduction in the constraining effect of the attached flow on the outer end of the root separation.

When the incidence is raised to 12·0 degrees, the flow pattern shows a vortex originating close to the outer end of the wire and following broadly the leading-edge outline, but with the sweep increasing as the tip is approached, so that it crosses the trailing edge in the region of 70 to 80 per cent semi span; the outer 10 per cent or so of the semi span appears to be a very nearly dead region. Near the root, surprisingly, the same type of flow which was observed at $\alpha = 10{\cdot}20$ degrees, appears to be re-established, but the mechanism by which this could happen is very difficult to visualize.

Flow visualization pictures taken at 160 ft/sec ($R_{\bar{c}} = 1{\cdot}02 \times 10^6$) are shown in Figs. 23–26. From these it will be seen, as would be expected, that the increase in Reynolds number reduces the extent of the separated region near the root, in both the wire-on and the wire-off cases. However, at this Reynolds number (on the basis of the pattern obtained at $\alpha = 11{\cdot}90$ degrees in Fig. 23 which is essentially similar to that at $\alpha = 10{\cdot}90$ degrees in Fig. 22) we may use similar arguments to those already presented to suggest that the basic stalling characteristics of the sections outboard of 20 per cent semi-span are exerting some influence on the overall stall pattern even in the wire-off case. This probably explains why, at this Reynolds number, the flow patterns at incidences up to $\alpha = 10{\cdot}70$ degrees are very similar, both wire-on and wire-off. Thus we may have some confidence that, in the wire-on case, the results obtained for the sections away from the immediate vicinity of the root are not dominated by the presence of the root separation.

The flow patterns obtained deep in the post-stall regime ($\alpha = 15{\cdot}1$ degrees Fig. 25 and $\alpha = 16{\cdot}70$ degrees Fig. 26) are very similar to each other but very different from those obtained at the lower Reynolds number. The secondary separation lines have now disappeared and the vortex which originates from the apex has a much lower sweep at this Reynolds number; moreover, the flow separation now appears to occur downstream of a short separation bubble near the leading edge, whereas previously the separation occurred at the leading edge. The last interesting feature of these pictures is the 'saddle' point which occurs near the leading edge; reverse flow approaching this on the inboard side returns inboard along the leading edge whilst reverse flow approaching on the outboard side turns and proceeds outboard along the separation line.

Having discussed the flow development on the wing with and without the wire, let us now turn our attention once again to the overall characteristics of the wing, and, in particular, to the pitching moment behaviour shown in Figs. 14 and 15. These show that, as the wing stalls, it experiences a strong nose-up change in pitching moment. In order to set this change in perspective some results from a conventional straight tapered planform wing of slightly lower sweep angle are shown for comparison. Although the straight tapered wing had a pronounced tip stall, the magnitude of the nose-up pitch change in the two cases is clearly comparable. Now this really is a most surprising result, in view of the fact that, on all the flow visualization evidence offered, it would normally be said that the present wing began to stall at the root, and so would be expected to pitch nose down; furthermore as can be seen from the lift curves of the straight tapered wing on Figs. 12 and 13 the $C_{L_{\max}}$ values attained by the two wings are also comparable, so that, in spite of the exaggerated treatment of the present wing, and the entirely different flow development on it, the overall results are essentially similar. However the results from the pressure plotting tests, to be given in the next section, will show clearly how this pitch-up arises, even though it will not be possible to produce an entirely non-controversial description of the flow mechanisms involved.

Lastly Figs. 16 and 17 show the overall drag results for this wing both wire-on and wire-off. Maskell[19] has shown that, in general, overall drag measurements cannot be analysed to give experimental values which are closely related to either the profile drag or the vortex drag, without additional information. Despite this, the breakdown of overall drag results into a constant plus a term dependent on the square of the lift coefficient can still be valuable, but, for cambered wings, it is more meaningful to use the relation

$$C_D = \check{C}_D + \frac{k}{\pi A}(C_L - \check{C}_L)^2,$$

where $\check{C}_D$ = minimum overall drag

and $\check{C}_L$ = lift coefficient for minimum overall drag,

than the more traditional relation

$$C_D = C_{D_0} + \frac{k}{\pi A}C_L^2.$$

Therefore the overall drag results have been analysed in this way in Fig. 17, using the value $\check{C}_L = 0{\cdot}04$. Since, as will be seen later, the spanwise loading is practically zero at zero lift, the occurrence of a minimum drag at other than zero lift must be associated with the lift dependence of the profile drag of the wing.

5. Results from the Pressure Plotting Tests

5.1. General Description

The pressure plotting results to be presented have been restricted to four out of the six cases for which overall load data were given in the previous section, i.e. all three values of Reynolds numbers with the wire-on, but only the highest Reynolds number with the wire-off. This restriction provides a worthwhile reduction in the quantity of data to be presented and facilitates both the presentation and the comparison between the cases, without making any significant difference to the information to be gained from the experiment. This is so, because it is fairly clear from what has already been shown, that all the wire-off cases are dominated by the root separation, and so are likely to be qualitatively similar, even though quantitative differences in, say, the size of the separated region are bound to exist between the differing Reynolds numbers. The data have also been further slightly limited by a decision, taken in the interests of reducing the tunnel occupancy time, not to take any pressure measurements outboard of 50 per cent semi span in the wire-off case.

This limitation has been of no significance as far as the understanding of the flow development in the wire-off case is concerned, but it has made it impossible to carry out the same type of analysis of the sectional stall behaviour that is presented for the wire-on cases in Section 6. Even this is no great loss, since the interference of the root separation on the stall characteristics of the sections near mid-semi span and outboard is so large that the analysis would, in any case, have been of little value.

Since we have begun by presenting the results of measurements of the overall forces and moments, and are only now presenting the results from the pressure measurements, this system of presenting results in order of increasing detail will be continued within this section also, so that, although the spanwise variation of sectional lift and pitching moment, C_{L_L} and C_{M_L}, might be described as an end product of the pressure measurements, these are presented first in Figs. 28–33. They are followed by a comparison between the measured overall forces and moments already presented, and those deduced from a spanwise integration of the local coefficients suitably weighted by the planform shape. These in turn are followed by the pressure distributions appearing on the wing at a set of selected incidences, the results for which have been interpolated from the raw pressure data.

Some difficulty was experienced in finding a suitable method for showing these distributions adequately, since the traditional way of presenting such data, in isobar form, is incapable of showing sufficient detail in regions of high pressure gradient, such as occur on this wing in the vicinity of the leading edge. Nevertheless it was not found possible to devise an alternative method which would show with comparable clarity the spanwise variations in the shape of the pressure distribution. For this reason, the pressure distributions have been presented in a composite form, in which isobar patterns are used to give an overall view of the spanwise development of the surface pressure distribution, and these are supplemented by a series of spanwise carpet plots of the pressure distribution over the forward 15 per cent of each section on which measurements were taken.

Finally, the development of the pressure distribution with incidence on three typical sections (one in the root region (1), one in the sheared wing region (2), one in the tip region (3) *see* Fig. 1) is shown, and the differences highlighted.

5.2. Sectional Lift and Moment Coefficients at the Design Condition

From the overall $C_L \sim \alpha$ results given in Figs. 12 and 13 it can be seen that the design C_L, with substantially attached flow over the wing, was achieved only in the wire-on condition at $R_{\bar{c}} = 1{\cdot}78 \times 10^6$ and $1{\cdot}02 \times 10^6$.

The spanwise C_{L_L} distribution at the design condition ($C_L = 0{\cdot}8$) at $R_{\bar{c}} = 1{\cdot}78 \times 10^6$ is shown in Fig. 29 by the line representing $\alpha = 11{\cdot}4$ degrees. It will be seen that the desired constant C_{L_L} distribution, has been achieved over most of the span, but over the outer 20 per cent an appreciable rise occurs. The design condition at $R_{\bar{c}} = 1{\cdot}02 \times 10^6$ is shown in Fig. 30 by the line for $\alpha = 12$ degrees and it can be seen that, in this case, the rise of C_{L_L} towards the tip is less, and, in consequence, the distribution is more uniform than at the higher Reynolds number. The reasons for the rise in C_{L_L} towards the tip and its variation with $R_{\bar{c}}$ are discussed later.

The corresponding pitching moment distributions at the design condition are shown in Figs. 33 and 34 by the lines representing $\alpha = 11{\cdot}4$ degrees and 12 degrees. In this case it can be seen that the main region of non-uniformity lies towards the root where the pitching moment about mid-chord decreases. It may thus be concluded that towards the root, the camber and twist distribution is not entirely successful in bringing the centre of pressure forward to the position it has near mid-semi span. In the same way since the pitching moment distribution towards the tip does not mirror the increase in lift coefficient in that region, it is reasonable to conclude that the centre of pressure is again aft of the position it has near mid-semi span. However, since on an uncambered wing the centre of pressure towards the tip would have been forward of the position at mid-semi span, it can only be concluded that the camber and twist distribution in this region over-corrects for the presence of the tip. The aft movement of the centre of pressure towards the root and tip can be seen also in the isobar patterns to be presented later.

It may be noticed that the incidence values quoted as representing the design condition in this section are different from those which would be deduced from Fig. 13. The values used are those which were obtained when the overall lift on the starboard half wing was deduced by chordwise and spanwise integration of the surface pressure distribution. The comparison between the measured overall forces and those deduced from the integration is shown in Fig. 38 and the differences are discussed in Section 5.5.

Although the regions where the measured loading deviates from that designed have been identified (and also the sense of the deviation) it is important that this does not convey the impression that the comparison is disappointing. Bearing in mind both the limitations of the theory used to design the wing geometry and the influence of the boundary layer (which is strong so close to the stall) it would be more correct to conclude that the comparison was encouraging. However it will be seen later that some of these deviations carry within them warnings that some modifications to the theory may have to be made if considerable increase in camber and C_L is required.

5.3. Sectional Lift Coefficients

Figures 28–31 show the spanwise variation of the local sectional lift coefficient in the four cases being considered. The most striking feature of these is the behaviour immediately prior to, and through the stall, and comparison between the various cases shows considerable differences between them.

In the wire-off case shown in Fig. 28 it will be seen that the initial development of the lift with increasing incidence, i.e. up to $\alpha \simeq 3$ degrees, is regular and as would be expected. (The spanwise variation of zero lift angle will be discussed later.) From $\alpha \simeq 3$ degrees to $\alpha \simeq 8$ degrees the lift over the inboard 20 per cent of the span proceeds to increase in a somewhat irregular fashion as the separation near the leading edge in that region grows, but nevertheless manages, broadly speaking, to keep pace with the lift development over the outboard 50 per cent of the span which appears to be very little affected by the inboard separation. From $\alpha \simeq 9$ degrees onwards, the lift development over the inboard 20 per cent becomes rather more regular and continues to increase, with a slightly increased slope, right up to the maximum incidence tested, approximately 14 degrees. However, over the outboard 60 per cent, the lift curve slope decreases quite markedly and the lift soon after begins to drop, having reached a low maximum in the region of $C_{L_L} = 0{\cdot}7$.

The wire-on case shown in Fig. 29 shows a distinctly different behaviour. Now, apart from the innermost section at $y/s = 0{\cdot}02$, the lift development with incidence is smooth and regular over the complete span up to an incidence of $\alpha \simeq 13$ degrees, which is well above the design incidence; in particular $C_{L_{\max}}$ values of around 0·9, or higher, are attained over the outboard 60 per cent of the span. It is thus apparent that the effect of the root separation on the lift is felt mainly, not in the region of the root as might be expected, but much further outboard.

Although the separation on a swept wing is a highly three-dimensional phenomenon, there is a natural tendency to assume that there will be a loss of lift at the spanwise station where the separation occurs.

But where leading-edge vortices are created by the separation, lift increments will appear as have been seen on this wing, inboard of 30 per cent semi span. However these results show that the separation can also cause a premature loss of lift further outboard where the flow is mainly attached. This demonstration of large spanwise interdependence underlines the difficulties associated with any attempt to create an analytical framework within which stall behaviour can be considered in the design stage.

Figures 30 and 31, which contain the results obtained from the tests at the two lower Reynolds numbers with the wire-on, not only enable us to see the trends with increase in Reynolds number when studied in combination with Fig. 29, but also contain additional information about the development of the flow as the stall is penetrated up to 18 degrees. In particular, the lift still continues to rise over the inboard 20 per cent with increasing incidence right up to $\alpha \simeq 18$ degrees and shows virtually no sign of approaching a maximum value. In contrast, over the outboard 30 per cent of the semi-span large losses of lift occur very rapidly after the local $C_{L_{\max}}$ is reached, the resulting low values of lift varying very little with further increase of incidence. This loss of lift coefficient outboard, coupled with the decreasing chord towards the tip and the rising lift inboard, adequately explain the high values of nose-up pitching moment that appear in Fig. 15 as the stall is penetrated.

However the most striking feature of these two figures is the behaviour of the sectional lift coefficient in the region from 30 to 50 per cent semi span just immediately post-stall. Here a rapid non-linear increase in lift is observed that is higher even than that occurring far inboard; this is followed soon after by a maximum and then a drop in lift. This behaviour invites comparison with the behaviour of slender wings with rounded leading edges as exemplified by the results given in Fig. 27, and is almost certainly associated with the development of the leading-edge vortex shown in the flow pattern for $\alpha = 12$ degrees in Fig. 22.

Having dealt briefly with the variation of lift coefficient both spanwise and with changes of incidence just prior to, through, and well past the stall, let us now turn our attention to the lift and pitching moment development at incidences where the flow may be thought of as being entirely attached. Dealing first with the lift and primarily with Fig. 29, at first sight it would appear that the design aim of a constant spanwise distribution of C_{L_L} has been achieved, within what might be termed 'engineering accuracy' bearing in mind the scale of deviations likely to be introduced by boundary layer effects. Now if this were true it would imply (a) that the chordwise downwash equation[1,2,4] is sufficiently accurate to account correctly for the overall effects of twist and camber, and (b) that the spanwise variations in the lift curve slope are well-enough predicted to enable a planform to be designed accurately to produce a given spanwise loading.

If now the spanwise distributions of C_{L_L} at constant incidence on Fig. 29 are looked at again in terms of (a) and (b) above, it becomes clear that two areas need some further investigation—(i) the spanwise variation in zero lift angle, which is directly related to (a) above, and (ii) the increase in C_{L_L} as the tip is approached from somewhere between $y/s = 0{\cdot}60$ and $0{\cdot}70$. This effect is directly related to (b) above.

Unfortunately, although the spanwise variation in zero lift angle shown in Fig. 29 would have been of significant interest had it been genuine, it is not at all clear that this is the case, since the variation shown is of the same order, and of approximately the same shape, as the variations in the pitch angle of the tunnel stream[21] measured somewhat later, and shown in Fig. 36.

In essence, of course, the appearance of such large non-uniformities in the flow must raise some doubts about the accuracy of the interrelation between the results presented in this Report and the geometry of the wing on which they were obtained, particularly in view of the difficulties experienced in achieving agreement between the positive and negative incidence tests of the basic aerofoil section[12], where the variation in flow direction across the tunnel appeared to be appreciably smaller than is the case for these tests. In spite of this, since we are mainly concerned with the behaviour at high incidence where small variations in flow direction are of less importance, it was not felt that any significant improvement in understanding would accrue through repeating the tests in an improved airflow, bearing in mind the general accuracy obtainable in a pressure plotting exercise of this type. It is worth pointing out that the mean pitch angle over the span of this wing was subsequently determined using an unswept wing and all the forces, moments, and incidences presented in this Report have been corrected by this angle ($\Delta\alpha \simeq 0{\cdot}57$ degrees). In contrast, it is unlikely that the rise in lift coefficient towards the tip is a spurious effect due to variations in the direction of the tunnel flow, since the magnitude of the rise increases with incidence (i.e. $\partial C_{L_L}/\partial\alpha$ increases towards the tip) which could only happen if the flow pitch angle varied significantly with height, this being picked up by the tip as incidence is increased; the results shown on Fig. 36 do not suggest that this is likely. Assuming then, that it is a genuine result there would appear to be three possible causes:

(a) differences between the actual downwash and the theoretical value arising from the presence of the tip vortex,

(b) boundary layer effect, and

(c) the R.A.E. Standard Method under-estimates the lift curve slope in the region of the tip.

Of these three, the last would seem to be the least likely since this would imply that the effect of the tip in raising $\partial C_{L_L}/\partial\alpha$ just inboard, is greater than if the wing were continued outboard of the tip with a swept forward panel (*see* Section 2) and this seems, on physical arguments, to be incorrect.

Although the effect of the boundary layer must always be to reduce the lift curve slope below the value in inviscid flow, the results shown on Fig. 29 could be interpreted as suggesting merely that the reduction in slope due to the boundary layer outboard is less than in the mid-semi span region. This could occur if the crossflow within the boundary layer increased as the tip was approached, thus reducing the effective displacement thickness[24]. However the results of Brebner and Wyatt[25] suggest that the converse is more likely to be true. Other suppositions could be made of how the boundary layer might cause this effect but none seem very convincing, and therefore it seems most likely that the explanation lies with the wing tip vortices.

Although the previous work on the effects of wing tip vortices[2,22,23,26] has been concerned mostly with wings of lowish aspect ratio ($A < 3$) having either finite tip chords or streamwise tips, so that there are no strictly comparable situations, nevertheless such results show that the effects of the tip vortices are similar to those obtained by adding end plates to the wing tips, and lead to an increase in C_{L_L} towards the tips and a slight decrease inboard. Furthermore there can be little doubt that the slope changes and the high values of $C_{L_{L_{\max}}}$ shown at the 98 per cent station on Figs. 29–31 are associated almost entirely with the presence of the tip vortex, which can be seen clearly in Fig. 22, $\alpha = 10{\cdot}90$ degrees, and is also discernible in Fig. 19, $\alpha = 9{\cdot}20$ degrees, Fig. 20, $\alpha = 6{\cdot}50$ degrees, Fig. 21, $\alpha = 10{\cdot}20$ degrees, Fig. 23, $\alpha = 7{\cdot}20$ and 8·70 degrees. Therefore, despite the closely elliptical shape of the planform outboard of 30 per cent semi span, it seems likely that a vortex of appreciable strength is shed from the leading edge near the tip. The effect of this vortex can be seen on the spanwise C_{L_L} distribution as far inboard as 70 per cent semi span, but the main effects are concentrated in the outer 10 per cent. The phrase 'tip vortex effect' should be taken to include the total rolling-up process and the resulting non-planar nature of the shed vorticity pattern. If the effects that have been discussed are truly ascribable solely to tip vortex effect then this suggests that much larger effects will be found on the span loading of an aircraft in a landing configuration where there are large discontinuities in the spanwise distribution of flaps and slats.

5.4. Sectional Pitching Moment Coefficients

Figures 32–35 show the variation of the local sectional pitching moment coefficients about the mid-chord point with incidence and spanwise position. The mid-chord point was selected, partially because the line through these points is the only straight line on the planform and so these plots can be simply used to deduce the overall pitching moment, but also because it is difficult to think of a totally suitable alternative. Viewing the results for each section in isolation, it would be natural to plot the pitching moments about the local aerodynamic centre; however this poses problems when plotting a spanwise carpet since the local aerodynamic centre varies across the span. Plotting about the quarter-chord point poses difficulties in presentation since near mid-semi span the carpet collapses into a series of nearly coincident horizontal lines.

In the wire-off case (Fig. 32) at low incidence there is a smooth variation of pitching moment in the spanwise direction increasing rapidly towards the root, as would be expected because of the increasing negative camber in that region. As incidence increases towards $\alpha = 6$ degrees the amount of spanwise variation decreases owing to the spanwise variation in $\partial C_{M_L}/\partial\alpha$, again as would be expected from the theory. Above 6 degrees significant changes take place in the development with incidence, particularly at the 8 and 10 per cent stations, although the development at 40 and 50 per cent does not appear to be affected until α is around 10 to 11 degrees. Above this incidence (which corresponds roughly to that for $C_{L_{L_{max}}}$ on the 40 and 50 per cent stations) the pitching moment continues to rise inboard but falls sharply in the mid-semi span region, suggesting that the suction peaks near the leading edges are maintained inboard, but collapse outboard.

When we come to the three wire-on cases, Figs. 33–35, we see again at low incidence the same spanwise variation of pitching moment towards the root, but the variation over the outboard half of the semi span can be seen to be rather irregular. There is also a small pitching moment at $\alpha = 0$ degrees at the mid-semi span station where the aerofoil section is symmetrical. The reason for this behaviour again arises from the spanwise variation of the tunnel flow direction which has been noted previously. Figure 37 shows a comparison between the measured and theoretical variation of C_{M_0} across the span, and it will be seen that, once allowance is made for the lift occurring outboard at $\alpha = 0$ degrees, reasonable agreement is obtained, and in particular the apparent occurrence of a C_{M_0} value at the 50 per cent station is explained. However the discrepancies between theory and experiment between the 7 and 20 per cent stations, and again between the 40 and 60 per cent stations, are worthy of comment; in both cases these differences could be interpreted in terms of the spanwise interpolation function λ, and some preliminary analysis of the sectional behaviour across the span, suggests that the effective shape of the λ curve on this wing is significantly different from the published one[1,2]. But it is not clear at the present time whether these differences arise as a fundamental difference between the potential flow over this wing and that over the wings from which the λ curve was derived, or whether they arise as boundary-layer effects, or even as a maldefinition of the camber line due to the way the thickness has been added.

Returning again to the basic pitching moment data, Fig. 33 shows that by the time the design lift coefficient has been attained ($\alpha \simeq 11{\cdot}4$ degrees) almost all the initial spanwise variation of pitching moment has disappeared and the spanwise variation of the chordwise pressure distribution would appear to be quite small. At the lower Reynolds numbers of Figs. 34 and 35 the spanwise variations of pitching moment at the higher incidences are rather larger than in Fig. 33, and, in comparison with the rest of the wing, there is quite a marked increase in positive pitching moment over the inboard 4 per cent as the Reynolds number is reduced. Once the stall begins, the pitching moment over the outboard section falls sharply, indicating a loss of leading-edge suction and a more even distribution of loading across the chord. However, close inboard the pitching moment continues to increase with incidence, suggesting that the leading-edge suction and the general form of the pressure distribution are being maintained.

Having carried out the chordwise integrations to evaluate C_{L_L} and C_{M_L}, it is a useful check upon the accuracy of the experiment to complete the task and integrate these values spanwise to yield overall coefficients which can be compared with the balance measurements of overall forces. The results of this final step for the three wire-on cases are shown in Figs. 38 and 39. These comparisons initially caused a little concern, since it is relatively easy to account for a situation in which the overall lift is greater than the integrated lift, in terms of lack of adequate definition of the pressure distribution, but a difference in the opposite sense is much harder to explain. Having searched diligently through the raw data, the only reasonable explanation that could be found was that the flow development on the two wings was not identical. On the basis of Fig. 36 alone this must be a plausible possibility, but Fig. 40 provides additional evidence, from which it would appear that the starboard wing stalls earlier than the port wing, but that pre-stall it carries more lift, just as would be expected from Fig. 38. Table 1 shows that only a limited number of pressure points were available on the port wing so that the integrated value of normal force in any one case was not very accurate; as against this, pressure readings at the 60 per cent station on the port wing were taken on nearly all runs, so that it was possible to deduce the values given in Fig. 40 for the port wing as the average over a large number of readings. It is thus expected that the final plotted values have an accuracy comparable to that obtained for the starboard wing values.

5.5. Overall Pressure Distributions

The overall pressure distributions in the two forms previously described (*see* Section 5.1) are shown in Figs. 41–66, and are so arranged as to give a ready comparison between the results from the four sets of test conditions at fixed incidences.

As we have already seen, the flow is orderly in all four cases at low incidence, so that only the data from $R_{\bar{c}} = 1{\cdot}78 \times 10^6$ with the wire-on are presented for incidences less than 4 degrees. Figure 41 shows the isobar pattern for $C_L = 0{\cdot}2$, and Fig. 42 shows the pressure distribution in the leading-edge region for $C_L = 0$ and $C_L = 0{\cdot}2$. As would be expected, the negative camber near the root generates suction peaks of appreciable magnitude even at zero lift, whilst the positive camber in the tip region displaces the isobars rearwards, but hardly reduces the level of the maximum suction. It is worth noting that the peak suctions near the root, over the incidence interval shown in Fig. 42, develop much more rapidly than those in the mid-semi span area, $\Delta C_p \simeq -1{\cdot}0$ at $y/s = 0{\cdot}02$ compared with $\Delta C_p \simeq -0{\cdot}35$ at $y/s = 0{\cdot}50$.

Figures 43 and 44 compare the pressure distributions with and without the wire at $\alpha = 5{\cdot}47$ degrees, $C_L \simeq 0{\cdot}40$. Whilst the isobar patterns show virtually no effect of the wire, Fig. 44 shows, even at this low incidence, fairly appreciable losses of peak suction inboard of the 4 per cent station in the absence of the wire, although stations outboard of this appear unaffected. The peak suctions near the root continue to develop more rapidly than in the mid-semi span region, $\Delta C_p \simeq -1{\cdot}10$ at $y/s = 0{\cdot}02$ compared with $\Delta C_p \simeq -0{\cdot}75$ at $y/s = 0{\cdot}50$ over the incidence interval 2·67 to 5·47 degrees.

Further increase of incidence to $\alpha = 8{\cdot}33$ degrees ($C_L \simeq 0{\cdot}60$) leads to the effects shown in Figs. 45 and 46, where it can be seen that fairly considerable losses of peak suction level and re-distribution of pressure occur in the wire-off case inboard of the 15 per cent station, the region outboard still appearing to be little affected although the local lift coefficient does not recover to the value achieved in the wire-on case until $y/s = 0{\cdot}50$. In the wire-on case we note that the peak suctions near the root continue to develop more rapidly than in the mid-semi span area, $\Delta C_p \simeq -1{\cdot}30$ at $y/s = 0{\cdot}02$ compared with $\Delta C_p \simeq -1{\cdot}10$ at $y/s = 0{\cdot}50$ in the incidence interval between 5·47 and 8·33 degrees.

Figures 47–50 show the pressure distributions for all four cases at $\alpha = 9{\cdot}77$ degrees which corresponds to $C_L = 0{\cdot}70$ for the wire-on case at $R_{\bar{c}} = 1{\cdot}78 \times 10^6$. Further deterioration in the flow conditions near the root can be seen in the wire-off case, the effect on the shape of the pressure distribution now extending out to the 30 per cent station and the lift of outboard stations is reduced below the wire-on case (Figs. 28–29). From the wire-on case it can be seen that the development of the peak suctions in the mid-semi span region now more closely matches the development near the root, $\Delta C_p \simeq -0{\cdot}75$ at $y/s = 0{\cdot}02$ and $\Delta C_p \simeq -0{\cdot}70$ at $y/s = 0{\cdot}50$ between $\alpha = 8{\cdot}33$ and 9·77 degrees; clearly though the differences between the levels of the peak suctions in the two regions have now become very large and the levels in the root region are such that it is scarcely surprising that the flow breakdown originates there. The comparison down the Reynolds number range afforded by Figs. 47, 49, 48a and 50a shows little difference in the root region between $R_{\bar{c}} = 1{\cdot}78 \times 10^6$ and $1{\cdot}02 \times 10^6$, but when the Reynolds number is further reduced to $0{\cdot}51 \times 10^6$ it would appear that the type of flow breakdown near the root observed at lower incidences in the wire-off case, is now becoming imminent in this case as well. It can also be seen that the peak suction levels over most of the span are measurably affected by reduction in the Reynolds number and, moreover, the laminar separation bubbles (which can be seen on the flow visualization pictures Figs. 19–26) provide a progressively larger perturbation on the measured pressure distribution.

In the wire-on case at $R_{\bar{c}} = 1{\cdot}78 \times 10^6$ the wing attains its design C_L at $\alpha = 11{\cdot}33$ degrees and the results for this incidence in all four cases are shown in Figs. 51–54. Looking first at the wire-on case at $R_{\bar{c}} = 1{\cdot}78 \times 10^6$, it can be seen that the design aim of achieving identical chordwise pressure distributions at all spanwise stations has been broadly achieved, apart from a region close to the leading edge on the inboard 20 per cent of the wing where high suction peaks are produced, and in a region comprising the outboard 10 per cent of the semi span in which the isobars sweep rapidly rearwards appearing to follow the leading edge of the planform, an effect which is probably produced by the wing tip vortex as discussed previously. The development of the peak suctions at the root and mid-semi span is still comparable, the ΔC_p in both cases being approximately $-0{\cdot}80$ between $\alpha = 9{\cdot}77$ and 11·33 degrees. The wire-off case at this incidence shows considerable flow separation inboard, and the pressure distributions on the outboard stations are noticeably affected, presumably due to the effect of the thickened boundary layer sweeping outboard, but this will be discussed further in Section 6.

The comparison down the Reynolds number range at $\alpha = 11{\cdot}33$ degrees again shows little difference between $R_{\bar{c}} = 1{\cdot}78 \times 10^6$ and $1{\cdot}02 \times 10^6$ except a general lowering of peak suction levels and a significant lengthening of the laminar separation bubbles on the outer 10 per cent of the semi span at the lower Reynolds number. However at $R_{\bar{c}} = 0{\cdot}51 \times 10^6$ a radical change has clearly overtaken the pressure distribution, the isobars in Fig. 51b suggesting the presence of a weak vortex originating in the region of 6 to 8 per cent semi span and passing over the trailing edge in the vicinity of the 70 per cent station. The pressure distribution in the forward part of the wing (Fig. 53b) still suggests a considerable chordwise extent of attached flow as might be expected from the flow visualization picture obtained at $\alpha = 10{\cdot}90$ degrees (Fig. 22).

At $\alpha = 12{\cdot}30$ degrees, the wire-on case at $R_{\bar{c}} = 1{\cdot}78 \times 10^6$ achieves a $C_L = 0{\cdot}85$ and the results at this incidence are given in Figs. 55–58. The isobars in Fig. 56 and the forward parts of the chordwise pressure distribution in Fig. 58 for the wire-on case at $R_{\bar{c}} = 1{\cdot}78 \times 10^6$ both show the beginnings of a flow separation in the root region; it will also be seen that the expected development of the pressure distribution above the design C_L which was outlined in Section 3.4, is not occurring. Instead of the peak suctions in the tip region rising more rapidly than elsewhere, there is a distinct decrease of peak suction levels in the outboard direction which reverses the trend which can be seen at the previous incidence $\alpha = 11{\cdot}33$ degrees. Furthermore there is no observable tendency for the isobar sweep to reduce in the tip region, all except the rearmost two isobars appearing to be dominated by the leading-edge shaping. It is difficult to know if the behaviour of the two most aft isobars on both this and the $R_{\bar{c}} = 1{\cdot}02 \times 10^6$ case indicates simply a boundary-layer separation near the trailing edge, or whether it is due to the increasing development of the tip vortex. Even the similar, but more marked, behaviour of these isobars at $\alpha = 13{\cdot}56$ degrees in Fig. 60a does not clarify the situation.

There is now scarcely any point in comparing the wire-on and wire-off cases as the flow regimes in the two cases are so dissimilar. Whereas the flow in the wire-on case is still primarily attached, the isobars in the wire-off case show a pattern which is strongly suggestive of a vortex springing from the apex, lying over the inner part of the wing, and passing over the trailing edge at about 35 per cent semi span. Outboard of this a more normal type of attached flow pressure distribution seems to be trying to re-establish itself, but the local C_{L_L} achieved and the general level of suctions over the upper surface are those appropriate to a much lower incidence than that at which this section must be operating, since the influence of the vortex will be to induce an upwash at this spanwise station, and thus to increase the effective incidence. It therefore appears likely that the boundary-layer displacement thickness over the stations outboard of the vortex has been unduly thickened by the addition of boundary-layer air from further inboard, which has been swept outboard by the crossflow component of the vortex.

When comparing down the Reynolds number range it is again apparent that there are no very striking differences between $R_{\bar{c}} = 1{\cdot}78 \times 10^6$ and $1{\cdot}02 \times 10^6$. Nevertheless the peak suction levels near the root are slightly higher at $R_{\bar{c}} = 1{\cdot}02 \times 10^6$ but they are lower by as much as $\Delta C_p = 0{\cdot}50$ out near the tip, so that the spanwise gradient of peak suction is rather steeper at the lower value of Reynolds number. The only other difference of note is the greater spanwise extent, at the lower Reynolds number, over which the $C_p = -0{\cdot}25$ isobar is displaced towards the trailing edge and this has already been discussed.

At $R_{\bar{c}} = 0{\cdot}51 \times 10^6$ (Fig. 57) the somewhat weak type of vortex flow apparent at the previous incidence has now strengthened, and the attached flow region which existed near the leading edge in the outboard half of the semispan has now given way to a completely detached flow with a substantially flat chordwise pressure distribution from near the leading edge. This isobar pattern is consistent with the evidence offered by the flow visualization pictures of Fig. 22, in that, between $\alpha = 11{\cdot}30$ and $12{\cdot}30$ degrees, the origin of the vortex moves out to close to the end of the wire and at the same time the sweep of the vortex increases, so that the point at which it crosses the trailing edge moves inboard slightly.

At $\alpha = 13{\cdot}56$ degrees, the wire-on case at $R_{\bar{c}} = 1{\cdot}78 \times 10^6$ achieves $C_L = 0{\cdot}90$ and the results at this incidence are shown in Figs. 59–62. The isobars in Fig. 60a and the forward parts of the pressure distribution in Fig. 62a show that, at this incidence, a stall is beginning to develop even with the wire-on at the highest Reynolds number. This initial stall development appears to be different from any of the other conditions and seems to consist of two separate breakdown areas,

(i) the inboard breakdown out to the 20 per cent station which seems qualitatively similar to that which has already been observed at lower incidences in other conditions, and particularly to the wire-off case at $\alpha = 8{\cdot}33$ degrees shown in Fig. 46b,

(ii) a further breakdown in the 30 to 40 per cent region leaving substantially attached flow conditions further outboard.

In addition there is a region outboard of 85 per cent in which the smaller-valued isobars are displaced strongly rearwards, the possible significance of which has already been discussed. Taken overall, these pressure measurements present a picture of an extremely complex process of flow breakdown which it is difficult to clarify further, in the absence of any flow visualization and any measurements of its further development.

However it is possible that (i) above, together with the differences between the flow breakdown over the outer wing at this and the two lower Reynolds numbers, indicate that we again have a situation in which the angle of incidence where sizeable flow separations occur inboard is lower than that at which sections out near mid-semi span would stall naturally, so that, just as in the wire-off case, the maximum lift capability of the wing is primarily determined by the inboard flow conditions. Clearly deductions of this type must be tentative where the results indicate such a complex flow; furthermore there must remain some doubt about the results at some of the spanwise stations (for example 30 and 40 per cent) since the balance measurements made simultaneously do record some scatter in the maximum lift values and it may well be that, for this incidence only, the pressure results do not all relate to the same flow condition. It may be noticed that results have not been included for the 80 per cent station since there was clear evidence that these results were untypical. In certain other cases too, results have been omitted for similar reasons, in all other situations all the data have been retained.

At $\alpha = 13{\cdot}56$ degrees the wire-off case (Figs. 60b and 62b) shows a strongly developed vortex flow inboard of 40 per cent semi span, whilst outboard of this exists, as before, a chordwise pressure distribution which, in two-dimensional flow, would suggest a substantial extent of separated flow towards the trailing edge. At this incidence (and at $\alpha = 12{\cdot}3$ degrees also) the initial path of the vortex is straight, so that the flow approximates to a conical form over this region, but subsequently the vortex turns fairly sharply and becomes much more closely aligned with the free stream direction. This behaviour, and, indeed, the whole flow configuration inboard of 40 per cent, is quite similar to that measured by Jaszlics and Trilling[27] near the root of a 45 degree swept sharp edged plate of high aspect ratio at 15 degrees incidence. Outboard of this root region, in their case, the flow was exactly as would be expected over an infinite swept sharp edge plate—the flow separating at the sharp edge to give a constant pressure over the whole of the upper surface, with a purely spanwise flow direction near the surface underneath the separated shear layer. We shall develop this theme further later, but this evidence plus the extremely sharp suction peaks measured in the wire-on cases in this root region, already indicate that the inboard flow separation on this wing in the absence of the wire, may be thought of as a swept version of the classical two-dimensional thin-aerofoil stall pattern[7].

At $R_{\bar{c}} = 1{\cdot}02 \times 10^6$ (Fig. 59a) the flow has developed a fairly weak vortex type pattern with some attached flow existing outboard near the leading edge, in a similar manner to that shown for $\alpha = 11{\cdot}33$ degrees at $R_{\bar{c}} = 0{\cdot}51 \times 10^6$ in Fig. 51b, although in this case the vortex appears to be rather stronger and crosses the trailing edge further inboard.

At $R_{\bar{c}} = 0{\cdot}51 \times 10^6$ (Fig. 59b) the vortex flow originating at the outer end of the wire ($y/s = 0{\cdot}10$) which was present at $\alpha = 12{\cdot}30$ degrees, has further strengthened and the sweep has increased so that it crosses the trailing edge further inboard, leaving an approximately constant pressure region outboard of 80 per cent semi span.

The pressure measurements made well into the post-stall regime at the two lower Reynolds numbers are shown in Figs. 63–66, Figs. 63–64 showing the results at $\alpha = 15$ degrees, and Figs. 65–66 showing the results at $\alpha = 17$ degrees. Both sets of results show that the very high peak suctions in close proximity to the root ($y/s < 0{\cdot}03$) are maintained even this far after the initial stall, but that further outboard the peak suction levels reduce with increasing incidence. The isobar patterns at $\alpha = 15$ degrees, Fig. 63a and b, are almost identical and show a tidy flow pattern which is essentially similar to those already shown for lower incidences at $R_{\bar{c}} = 0{\cdot}51 \times 10^6$. In comparison with these results it will be seen that the suction levels induced by the vortex have not changed measurably but the path of the vortex has become more highly swept, so that, although it still originates close to the end of the wire at the 10 per cent station, it now crosses the trailing edge further inboard.

In contrast the results obtained at $\alpha = 17$ degrees (Figs. 65 and 66) do not present anything like such an orderly pattern and, in particular, the isobars no longer run parallel and close together along the inboard edge of the vortex, but are much more widely spaced. The flow visualization pictures do not give much assistance in explaining this development. Rather do they tend to confuse the issue, since the last picture on Fig. 22 shows the main vortex apparently springing from the apex and not, as appears from the isobar pattern, from the end of the wire. In this situation any attempted explanations must be tentative; we will present below three possible explanations which seem to fit the available facts:

(a) A second vortex has begun to be shed from the apex (as suggested by the flow visualization) and, because it soon ceases to be fed by a vortex sheet from the leading edge, it is drawn into the main vortex flow originating near the 10 per cent station.

(b) Vortex breakdown is occurring. This might account for the sudden appearance of the violent pitching oscillation which was encountered at high incidence at $R_{\bar{c}} = 1{\cdot}78 \times 10^6$ and referred to early in Section 4. Unfortunately no measurements of vortex breakdown are available for sweep back angles of 35 degrees, but extrapolation of results obtained at higher sweep angles suggests that, for a plane sharp edged wing, vortex breakdown would occur in the range 2 degrees $< \alpha <$ 8 degrees. If, in our case, we identify the above incidence being measured from the incidence at which the vortex first formed, as has been done for other round edged wings, then $\alpha = 17$ degrees is equivalent to some 5 degrees incidence on a plane sharp edged wing, which is clearly within the expected range.

(c) The vortex height above the wing is increasing rapidly enough with incidence for the pressure gradients induced on the wing to be reduced. This is not a very attractive explanation since on a slender wing the vortex position is a smooth function (almost linear) of incidence and no such tendency has been noted at lower incidences.

5.6. Chordwise Pressure Distributions at Particular Spanwise Stations

The development of the pressure distribution over the complete upper surface of the wing at particular incidences has already been shown, but it is also of interest to study the development of the chordwise pressure distribution at particular stations with increasing incidence, in a little more detail. Accordingly the results at the 3, 40 and 85 per cent stations are presented in Figs. 67–80 inclusive. Beginning with the wire-on condition at $R_{\bar{c}} = 1{\cdot}78 \times 10^6$, Fig. 68 shows the development of the chordwise pressure distribution with incidence at the 3 per cent station; at low incidence can be seen the typical chordwise pressure distribution on a negatively cambered aerofoil near zero lift—a suction peak on the upper surface near the leading edge giving positive lift on the forward part of the aerofoil, followed by a rapid decrease in suction on the upper surface and a rapid rise of suction on the lower surface producing a small negative lift over a substantial part of the rear of the chord. The rapid rise of the peak suction with increasing incidence at this spanwise station, and the extremely high adverse pressure gradients on the rear edge of the very narrow suction peak are all very evident. Just beyond $\alpha = 12$ degrees, the local separated region near the leading edge begins to perturb the chordwise pressure distribution; this perturbation grows with increasing incidence and is associated with a progressive decrease in the level of the peak suction. The same pressure data are shown plotted against z/c in Fig. 67 and here the small size of the suction loop should be noted, this being associated with the large drag increment which is known to exist towards the root of a swept wing, and which is balanced, in potential flow, by a thrust increment near the tip^2.

Figure 70 shows the development of the chordwise loading with incidence at the 40 per cent station; here, the camber is very small and the pressure distributions on the upper and lower surfaces at zero lift are almost identical. With increasing incidence the peak suction level increases more slowly than in the previous case and the suction peak is wider; the peak suction continues to rise until $\alpha \simeq 13$ degrees and with further increase of incidence the suction peak then collapses, much more dramatically than at the 3 per cent station. Figure 69 shows the pressure data at this station plotted against z/c and the increase in size of the suction loops in comparison with Fig. 67 will be obvious.

Figures 71 and 72 show the corresponding results for the 85 per cent station. In this case, because the section has positive camber, a small region of negative lift can be seen near the leading edge at the lowest incidence, and this is counterbalanced by a smaller level of positive lift existing over the remainder of the chord. The rate of increase of the peak suction is the lowest of the three cases at intermediate incidences, but shows evidence of increasing much more rapidly past the design incidence, as would be expected. The suction peaks are wider than at either of the two previous stations and the perturbation provided by the laminar separation bubble is much larger. The post-stall collapse of the suction peak does not start until $\alpha \simeq 13{\cdot}5$ degrees and, unlike conditions at the 40 per cent station, is relatively mild. When these pressure-data are plotted against z/c (Fig. 71) a very large increase in the suction loop and a decrease in the pressure loop are found, demonstrating the counterbalancing thrust force mentioned above.

The chordwise pressure distributions in the wire-off case at $R_{\bar{c}} = 1{\cdot}78 \times 10^6$ are shown in Figs. 73 and 74. At the 3 per cent station (Fig. 73) the development with incidence is very similar to the wire-on case up to around $\alpha = 5$ degrees, but for a few degrees after this the peak suction level drops and the suction peak becomes wider. Above about $\alpha = 9$ degrees the peak suction level begins to rise again and a secondary suction peak is formed just in front of an extremely high adverse pressure gradient. This secondary suction peak ultimately becomes higher than the primary one, suggesting strongly the existence of a vortex. The behaviour below $\alpha \simeq 9$ degrees is essentially similar to that observed on a two-dimensional aerofoil in the initial phases of a thin aerofoil stall, and thus tends to support our initial assumption that the separation near the root can be thought of in terms of a 'long bubble'.

At the 40 per cent station (Fig. 74) the chordwise pressure distributions are very similar in shape to those in the wire-on case and the local stall still occurs in the region of $\alpha = 13$ degrees. However the general rate of increase in the upper surface suctions beyond $\alpha = 7$ degrees is much reduced in comparison to the wire-on case. This behaviour, of course, has already been noted when discussing the variation of the overall pressure distribution, but this figure does show the effect very clearly.

The results at $R_{\bar{c}} = 1{\cdot}02 \times 10^6$ and $R_{\bar{c}} = 0{\cdot}51 \times 10^6$ at the 3 per cent station are shown in Figs. 75 and 76, and these, in comparison with Fig. 68, show the response of the pressure distribution at this station to changes in Reynolds number. The most interesting feature shown by these three figures is the apparent adverse effect on the local stalling incidence of increasing the Reynolds number above $1{\cdot}02 \times 10^6$. On Fig. 76 at $R_{\bar{c}} = 0{\cdot}51 \times 10^6$ the initial flow breakdown occurs around $\alpha = 10{\cdot}6$ degrees; by the time the Reynolds number has risen to $1{\cdot}02 \times 10^6$ on Fig. 75, this breakdown is delayed until around $\alpha = 13{\cdot}8$ degrees; further increase of Reynolds number to $R_{\bar{c}} = 1{\cdot}78 \times 10^6$ (Fig. 68) results in the incidence at which breakdown occurs, falling to around $\alpha = 12$ degrees. However this adverse effect is found only in terms of the incidence at which flow breakdown occurs; at a fixed incidence below the breakdown value, the Reynolds number effect on both the peak suction levels and the local lift coefficient C_{L_L} is still favourable. In fact, despite the difference between the incidence values at which breakdown occurs at $R_{\bar{c}} = 1{\cdot}02 \times 10^6$ and $R_{\bar{c}} = 1{\cdot}78 \times 10^6$, the C_{L_L} in each case is close to 0·92. It is thus possible that the apparent adverse effect on incidence is primarily a function of the increased lift curve slope at the higher Reynolds number. However other possible causes (e.g. the increased Mach number or the possibility of the wire diameter being too large at $R_{\bar{c}} = 1{\cdot}78 \times 10^6$) should, perhaps, be borne in mind. Lastly on Fig. 76 there is a check in the rise of the peak suction just after $\alpha = 6$ degrees which is similar to that in the wire-off case.

The comparison of stall pattern at the 40 per cent station provided by Figs. 70, 77 and 78 shows clear evidence of changes within this Reynolds number range. If we think in terms of the four two-dimensional stall patterns[7], then, at the two lower Reynolds numbers, the post-stall pressure distributions suggest a leading-edge stall pattern, with only a slight tendency for there to be a lack of pressure recovery towards the trailing edge just prior to the flow breakdown. However the suction level of the plateau on all the post-stall distributions except at $\alpha = 17{\cdot}8$ degrees is much higher than would be experienced under two-dimensional conditions, so much so that after the flow breakdown, the local lift force rises as shown in Figs. 30 and 31. From this evidence we may begin to suspect that, even if we can establish a strong connection between the pre-stall behaviour of the section in two-dimensional flow and on a swept wing, it is unlikely that there will be any connection between the post-stall behaviours. Even in the highest Reynolds number case where there is evidence of a trailing-edge stall pattern the post-stall pressure distributions shown in Fig. 70 are quite unlike anything observed in two-dimensional flow.

In contrast, when we come to inspect the results down the Reynolds number range at the 85 per cent station, the similarity of the post-stall pressure distributions to those found in two-dimensional flow is quite striking. In Fig. 80, at $R_{\bar{c}} = 0{\cdot}51 \times 10^6$, the pressure distribution just before the stall shows a large short bubble and a good trailing-edge pressure recovery; post-stall, the upper surface pressure distribution is almost constant and has a suction level very similar to that which would be achieved under two-dimensional conditions—in short, a classical demonstration of a leading-edge stall pattern. Moving up to $R_{\bar{c}} = 1{\cdot}02 \times 10^6$ in Fig. 79, we see the classical shortening of the short bubble with increasing incidence, the beginnings of a trailing-edge separation shown by a lack of pressure recovery towards the trailing edge on the $\alpha = 12{\cdot}85$ degrees distribution, to be followed again by a complete collapse of the upper surface suction peak down to a low level, just as would be seen in a two-dimensional mixed leading-edge/trailing-edge stall[7]. At $R_{\bar{c}} = 1{\cdot}78 \times 10^6$ on Fig. 72, the stalled region is not penetrated very deeply but the behaviour shown is just as would be found in a two-dimensional trailing-edge stall pattern, and once again the shrinking of the short bubble with increasing incidence, prior to the stall, can be seen.

6. Further Analysis of Sectional Stalling Behaviour

Starting from the linearised downwash equation for a lifting surface and associated trailing vortex sheet, and making the assumptions of high aspect ratio and zero sweep, it can be shown[11]

(a) that the downwash distribution due to the trailing vorticity is constant across the chord, thus leading to the concept of an induced angle of incidence, α_i, and

(b) that the shape of the chordwise loading is the same as in two-dimensional flow (i.e. determined solely by the bound vorticity), its magnitude being determined by the 'effective angle of incidence', α_e, where

$$\alpha_e = \alpha - \alpha_i \tag{1}$$

(α = geometric angle of incidence measured from zero lift).

When we come to consider finite swept wings, we first make the assumption that the spanwise distribution of α_i at the wing, for a given aspect ratio, depends only on the spanwise lift loading, independent of the sweep angle. Thus, as for wings of zero sweep,

$$\alpha_i = \frac{\omega}{U_0} = \frac{\omega}{8\pi}\frac{\bar{c}}{s}\int_{-1}^{+1} \frac{d(C_{L_L}c/\bar{c})/d(y/s)}{(y/s) - (y'/s)}\, d(y'/s) \tag{2}$$

(where ω = downwash factor due to Küchemann[2], which is a function of aspect ratio).

The shapes of the chordwise loadings and the local relationship between C_{L_L} and α_e, can then be determined purely in terms of the bound vorticity, as before, and lead to the variations across the span described in Section 2. According to these assumptions, provided the wing has an aspect ratio greater than 3 or 4, there will be a portion of the wing, disposed about mid-semi span, where the chordwise loading will be the same as that on an infinite sheared wing, once due allowance has been made for α_i. Furthermore, well known transformations[11] exist by which conditions on an infinite sheared wing may be related to those in two-dimensional flow. Our present wing has an aspect ratio of 7, and has been twisted and cambered so as to almost eliminate the root and tip effects near $C_{L_{\max}}$, so that, at high lift, the sheared wing region corresponds to that on an uncambered wing of very large aspect ratio; hence it is particularly suitable for making a comparison between the performance of sections near mid-semi span and the same section in two-dimensional flow.

In order to make this comparison the following transformations were applied to the swept wing data in order to present it in the same form as that in the two-dimensional test of the aerofoil[12],

$$\bar{\alpha} = (\alpha - \alpha_i - \alpha_0)\sec\phi \tag{3}$$

and

$$\overline{C_L} = (C_{N_L}\cos\bar{\alpha} - C_{T_L}\sin\bar{\alpha})\sec^2\phi, \tag{4}$$

where $\bar{}$ signifies a parameter converted to equivalent two-dimensional conditions.

α = geometric angle of incidence of the swept wing,

and α_0 = experimentally measured zero lift angle on a particular spanwise section.

The induced downwash α_i was calculated from the experimental C_{L_L} distributions (Figs. 29–31). The computer program which performed this calculation utilized a cubic spline procedure to estimate the first and second derivatives of the spanwise loading, and performed the integration of equation (2) numerically, after transformation to an angular variable, by the trapezoidal folding technique used by Grey-Wilson in the program for the R.A.E. Standard Method[28]. Some typical results are shown in Figs. 81–83. From these it can be seen that very large and rapid changes in the spanwise distribution of downwash occur through the stall at the two lower Reynolds numbers, primarily due to the large non-linear lift increments that occur around mid-semi span when the wing stalls. These lift increments lead to a spanwise load distribution which exhibits a pronounced peak in the region of 40 to 50 per cent semi span, so that the spanwise load gradients on either side are such as to generate a downwash in the region of the peak load, thus leading to the very high downwash values shown.

The calculated downwash figures were then used in conjunction with equations (4) and (3) and the basic integrated pressure values of C_{N_L} and C_{T_L}, to generate a set of quasi-two-dimensional results from the spanwise stations 40, 50, 60 and 70 per cent, at all three wire-on Reynolds numbers. These are compared with the behaviour of the basic aerofoil section in two-dimensional flow[12], in Figs. 84–86.

Figure 84 shows the results obtained from the swept wing at $R_{\bar{c}} = 1{\cdot}78 \times 10^6$ compared with the two-dimensional results at $R_{\bar{c}} = 1{\cdot}33 \times 10^6$ thus giving fairly close correspondence between the values of R_y (*see* Fig. 4) for the swept wing results and the Reynolds number of the two-dimensional test. It will be seen that although the lift curve slopes and the maximum C_L values derived from the swept wing results are slightly higher than those from the two-dimensional tests[12], nevertheless there is broad agreement between the two, notably prior to the stall but post-stall as well. In contrast, some of the results derived from the swept wing at $R_{\bar{c}} = 1{\cdot}02 \times 10^6$ and shown in Fig 85, are clearly farcical and bear no resemblance to any behaviour ever observed in two-dimensional flow. These results come from the stations on which large vortex-induced lift increments arise when the wing stalls; so far as the quasi-two-dimensional results are concerned these lift increments distort the spanwise loading in such a way that, according to linearized wing theory, large increases in induced downwash occur at those stations, thus substantially reducing the 'effective incidence'. The eventual outcome is then as shown on Fig. 85. Clearly in this post-stall flow configuration we have passed far beyond the range of applicability of the concepts and assumptions involved in linearized finite wing theory, so that although very high values of $C_{L_{max}}$ appear to be generated, these are not relevant to the performance of the section in attached flow. In our case this does not pose much of a difficulty, since it is reasonably clear at what value of C_L flow separation sets in, and it is this value which will be used in the ensuing discussion of $C_{L_{max}}$ values. So far as the attached flow part of the comparison shown in Fig. 85 is concerned, we again note that the swept wing results have a higher $C_{L_{max}}$ and lift curve slope than the corresponding two-dimensional results. Finally the results derived from the swept wing at $R_{\bar{c}} = 0{\cdot}51 \times 10^6$ are shown in Fig. 86 and compared with the two-dimensional results at $R_{\bar{c}} = 0{\cdot}55 \times 10^6$. Once again we have the bizarre post-stall behaviour at the 40 and 50 per cent stations and also a small amount of a similar nature at 60 per cent. In this case, two-dimensional results are not available down to a Reynolds number quite as low as the values of R_y, so direct comparison is not strictly possible. However the general level of the swept wing results suggests that, at this Reynolds number, they are more similar to the two-dimensional results than was the case on the two previous figures.

In order more readily to make comparison between the sectional $C_{L_{max}}$ values achieved on the swept wing and those achieved in two-dimensional flow, $C_{L_{max}}$ has been plotted against Reynolds number in Fig. 87. Ignoring the open symbols for the moment, the results obtained at $R_{\bar{c}} = 0{\cdot}51 \times 10^6$, where the stall patterns on the swept wing can be plausibly related to the leading-edge type, correlate well with the two-dimensional results. But the results from the other two Reynolds numbers, where the sectional stall patterns are tending to be more influenced by separation near the trailing edge, are all higher than the two-dimensional results. Where the stall is determined primarily by flow breakdown near the leading edge, it is likely on several counts (e.g. the independence principle in laminar boundary layers, the streamline paths around the leading edge, and the results obtained by Horton[31] in swept short bubbles) that R_y is the relevant Reynolds number. This concept is supported by the results. However when the stall is primarily determined by turbulent separation towards the trailing edge, the definition of the relevant Reynolds number is not at all clear, but, if one studies the path of the external flow streamlines between the attachment line and the trailing edge, it is not implausible to suggest that R_s might be a more representative value. Following this argument the sectional $C_{L_{\max}}$ values obtained on the swept wing have also been plotted against R_s on Fig. 87 as the open symbols, and this now provides good correlation with the two-dimensional results obtained at $R_{\bar{c}} = 1{\cdot}02 \times 10^6$, but the results obtained at $R_{\bar{c}} = 1{\cdot}78 \times 10^6$ now fall below the line, representing the two-dimensional behaviour. Whether or not these last values are too low because of the tendency for the stall at $R_{\bar{c}} = 1{\cdot}78 \times 10^6$ to be controlled by the conditions near the root, we leave as an open question.

Thus in general terms, reasonable correlation can be shown between the values of sectional $C_{L_{\max}}$ achieved in the mid-semi span region of this particular swept wing and those achieved on the same section in two-dimensional flow by making use of the accepted concepts of induced downwash and the flow over an infinite sheared wing. However this is contrary to results from some N.A.C.A. investigations[29,30] which were undertaken with very much the same end in view. These results showed that the sectional $C_{L_{\max}}$ values achieved on the swept wing were, in the main, substantially higher than the two-dimensional results would have suggested, although the level decreased outboard. In view of the large vortex induced lift increments observed on the present wing, and the possible improvement in correlation obtained by using R_s instead of R_y, the N.A.C.A. results have been re-assessed to see if they could be made to support the present results. For the sake of completeness, a short description of the experiment performed by N.A.C.A. and the way in which the results have been re-assessed is given in Appendix II. The re-assessed data converted to two-dimensional values using the mid-chord sweep of $\phi = 43{\cdot}4$ degrees, are shown in Fig. 88, and compared with the measured performance of the basic sections in two-dimensional flow. It will be seen that neither the re-assessment, nor the use of R_s as the correlating Reynolds number, have resulted in a degree of correlation between these data which is comparable to that shown in Fig. 87, and to this extent we are faced with a considerable dilemma in our interpretation of these two sets of results in combination.

On the one hand we have our own data, which has been obtained from a wing on which a high degree of uniformity in the spanwise distribution of pressure has been achieved, and which has been collected and analysed in considerable detail, but about which some doubt remains as to the efficacy of the wire in entirely suppressing the adverse effects of the root separation. On the other hand, there are the N.A.C.A. data in which there are no worries about the condition of the flow in the root of the wing but which have been obtained on wings where no attempt has been made to secure spanwise uniformity of pressure distribution, although two very different spanwise distributions of local C_{L_L} have been tested, and both have given similar results. On this basis it could be argued that the spanwise C_{L_L} distribution is not a dominant variable, although intuitively one would expect that changes in spanwise loading would produce measurable and consistent trends. Furthermore the N.A.C.A. data is much more sparse than our own and has been collected according to somewhat different concepts, so that it is impossible to analyse it in exactly the same way, although it would be somewhat surprising if either of these factors were large enough to account for the differences that have been shown. In short, we are faced with a situation which, at the present time, is difficult to interpret, and which is only likely to be resolved by the appearance of additional data.

Finally Figs. 89–92 show, in different ways, the extent to which the two-dimensional pressure distributions are repeated on sections in the sheared wing region. The first three figures (89–91) show a comparison between the variation of sectional pitching moment with local lift coefficient; it will be noted that the data for the 40 per cent station shows a small positive value of C_{M_0}, and that for the 60 per cent station shows a small negative C_{M_0} as would be expected from the camber which these sections have. Nevertheless, by the time the stalling C_L is being approached, the results for both these stations, and the 50 per cent station, are all showing closely similar values of C_M, which in turn are closely matched by the values from the two-dimensional tests, thus indicating close similarity between the chordwise pressure distributions. This is confirmed by the direct comparison of the pressure distributions shown in Fig. 92. Here the pressure distribution for a C_L about 0·2 below $C_{L_{max}}$ in two-dimensional flow has been converted to an equivalent chordwise pressure distribution on the swept wing by multiplying all C_p values by $\cos^2 \phi$, and is compared with the results obtained from the 50 per cent station at the same equivalent C_L. Clearly the agreement between the two is very good, apart from discrepancies which are noticeable in the region of the suction peak, the re-attachment point of the short bubble, and near the trailing edge on the upper surface. The differences near the attachment line of the main flow can be attributed to the difference between the mid-chord sweep and the local sweep at the leading edge, and this could be removed by applying rigorously the local sweep ideas implicit in the R.A.E. Standard Method.

7. Summary of the Stall Behaviour of the Wing

7.1. Introduction

Having presented the results of balance measurements, flow visualization, and pressure plotting in detail, it now seems worth while to draw all these together to give a summary description of the different stall processes on this wing. However, a large part of the description depends upon the interpretation that we place upon the flow visualization of the root separation, and our interpretation is different from that put forward by Isaacs[10], for instance, in a similar case.

In Fig. 22, within the first three pictures, two distinct flow configurations can be distinguished as we have already noted earlier; for greater clarity the main features of the flow near the root on these three photographs have been sketched in Fig. 92. In the first and third photographs (i.e. at α = 10·2 and 12·0 degrees) a re-attachment line can be seen originating at the wing apex and continuing outboard at a high angle of sweep until it bends back sharply towards the leading edge, terminating there at a 'saddle point', in the region of $y/s = 0{\cdot}1$, to enclose a region of separated flow which, in plan view, resembles the shape of a human ear. Within this region the flow lines indicate a circulatory flow in plan view and none of the flow lines have points of inflexion in them as do the flow lines produced by a vortex springing from the leading edge of a highly swept or slender wing. Behind the re-attachment line and inboard of the 'streak', although there is evidence of considerable cross flow, the flow pattern does not suggest the presence of a vortex. In contrast to this, the pattern shown in the second photograph of Fig. 22 (and also α = 10·2 and α = 11·70 degrees in Fig. 21) shows no forward movement of the re-attachment line and the flow pattern suggests the presence of a vortex. The transition from the first flow configuration to the second appears to take place smoothly, and in the intermediate region it may be difficult to distinguish between them as can be inferred by comparing α = 9·20 degrees (Fig. 19) and α = 10·20 degrees (Fig. 21). It is this first type of flow pattern which we believe is characteristic of a swept version of a long bubble (in this case terminated at its outer end by a short bubble) in which little or no vorticity is shed downstream, except of course at the trailing edge; only in the second case is a vortex formed which can in any way be compared to that occurring on a slender wing. It must be admitted that, at this time, we lack the evidence from detailed boundary layer traverses which would be necessary in order to be certain of this interpretation, and, moreover, that it is different from that of Isaacs[10], who observed an extremely similar ear-shaped separation region on a model of the Trident wing, and concluded that 'the leading-edge separation has formed a coiled vortex sheet in the manner of the leading-edge separation on more highly swept wings'. He accepts that this flow is set up by the inability of the flow to negotiate, by means of a short bubble, the high adverse pressure gradients that exist locally (which is the mechanism by which a long bubble would be produced on an unswept wing) but rejects the idea that the resulting flow on the swept wing is any more than superficially similar to a long bubble, on the grounds that the velocities within a long bubble are low. Recent research[33,34] has confirmed earlier measurements[32] in showing that the reverse flow within most of the length of a long bubble is much the same fraction of the external velocity (about 15 per cent) as the reverse flow near the re-attachment point of a short bubble. At reasonable tunnel speeds this is enough to produce a visible oil pattern even taking into account the lower external velocity that is likely near the re-attachment point of a long bubble. Furthermore, Fig. 94 (which is abstracted from Ref. 34) shows a sketch of an oil flow pattern obtained beneath a long bubble formed on a plate bounded by two parallel walls. Due to the influence of the walls, the bubble is significantly shorter at its outer ends producing a curved re-attachment line similar to that on our swept wing, and showing internal flow lines which indicate that the flow circulates in plan view as well as within a vertical section of the bubble. Lastly, flow patterns obtained on the unswept portion of the Bristol 188 wing[37] also show similar features. We feel that this evidence, plus the behaviour of the pressure distribution on sections near the root (*see* Section 5.6) is adequate support for our hypothesis that the 'ear-shaped' region is much more like a part-span swept version of a long bubble, than a vortex flow. Accordingly, this is used as a basis on which to explain the stalling behaviour of this wing.

7.2. Wire-Off Stall Behaviour

Following the above hypothesis we suggest that, without the wire, the stall of the wing begins as a thin-aerofoil stall at about $\alpha = 4$ degrees in the region of 3 to 5 per cent of the semi span. At $R_{\bar{c}} = 0{\cdot}51 \times 10^6$ the oil flow suggests the resulting long bubble expands rapidly, both spanwise and chordwise, with increase of incidence, until a fully-fledged vortex is formed springing from the apex, leaving the wing outboard of the vortex covered by a fully separated flow from the leading edge. At $R_{\bar{c}} = 1{\cdot}02 \times 10^6$ and $1{\cdot}78 \times 10^6$ the outward spread of the long bubble is restricted directly by the effect of the increased Reynolds number on its size, and indirectly by the increased stability of the boundary layer outboard of the bubble. The turbulent boundary layer outboard of the bubble originates from a short bubble near the leading edge; the short bubble is reduced in size by the increase in Reynolds number and this in turn reduces the re-attachment boundary layer thickness (i.e. the starting thickness of the turbulent boundary layer) and improves the ability of the resulting turbulent boundary layer to overcome an adverse pressure gradient. It appears that the combination of this effect with the smaller size of the long bubble at any given incidence, results in the spanwise spread of the long bubble being quite strongly curtailed in comparison with the results at $R_{\bar{c}} = 0{\cdot}51 \times 10^6$. Under these circumstances, the interference from the inboard long bubble with flow over the remainder of the wing, appears to arise from the thick boundary layer which exists behind the re-attachment line. From the flow pictures it appears that this thick boundary layer (which starts with strong cross flow components near the re-attachment line) sweeps outboard as it moves rearward and penetrates beneath the boundary layer which originates from the short bubble near the leading edge, resulting in a large displacement thickness near the trailing edge. This type of occurrence has been shown before, for example Fig. 4 of Ref. 36.

Thus the chordwise pressure distribution in the mid-semi span region retains basically its characteristic attached flow shape but the lift is less than it would be if the root separation were suppressed. This effect can be seen by studying the development of the incidence loading at a spanwise station just inboard of mid-semi span; we have chosen 40 per cent semi span and the results are shown in Figs. 95–97. These results are presented in the manner of method (3) that was used to analyse the pressure loadings obtained on the two-dimensional section, and is fully described in Ref. 12. Basically, it involves inserting the experimental values of the pressure loading, ΔC_p, into the expression for calculating ΔC_p in potential flow, and then, changing the values of the parameter n in the term $[(1 - x)/x]^n$ and the incidence α, to obtain the best agreement. In order to do this we effectively invert the equation and take logarithms of both sides, so that in the two-dimensional case we obtain the expression

$$\log[-\Delta C_p(x)\chi(x)] = \log\left[2\sin 2\alpha\frac{\alpha_b}{\alpha}\right] + n\log\left(\frac{1-x}{x}\right)$$

where $\Delta C_p(x)$ = the chordwise pressure loading from experiment,
$\chi(x)$ = composite function of the aerofoil section geometry obtained from the S-functions,
α_b/α, n = two unknown constants obtained by plotting $\log[-\Delta C_p\chi]$ against $\log[(1 - x)/x]$ and, in the two-dimensional case, interpreting these in terms of the effect of the boundary layer on the incidence loading.

In the case of the results of the swept wing, we have manipulated the incompressible form of the chordwise loading equation in the R.A.E. Standard Method[1] in much the same way, taking the change in the loading from some datum incidence to be the incidence loading, in order to remove the chordwise loading due to camber. The results so obtained are plotted in Fig. 95 where, since the χ-function is significantly different from the two-dimensional case we have denoted the derived pressure loading by ΔC_{p_T}, indicating that it bears some resemblance to a thin wing loading, in that the thickness effects of the profile shape have been removed.

In Fig. 95, for incidences up to $\alpha = 3{\cdot}75$ degrees, the results form as good a straight line as was obtained from the two-dimensional results, but above this, up to $\alpha = 8{\cdot}90$ degrees, there is a progressive deterioration in the form of reduced loading over the rear half of the aerofoil. This we interpret as being due to increasing interference from the thick boundary layer behind the long bubble, which, pushing its way underneath the thinner boundary layer forward on the section, effectively applies a sudden negative camber, thus unloading the trailing edge. Ultimately the majority of the section becomes affected by the outflowing thick boundary layer from the root, and then the trailing-edge loading returns, but at the same time the effective incidence decreases rapidly as can be seen from Fig. 97b. [The ratio α_b/α is significantly less than unity because no allowance has been made in this analysis for the induced downwash α_i.] Finally the long bubble near the root breaks out into a well-developed vortex flow between $\alpha = 11{\cdot}33$ degrees and $\alpha = 12{\cdot}30$ degrees (Figs. 52 and 56) and this causes a radical chordwise re-distribution of pressure at this station.

The outflowing boundary layer spoiling the lift of the outboard sections produces a mild nose-up pitch at incidences just below that at which the vortex becomes clearly apparent, but as soon as the vortex becomes strong the nonlinear lift which it induces on the inboard sections produces the dominant nose-up increment (Fig. 14).

7.3. Wire-On Stall Behaviour

With the wire fitted to the wing, the breakdown of the flow near the root to a long-bubble configuration is delayed to a much higher incidence (Figs. 68 and 73); in consequence the boundary layer over the mid-semi span region and outboard is much thinner than in the wire-off case, as can be seen from the derived chordwise loadings in Figs. 96, 98 and 99, where, in general, the data towards the trailing edge follows the lines from the pressure distribution over the forward 50 per cent of the chord to around 75 to 80 per cent of the chord, just as was observed in the two-dimensional tests. In Fig. 97 the parameters n and α_b/α are compared with the values obtained in the wire-off case, and it can be seen that (below the wire-off stalling incidence) the value of n is nearer 0·5 and the value of α_b/α is higher, both indicative of a thinner boundary layer. At higher incidences n begins to rise and α_b/α to fall as was observed in two-dimensional flow, but n never attains values as high as those observed in two-dimensional flow.

At $R_{\bar{c}} = 0{\cdot}51 \times 10^6$ the adverse effects of the long bubble near the root are not entirely suppressed, but only delayed to a higher incidence; because of this, initially a vortex is again formed springing from the apex as in the wire-off case ($\alpha = 10{\cdot}90$ degrees, Fig. 22), but this very soon gives way to a vortex which springs from the end of the wire caused by the leading-edge stall of the mid-semi span region ($\alpha = 12{\cdot}00$ degrees, Fig. 22) and then a long bubble flow is re-established near the root. Deep into the post-stall regime, the vortex origin again moves into the apex and the flow configuration is indistinguishable from the wire-off case.

At $R_{\bar{c}} = 1{\cdot}02 \times 10^6$ it is plausible to suggest that the stall originates as a mixed leading- and trailing-edge stall from sections in the mid-semi span region, since large vortex induced lift increments are produced just as they were at $R_{\bar{c}} = 0{\cdot}51 \times 10^6$. At both these lower Reynolds numbers the onset of the part-span vortex flow produces large lift increments towards the root and thus creates large nose-up pitching moment changes.

The stall pattern at $R_{\bar{c}} = 1{\cdot}78 \times 10^6$ is rather difficult to interpret; the first lift loss occurs out in the tip region, but there is some evidence to suggest that this may arise as a result of the wire near the root being rather too large and re-introducing a thickened outflowing boundary layer similar to that in the wire-off cases.

8. Conclusions

The conclusions to be drawn from this investigation may be conveniently listed under the three initial objectives,

(a) to investigate the stall behaviour of a wing designed, according to the R.A.E. Standard Method, to have uniform spanwise and chordwise pressure distributions at an incidence close to that for $C_{L_{\max}}$,

(b) to check the applicability of the R.A.E. Standard Method to a high C_L, non-planar case,

(c) to attempt to relate the stalling behaviour of sections near mid-semi span to that in two-dimensional flow, by making use of the twin concepts of induced incidence (α_i) and an infinite sheared wing.

Under the first heading, it has been found possible to suggest consistent explanations for the varying stall patterns observed on this wing in terms of known stall behaviour in two-dimensional flow, and the detailed description is given in Section 7. In particular, our interpretation of the results suggests that it is possible to observe swept counterparts of thin-aerofoil, leading-edge, mixed leading/trailing edge, and trailing-edge stall patterns. But it is very often extremely difficult to assess accurately which of these stall mechanisms is at work on a swept wing, because of the strong spanwise influences that occur, especially when the stall originates inboard.

Under the second heading it is concluded that, in general, the R.A.E. Standard Method copes with the high C_L, non-planar case very well, apart from regions close to the leading edge in both the root and tip regions, where the camber effects appear to be exaggerated, although this may be connected with difficulties encountered in placing the thickness distribution around camber lines with high curvature. Because of this, care may be needed in using the method to predict the effects of leading-edge flaps.

Under the third heading, good correlation between $C_{L_{\max}}$ values in two- and three-dimensional flow has been obtained, and also between the sectional stall patterns. But this result is in contradiction to some previous N.A.C.A. tests, and this is a field which requires further investigation. Our present results agreed with the N.A.C.A. tests in showing good agreement between the chordwise pressure distributions prior to the stall in two- and three-dimensional flow, when interrelated via the concept of an infinite sheared wing, and also in suggesting that the root of a swept wing can support very high values of $C_{L_{\max}}$.

LIST OF SYMBOLS

A	Aspect ratio
c	chord
$\bar{c}$	Standard mean chord $= S/2s$
$\bar{\bar{c}}$	Aerodynamic mean chord
d	Diameter of transition wire
C_L	Lift coefficient $= \text{Lift}/\frac{1}{2}\rho U_0^2 S$
C_D	Drag coefficient $= \text{Drag}/\frac{1}{2}\rho U_0^2 S$
C_M	Pitching moment coefficient $= \text{Pitching Moment}/\frac{1}{2}\rho U_0^2 S\bar{\bar{c}}$
C_N	Normal force coefficient (positive in lift sense)
C_p	Pressure coefficient $= (p - p_0)/\frac{1}{2}\rho U_0^2$
ΔC_{p_T}	Thin wing incidence loading
C_T	Axial force coefficient (positive in drag sense)
k	Lift dependent drag factor $C_D = \check{C}_D + \frac{k}{\pi A}(C_L - \check{C}_L)^2$
n	Index of chordwise loading due to incidence on a thin wing $\left(\frac{1-x}{x}\right)^n$
p	Static pressure
p_0	Free-stream static pressure
R	Reynolds number
$R_{\bar{c}}$	$\frac{U_0\bar{c}}{\nu}$
R_s	Local chordal Reynolds number in free-stream direction (i.e. sheared) $= \frac{U_0 c}{\nu}$
R_y	Local chordal Reynolds number normal to mean sweep (i.e. yawed) $= \frac{U_0\hat{c}\cos\phi}{\nu} = R_s\cos^2\phi$
R_w	$\frac{U_0 d}{\nu}$
S	Wing area
s	Wing semi-span
t	Aerofoil thickness/chord ratio
U_0	Free-stream velocity
x	Distance along chord
y	Distance spanwise
z	Distance normal to chord
α	Incidence

α_b	Incidence value determined from analysis of pressure distribution
λ	Spanwise interpolation function for centre and tip effect
ϕ	Mean sweep angle
ν	Kinematic viscosity
χ	Composite function of aerofoil section geometry

Suffices

i	Conditions induced by trailing vorticity
L	Local conditions on the swept wing
0	Conditions at zero overall lift

Superscripts

$\hat{}$	Conditions measured normal to mean sweep (i.e. yawed wing)
$\check{}$	Conditions measured at minimum drag
$\bar{}$	Conditions in equivalent two-dimensional flow (except for $\bar{c}$ *see* before)

REFERENCES

No.	*Author(s)*	*Title, etc.*
1	—	Method for predicting the pressure distribution on swept wings with subsonic attached flow. Roy. Aero. Soc., Transonic Data Memorandum 6312.
2	D. Küchemann	A simple method for calculating the span- and chordwise loadings on straight and swept wings of any given aspect ratio at subsonic speeds. R. & M. 2935 (1952).
3	G. G. Brebner	The design of swept wing planforms to improve tip stalling characteristics. R.A.E. Report Aero 2520 (A.R.C. 17264) (1954).
4	G. G. Brebner	The application of camber and twist to swept wings in incompressible flow. A.R.C., C.P. 171 (1952).
5	J. Weber	The calculation of the pressure distribution on the surface of thick cambered wings and the design of wings with given pressure distribution. A.R.C., R. & M. 3026 (1955).
6	J. A. Hay and W. J. Eggington	An exact theory of a thin aerofoil with large flap deflection. *Journal of the Roy. Aero. Soc.*, November 1956.
7	D. E. Gault	A correlation of low speed aerofoil section stalling characteristics with Reynolds number and aerofoil geometry. N.A.C.A. Technical Note 3963 (1957).
8	L. F. Crabtree	Effects of leading edge separation. Thin wings in two-dimensional incompressible flow. *Journal Aero. Sci.*, Vol. 24, No. 8, pp. 597–604 (1957).
9	G. G. Brebner and L. A. Wyatt	Boundary layer measurements at low speed on two wings of 45° and 55° sweep. A.R.C. C.P. 554 (1960).
10	D. Isaacs	Wind tunnel measurements of the low speed stalling characteristics of a model of the Hawker-Siddeley Trident 1C. A.R.C., R. & M. 3608 (1968).
11	B. Thwaites, Ed.	*Incompressible aerodynamics.*
12	D. S. Woodward	The two-dimensional characteristics of a 12·2 per cent thick R.A.E. 100 aerofoil section. A.R.C., R. & M. 3648, 31374 (1969).
13	P. R. Owen and L. Klanfer	On the laminar boundary layer separation from the leading edge of a thin aerofoil. A.R.C., C.P. 220 (1953).
14	N. Curle and S. W. Skan (Miss)	Calculated leading edge laminar separations from some R.A.E. aerofoils. A.R.C., C.P. 504 (1959).

15	G. G. Brebner	Low speed wind tunnel tests on the effect of planform design, and camber and twist, on swept back wing characteristics. R.A.E. Technical Report 65145 (A.R.C. 27488) (1965).
16	J. R. Cole	A pneumatic switch for isolating pressure lines in a wind tunnel pressure recording system. Unpublished M.O.D. (P.E.) material.
17	D. S. Woodward	On the integration of functions specified only as discrete data points, with special reference to the processing of wind tunnel pressure measurements. R.A.E. Technical Report 67151 (A.R.C. 29885) (1967).
18	D. S. Woodward	A complete program for processing wind tunnel pressure data. Unpublished M.O.D. (P.E.) material.
19	E. C. Maskell, D. A. Kirby and J. Y. G. Evans	Aerodynamic research to improve the low-speed performance of transport aircraft for short and medium ranges. Unpublished M.O.D. (P.E.) material.
20	J. Weber	Some effects of flow separation on slender delta wings. R.A.E. Technical Note Aero 2425 (A.R.C. 18073) (1953).
21	A. R. Beauchamp	An investigation into the quality of the flow in the R.A.E. No. 2 $11\frac{1}{2} \times 8\frac{1}{2}$ ft wind tunnel. R.A.E. Report to be published.
22	D. Küchemann and D. J. Kettle	The effects of end plates on swept wings. A.R.C., C.P. 104 (1951).
23	D. Küchemann, J. Weber and G. G. Brebner	Low speed tests on wings of 45° sweep. Pt. II—Balance and pressure measurements on wings of different aspect ratios. A.R.C., R. & M. 2882 (1951).
24	M. J. Lighthill	On displacement thickness. *Journal of Fluid Mechanics*, Vol. 4, Pt. 4 (1958).
25	G. G. Brebner and L. A. Wyatt	Boundary layer measurements at low speed on two wings of 45° and 55° sweep. A.R.C., C.P. 554 (1960).
26	J. Weber	Low speed measurements of the pressure distributions and overall forces on wings of small aspect ratio and 53° sweep back. R.A.E. Technical Note Aero 2017 (A.R.C. 12878) (1949).
27	I. Jaszlics and L. Trilling	An experimental study of the flow field about swept and delta wings with sharp leading edges. *Journal Aero. Space Sci.*, Vol. 26, No. 8 (1959).
28	A. F. Jones, P. V. Grey-Wilson and D. A. Treadgold	Notes on computer programmes for the prediction of pressure distributions on swept wings with subsonic attached flow. Unpublished M.O.D. (P.E.) material.
29	L. W. Hunton	Effects of finite span on the section characteristics of two 45° swept back wings of aspect ratio 6. N.A.C.A. T.N. 3008 (1953).
30	L. W. Hunton and H. A. James	Use of two-dimensional data in estimating loads on a 45° swept back wing with slats and partial-span flaps. N.A.C.A. T.N. 3040 (1953).

31 H. P. Horton — Laminar separation bubbles in two- and three-dimensional incompressible flow.
Ph.D. Thesis Q.M.C. London University (1968).

32 D. E. Gault — An investigation at low speed of the flow over a simulated flat plate at small angles of attack using pitot-static and hot-wire probes.
N.A.C.A. T.N. 3876 (1957).

33 D. S. Woodward — An investigation of the parameters controlling the behaviour of laminar separation bubbles.
Unpublished M.O.D. (P.E.) material.

34 D. S. Woodward — Further work on separation bubbles.
Ph.D. Thesis Q.M.C. London (1969).

35 E. J. Jacobs and A. Sherman — Aerofoil section characteristics as affected by variations of the Reynolds number.
N.A.C.A. Tech. Report 586 (1937).

36 D. Küchemann — Boundary layers on swept wings: their effects and their measurement.
AGARD AG19/P9, p. 69, Ottawa, June 1955.
(R.A.E. Technical Note Aero 2370).

37 J. A. Lawford and A. R. Beauchamp — Low-speed wind-tunnel measurements of pressure fluctuations on the wing of a twin-jet aircraft (Bristol 188).
A.R.C., R. & M. 3551 (1966).

APPENDIX I

Description of the Experimental Installation and Method

I.1. The Wind-Tunnel Model

The model was constructed of a glass fibre and araldite cladding around a steel spar which was continuous across the centre section. The spar was made up from two sections bolted together so as to lie within the complicated surface geometry, and at the root a 1 in. square (25·4 mm) I-section tail-string was attached, which was angled downwards at 5 degrees to the wing chord plane. The pressure plotting within the wing was achieved by running 0·048 in. od × 0·028 in. id (1·22 mm od × 0·71 mm id) cupro-nickel tubing spanwise along approximately constant percentage chord lines, 0·02 in (0·5 mm) below the surface. These pipes were taken out of the wing by running them down the tail sting between the flanges of the I-section and terminating them in a distribution plate at the rear of the sting. 0·0177 in. (45 mm) diameter holes were drilled at 22 spanwise stations in the pipes on the starboard wing as listed in Table 1, which also shows the distribution of the points between the upper and lower surfaces. Near the tip the total number of points had to be reduced because of the small chord, and near the root the sting obscured the two innermost stations over the rear of the chord on the lower surface. A smaller number of pipes were also placed in the port wing, but holes were drilled in these only at the 60 per cent semi-span station, the intention being that the pressures recorded by these holes should be used as a check upon the repeatability of the incidence settings from one run to another. In fact they turned out to be not very useful from this point of view but were invaluable in showing that the flow development on the two halves of the wing was not identical.

The size of the pipes used for the pressure plotting was dictated by the point density required near the leading edge in order adequately to measure the suction peaks generated there. The density obtained on this model was adequate over most of the wing except in the outermost sections, but this was obtained only at the price of rather long lags between changes in model incidence and the final settling of the manometers. A two minute settling time was allowed for most of the runs although this was slightly reduced when measuring very near the root and extended when near the tip.

I.2. The Installation of the Model in the Tunnel

Front and rear views of the model in the tunnel are shown in Figs. 8 and 9. The wing was mounted on a pair of streamlined struts above the lower, virtual centre, balance of the No. 2 11½ ft × 8½ ft tunnel at R.A.E. Farnborough. The attachments of the struts to the wing were designed so that the pivots were completely buried in the model, the struts themselves being tapered as much as possible, and the strut guards covering only half the strut height, so that the interference of the supports on the wing flow was kept small. Because of this the struts themselves were too slender to give adequate lateral stiffness to the rig, so this was provided by wire cross-bracing. The other wire which can be seen attached to the apex of the wing carried a number of weights immersed in an oil bath in an attempt to provide some damping to the pitching oscillations which developed at, and beyond, the stall, at the highest tunnel speed.

The model was constrained in pitch by the tail strut which was attached to the screwjack used to provide incidence adjustment. The screwjack was driven in either direction by a two-speed three-phase electric motor operating through a gear train and a worm and pinion. A DC transmitter, driven from the final pinion, operated a remote counter which indicated the position of the screwjack to ±0·005 in. (±0·01 mm) and this was used throughout the test to set the model incidence. Wind-off counter values were recorded at one degree intervals, the wing incidence being set by means of an inclinometer positioned on detachable datum pads above the wing. The stiffness of the sting was then measured by applying a known pitching moment (via a wire, weights and a pulley) and recording the incidence change produced. When reducing the results, the rotation of the wing due to the deflection of the sting was calculated from the net pitching moment (i.e. measured-tare) and the sting stiffness, and this was added to the incidence value indicated by the counter reading.

I.3. The Pressure Plotting System

Inside the tail strut, which was made from a standard streamline section tube, were packed 80 0·078 in. od × 0·048 in. id (1·98 mm od × 1·22 mm id) cupro-nickel tubes, the inside finally being filled with casting araldite to give a solid entity. At the top of this strut, short lengths of 0·048 in. od (1·22 mm od) tube identical to that in the wing were let into the larger tubes so that connection between the wing tubes at the end of the sting and the larger pipes running down the tail strut could be made with small bore PVC tube. In this way a simple and small flexible joint in the pressure tubing was made as can be seen in Fig. 9. At the bottom of the strut the tubes inside the strut were terminated in tapered connectors suitable for taking 4 mm id PVC tube and this type of tubing was used for the remainder of the pressure piping which ran from the base of the strut, through a switching box, to three manometers.

The pressure switching box[16] was identical in design to that used in the 8 ft × 6 ft tunnel for switching pressures between various banks of Midwood manometers; the principle of operation is shown in Fig. 10. Four pressure switching boxes were used as shown schematically in Fig. 11, three of these boxes were used for switching in, or isolating, the three manometers, whilst the fourth was arranged so that all pressure lines from the model and any of the manometers could be vented to atmosphere. In operation these switching boxes proved to be a great success, giving an excellent seal, and materially assisted the large amount of leak and blockage testing which was a necessary part of this test technique, due to the method adopted for obtaining a pressure survey across the semi-span (*see* below).

Three manometers were used in order to cope with the Reynolds number range required. Each manometer was approximately 40 in. square (1·017 m) and contained 86 manometer tubes; a 35 mm recording camera was mounted on a light rigid frame about 5 ft 6 in. (1·65 m) away from the plane of the tubes on each manometer; adequate lighting for photography was obtained from eight 40 W fluorescent lighting tubes mounted approximately 12 in. (0·305 m) behind the plane of the manometer tubes in each case, the lighting being distributed by a frosted perspex panel mounted immediately behind the tubes. The first manometer was used for making measurements at windspeeds around 80 ft/sec (24·4 m/sec) ($R_{\bar{c}} = 0{\cdot}51 \times 10^6$) and was fitted with glass tubes, the plane of the tubes being inclined at 20 degrees to the horizontal; ethyl alcohol (sg $\simeq$ 0·8), dyed blue, was used as the manometric fluid. The second manometer was used for making measurements at windspeeds around 160 ft/sec (48·8 m/sec), ($R_{\bar{c}} = 1{\cdot}02 \times 10^6$); it again used glass tubes but was filled with carbon tetrachloride (sg $\simeq$ 1·6) and mounted vertically. No dye was used in the liquid of this manometer, instead the menisci were marked for photographic purposes by floating a black perspex ball on the top of the liquid in each tube. The third manometer was used for taking measurements at windspeeds around 300 ft/sec (91·4 m/sec), ($R_{\bar{c}} = 1{\cdot}80 \times 10^6$), and in this case the manometer tubes were formed in blocks of cast araldite by using a mould employing tensioned metal rods coated in release agent to form the tubes. This method produced extremely straight and even bored tubes so that zero variations were much reduced when the plane of the tubes was close to the horizontal. Mercury (sg $\simeq$ 13·6) was used as the manometric fluid, oxidation of the surface of the meniscus being prevented by the addition of a little orthophosphoric acid in each tube, and the plane of the manometer tubes was inclined at 20 degrees to the horizontal.

When pressure measurements were being taken the holes in all except one spanwise station were filled with commercially available modelling wax (Glitterwax) so as to present as smooth a wing surface as possible and to minimise the effects of the movement of the measuring station upon the stalling behaviour. [Unfortunately, even so, there is evidence of small changes in flow development and $C_{L_{\max}}$ as the measuring station was moved spanwise, which serves to underline the practical difficulties involved in an investigation of this type.] The wax was removed by slightly pressurizing all tubes and warming the wax with a mains soldering iron run off approximately 35 V supplied from a variable transformer; re-sealing was accomplished by melting the wax into the holes in the same way. Some trouble was experienced with the wax running into, and thus blocking, the pipes, but this was relatively easily removed by warming the pipe through the araldite surface of the model whilst keeping a pressure of about 2 psi (140 mb) inside the pipes so that as soon as the wax melted it was blown out of the nearest downstream pressure hole.

I.4. Tare Loads on the Support System

The tare drag and pitching moment of the main struts and their cross bracing were measured in the absence of the model. Surprisingly, a small tare lift ($C_L \simeq 0{\cdot}005$) was also measured, which appeared to arise from a suction generated over the open top of the strut guard acting on a flange on the strut which was just below the top of the guard. This suction decreased slightly with model lift so the lift tare that was subtracted from the readings was similarly altered as the incidence was varied.

The tare loads due to the tail strut were estimated by replacing the strut with a wire system, calculating the tare loads due to the wires from standard wire data, and thus deducing the loads on the strut. No measurable lift load was found and the effective point of action of the drag load was very close to the centre of the strut at all incidences.

The tare loads on the sting were estimated by measuring the pressures on both the upper and lower surfaces using 'creeper' tubes; the normal force thus found was virtually constant along the length of the sting and was almost indistinguishable from the result of assuming that the load was generated solely by the component of the airstream velocity normal to the sting and using a drag coefficient of unity. A small tare contribution from the blunt base of the sting was estimated by measuring the base pressure behind it, and this, again, was found to be little influenced by variation of incidence within the range used.

I.5. Data Reduction

The values of the pressures on the model were deduced from the photographs of the manometers by measuring the manometric heights on a large film reader (Benson–Lehner Boscar) in the same way as was used in the previous two-dimensional tests[12]. However in this case the quantity of data was such that a computer program was clearly called for to evaluate the sectional coefficients[18] and this required the development of some special techniques[17].

When the model was inspected before the tests began, some of the sections were found to be somewhat outside the specified tolerances. However considering all the unknown factors involved in specifying the geometry in the first place, it was decided to proceed with the test and to derive the ordinates of the pressure points from the measured shape of the wing. This was clearly simple for the chordwise location of each pressure point but it was much more complicated to measure the thickness ordinate. In fact no effort was made to do this, instead the required ordinates were interpolated from the measured sectional shapes using the method outlined in Ref. 17.

As well as measuring the overall characteristics of the wing on the balance before the pressure plotting was connected (and it was done in this way in order to avoid possible trouble with constraint effects of the large number of pressure tubes bridging from the balance to earth) balance loads were recorded throughout each pressure plotting run. From these figures the true geometric incidences were calculated as described previously; the tunnel constraint was calculated and added to the incidence value in each case, and the total blockage was calculated and incorporated in the determination of the C_p values. By comparing the $C_L - \alpha$ curves obtained from these readings it was found that in general, incidence values were repeated to $\pm 0{\cdot}02$ degree.

APPENDIX II

Description of N.A.C.A. Swept Wing Tests and their Re-Assessment

In all, three sets of tests were conducted in the Ames 40 ft × 80 ft tunnel on a half model of a wing and a fuselage[29,30]. The wing had a straight tapered planform with a taper ratio of 0·5, an aspect ratio of 6, and a quarter-chord sweep back angle of 45 degrees. All the pressure plotting results that have been used in this re-assessment were obtained along lines normal to the quarter-chord line, i.e. at 45 degrees to the free stream direction. The model for the first test had an untwisted wing of N.A.C.A. 64A010 section normal to the quarter-chord line, and the results for this wing show clear indications of the same type of non-linear lift increments as were obtained on the present model, and so the $C_{L_{\max}}$ values, relative to the limit of attached flow, were re-estimated. This was not quite so easy as in our case, since insufficient data were presented to allow the data to be analysed in the same way as shown in Section 6, and so the relevant values of $C_{L_{\max}}$ had to be assessed from the local $C_{L_L} \sim \alpha$ curves for the finite wing and then multiplied by the appropriate sweep factors; this meant that true sectional C_L values perpendicular to the effective wind direction were not attainable, furthermore we suspect that the figures given are C_{N_L} and not C_{L_L}, although neither of these factors is likely to be of large significance. It is possible that they might have been more significant on the second wing which had 10 degrees of washout between root and tip and used a cambered section N.A.C.A. 64A810. The large twist gave a C_{L_L} distribution with a maximum at the root decreasing steadily outboard, in contrast to the first wing where the C_{L_L} distribution increases from the root to about 85 per cent semi span. The cambered section in two-dimensional flow had a gentle stall arising from a progressive forward movement of the turbulent separation point, the initial separation occurring before $C_{L_{\max}}$. Under these circumstances it was felt to be preferable to use the figures relating to the first onset of separation rather than the observed $C_{L_{\max}}$, both values having been quoted in the original report.

The third model had a part-span double slotted flap and a full-span slat and the general flow situation on this wing is too complex for us to attempt to improve, with any confidence, on the original analysis, so these results have been ignored. It is worth noting that the original analysis showed similar increases in sectional $C_{L_{\max}}$ to those measured on the first two wings.

TABLE 1

Station number (starboard wing)	1	2	3	4	5	6	7	8	9	10	11	12	13	14	15	16	17	18	19	20	21	22
Percentage of semispan	0	1	2	3	4	5	6	8	10	15	20	30	40	50	60	70	80	85	90	94	96	98
Pressure holes on upper surface	12	35	37	37	37	37	37	37	37	36	36	36	36	36	36	36	29	29	28	26	25	20
Pressure holes on lower surface	7	9	19	19	19	19	19	19	19	19	19	19	19	19	19	19	19	18	16	14	13	11
Sectional coefficients obtained	No	No	← Yes →																			
Port wing station pressure plotted at same time (% y/s)	60	60	60	60	60	60	60	60	60	60	60	60	60	60	60	60	60	60	90	94	96	98
Number of pressure holes on port wing	22	22	22	22	22	22	22	22	22	22	22	22	22	22	22	22	22	22	21	21	18	18

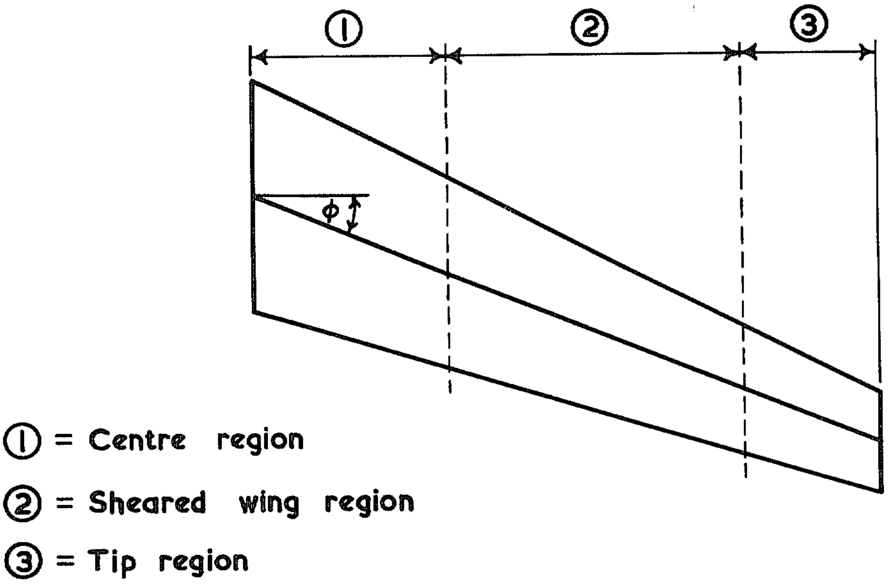

FIG. 1. Important regions of typical swept wing.

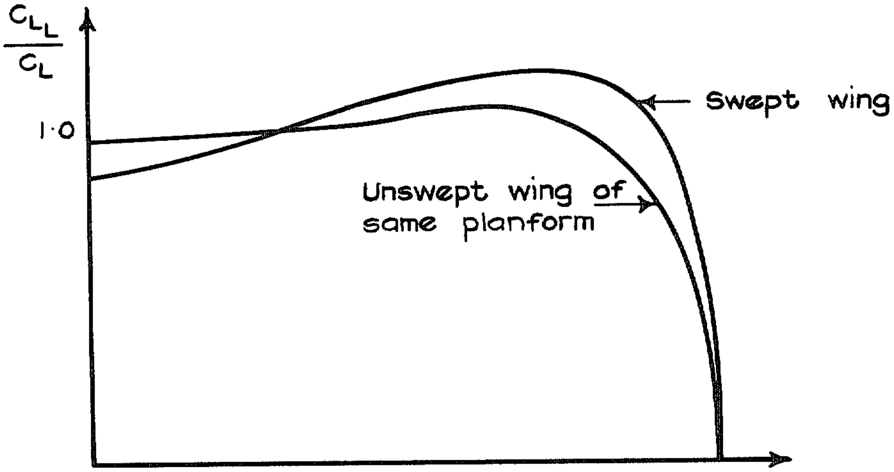

FIG. 2. Schematic local C_{L_L} distributions on swept and unswept wings.

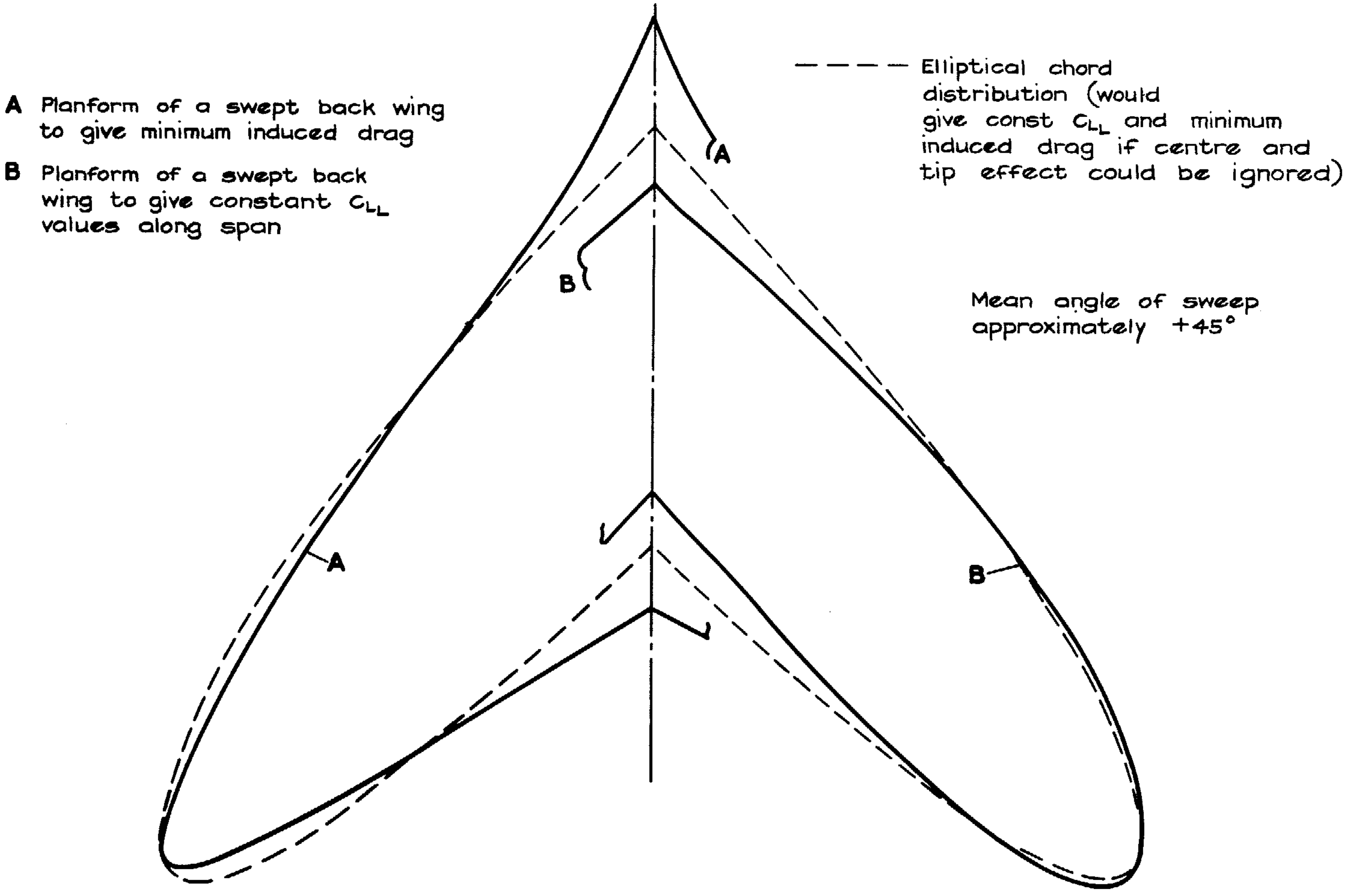

FIG. 3. Comparison of planforms to produce given spanwise loadings.

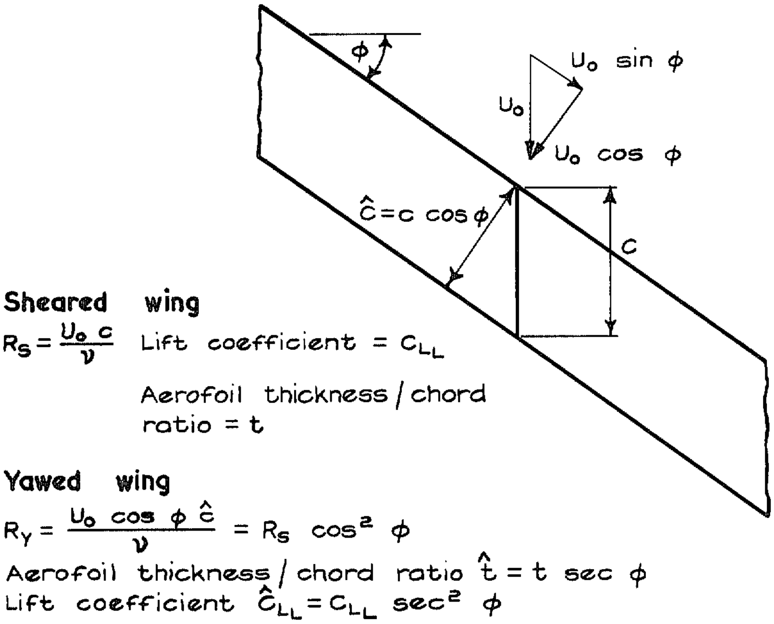

FIG. 4. Definition of sheared and yawed wing conditions on a swept wing.

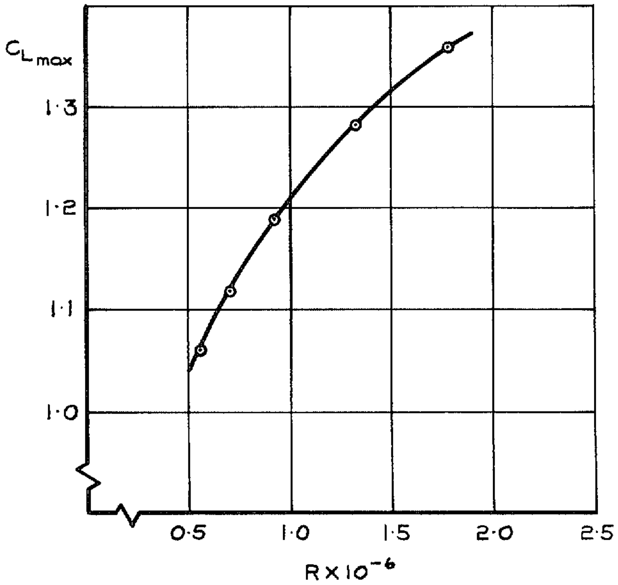

FIG. 5. Measured variation of $C_{L_{max}}$ with Reynolds number for 12·2 per cent thick R.A.E.100 aerofoil in two-dimensional flow.

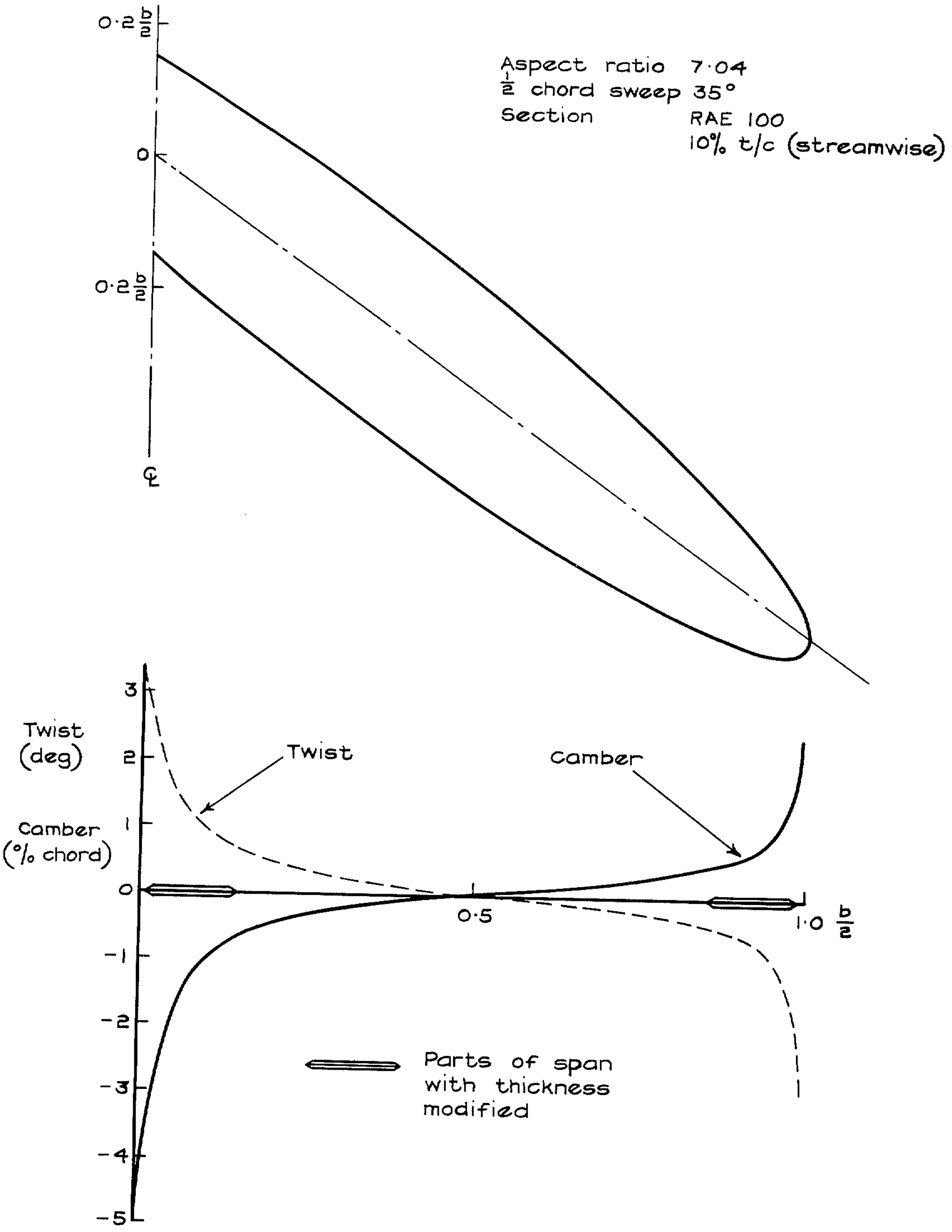

FIG. 6. Wing designed for uniform pressure distribution at $C_L = 0{\cdot}8$.

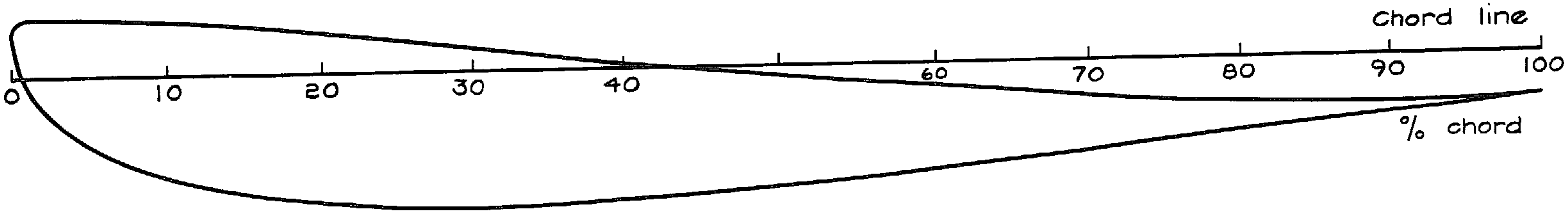

a Root section twist = 3·35 degrees camber = $-4{\cdot}96\%$ thickness modified

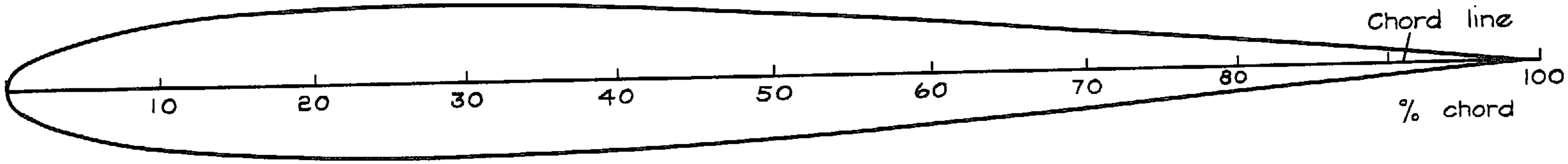

b Sheared wing section no camber or twist 10% t/c RAE 100 thickness form

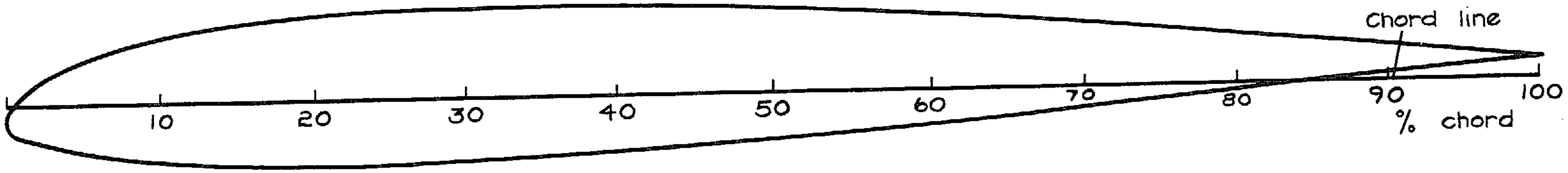

c 98% semi-span section twist = $-1{\cdot}46$ degrees camber = $1{\cdot}44\%$ thickness modified

FIG. 7a–c. Wing sections at root, mid-semi span, and near the tip.

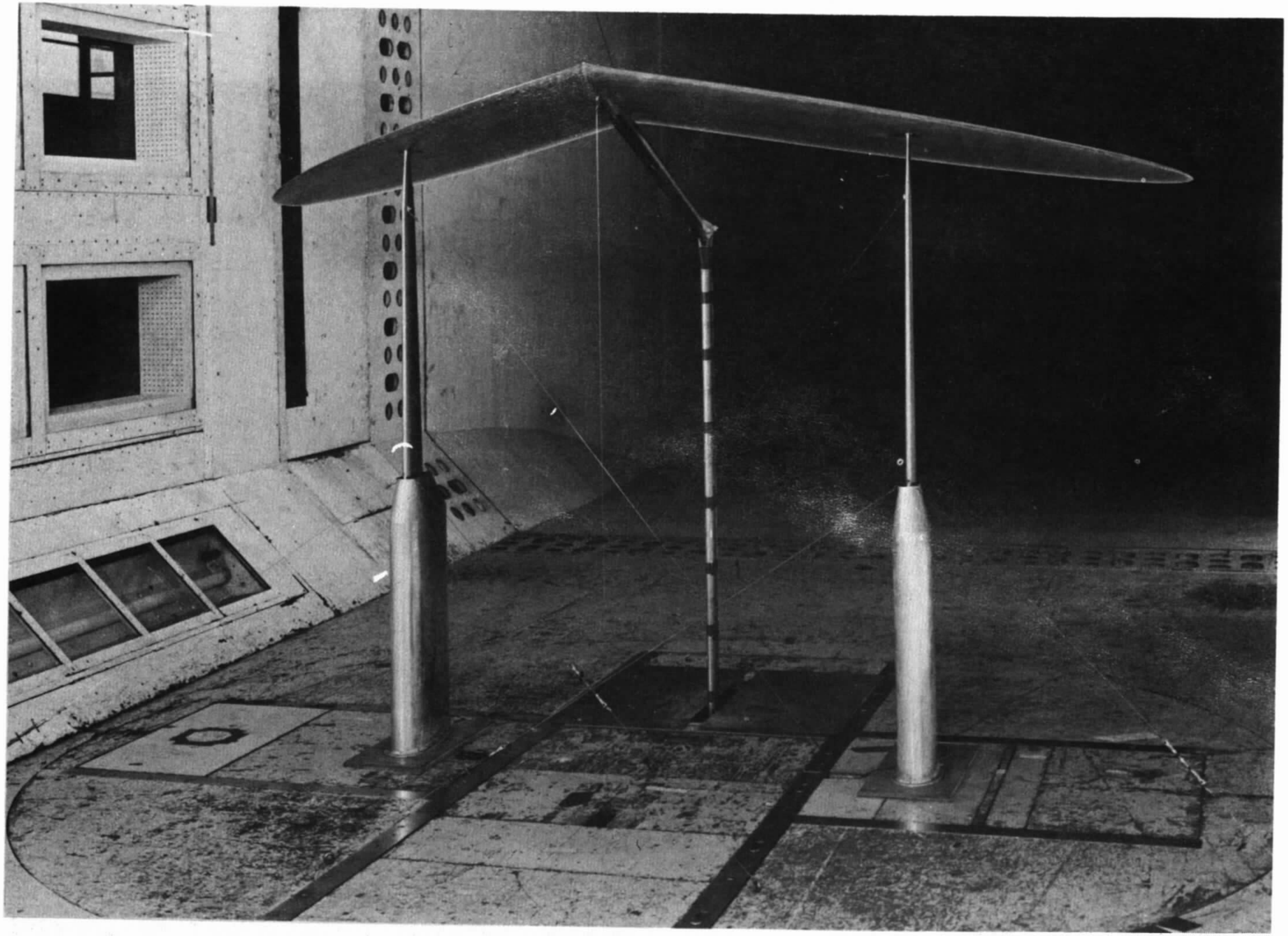

FIG. 8. Front view of model installed in wind tunnel.

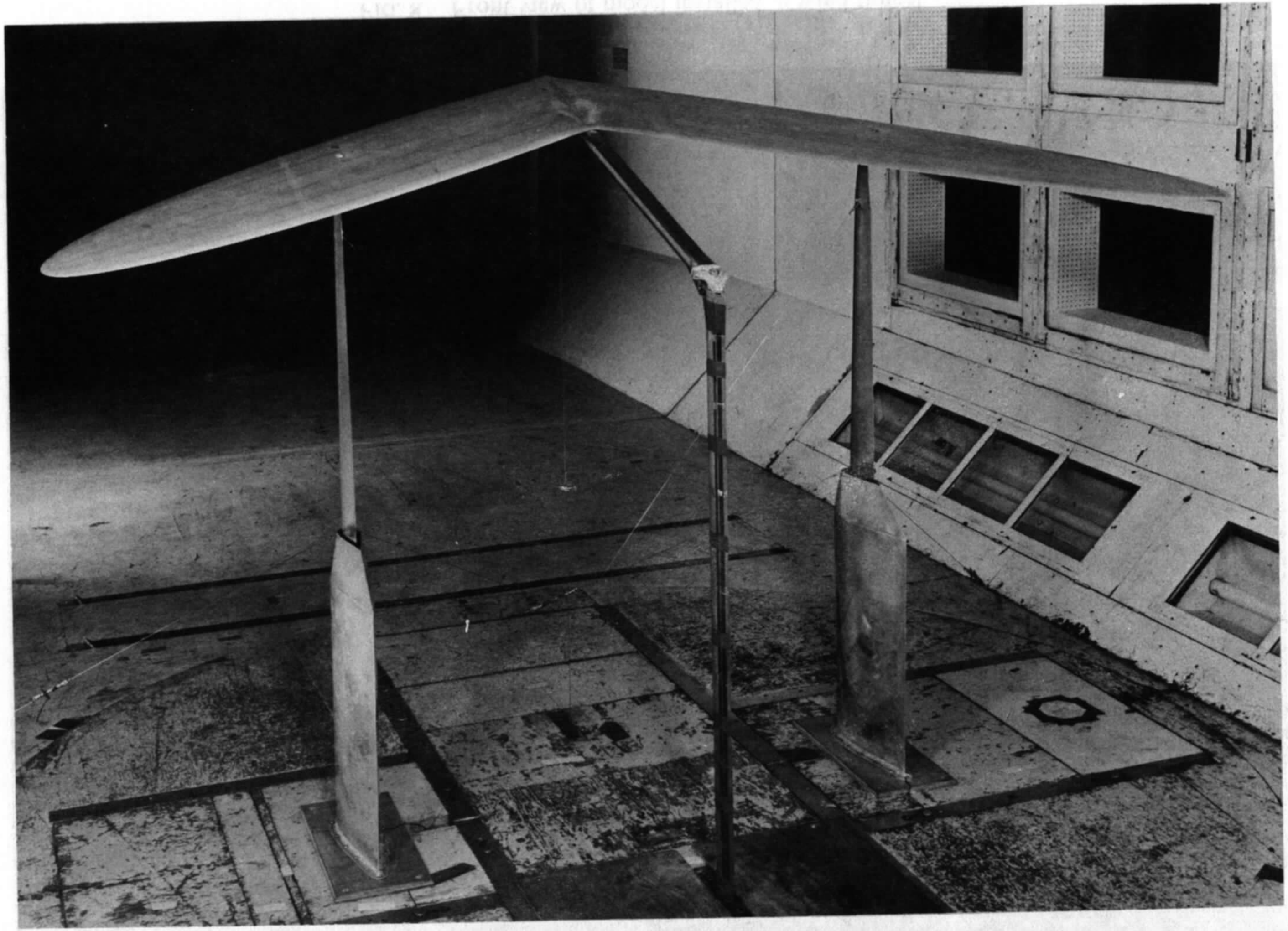

FIG. 9. Rear view of model installed in wind tunnel.

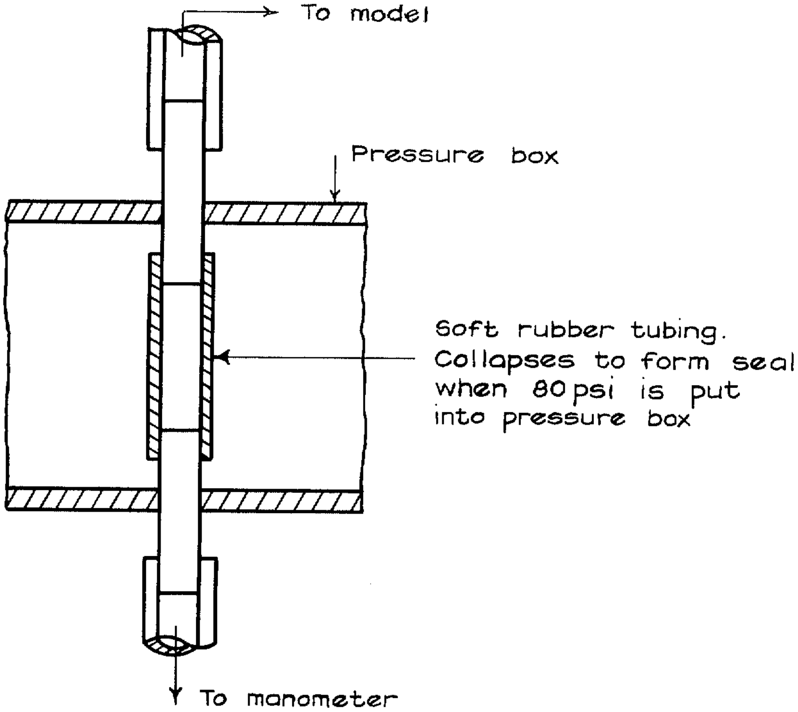

FIG. 10. Principle of pressure switch.

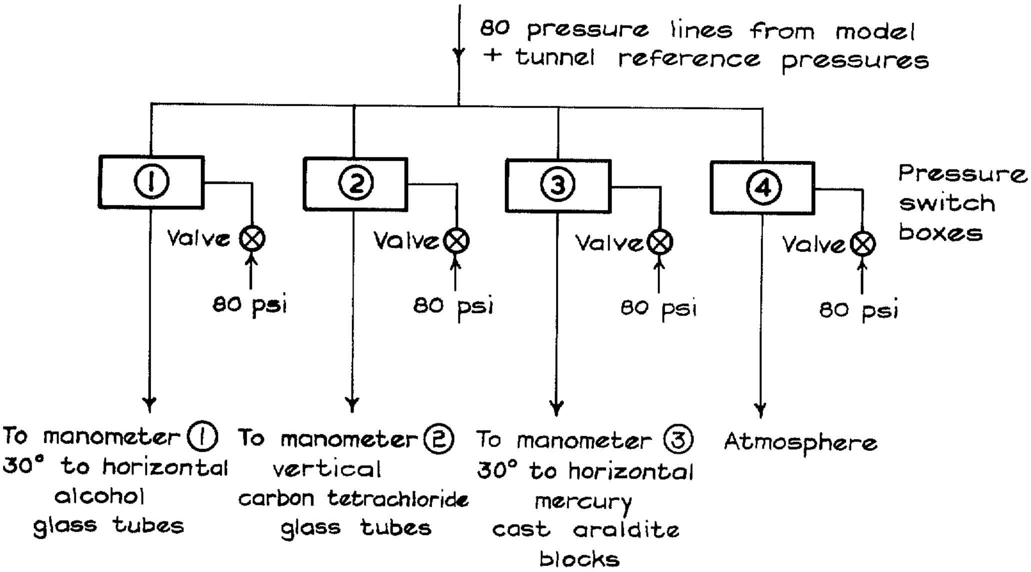

FIG. 11. Schematic layout of pressure measuring system.

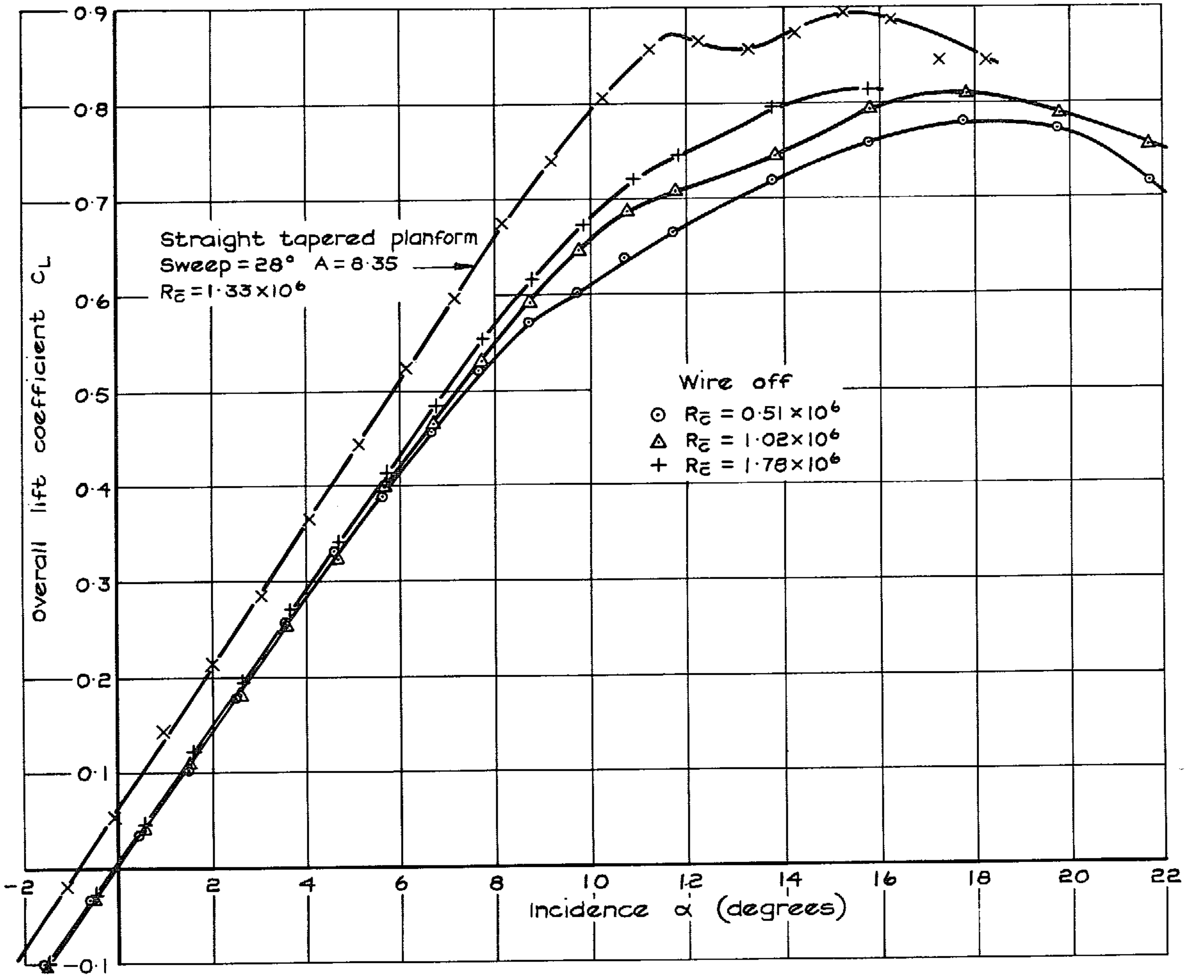

FIG. 12. Lift-incidence characteristics through the Reynolds number range wire-off.

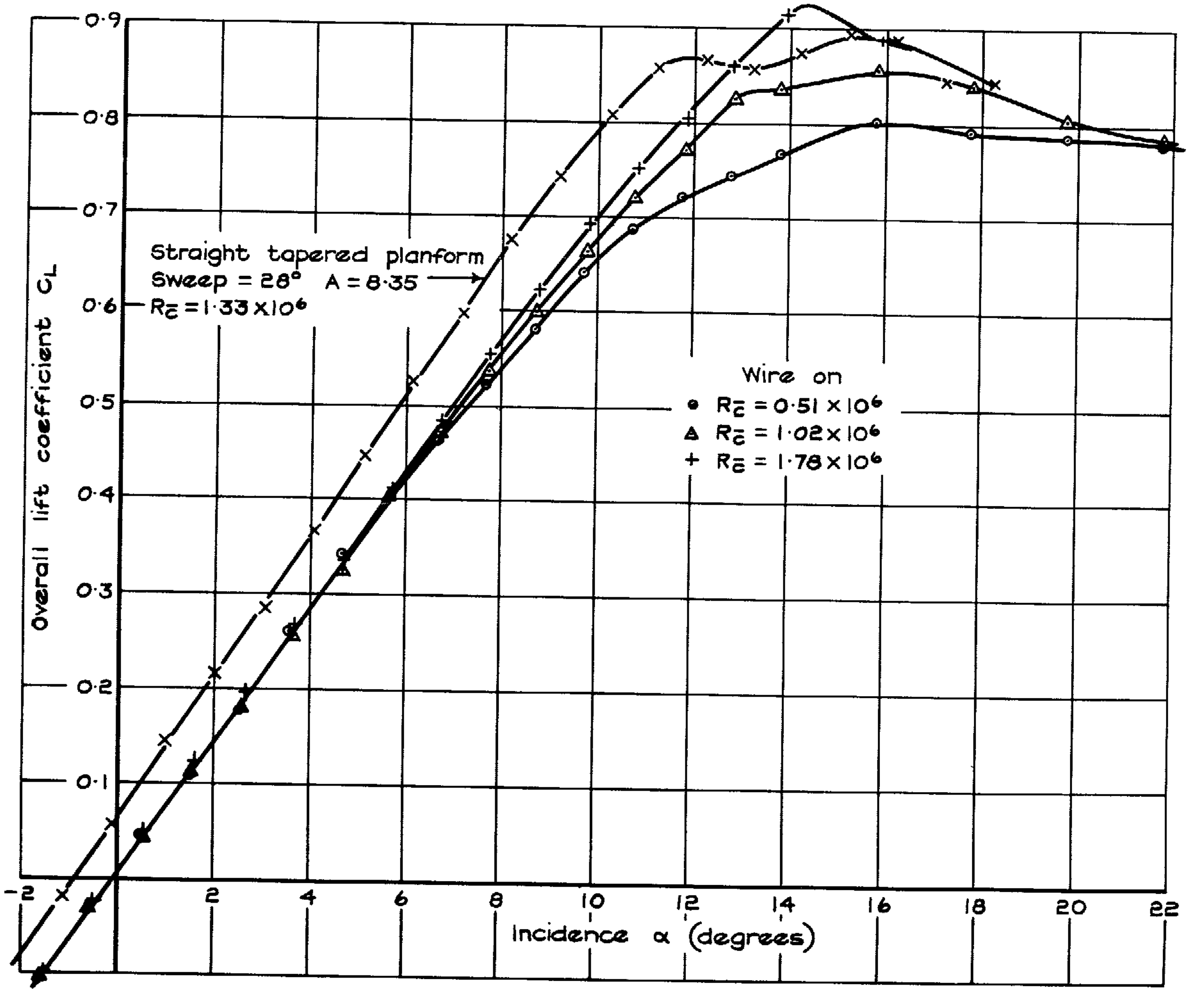

FIG. 13. Lift-incidence characteristics through the Reynolds number range wire on.

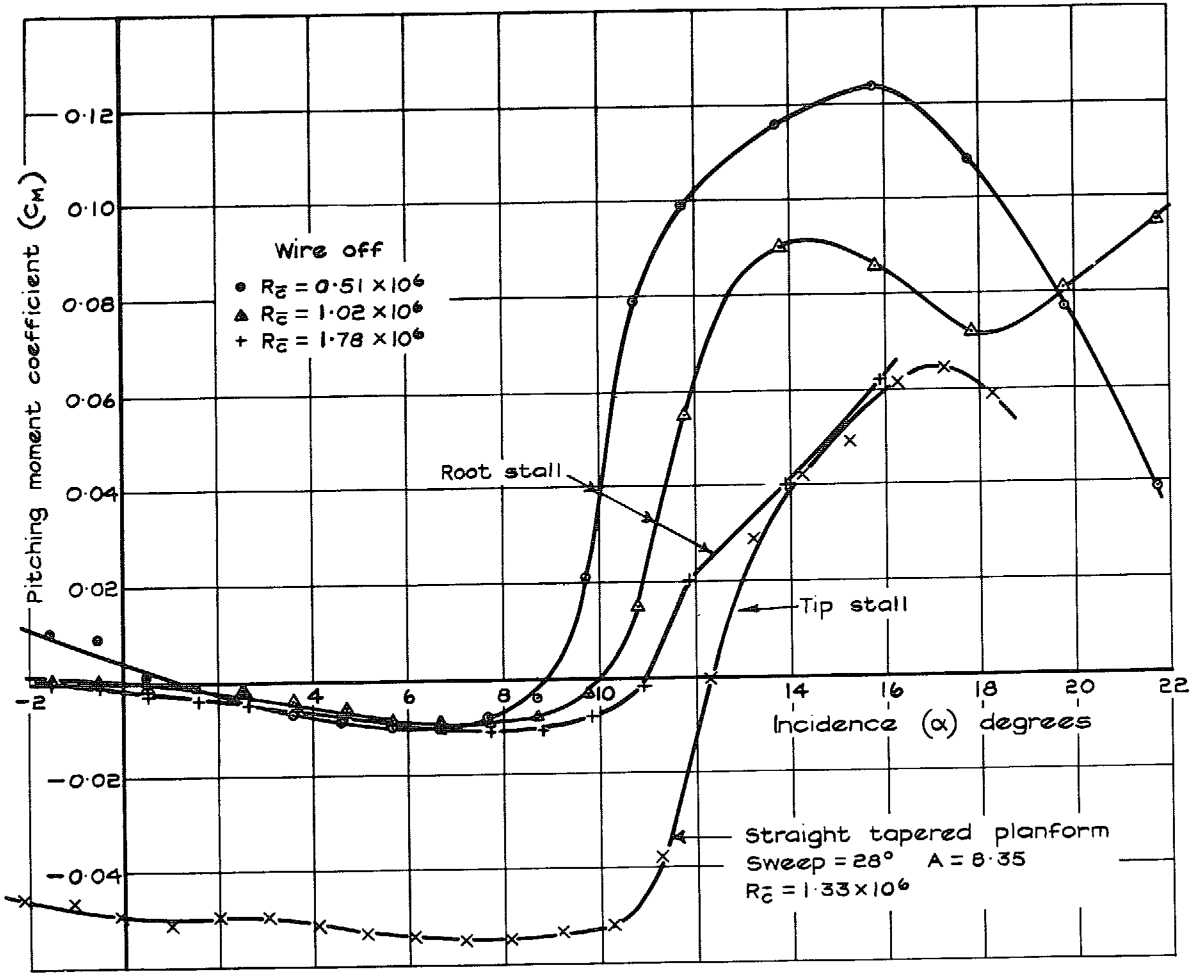

FIG. 14. Pitching moment characteristics about mean aerodynamic $\frac{1}{4}$ chord point through the Reynolds number range wire off.

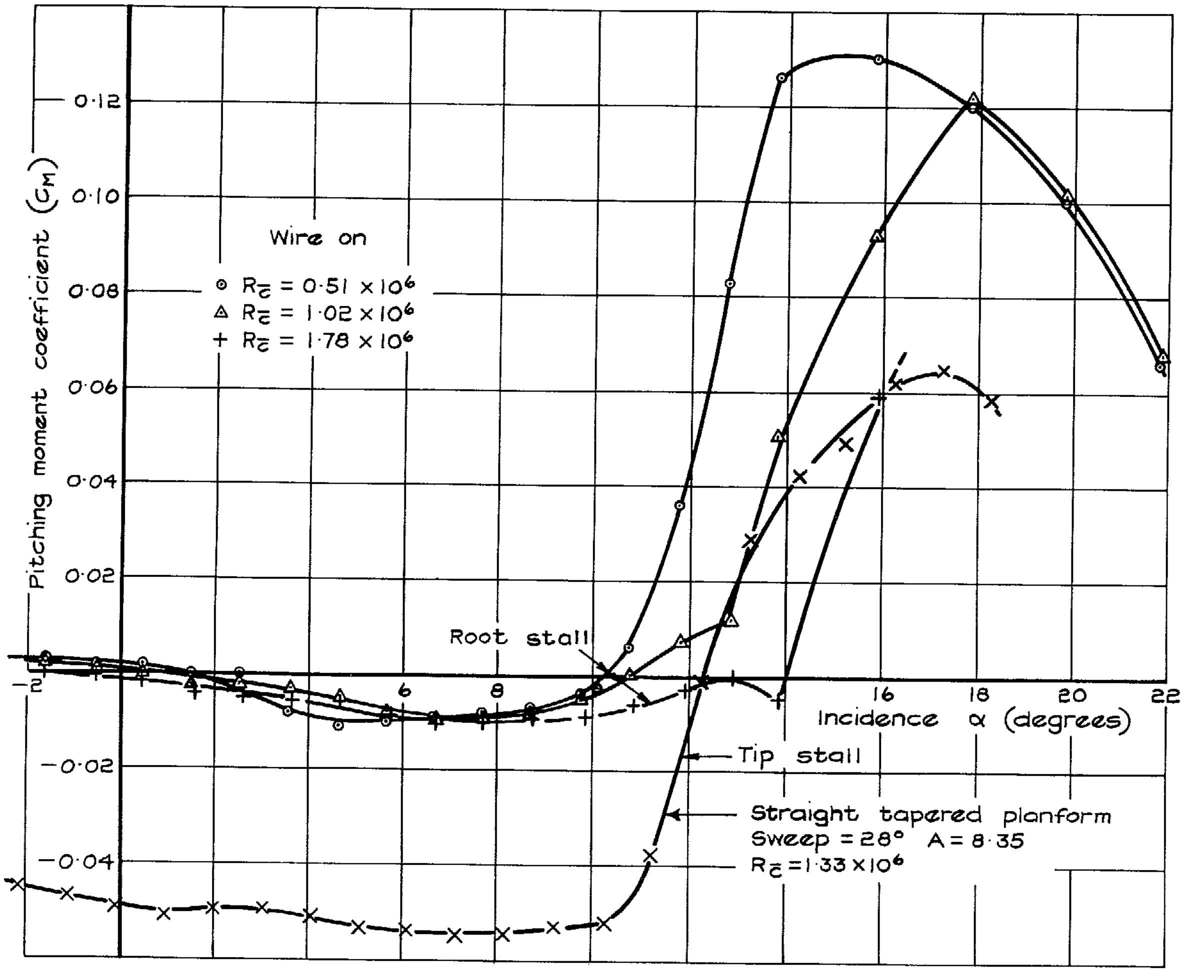

FIG. 15. Pitching moment characteristics about mean aerodynamic $\frac{1}{4}$ chord point through the Reynolds number range wire on.

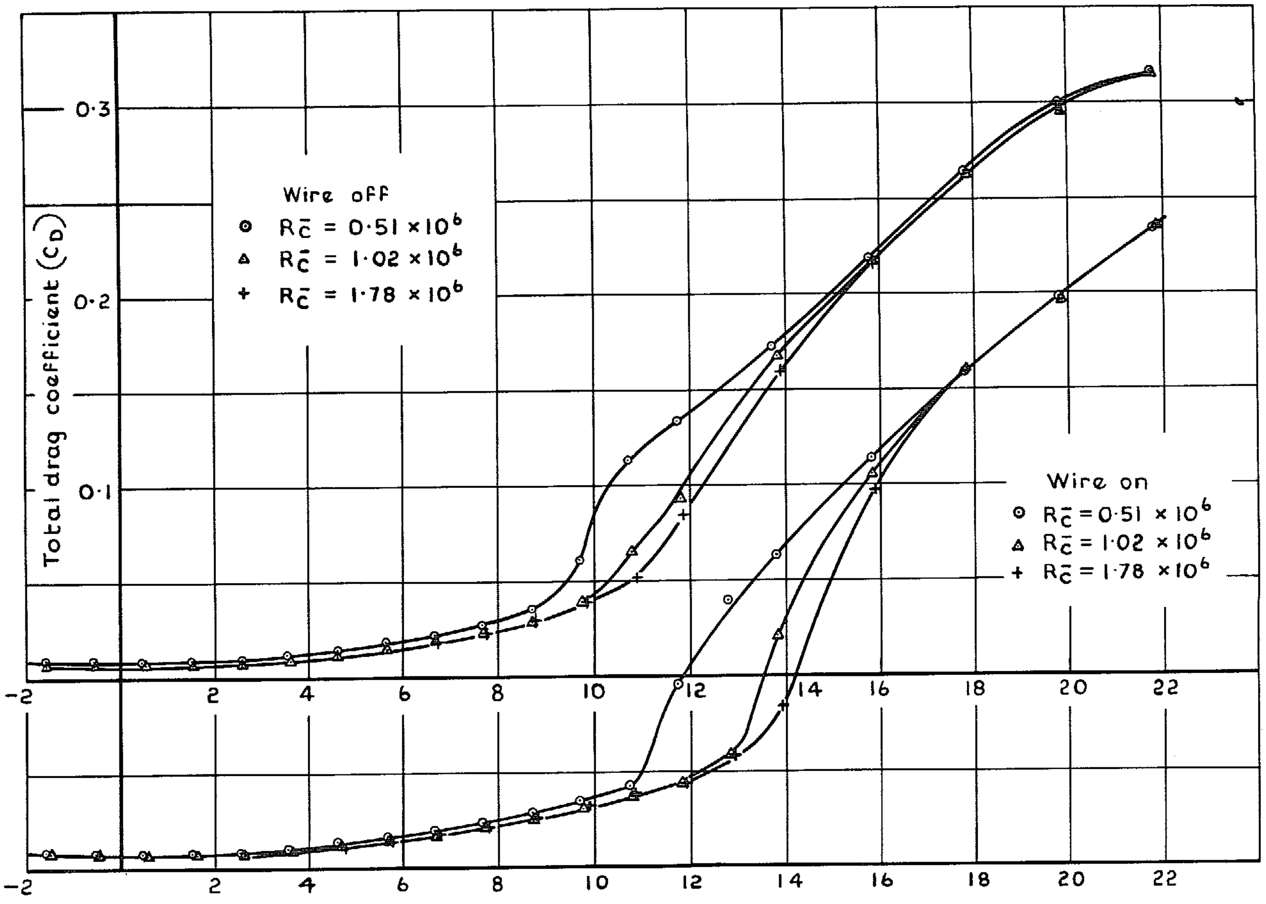

FIG. 16. Comparison of drag of wing with and without wire over the Reynolds number range.

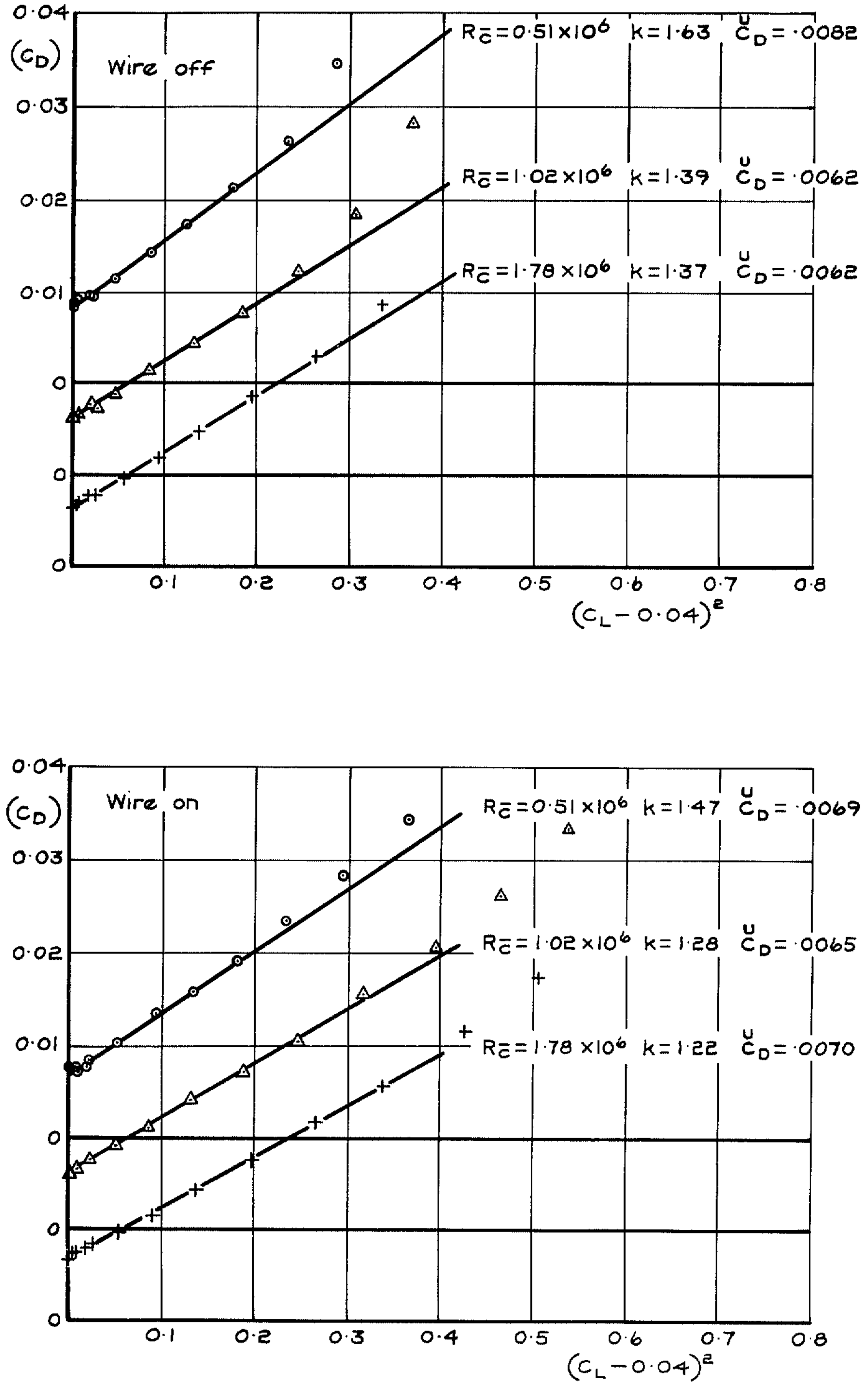

FIG. 17. Comparison of induced drag characteristics with and without wire over the Reynolds number range.

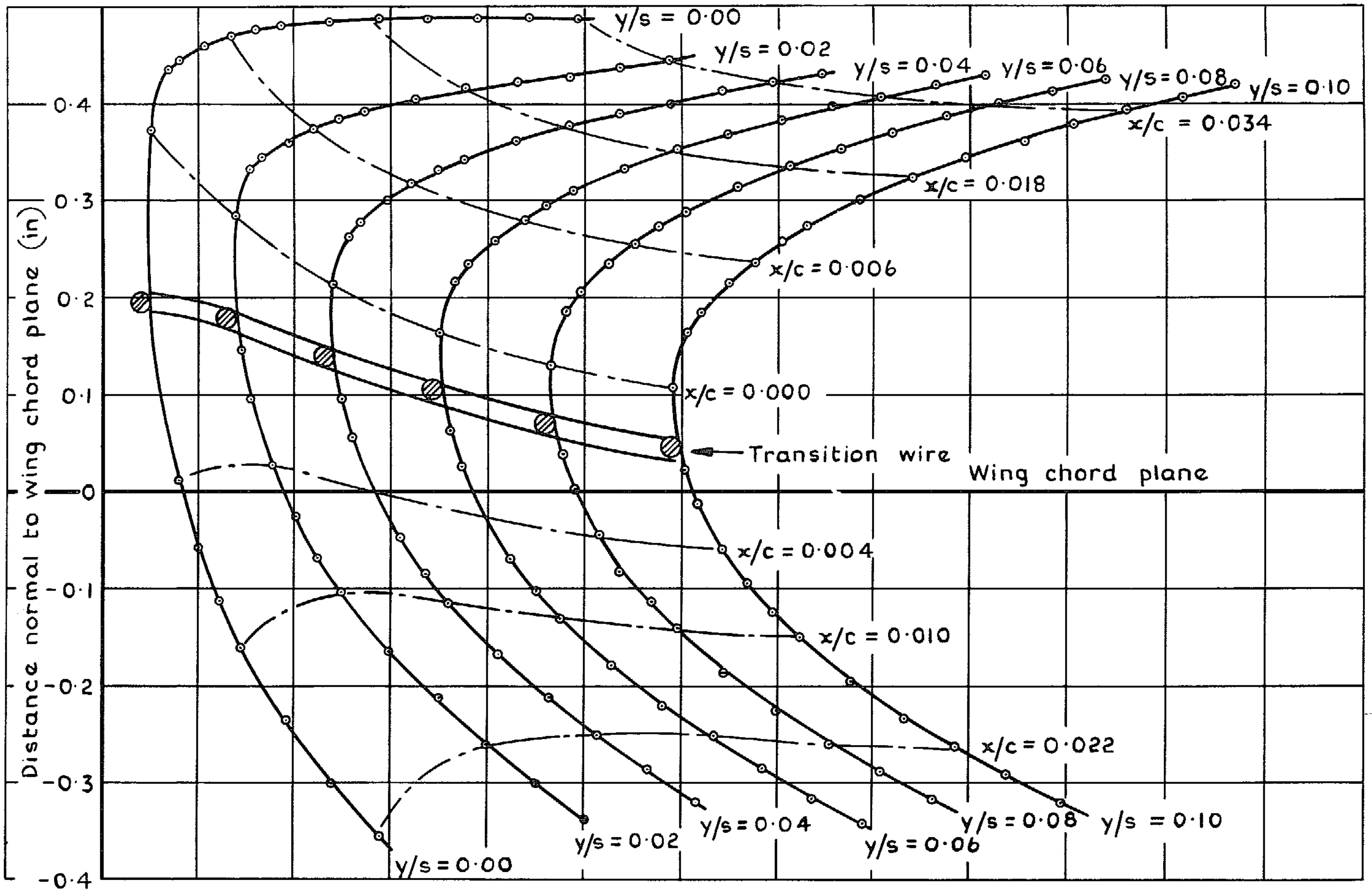

FIG. 18. Horizontal projection of leading edge geometry near the wing root showing transition wire.

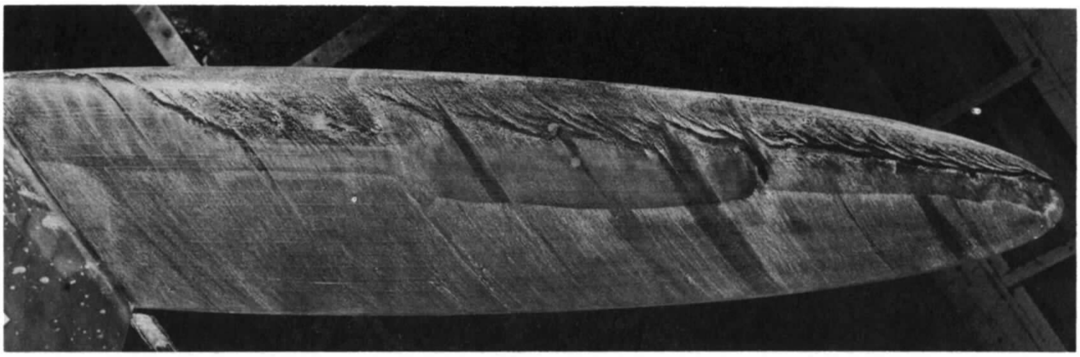

$\alpha = 3.60$ degrees

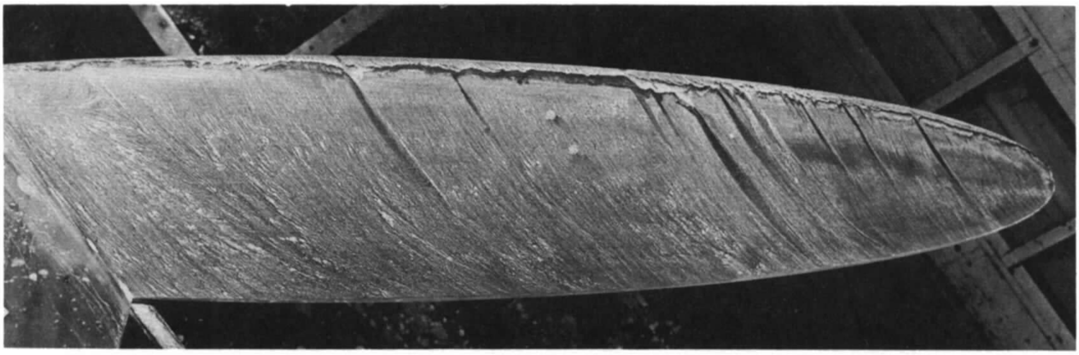

$\alpha = 6.50$ degrees

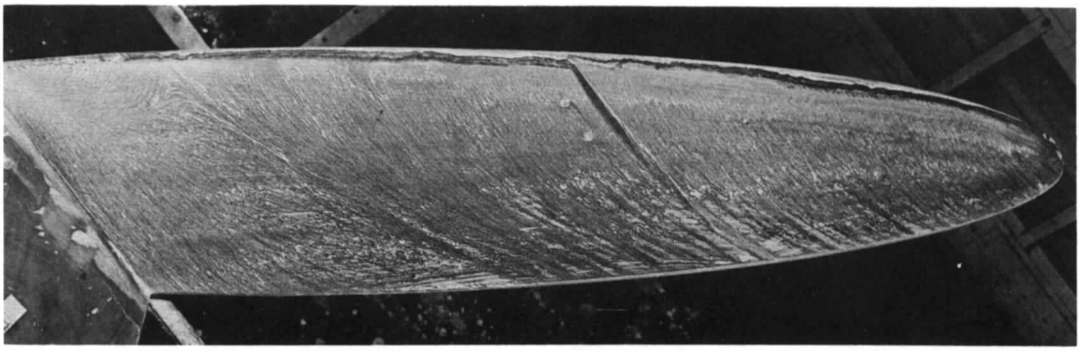

$\alpha = 8.10$ degrees

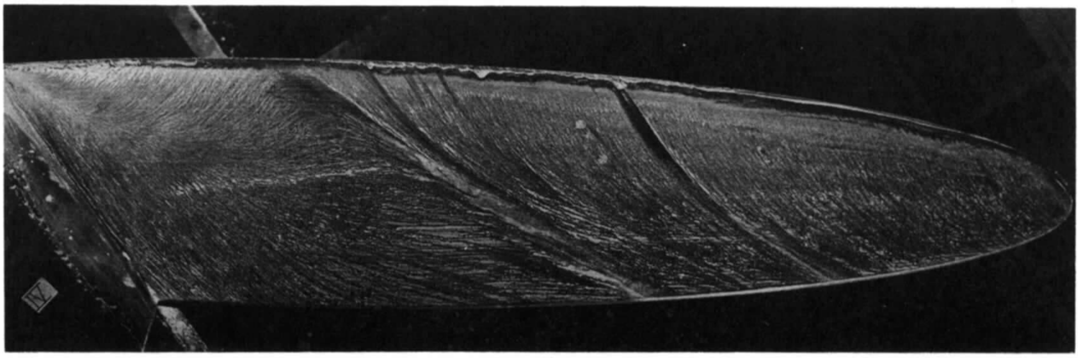

$\alpha = 9.20$ degrees

FIG. 19. Flow visualization at $R_{\bar{c}} = 0{\cdot}51 \times 10^6$ wire off.

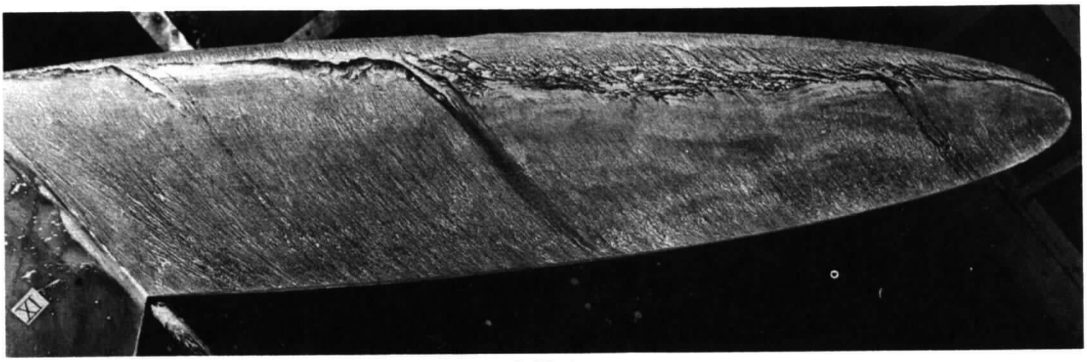

α = 3.60 degrees

α = 6.50 degrees

α = 8.10 degrees

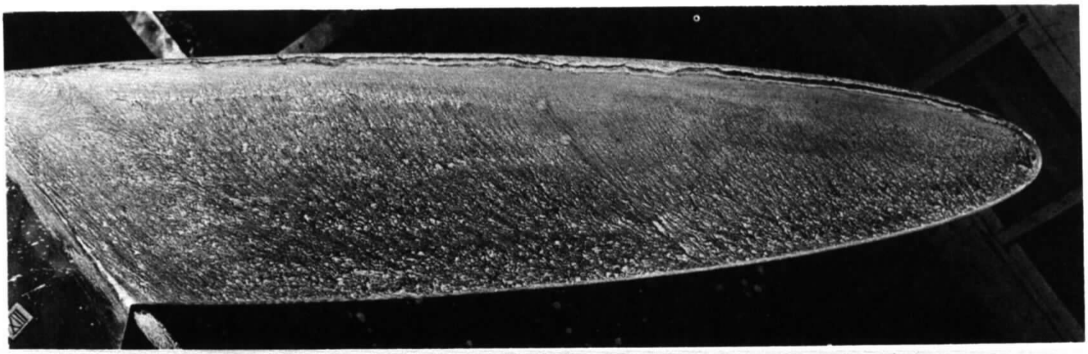

α = 9.20 degrees

FIG. 20. Flow visualization at $R_{\bar{c}} = 0{\cdot}51 \times 10^6$ wire on.

a = 10.20 degrees

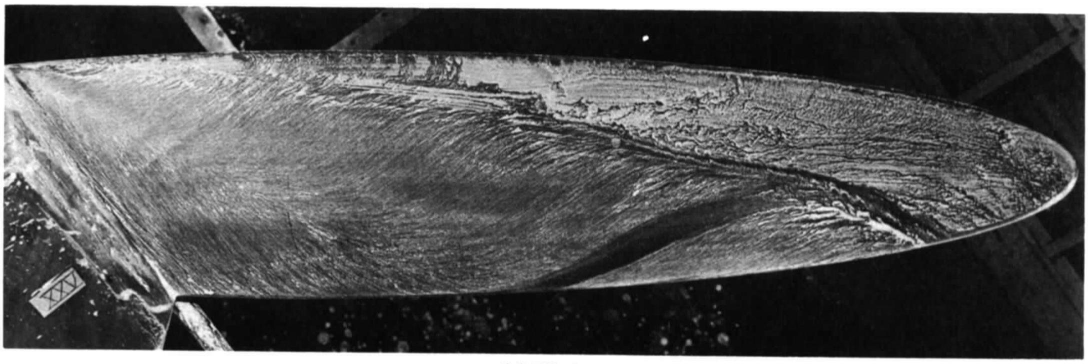

a = 11.70 degrees

a = 17.90 degrees

FIG. 21. Flow visualization at $R_{\bar{c}} = 0{\cdot}51 \times 10^6$ wire off.

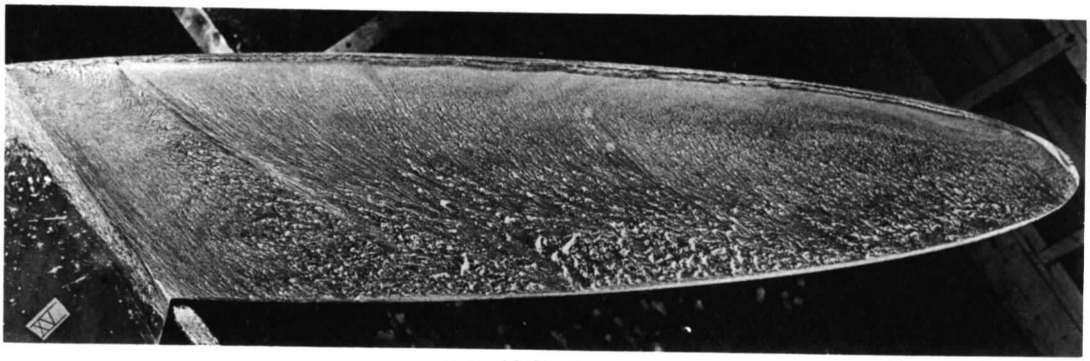

α = 10.20 degrees

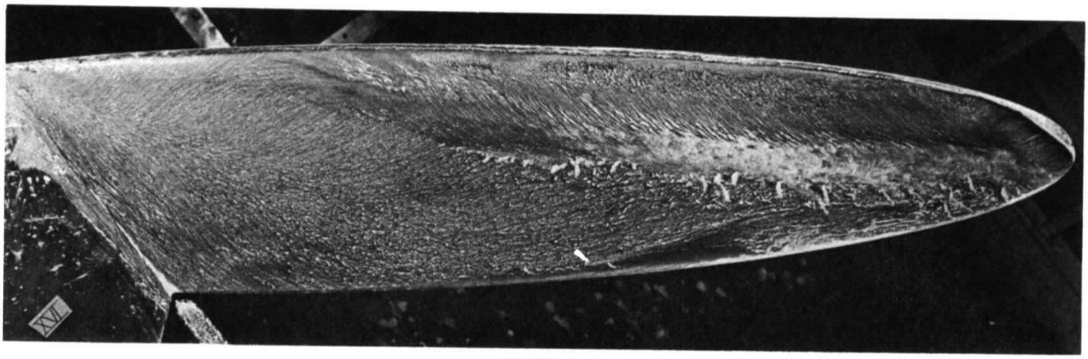

α = 10.90 degrees

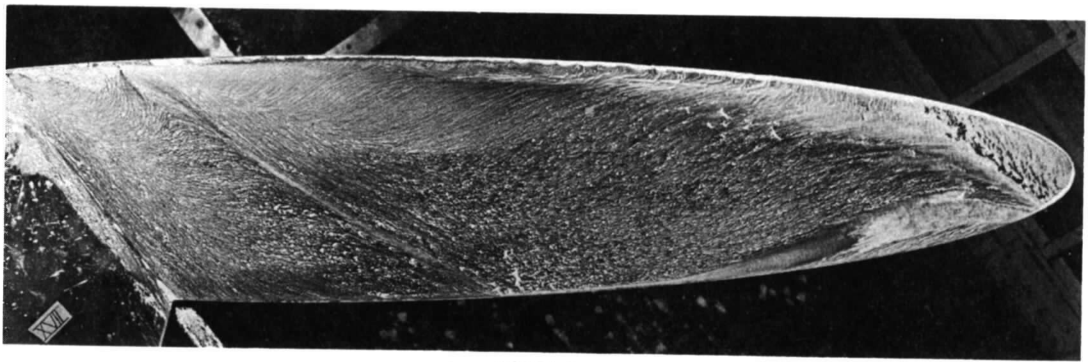

α = 12.00 degrees

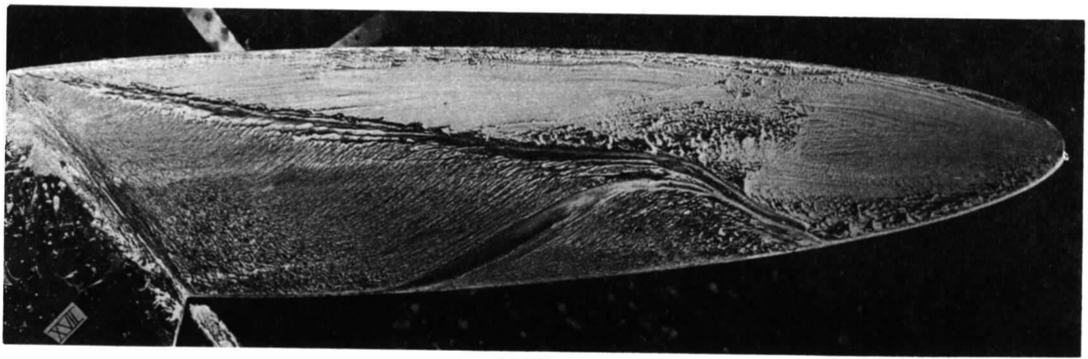

α = 16.60 degrees

FIG. 22. Flow visualization at $R_{\bar{c}} = 0{\cdot}51 \times 10^6$ wire on.

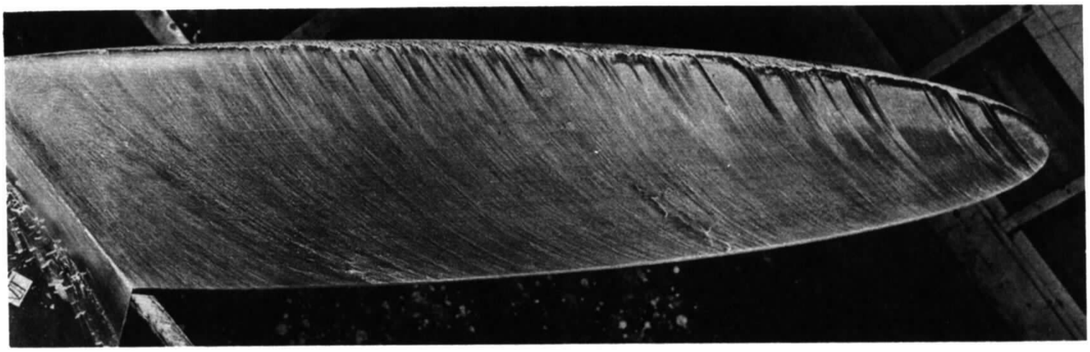

a = 7.20 degrees

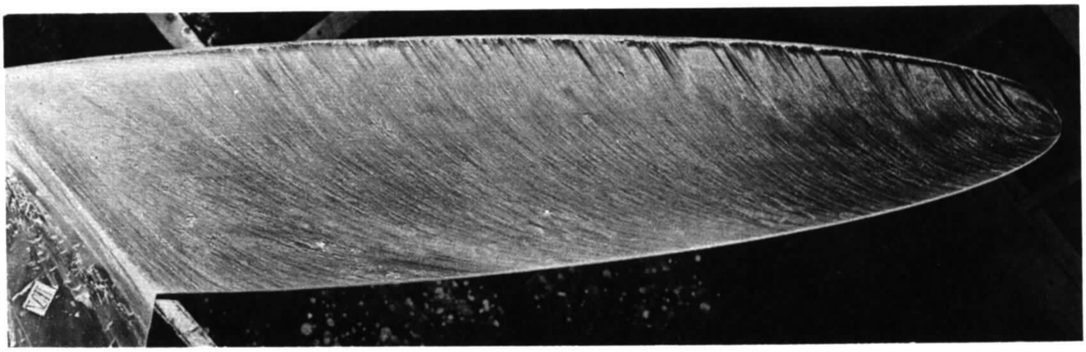

a = 8.70 degrees

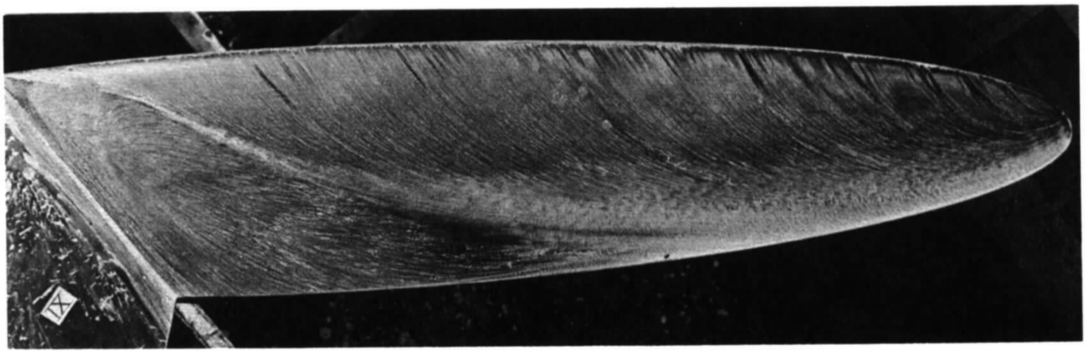

a = 10.70 degrees

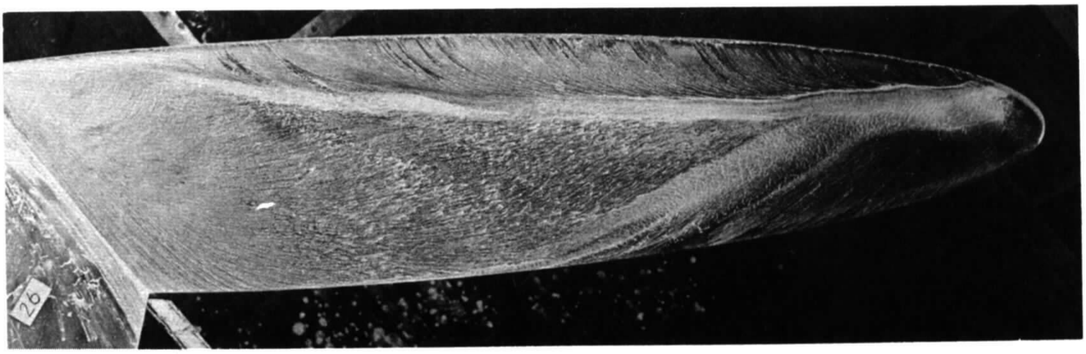

a = 11.90 degrees

FIG. 23. Flow visualization at $R_{\bar{c}} = 1{\cdot}02 \times 10^6$ wire off.

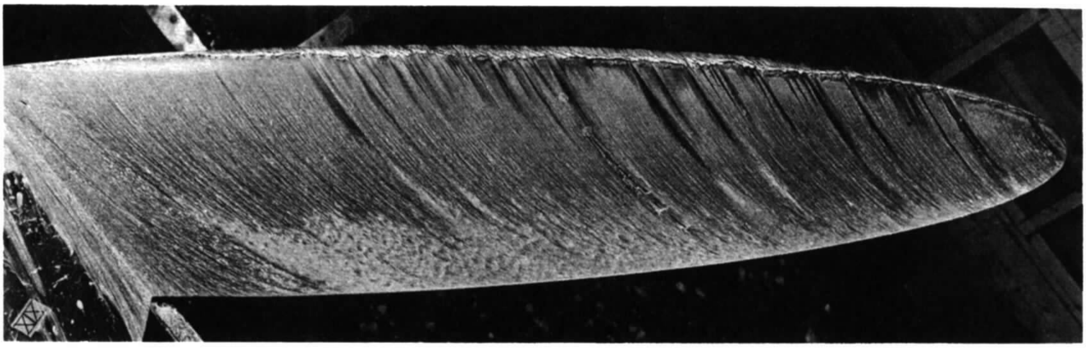

α = 7.20 degrees

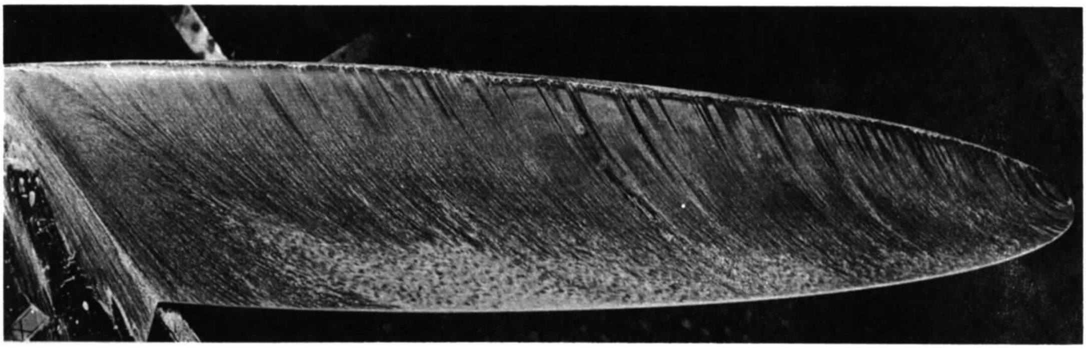

α = 8.70 degrees

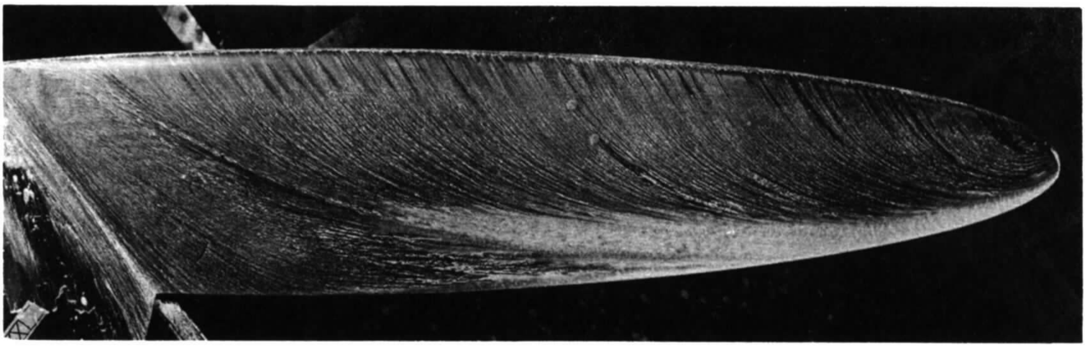

α = 10.70 degrees

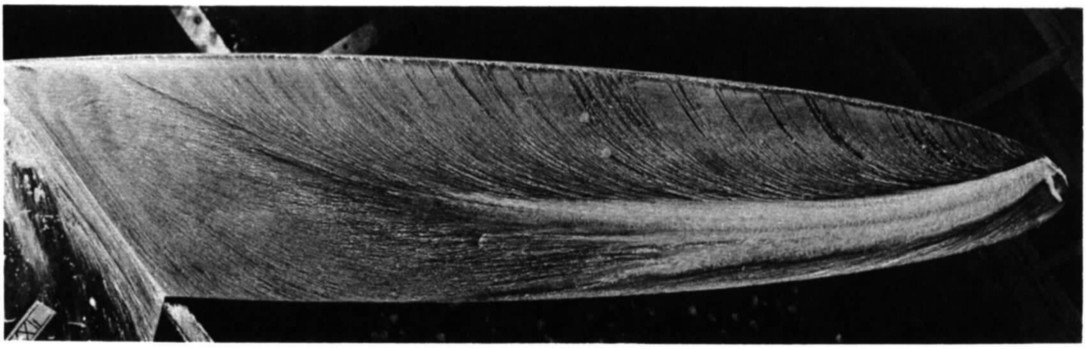

α = 11.80 degrees

FIG. 24. Flow visualization at $R_{\bar{c}} = 1{\cdot}02 \times 10^6$ wire on.

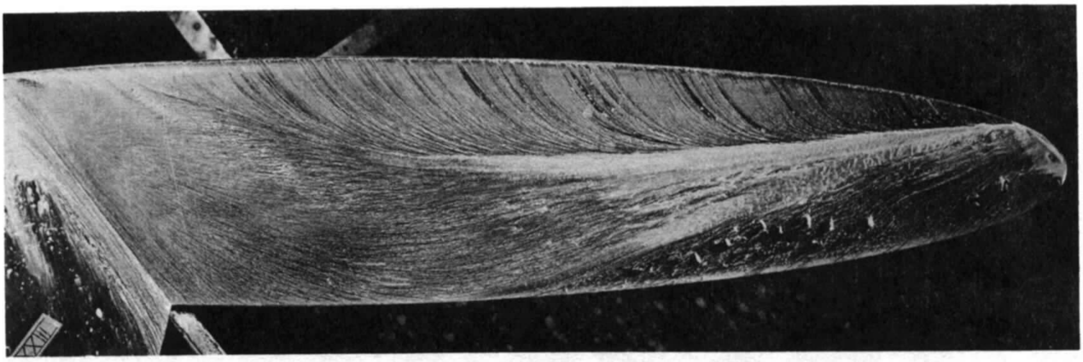

a = 12.80 degrees

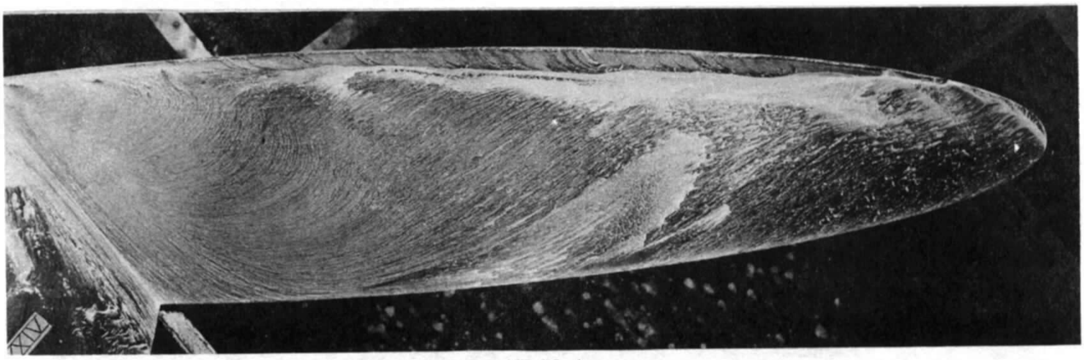

a = 15.10 degrees

FIG. 25. Flow visualization at $R_{\bar{c}} = 1{\cdot}02 \times 10^6$ wire on.

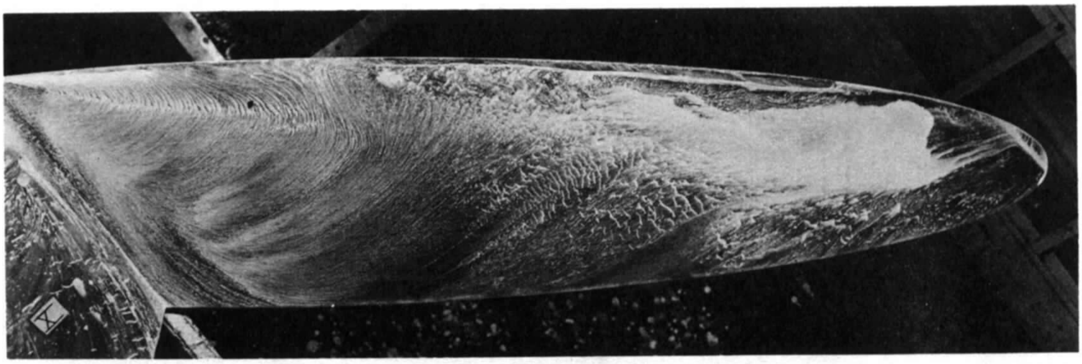

a = 16.70 degrees

FIG. 26. Flow visualization at $R_{\bar{c}} = 1{\cdot}02 \times 10^6$ wire off.

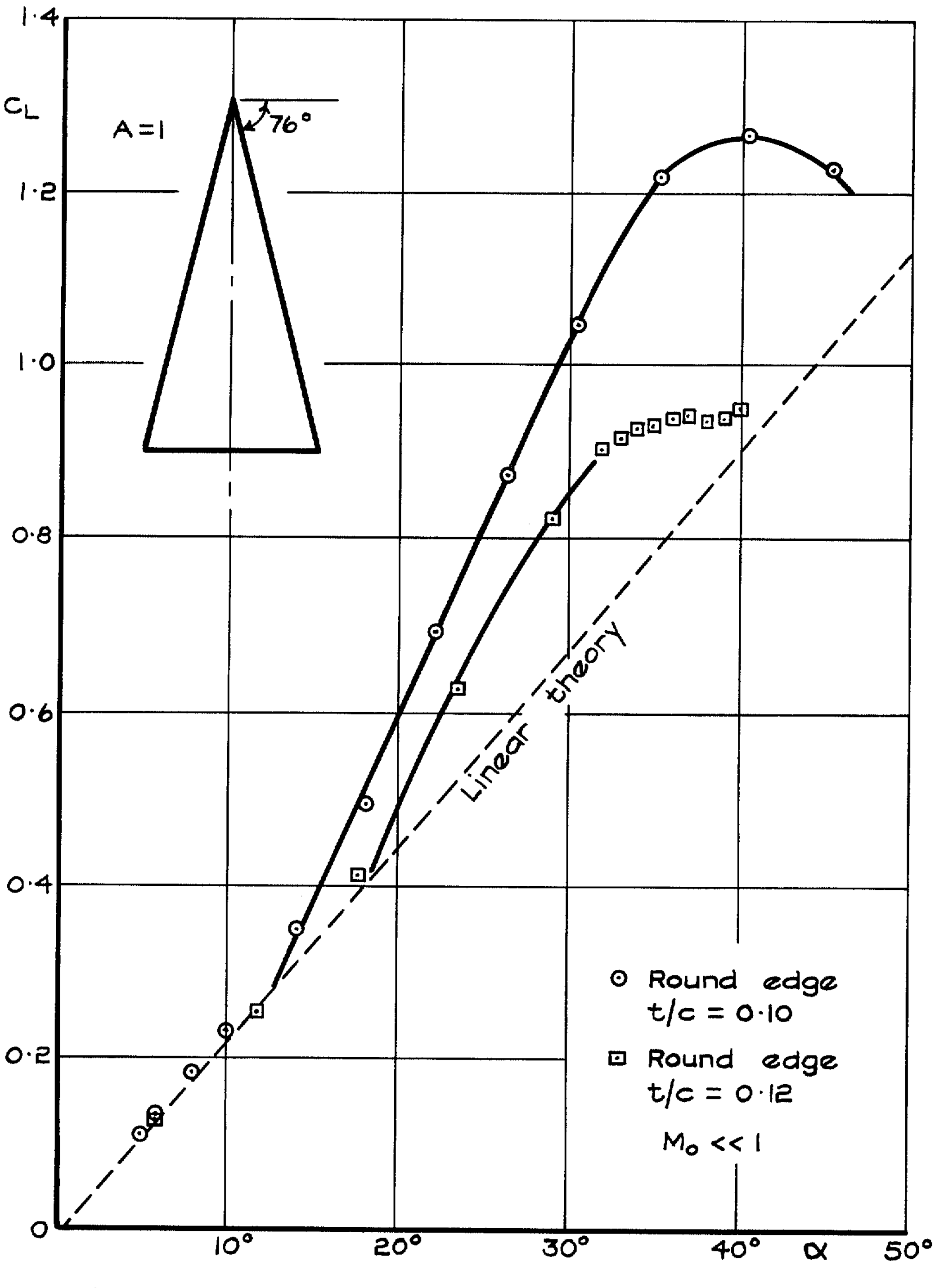

FIG. 27. Typical lift-incidence relation for a delta wing with a round leading edge (abstracted from Ref. 20).

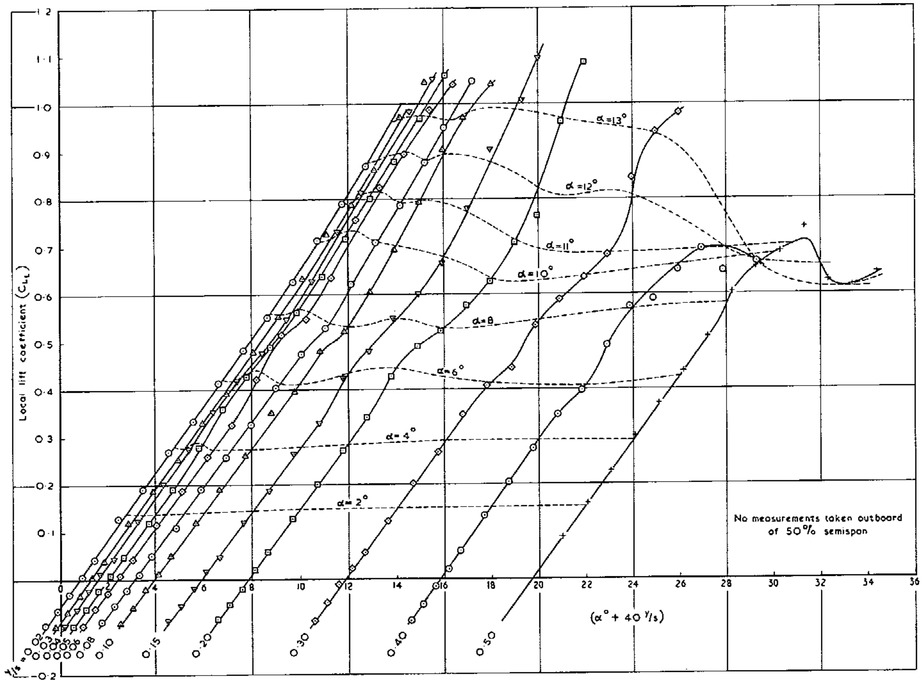

FIG. 28. Variation of local lift coefficient with spanwise position and incidence $R_{\bar{c}} = 1{\cdot}78 \times 10^6$ wire off.

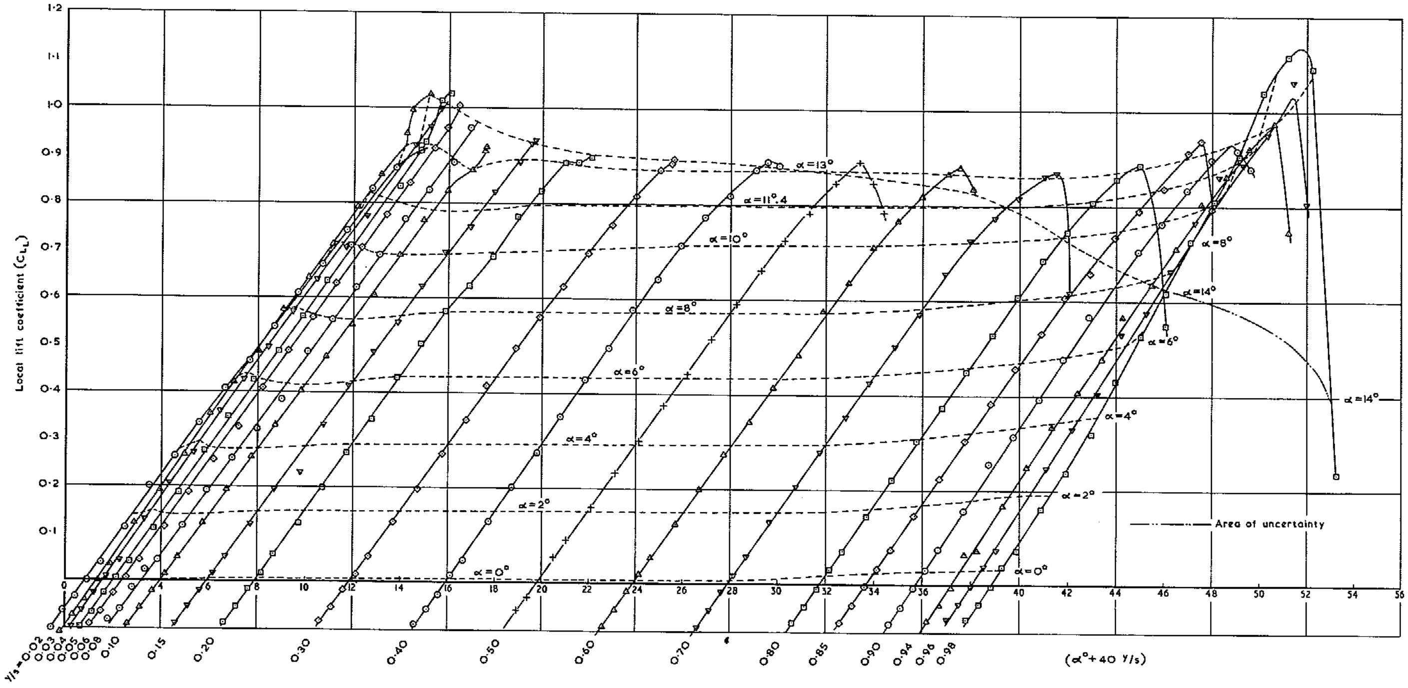

FIG. 29. Variation of local lift coefficient with spanwise position and incidence $R_{\bar{c}} = 1{\cdot}78 \times 10^6$ wire on.

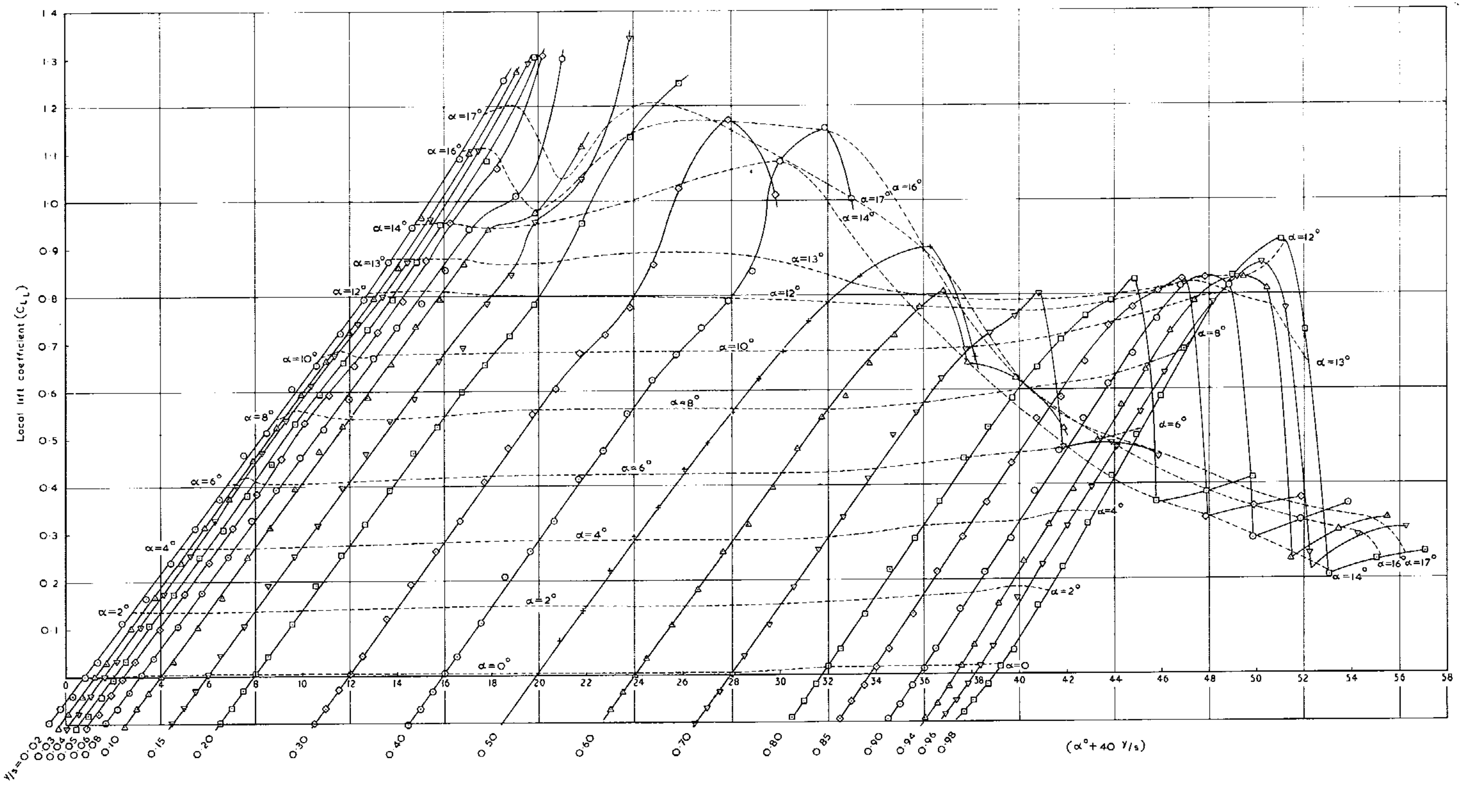

FIG. 30. Variation of local lift coefficient with spanwise position and incidence $R_{\bar{c}} = 1{\cdot}02 \times 10^6$ wire on.

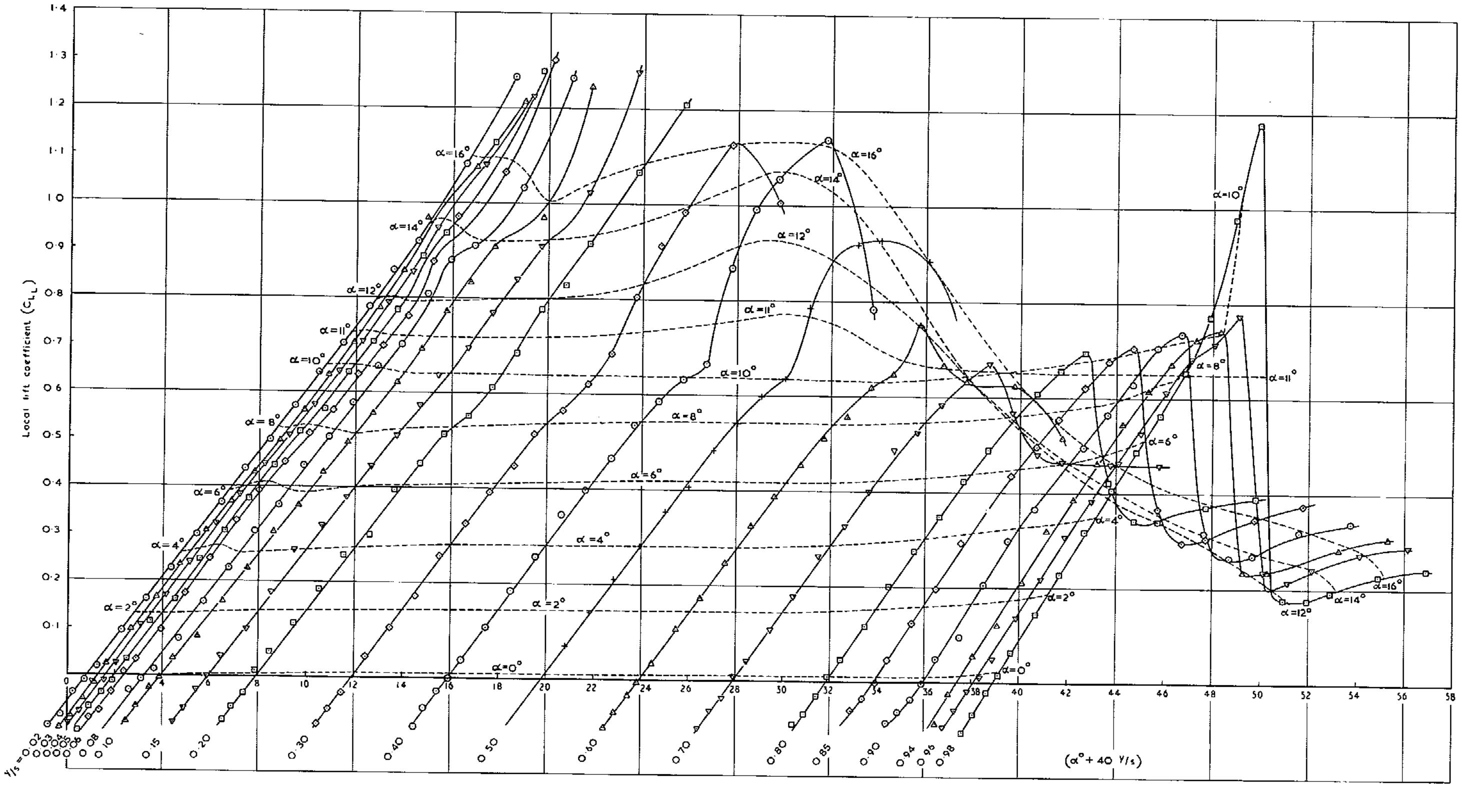

FIG. 31. Variation of local lift coefficient with spanwise position and incidence $R_{\bar{c}} = 0{\cdot}51 \times 10^6$ wire on.

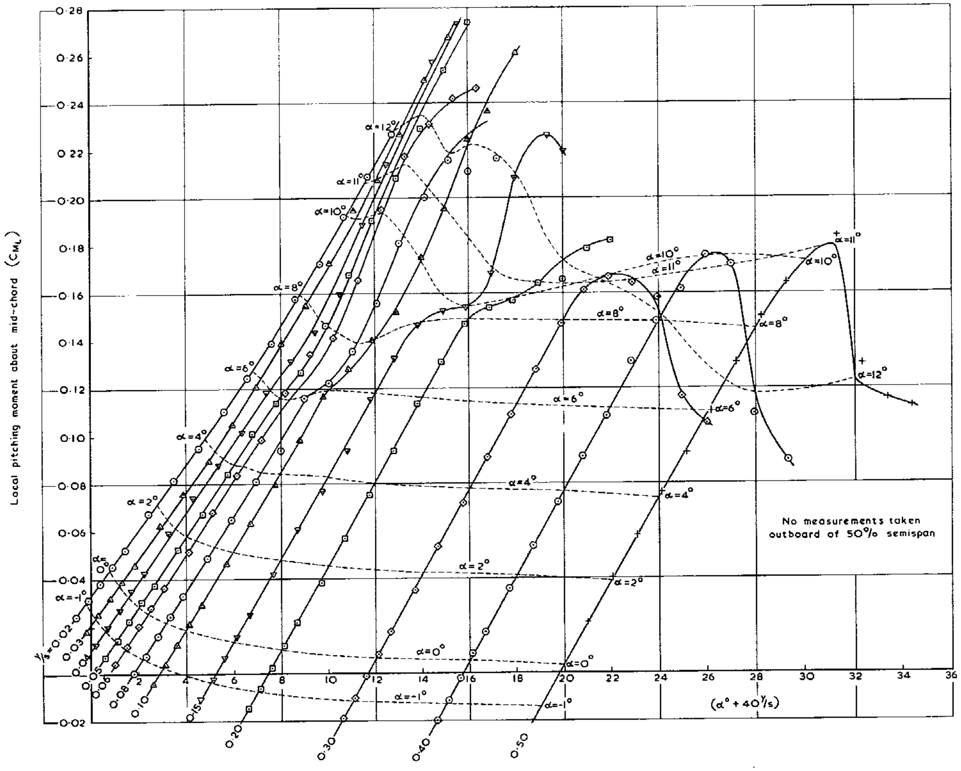

FIG. 32. Variation of local pitching moment about mid-chord with spanwise position and incidence $R_{\bar{c}} = 1{\cdot}78 \times 10^6$ wire off.

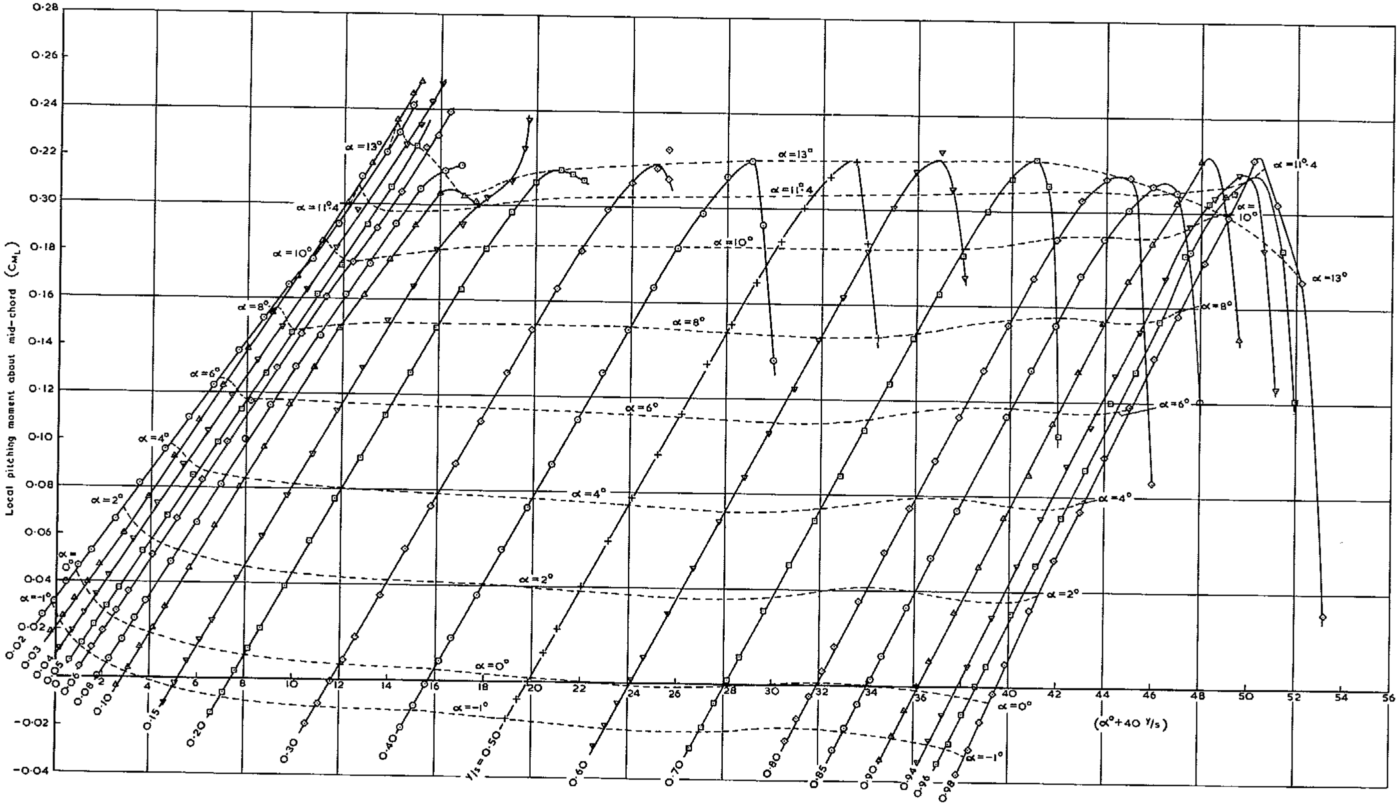

FIG. 33. Variation of local pitching moment about mid-chord with spanwise position and incidence $R_{\bar{c}} = 1{\cdot}78 \times 10^6$ wire on.

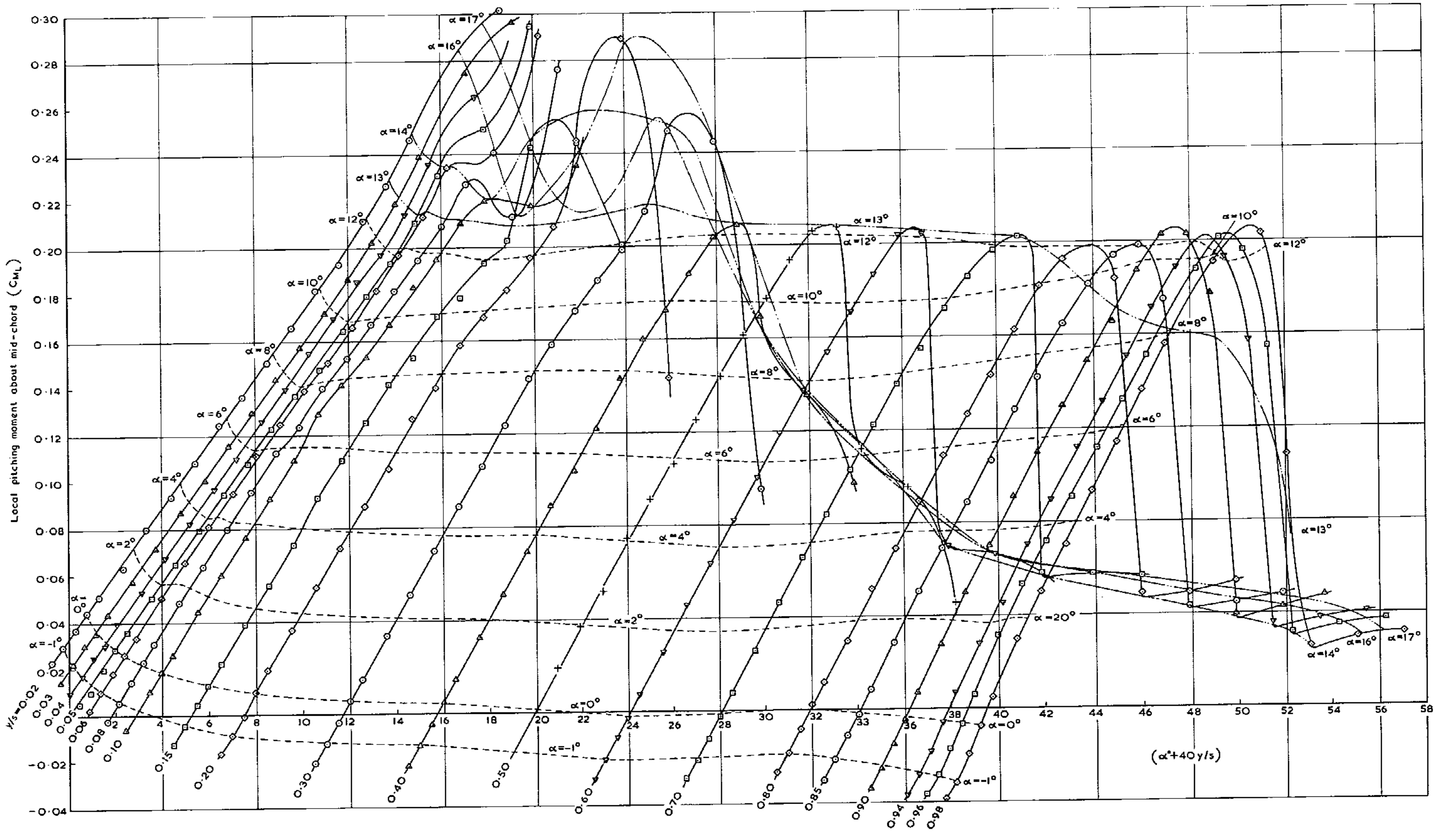

FIG. 34. Variation of local pitching moment about mid-chord with spanwise position and incidence
$R_{\bar{c}} = 1{\cdot}02 \times 10^6$ wire on.

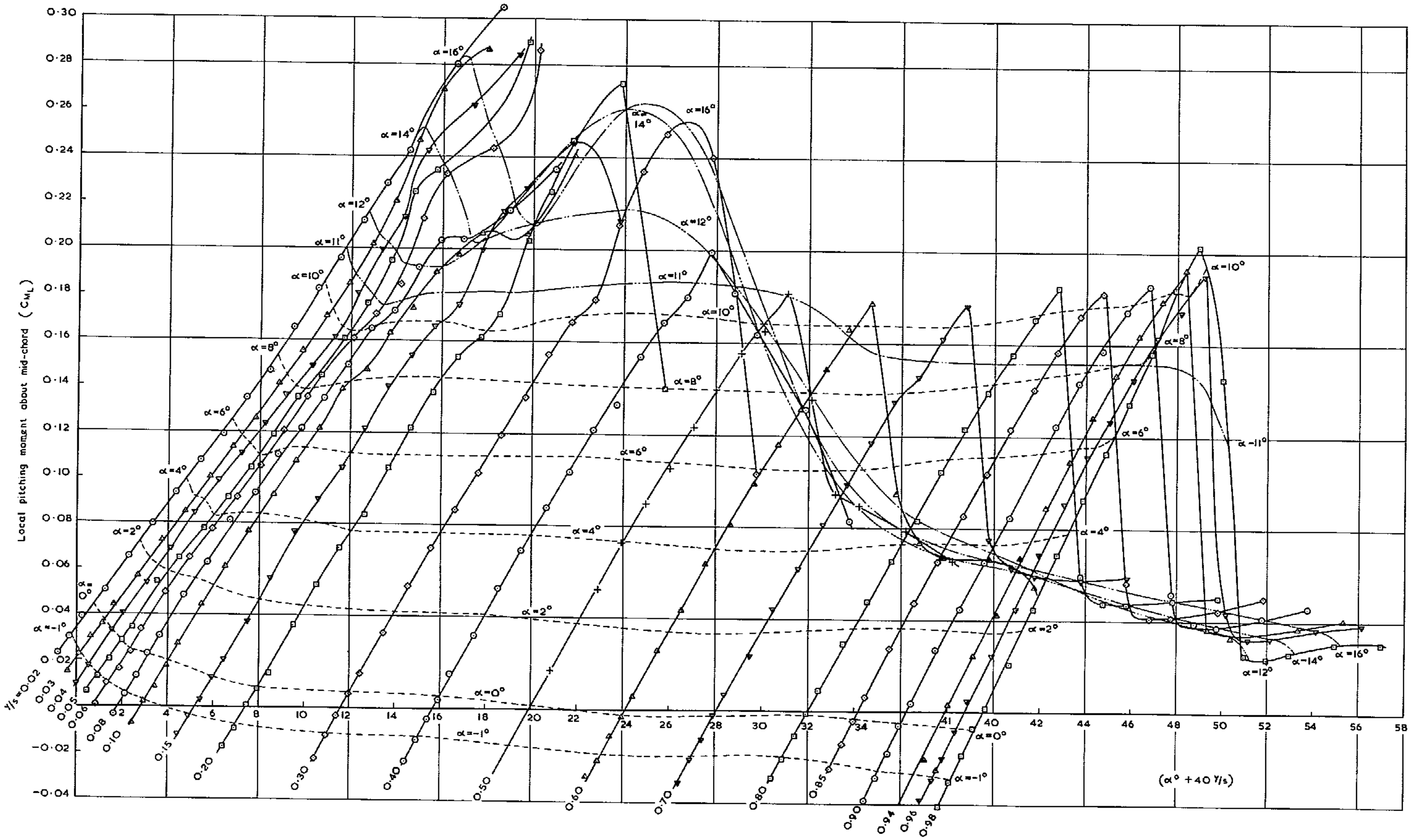

FIG. 35. Variation of local pitching moment about mid-chord with spanwise position and incidence $R_{\bar{c}} = 0{\cdot}51 \times 10^6$ wire on.

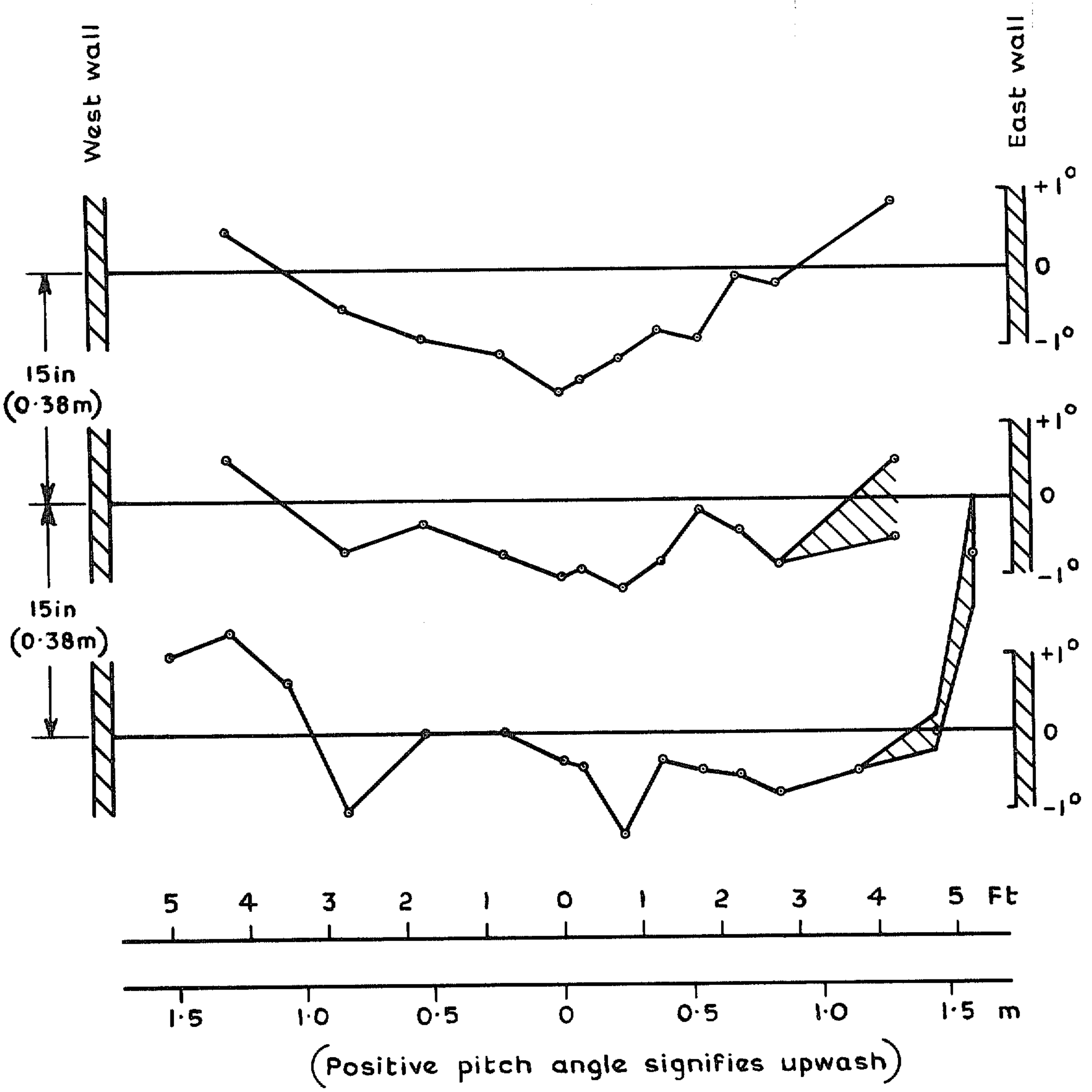

FIG. 36. Spanwise variations of pitch angle in the tunnel at three heights as determined by long tufts (calibration carried out 6 months after pressure plotting tests) (abstracted from unpublished work, A. R. Beauchamp).

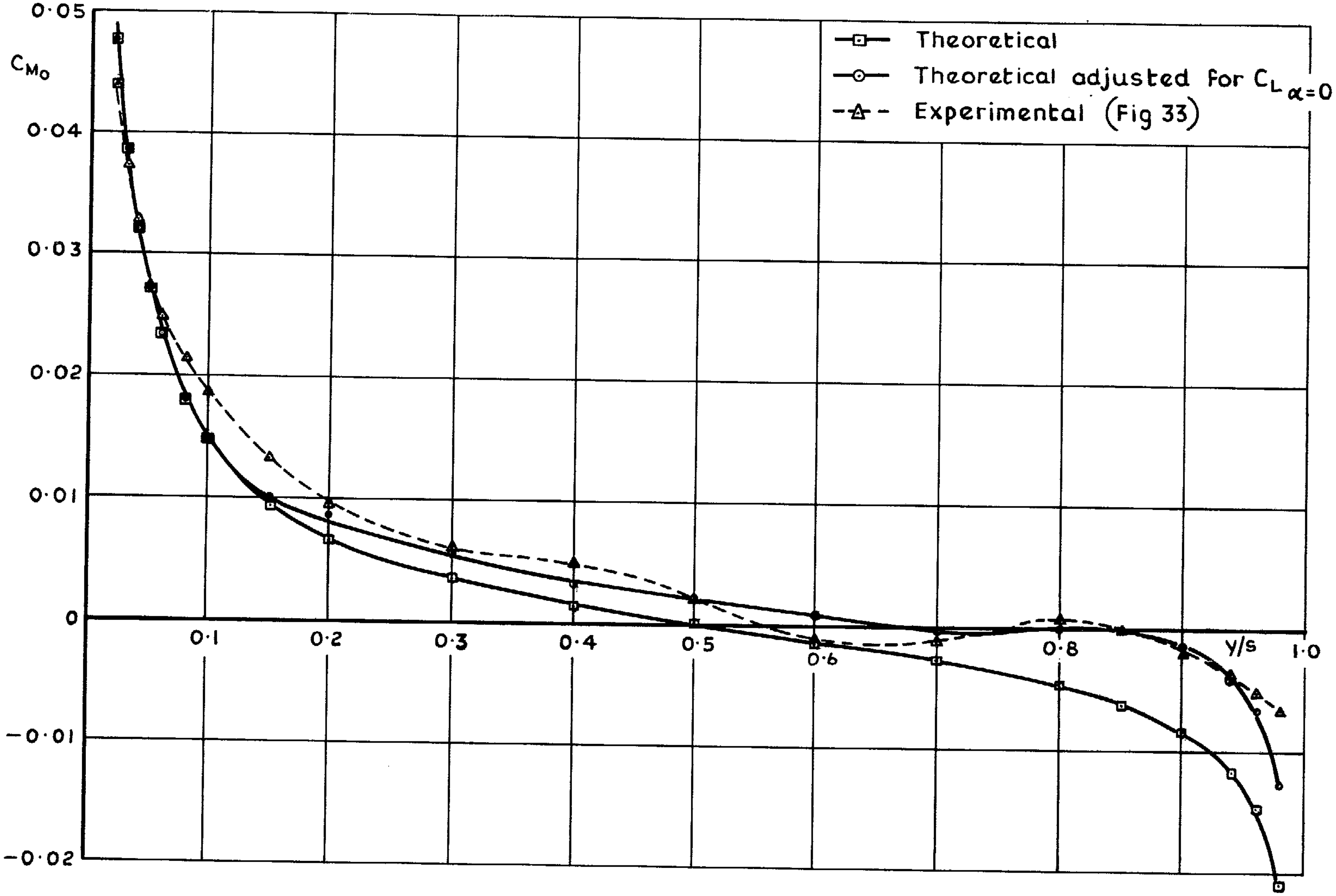

FIG. 37. Comparison between measured and theoretical spanwise distributions of C_{M_0}.

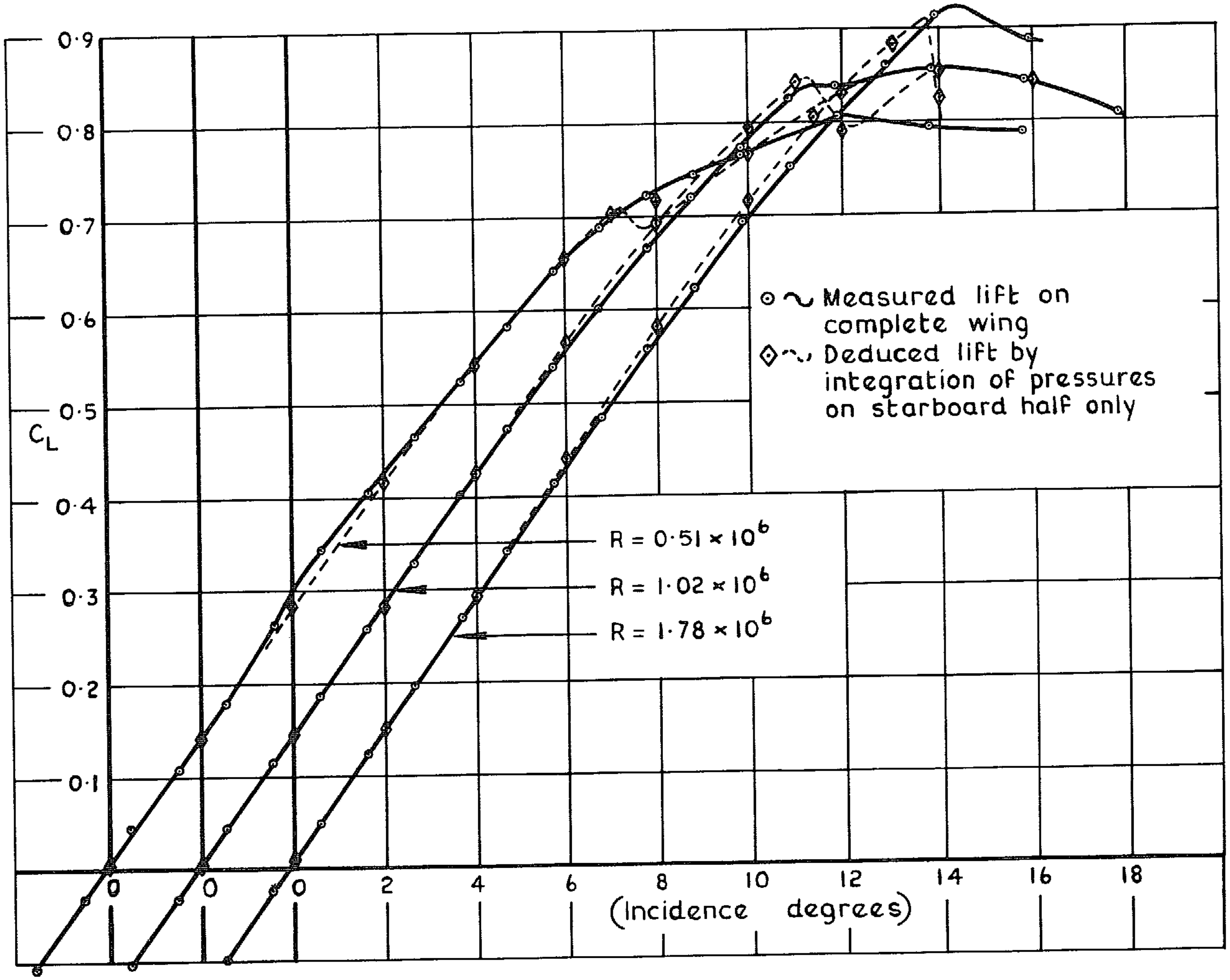

FIG. 38. Comparison of measured lift on complete wing with lift deduced from integration of pressures on starboard wing only (wire on).

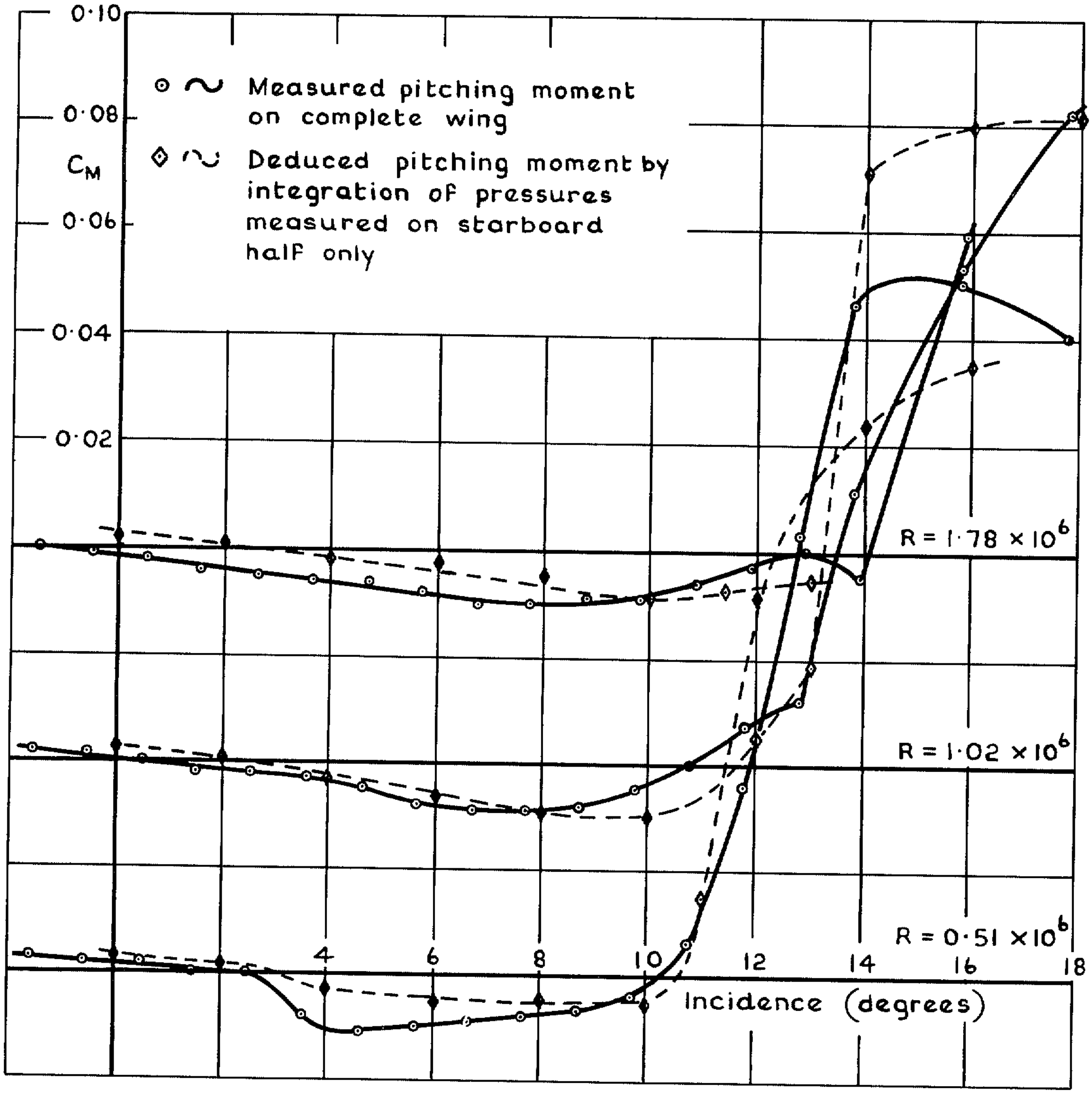

FIG. 39. Comparison of measured pitching moments on complete wing with those deduced from integration of pressures on starboard wing only (wire on).

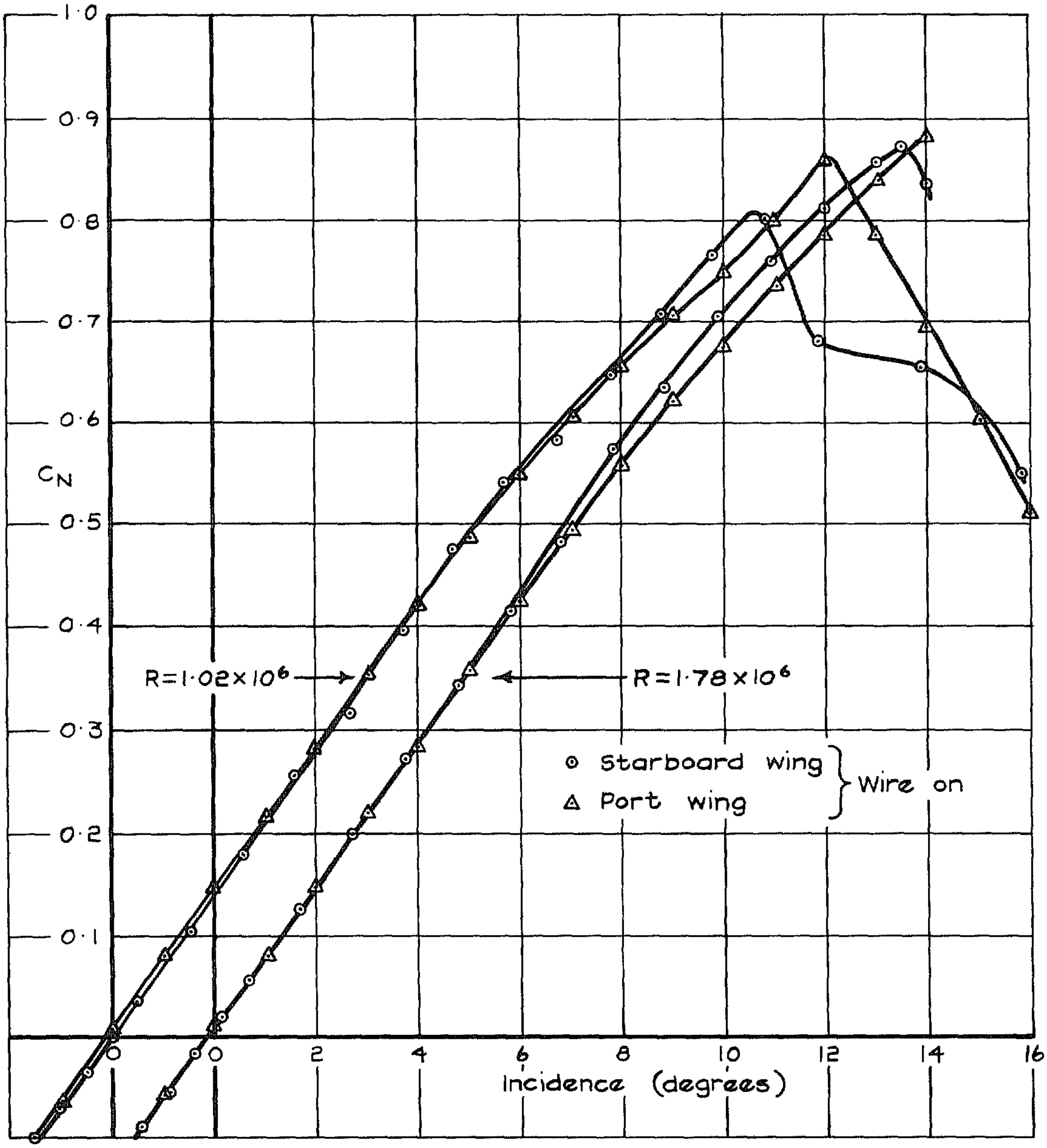

FIG. 40. Comparison of lifting behaviour of sections at 60 per cent semi-span on port and starboard wings.

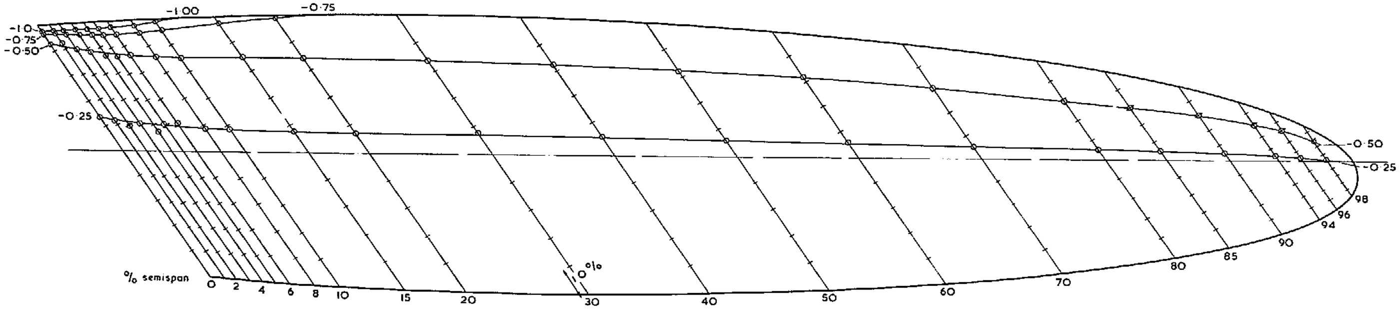

a $\alpha = 2°·67$ ($C_L \simeq 0·20$) $R_{\bar{c}} = 1·78 \times 10^6$ wire on

FIG. 41a. Isobar pattern at low incidence.

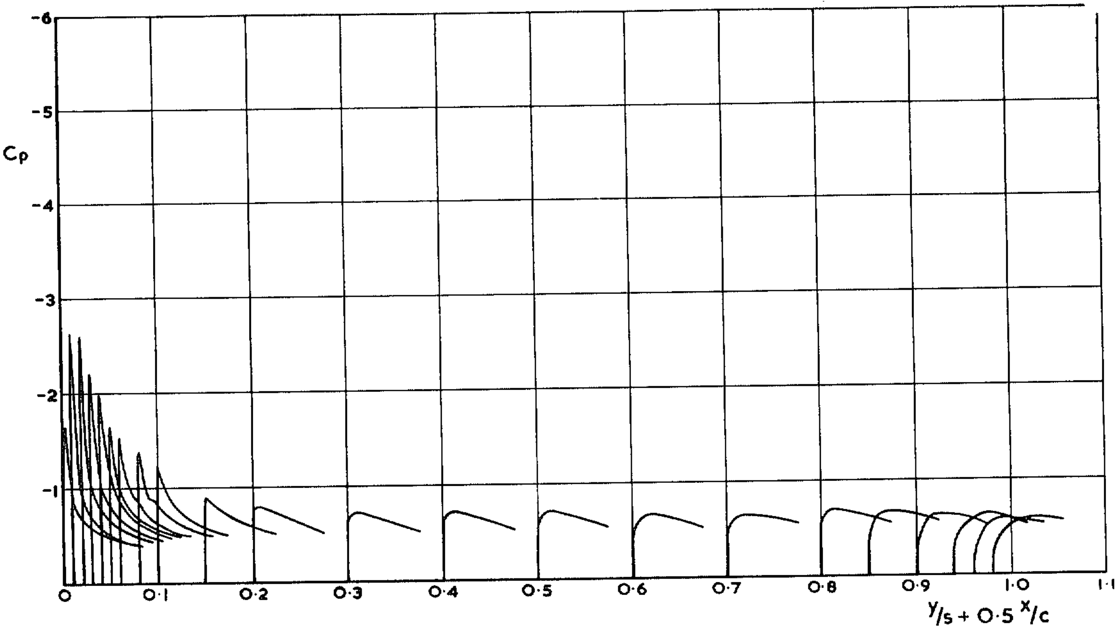

a $\alpha=2\cdot67°$ $(C_L \simeq 0\cdot2)$, $R_{\bar{c}}=1\cdot78\times10^6$ wire on

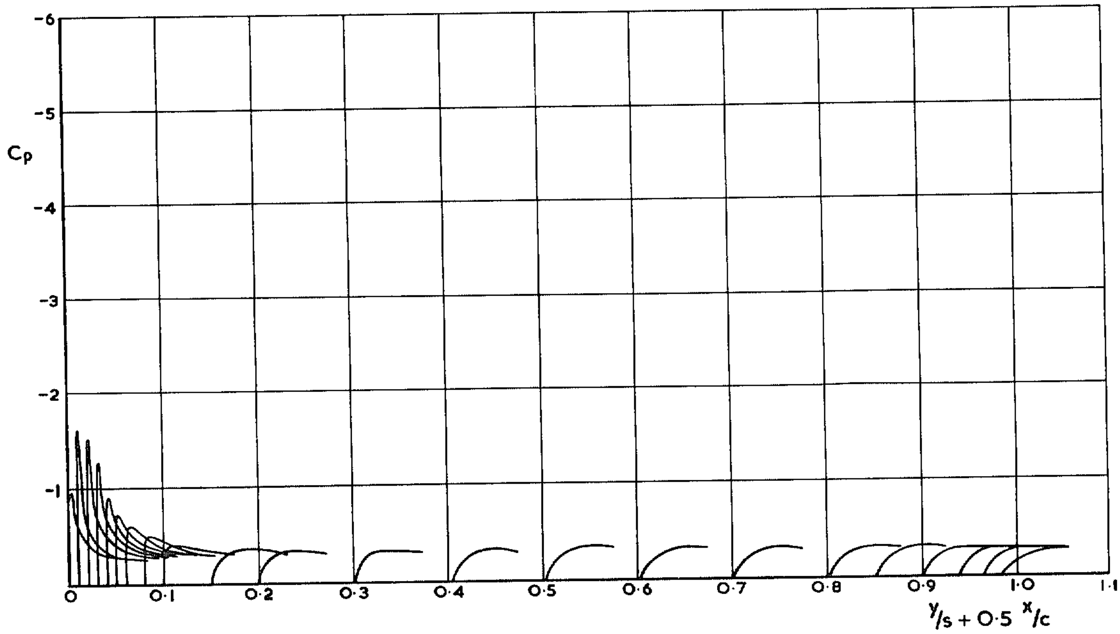

b $\alpha=-0\cdot1°$ $(C_L \simeq 0)$, $R_{\bar{c}}=1\cdot78\times10^6$ wire on

FIG. 42a–b. Spanwise variation of pressure distribution over forward 15 per cent of chord.

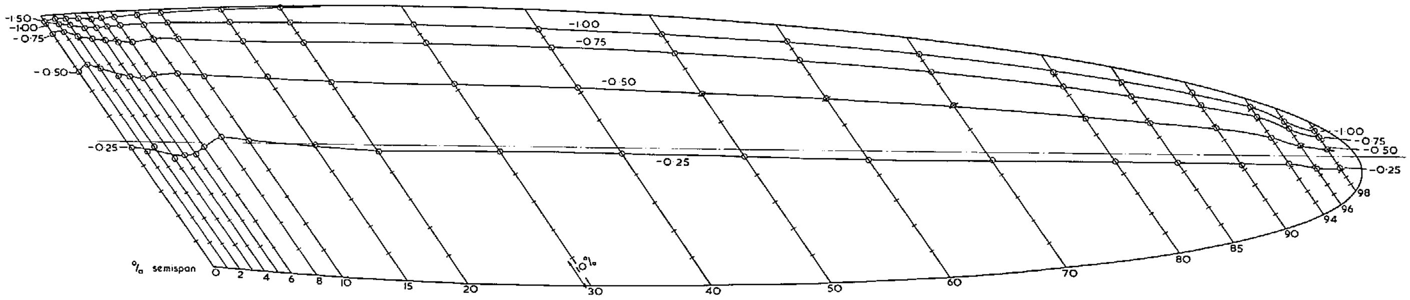

a α = 5°·47 ($C_L \simeq 0·40$) $R_{\bar{c}}$ = 1·78 × 10^6 wire on

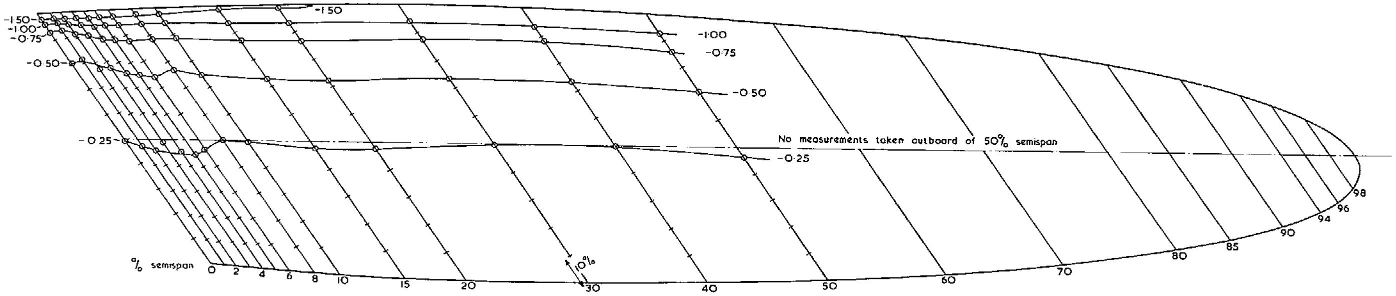

b α = 5·47 ($C_L \simeq 0·40$) $R_{\bar{c}}$ = 1·78 × 10^6 wire off

FIG. 43a–b. Comparison of isobar patterns with and without wire at $\alpha = 5·47°$, $R_{\bar{c}} = 1·78 \times 10^6$.

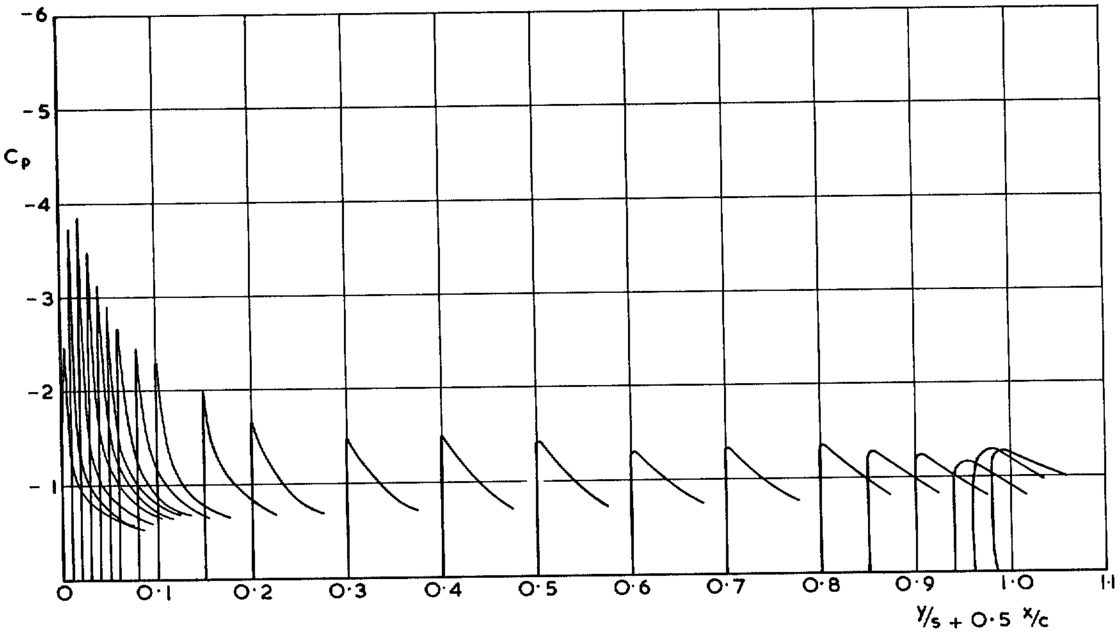

a $\alpha = 5·47° (C_L \simeq 0·4)$, $R_{\bar{c}} = 1·78 \times 10^6$ wire on

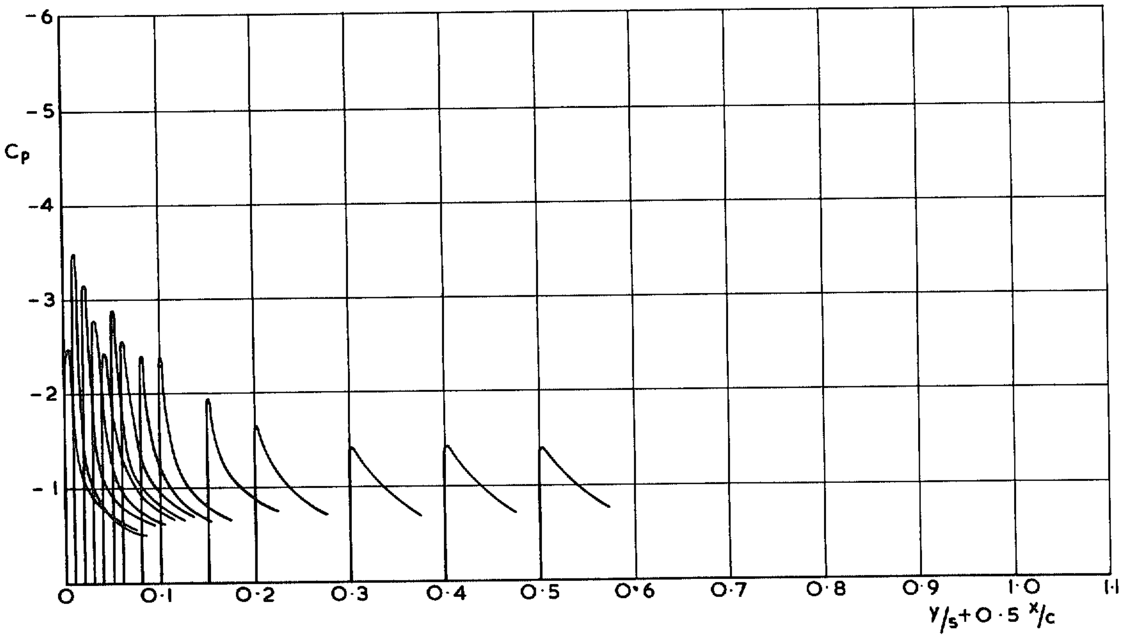

b $\alpha = 5·47° (C_L \simeq 0·4)$, $R_{\bar{c}} = 1·78 \times 10^6$ wire off

FIG. 44a–b. Spanwise variation of pressure distribution over forward 15 per cent of chord.

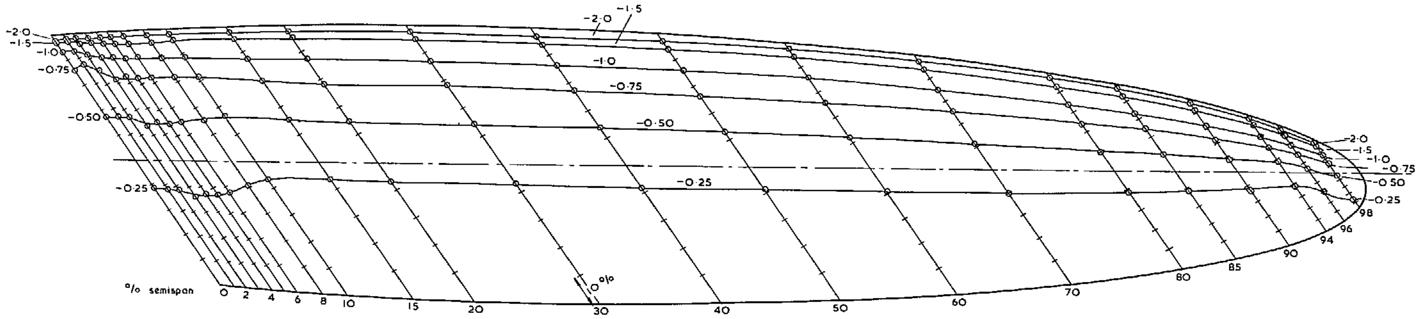

a $\alpha = 8^\circ\cdot33$ ($C_L \simeq 0\cdot60$) $R_{\bar{c}} = 1\cdot78 \times 10^6$ wire on

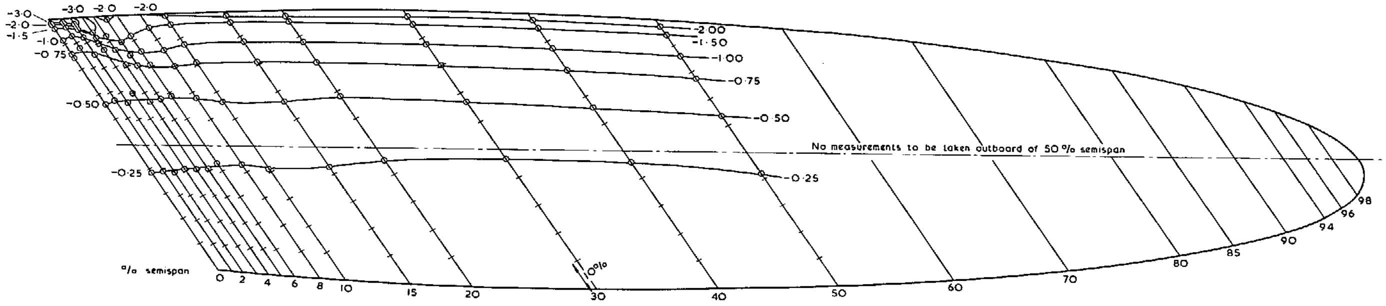

a $\alpha = 8^\circ\cdot33$ ($C_L \simeq 0\cdot59$) $R_{\bar{c}} = 1\cdot78 \times 10^6$ wire off

FIG. 45a–b. Comparison of isobars with and without wire at $\alpha = 8{\cdot}33^\circ$, $R_{\bar{c}} = 1{\cdot}78 \times 10^6$.

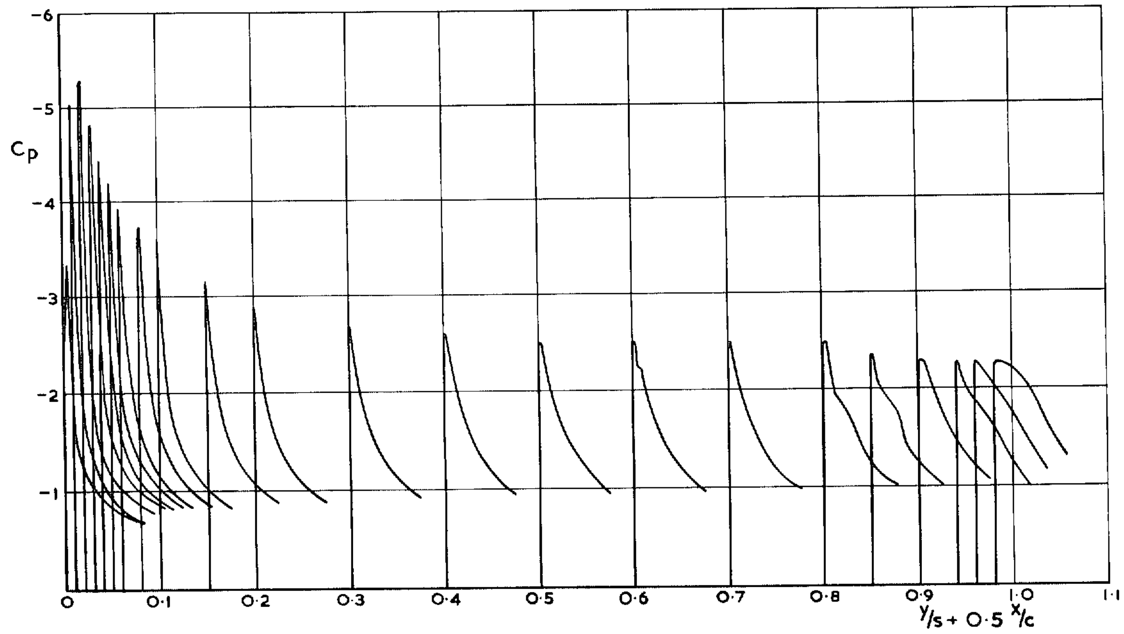

a $\alpha = 8{\cdot}33^\circ$ ($C_L \simeq 0{\cdot}6$), $R_{\bar{c}} = 1{\cdot}78 \times 10^6$ wire on

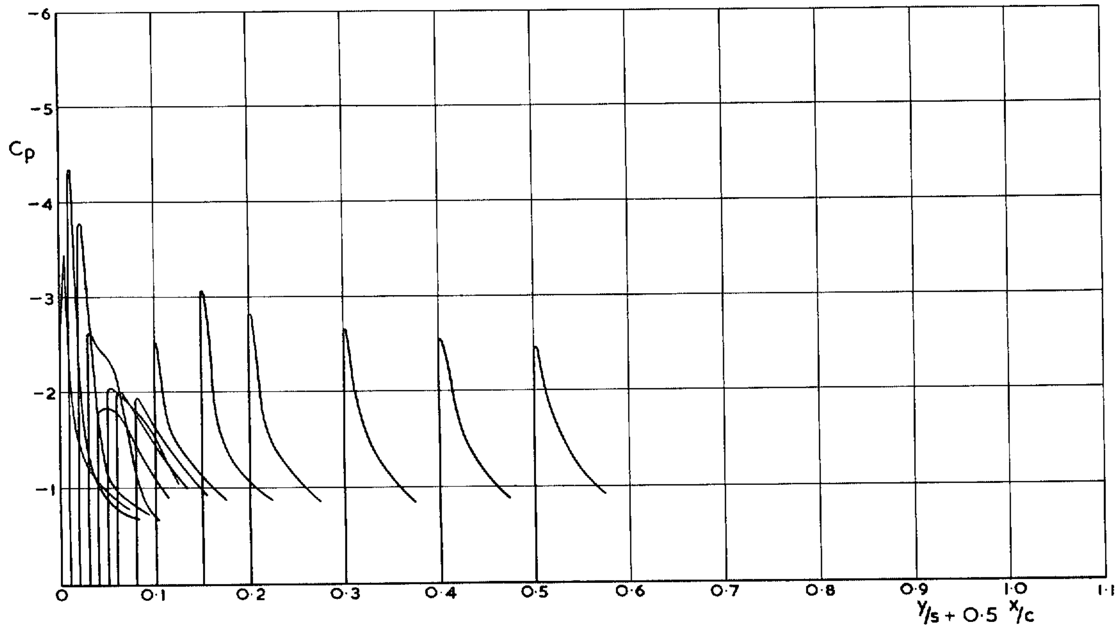

b $\alpha = 8{\cdot}33^\circ$ ($C_L \simeq 0{\cdot}59$), $R_{\bar{c}} = 1{\cdot}78 \times 10^6$ wire off

FIG. 46a–b. Spanwise variation of pressure distribution over forward 15 per cent of chord.

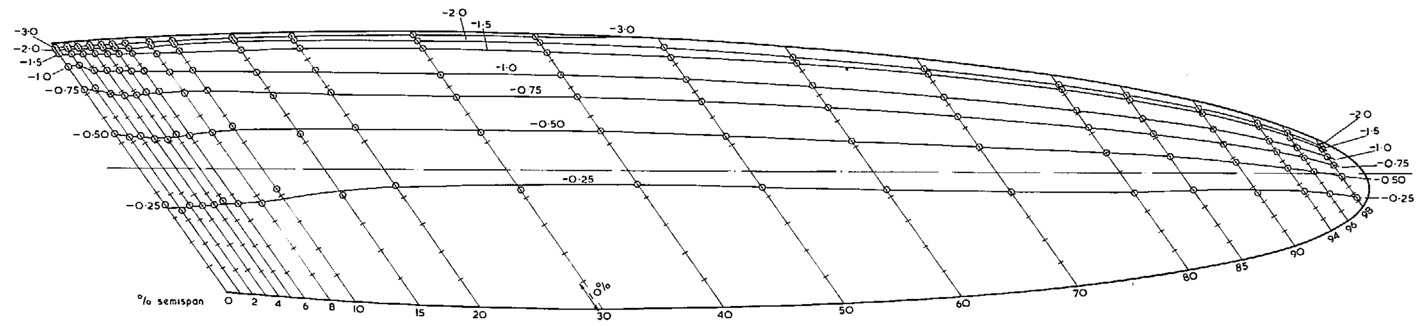

a α=9°·77 ($C_L \simeq 0·68$) $R_{\bar{c}}$ =1·02 x 10^6 wire on

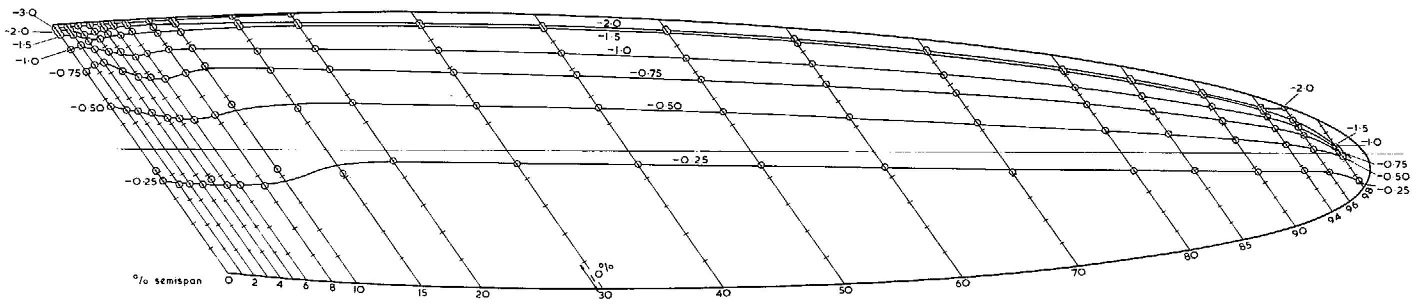

b α=9°·77 ($C_L \simeq 0·65$) $R_{\bar{c}}$=0·51 x 10^6 wire on

FIG. 47a–b. Comparison of isobar patterns at the two lower Reynolds numbers, α = 9·77°, wire on.

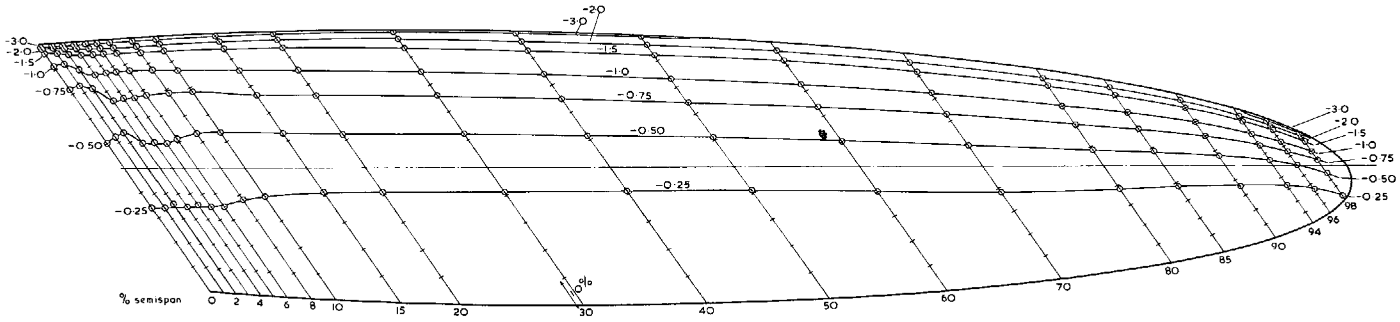

a $\alpha = 9°{\cdot}77$ ($C_L \simeq 0{\cdot}70$) $R_{\bar{c}} = 1{\cdot}78 \times 10^6$ wire on

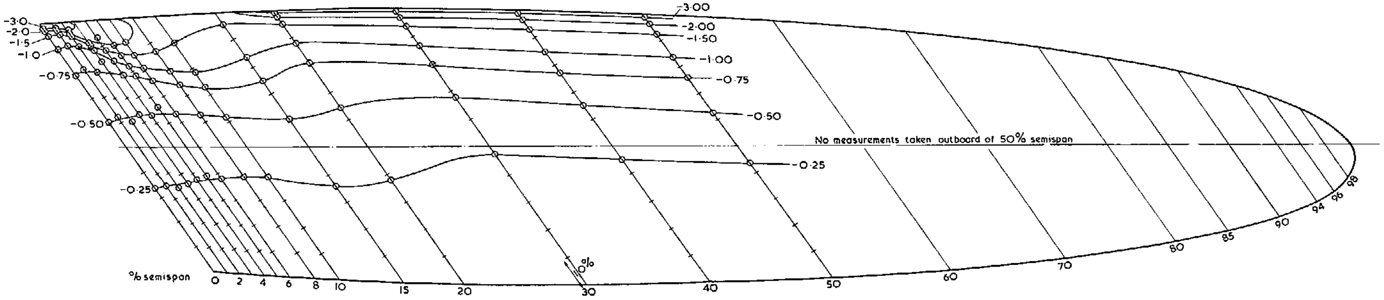

b $\alpha = 9°{\cdot}77$ ($C_L \simeq 0{\cdot}67$) $R_{\bar{c}} = 1{\cdot}78 \times 10^6$ wire off

FIG. 48a–b. Comparison of isobar patterns with and without wire at $\alpha = 9{\cdot}77°$, $R_{\bar{c}} = 1{\cdot}78 \times 10^6$.

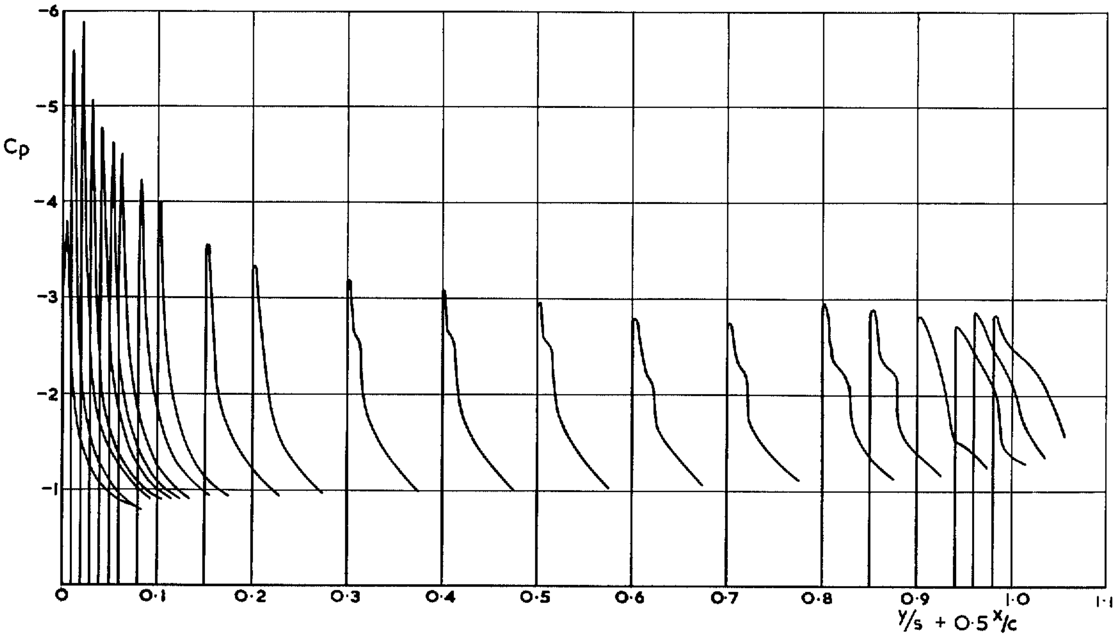

a $\alpha = 9{\cdot}77°$ $(C_L \simeq 0{\cdot}68)$, $R_{\bar{c}} = 1{\cdot}02 \times 10^6$ wire on

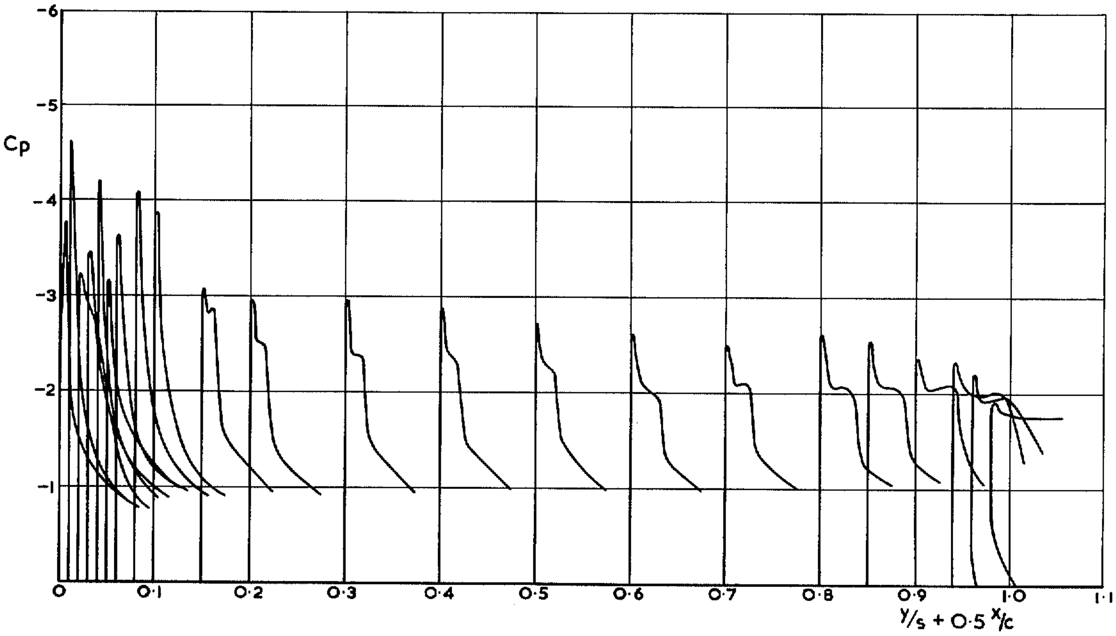

b $\alpha = 9{\cdot}77°$ $(C_L \simeq 0{\cdot}65)$, $R_{\bar{c}} = 0{\cdot}51 \times 10^6$ wire on

FIG. 49a–b. Spanwise variation of pressure distribution over forward 15 per cent of chord.

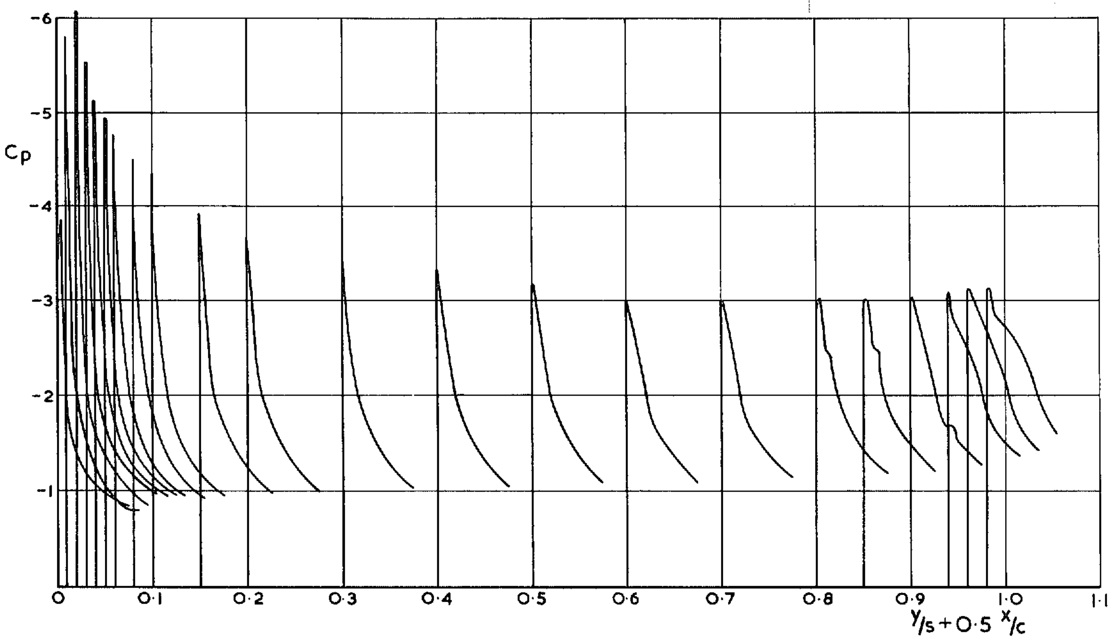

a $\alpha = 9{\cdot}77^\circ$ ($C_L \simeq 0{\cdot}7$), $R_{\bar{c}} = 1{\cdot}78 \times 10^6$ wire on

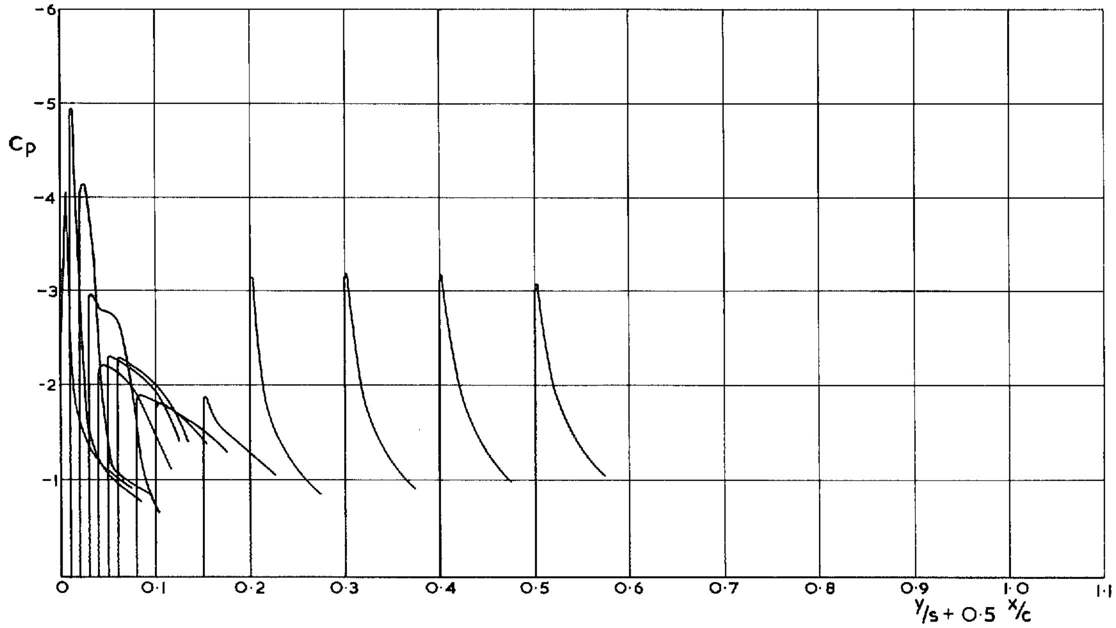

b $\alpha = 9{\cdot}77^\circ$ ($C_L \simeq 0{\cdot}67$), $R_{\bar{c}} = 1{\cdot}78 \times 10^6$ wire off

FIG. 50a–b. Spanwise variation of pressure distribution over forward 15 per cent of chord.

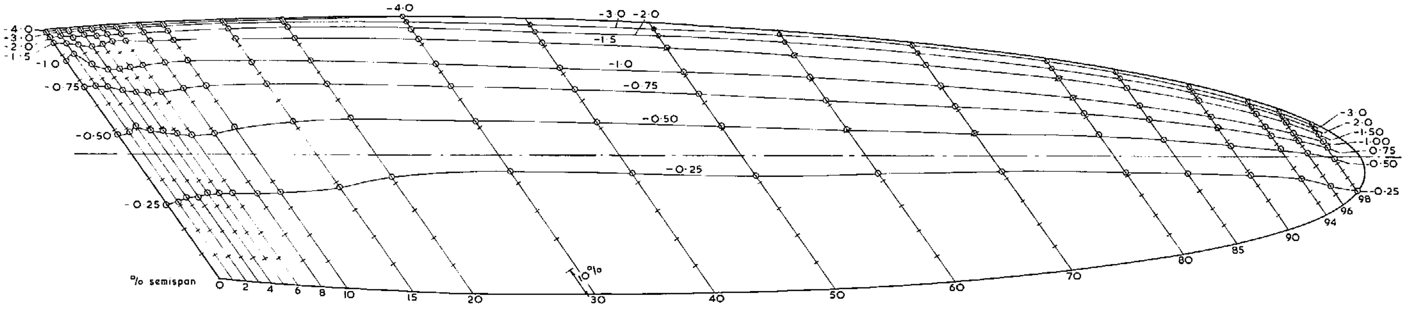

a α=11°·33 ($C_L \simeq 0{\cdot}76$) $R_{\bar{c}} = 1{\cdot}02 \times 10^6$ wire on

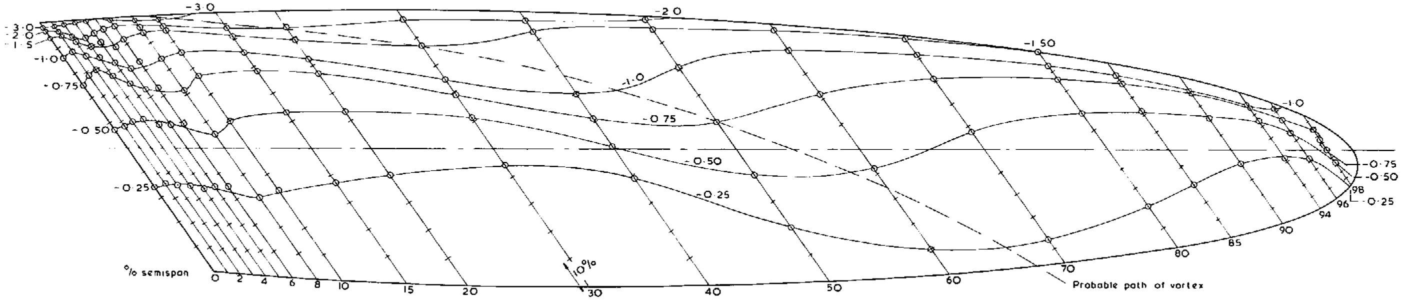

b α=11°·33 ($C_L \simeq 0{\cdot}70$) $R_{\bar{c}}=0{\cdot}51\times10^6$ wire on

FIG. 51a–b. Comparison of isobar patterns at the two lower Reynolds numbers, α = 11·33°, wire on.

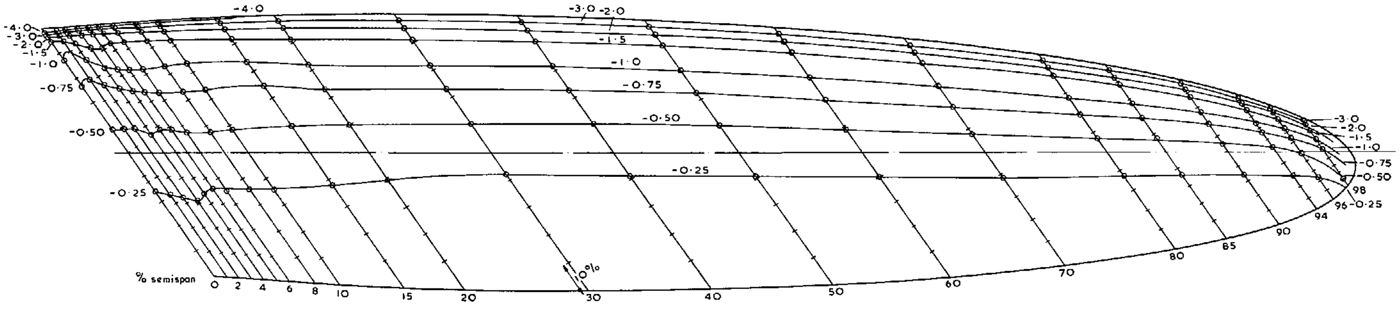

a α = 11°.33 ($C_L \simeq 0{\cdot}80$) $R_{\bar{c}} = 1{\cdot}78 \times 10^6$ wire on

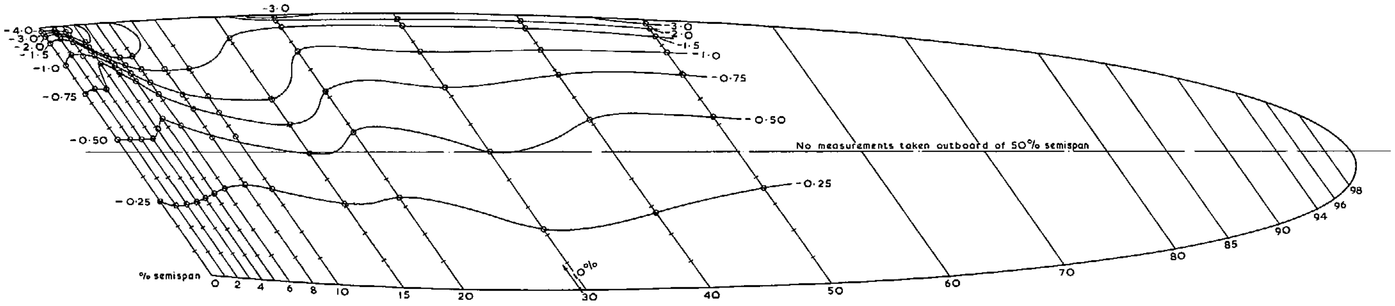

b α = 11°.33 ($C_L \simeq 0{\cdot}73$) $R_{\bar{c}} = 1{\cdot}78 \times 10^6$ wire off

FIG. 52a–b. Comparison of isobar patterns with and without wire at $\alpha = 11{\cdot}33°$, $R_{\bar{c}} = 1{\cdot}78 \times 10^6$.

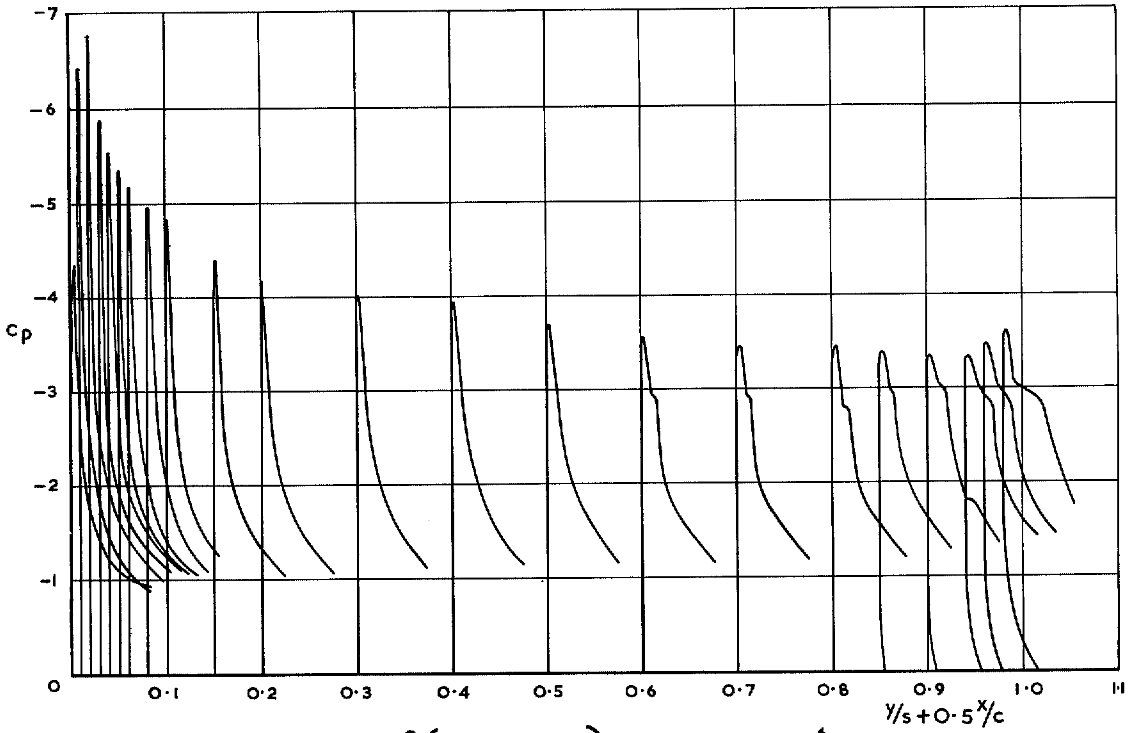

a $\alpha = 11 \cdot 33^{\circ} (C_L \simeq 0 \cdot 76)$, $R_{\bar{c}} = 1 \cdot 02 \times 10^6$ wire on

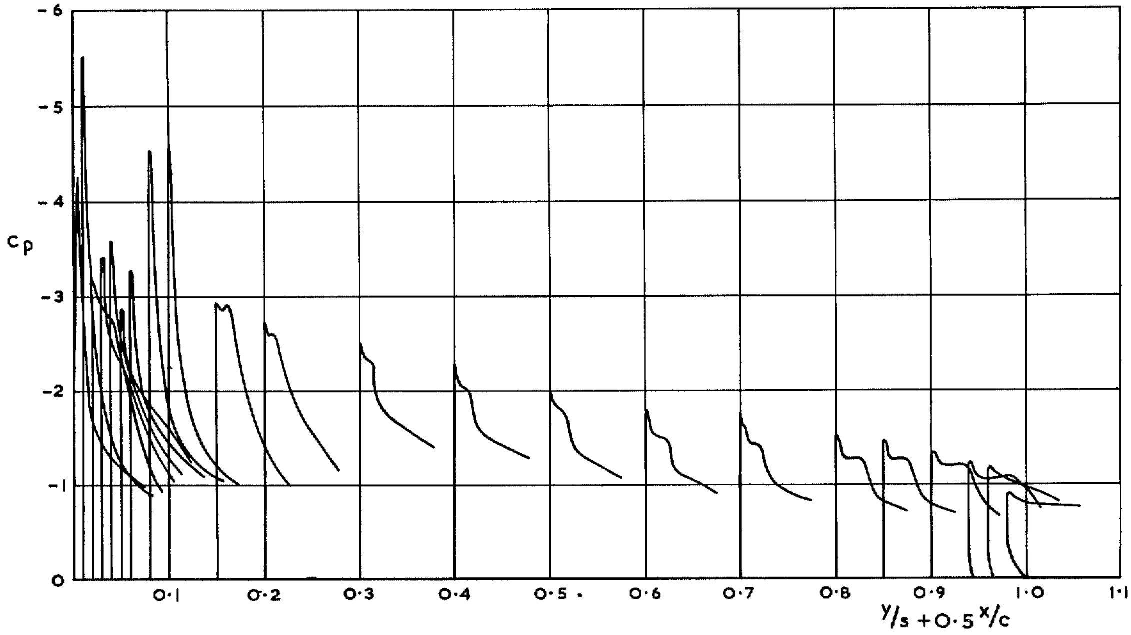

b $\alpha = 11 \cdot 33^{\circ} (C_L \simeq 0 \cdot 70)$, $R_{\bar{c}} = 0 \cdot 51 \times 10^6$ wire on

FIG. 53a–b. Spanwise variation of pressure distribution over forward 15 per cent of chord.

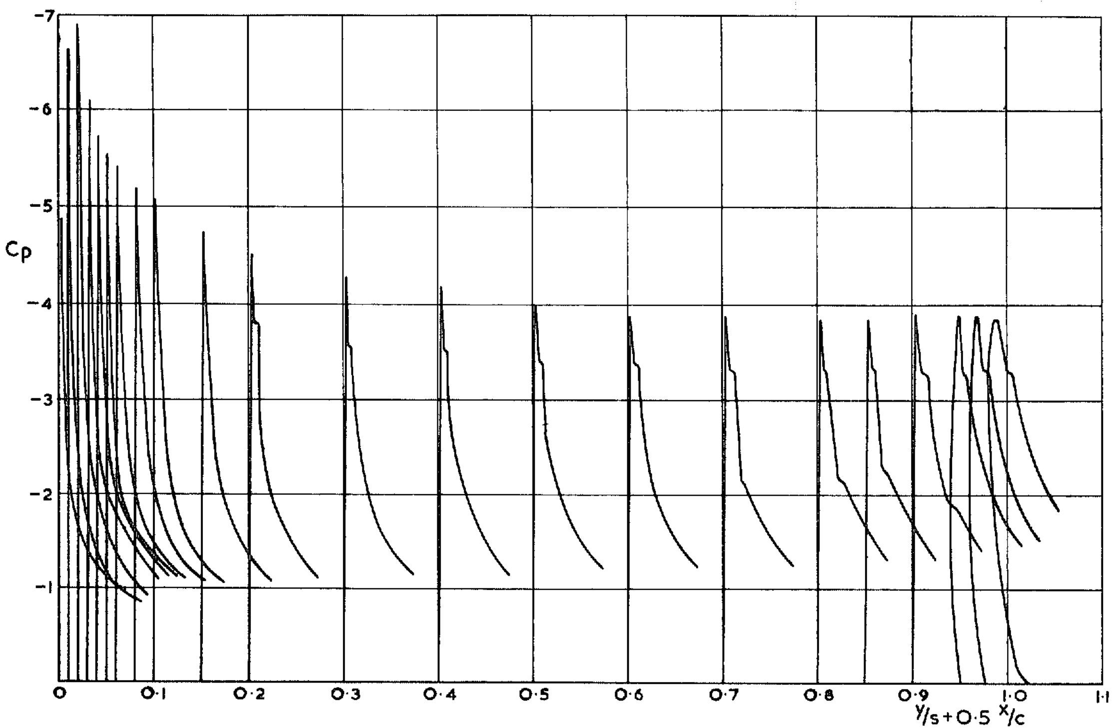

a $\alpha = 11\cdot33^\circ$ ($C_L \simeq 0\cdot8$), $R_{\bar{c}} = 1\cdot78 \times 10^6$ wire on

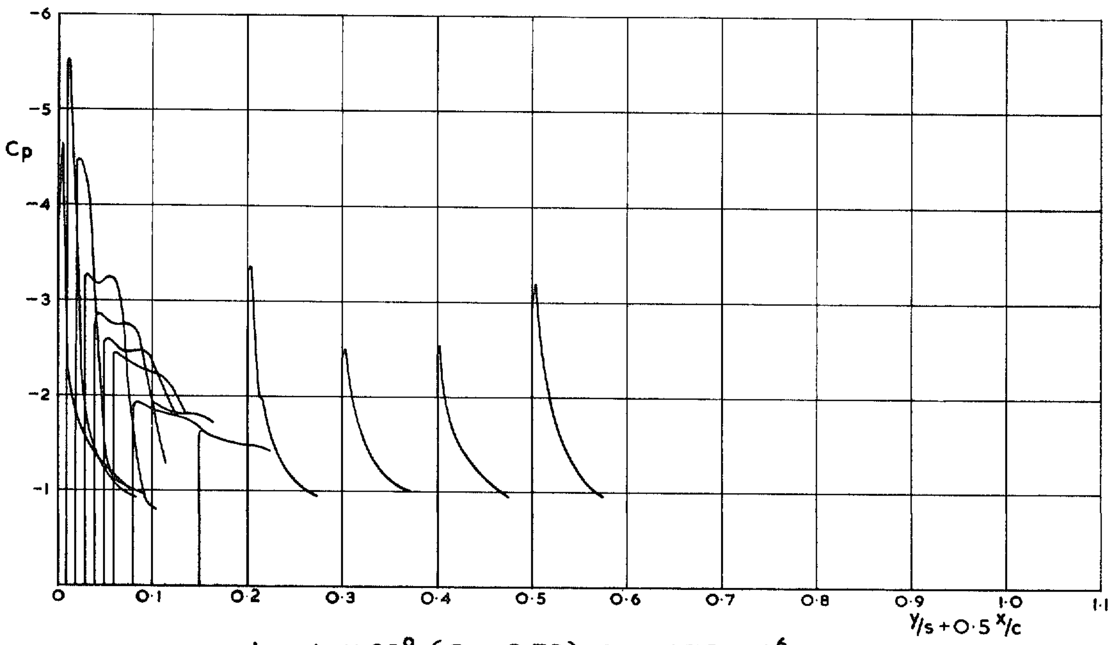

b $\alpha = 11\cdot33^\circ$ ($C_L \simeq 0\cdot73$), $R_{\bar{c}} = 1\cdot78 \times 10^6$ wire off

FIG. 54a–b. Spanwise variation of pressure distribution over forward 15 per cent of chord.

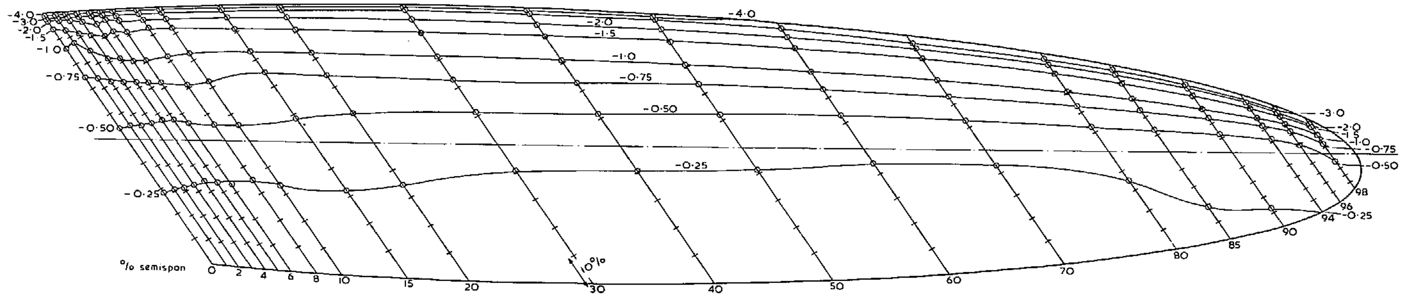

a $\alpha = 12°\cdot30$ ($C_L \simeq 0\cdot81$) $R_{\bar{c}} = 1\cdot02 \times 10^6$ wire on

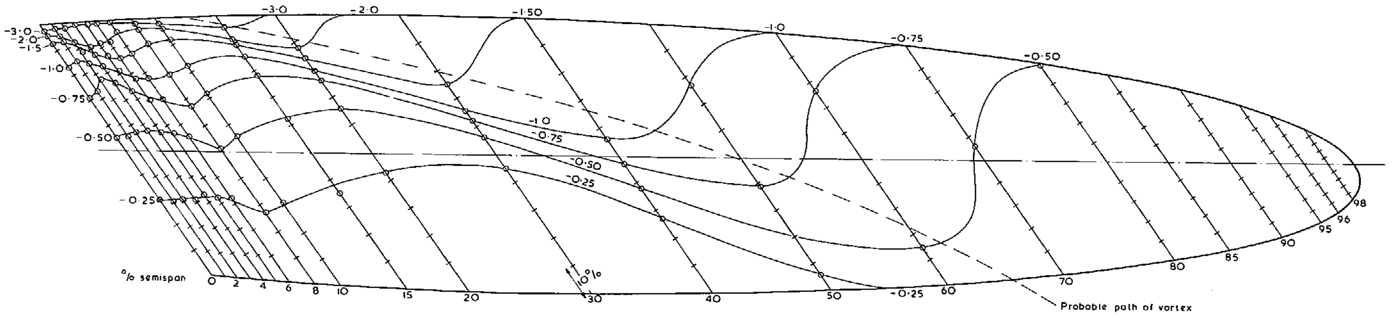

b $\alpha = 12°\cdot30$ ($C_L \simeq 0\cdot71$) $R_{\bar{c}} = 0\cdot51 \times 10^6$ wire on

FIG. 55a–b. Comparison of isobar patterns at the two lower Reynolds numbers, $\alpha = 12\cdot30°$, wire on.

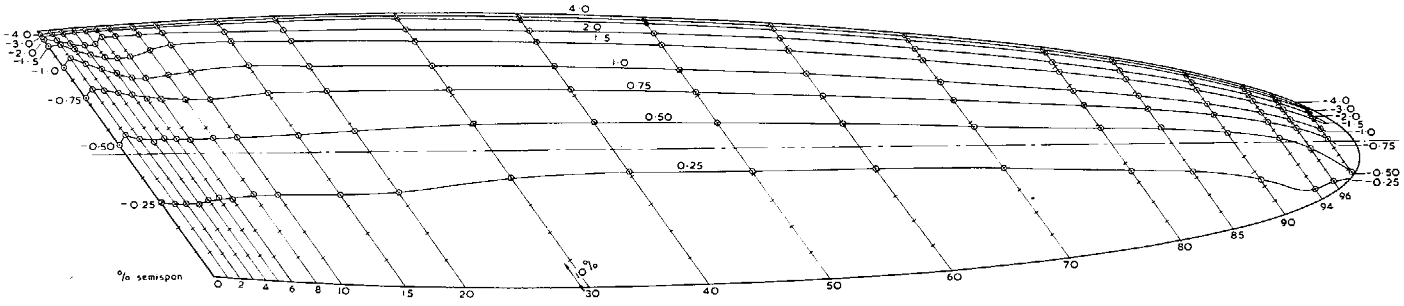

a $\alpha = 12^{\circ}30$ ($C_L \simeq 0.85$) $R_{\bar{c}} = 1.78 \times 10^6$ wire on

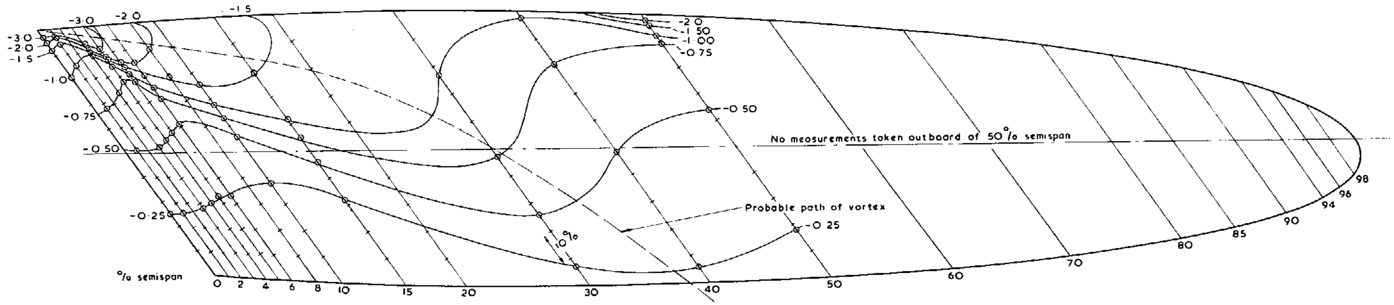

b $\alpha = 12^{\circ}30$ ($C_L \simeq 0.76$) $R_{\bar{c}} = 1.78 \times 10^6$ wire off

FIG. 56a–b. Comparison of isobar patterns with and without wire at $\alpha = 12{\cdot}30^{\circ}$, $R_{\bar{c}} = 1{\cdot}78 \times 10^6$.

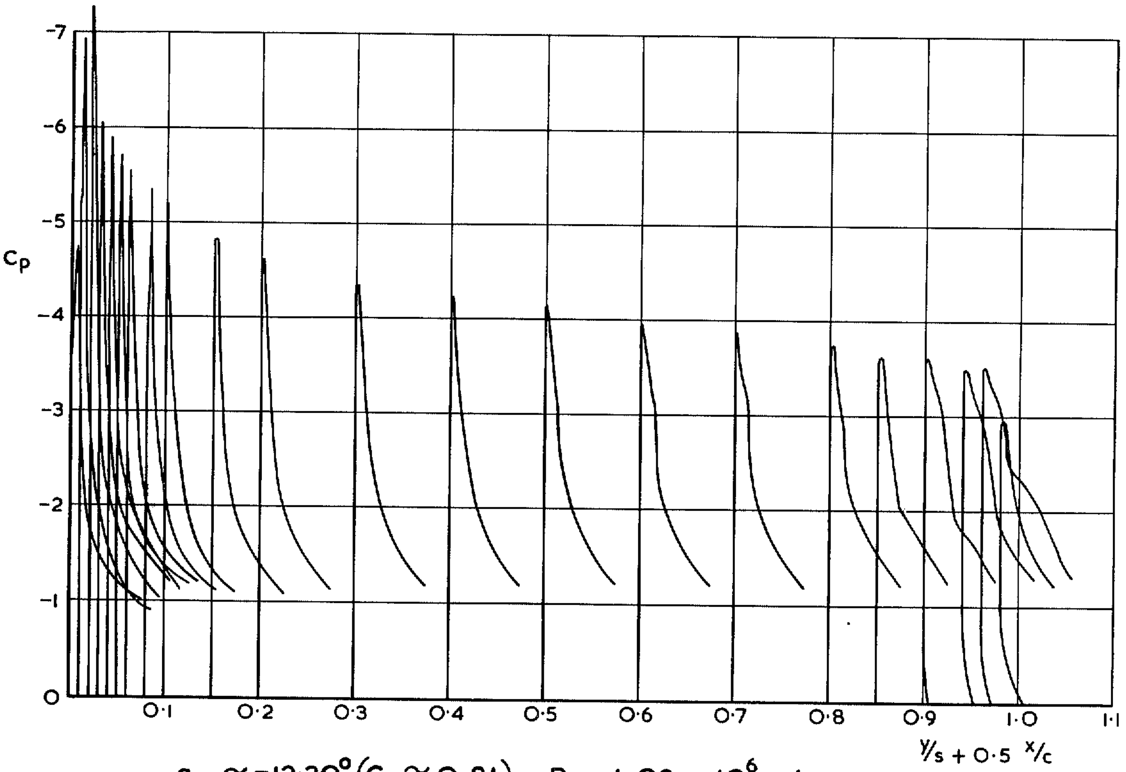

a $\alpha = 12{\cdot}30^\circ (C_L \simeq 0{\cdot}81)$, $R_{\bar{c}} = 1{\cdot}02 \times 10^6$ wire on

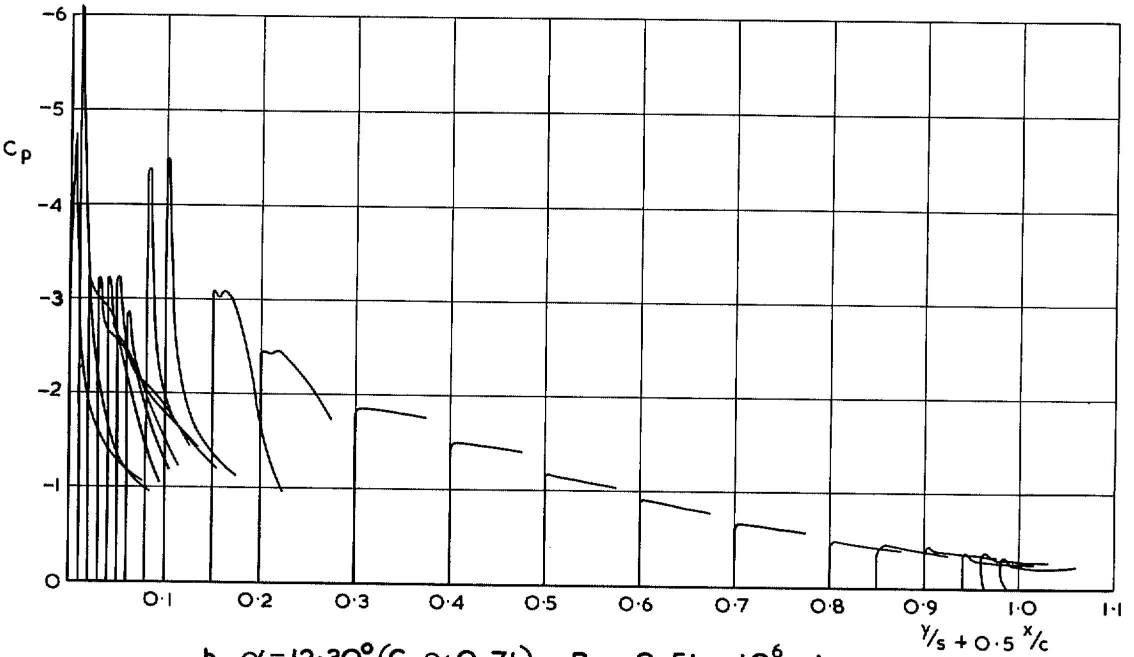

b $\alpha = 12{\cdot}30^\circ (C_L \simeq 0{\cdot}71)$, $R_{\bar{c}} = 0{\cdot}51 \times 10^6$ wire on

FIG. 57a–b. Spanwise variation of pressure distribution over forward 15 per cent of chord.

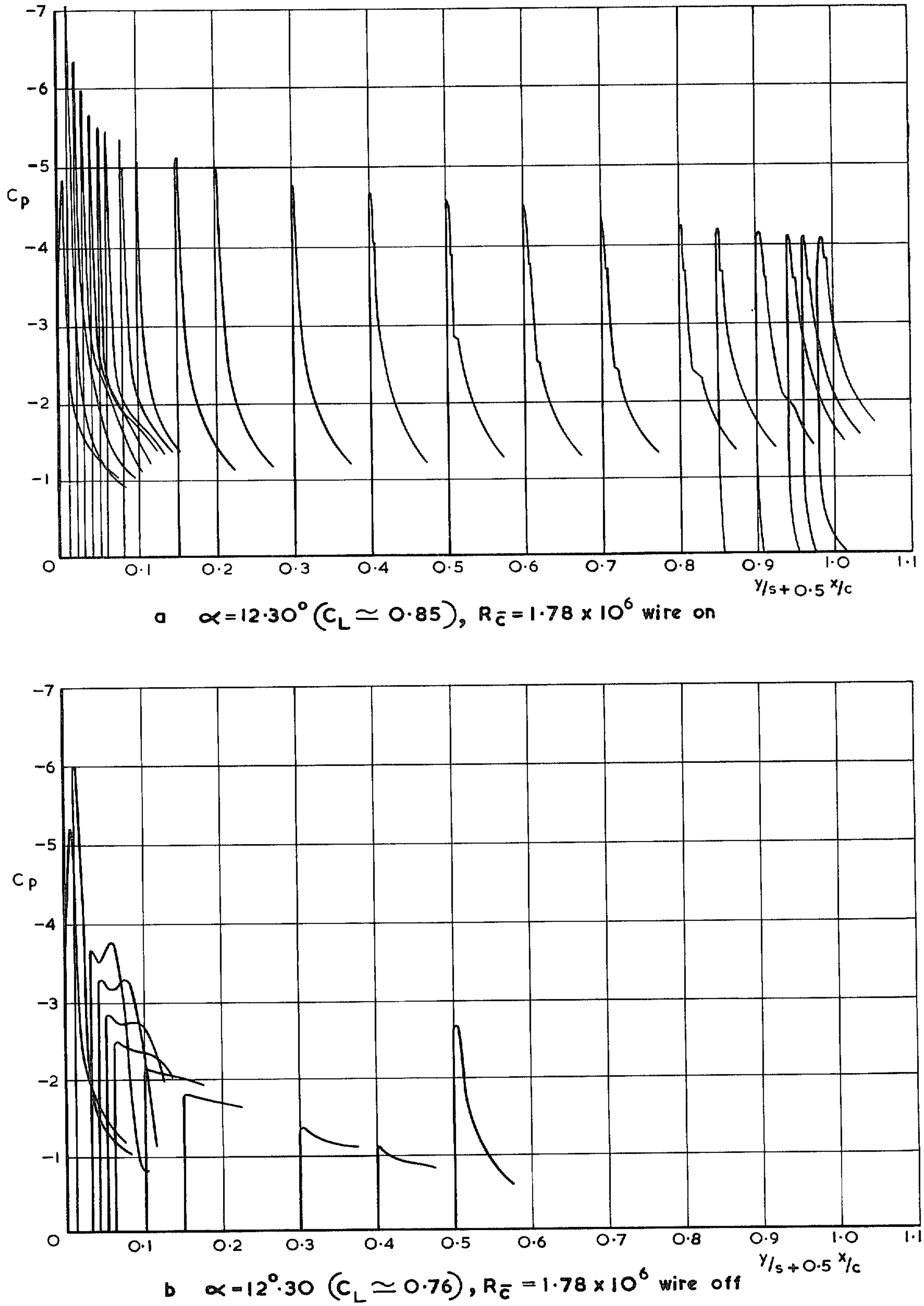

FIG. 58a–b. Spanwise variation of pressure distribution over forward 15 per cent of chord.

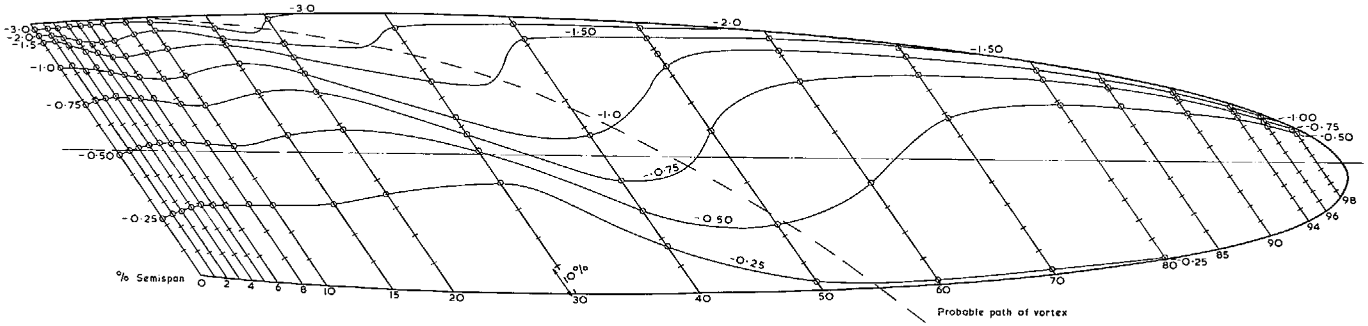

a $\alpha = 13^\circ{\cdot}56$ ($C_L \simeq 0{\cdot}82$) $R_{\bar{c}} = 1{\cdot}02 \times 10^6$ wire on

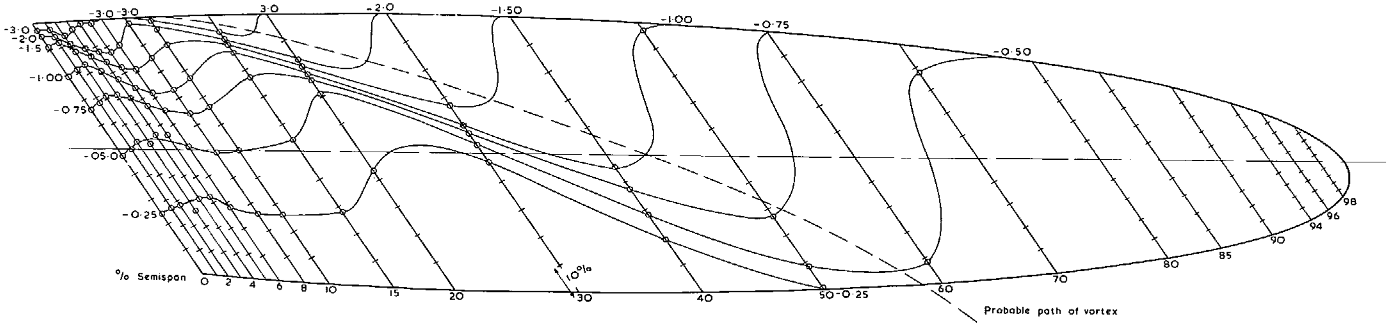

b $\alpha = 13^\circ{\cdot}56$ ($C_L \simeq 0{\cdot}75$) $R_{\bar{c}} = 0{\cdot}51 \times 10^6$ wire on

FIG. 59a–b. Comparison of isobar patterns at the two lower Reynolds numbers, $\alpha = 13{\cdot}56^\circ$, wire on.

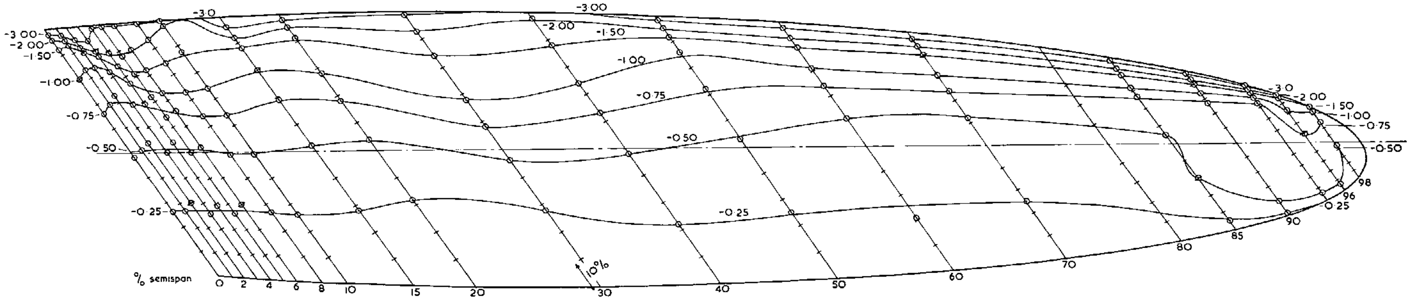

a $\alpha = 13^\circ{\cdot}56$ ($C_L \simeq 0{\cdot}90$) $R_{\bar{c}} = 1{\cdot}78 \times 10^6$ wire on

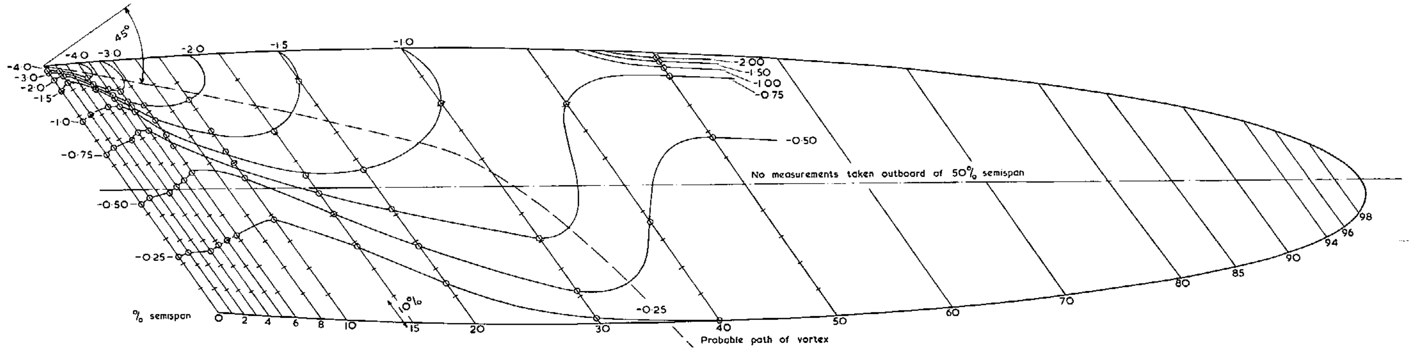

b $\alpha = 13^\circ{\cdot}56$ ($C_L \simeq 0{\cdot}79$) $R_{\bar{c}} = 1{\cdot}78 \times 10^6$ wire off

FIG. 60a–b. Comparison of isobar patterns with and without wire at $\alpha = 13{\cdot}56^\circ$, $R_{\bar{c}} = 1{\cdot}78 \times 10^6$.

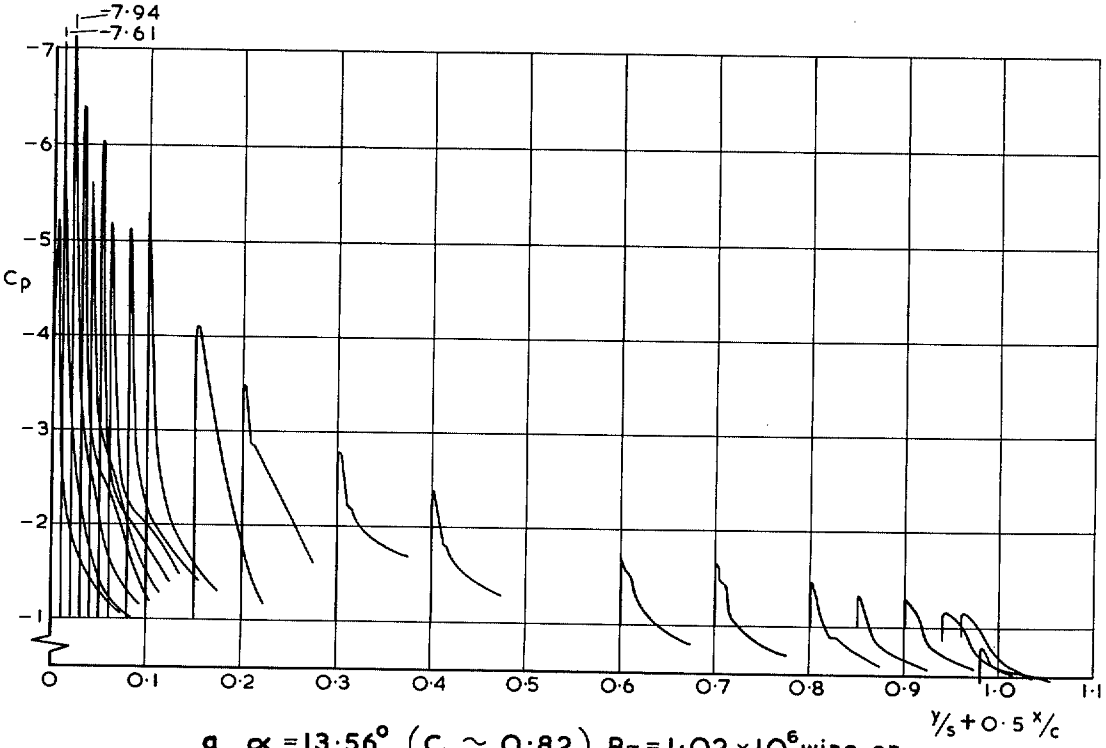

a $\alpha = 13{\cdot}56^\circ$ $(C_L \simeq 0{\cdot}82)$, $R_{\bar{c}} = 1{\cdot}02 \times 10^6$ wire on

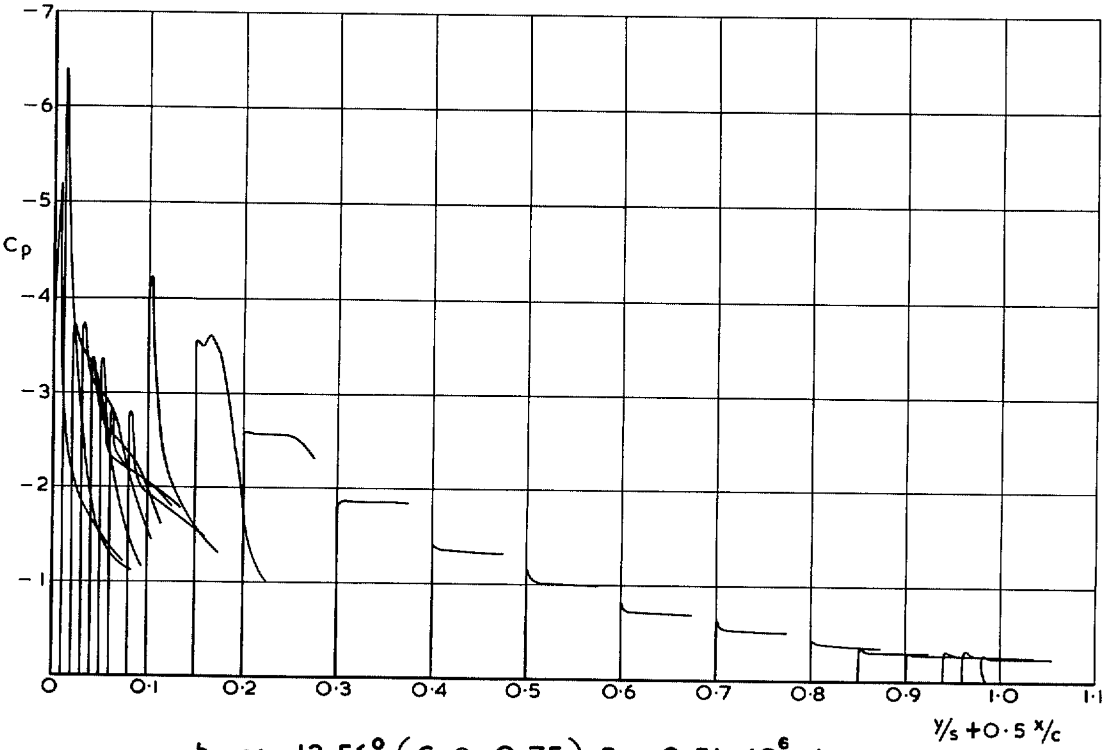

b $\alpha = 13{\cdot}56^\circ$ $(C_L \simeq 0{\cdot}75)$, $R_{\bar{c}} = 0{\cdot}51 \times 10^6$ wire on

FIG. 61a–b. Spanwise variation of pressure distribution over forward 15 per cent of chord.

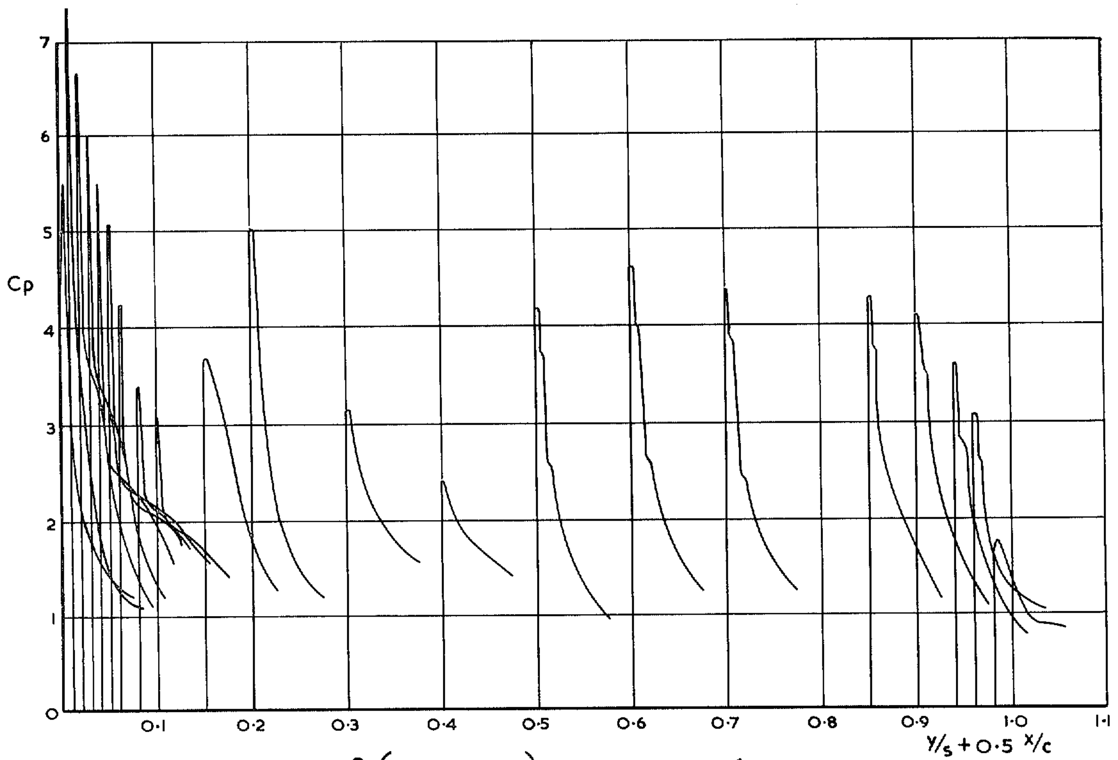

a $\alpha = 13{\cdot}56^\circ$ $(C_L \simeq 0{\cdot}90)$, $R_{\bar{c}} = 1{\cdot}78 \times 10^6$ wire on

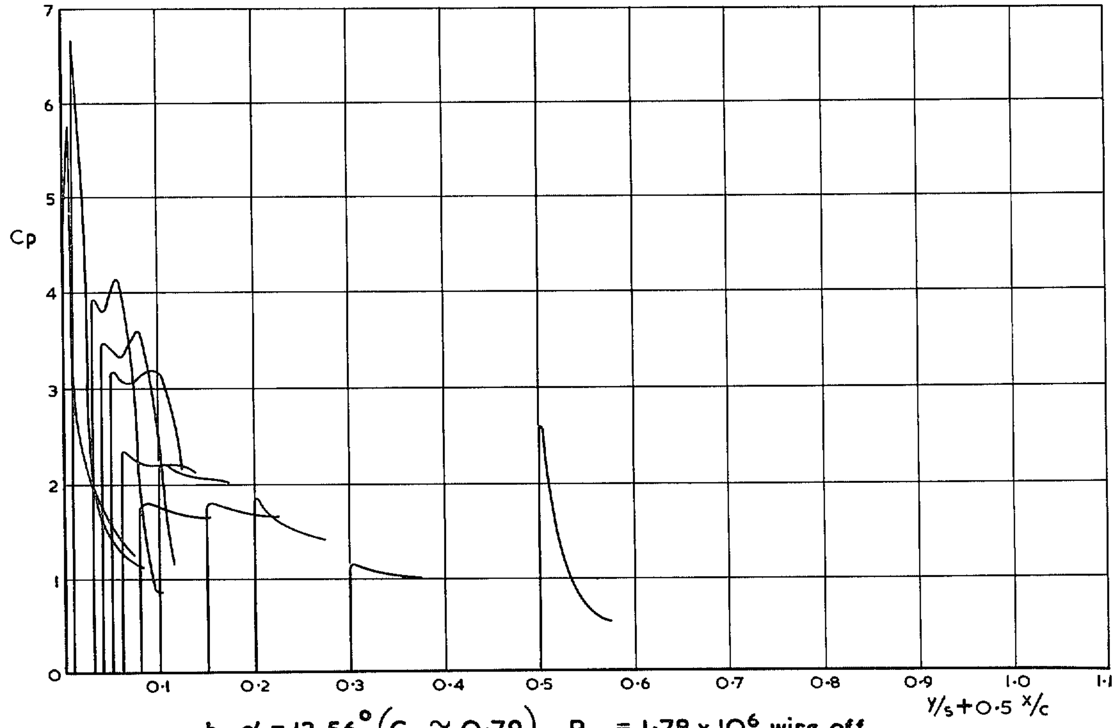

b $\alpha = 13{\cdot}56^\circ$ $(C_L \simeq 0{\cdot}79)$, $R_{\bar{c}} = 1{\cdot}78 \times 10^6$ wire off

FIG. 62a–b. Spanwise variation of pressure distribution over forward 15 per cent of chord.

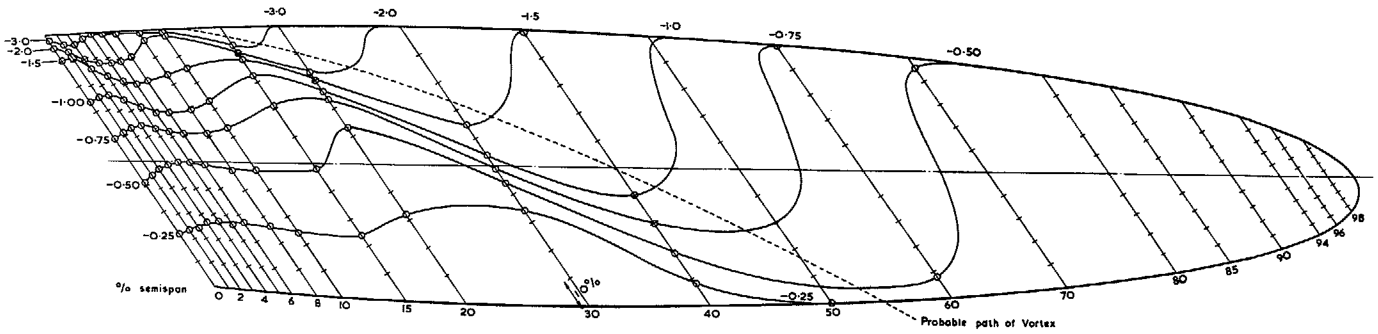

a $\alpha = 15^\circ$ ($C_L = 0{\cdot}82$) $R_{\bar{c}} = 1{\cdot}02 \times 10^6$ wire on

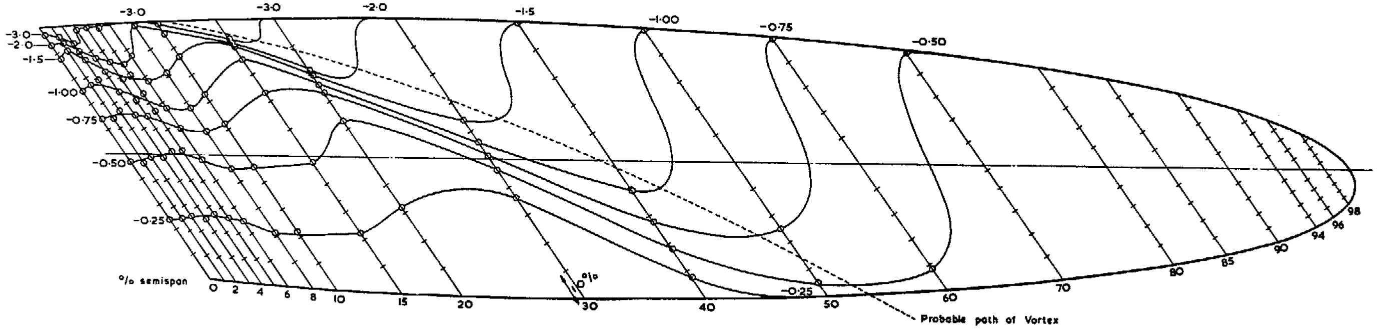

b $\alpha = 15^\circ$ ($C_L = 0{\cdot}80$) $R_{\bar{c}} = 0{\cdot}51 \times 10^6$ wire on

FIG. 63a–b. Comparison of isobar patterns in the post-stall regime, $\alpha = 15^\circ$, wire on.

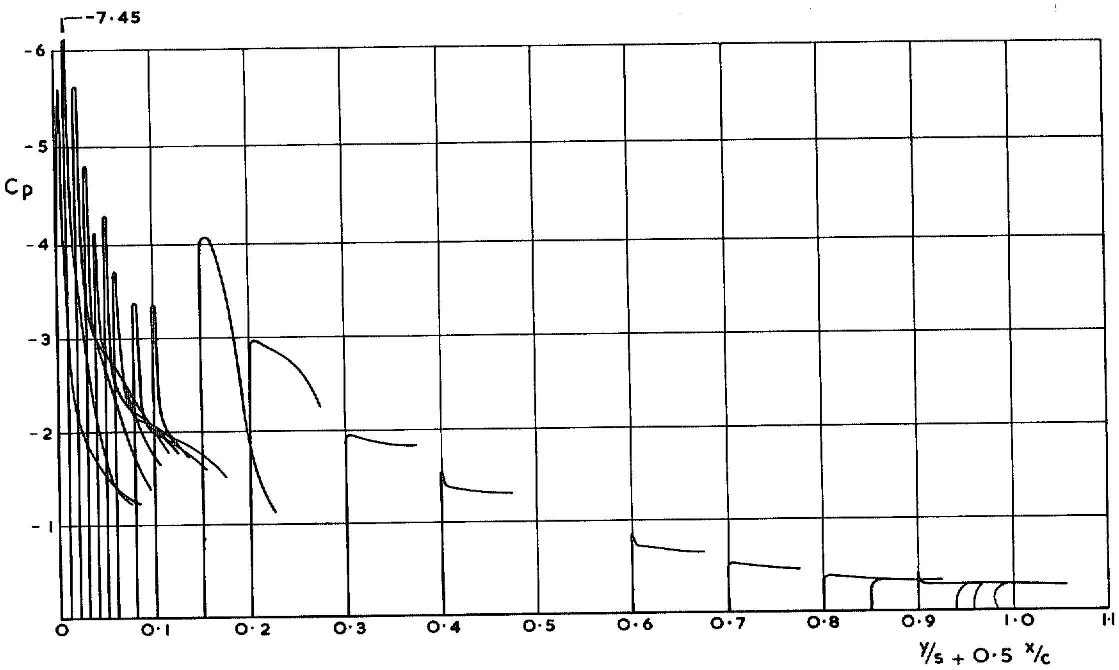

a $\alpha = 15^\circ$ ($C_L \simeq 0{\cdot}82$), $R_{\bar{c}} = 1{\cdot}02 \times 10^6$ wire on

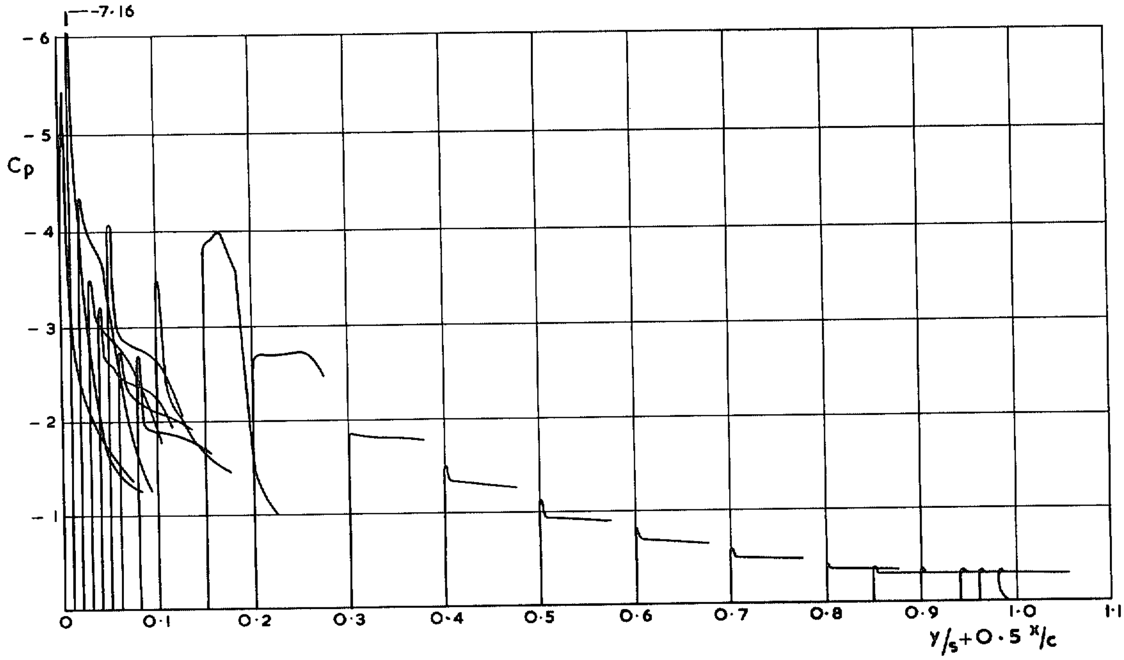

b $\alpha = 15^\circ$ ($C_L \simeq 0{\cdot}80$), $R_{\bar{c}} = 0{\cdot}51 \times 10^6$ wire on

FIG. 64a–b. Spanwise variation of pressure distribution over forward 15 per cent of chord.

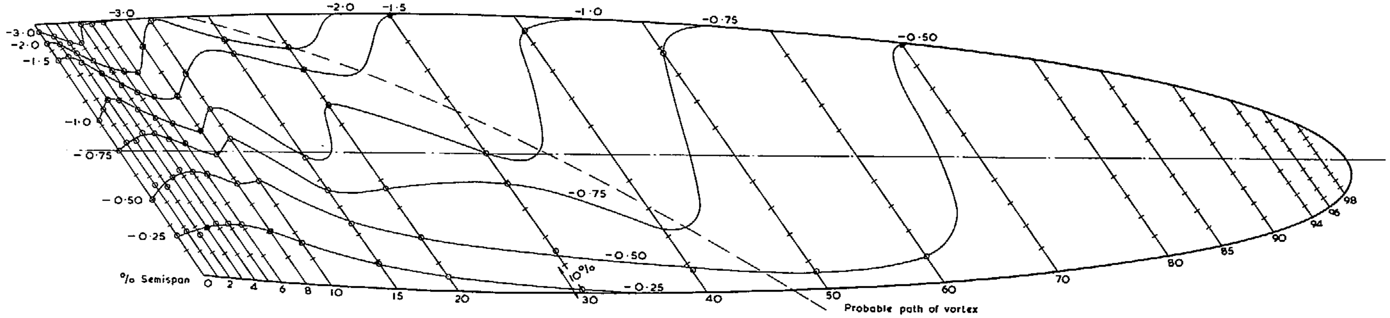

a $\alpha = 17^\circ$ ($C_L \triangleq 0{\cdot}85$) $R_{\bar{c}} = 1{\cdot}02 \times 10^6$ wire on

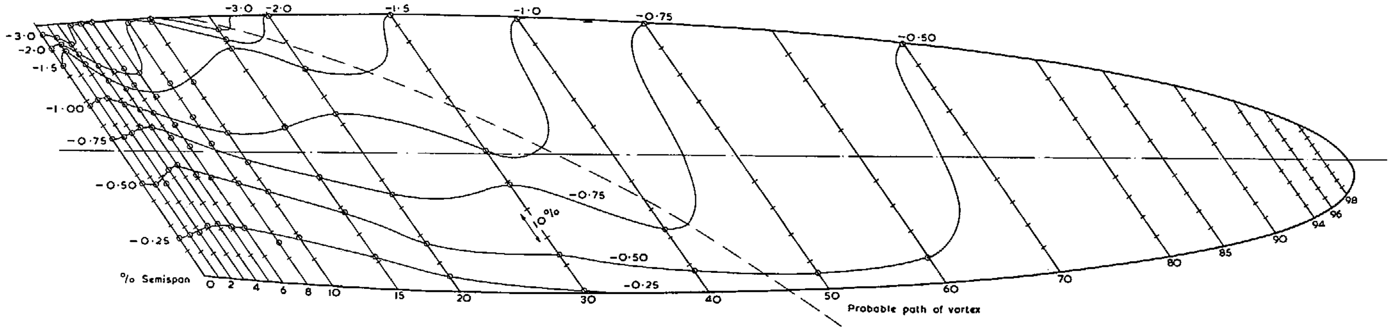

b $\alpha = 17^\circ$ ($C_L \triangleq 0{\cdot}81$) $R_{\bar{c}} = 0{\cdot}51 \times 10^6$ wire on

FIG. 65a–b. Comparison of isobar patterns in the post-stall regime, $\alpha = 17^\circ$, wire on.

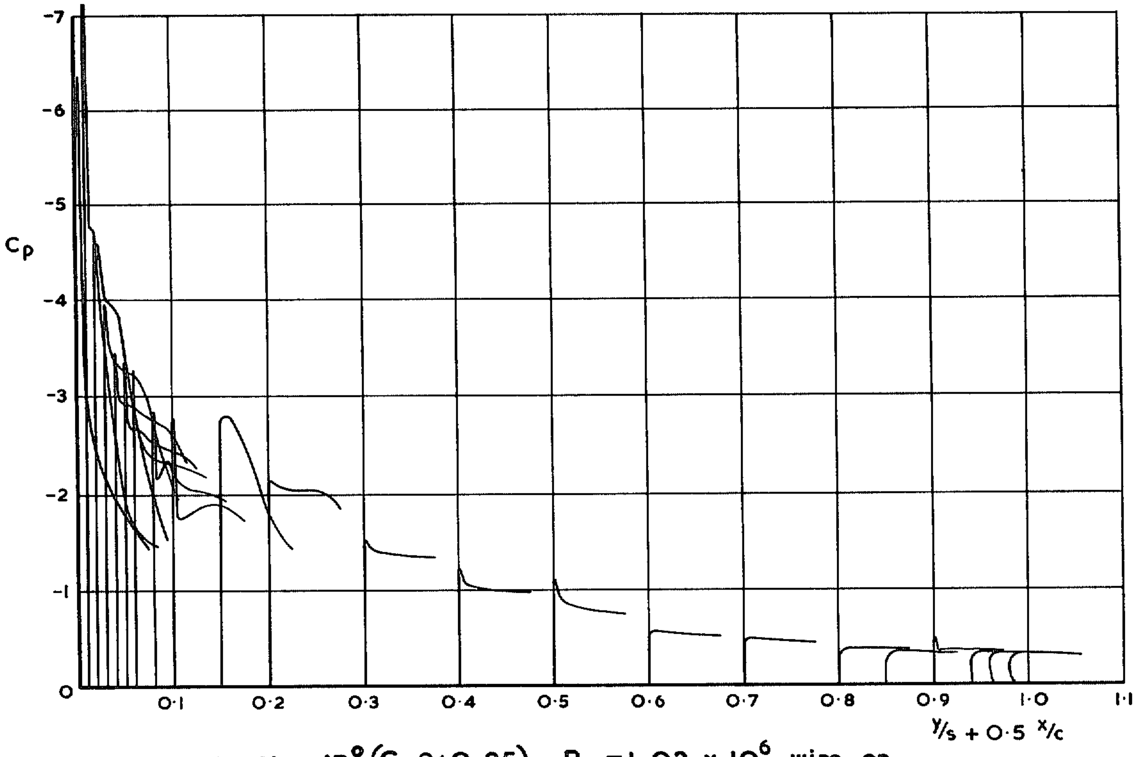

a $\alpha = 17°$ ($C_L \simeq 0{\cdot}85$), $R_{\bar{c}} = 1{\cdot}02 \times 10^6$ wire on

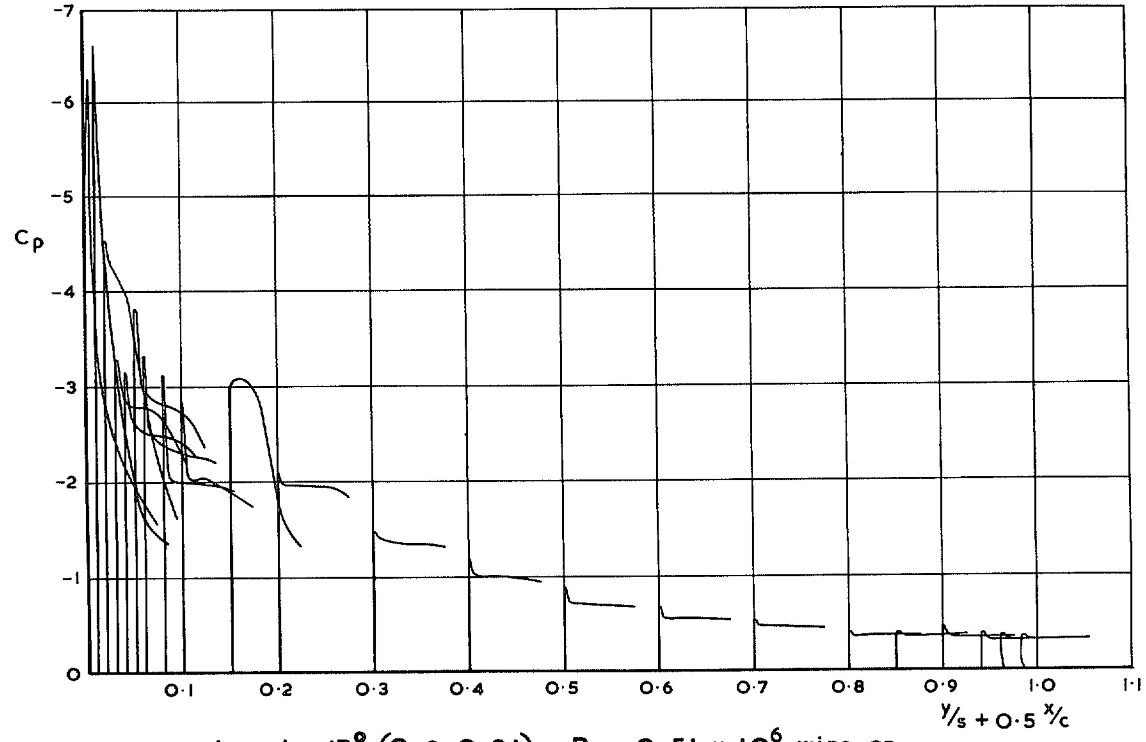

b $\alpha = 17°$ ($C_L \simeq 0{\cdot}81$), $R_{\bar{c}} = 0{\cdot}51 \times 10^6$ wire on

FIG. 66a–b. Spanwise variation of pressure distribution over forward 15 per cent of chord.

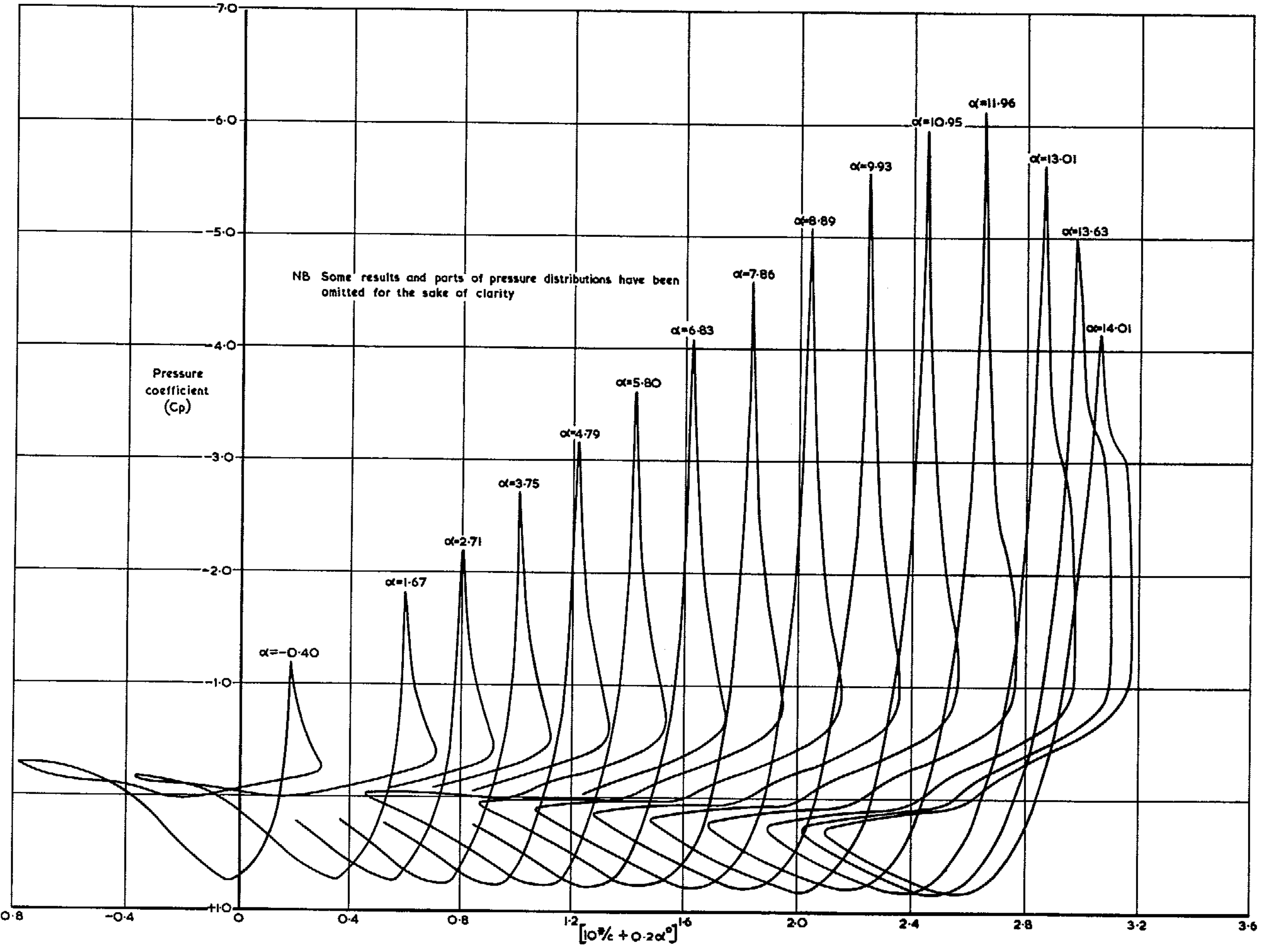

FIG. 67. Variation of axial pressure distribution with incidence at 3 per cent semispan station. $R_{\bar{c}} = 1{\cdot}78 \times 10^6$, wire on.

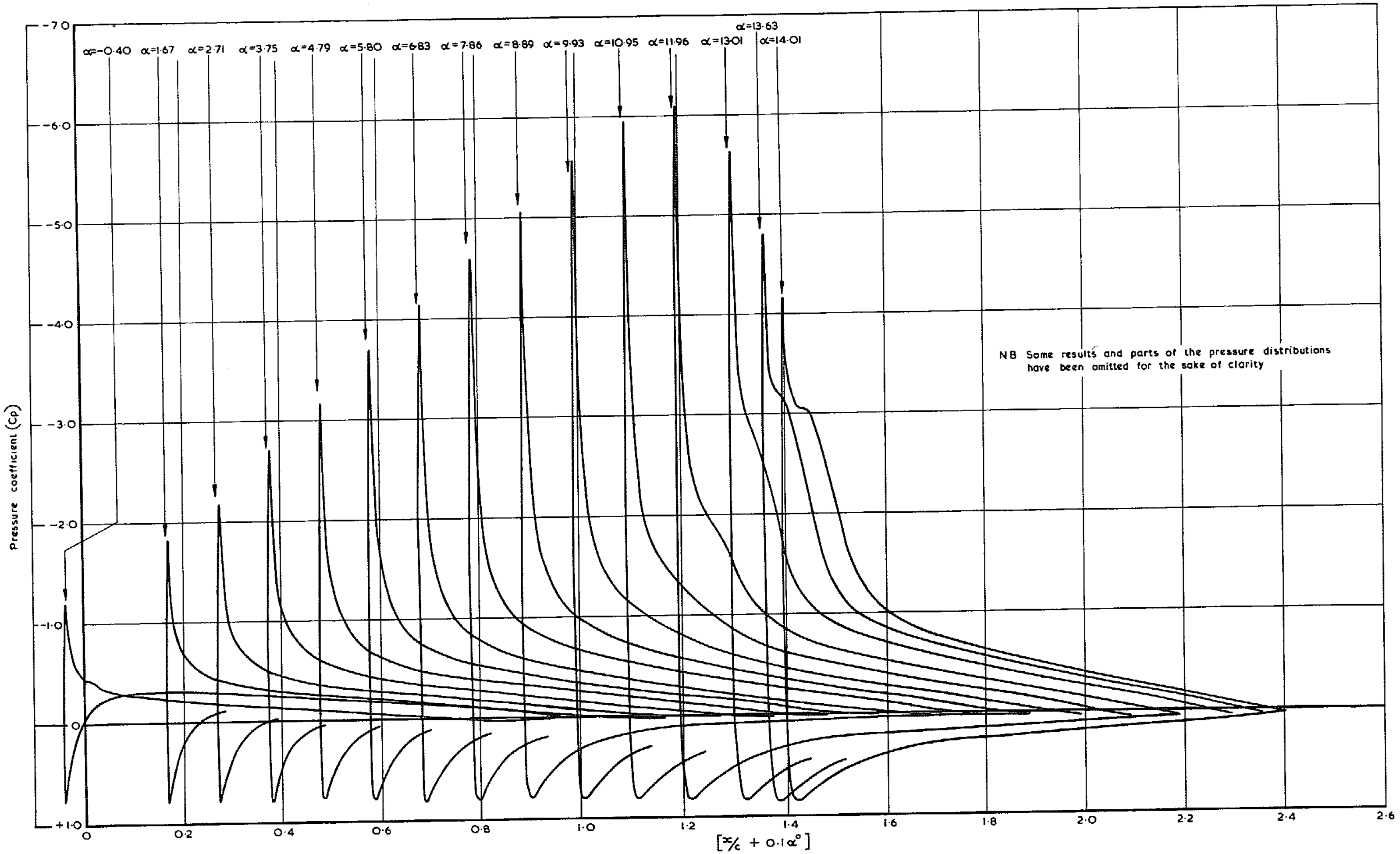

NB Some results and parts of the pressure distributions have been omitted for the sake of clarity

FIG. 68. Variation of chordwise pressure distribution with incidence at 3 per cent semispan station. $R_{\bar{c}} = 1{\cdot}78 \times 10^6$, wire on.

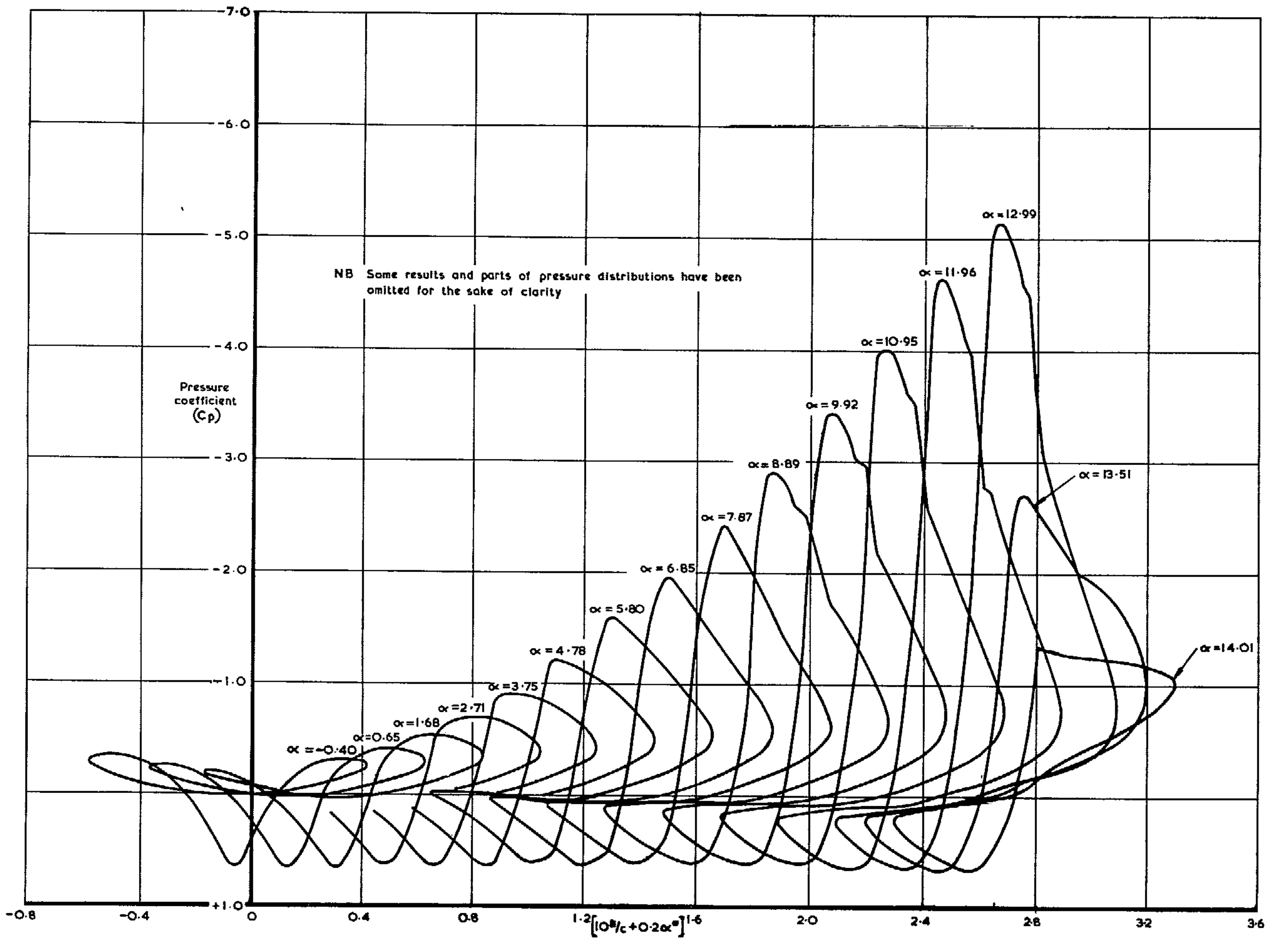

FIG. 69. Variation of axial pressure distribution with incidence at 40 per cent semispan station. $R_{\bar{c}} = 1{\cdot}78 \times 10^6$, wire on.

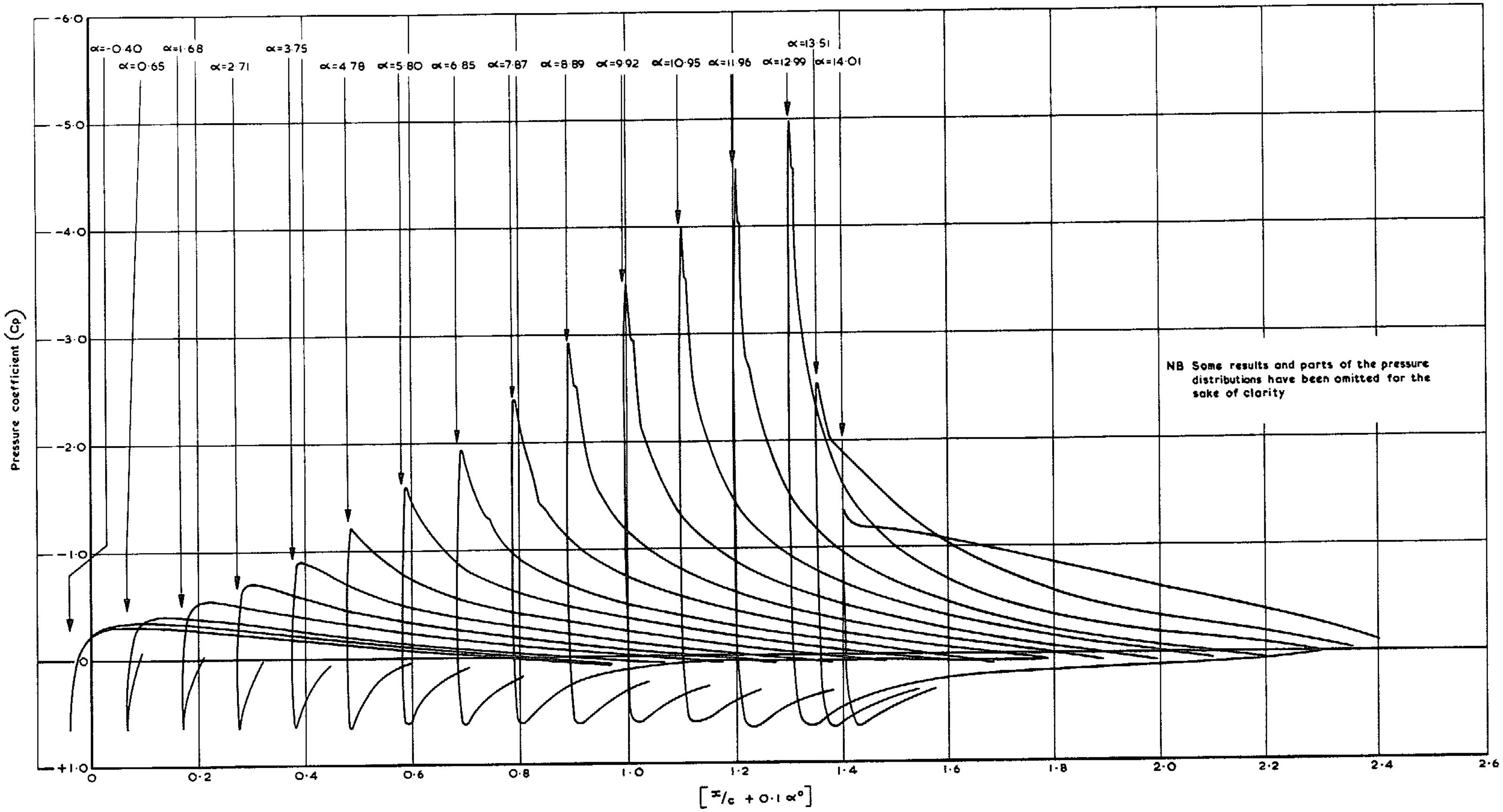

NB Some results and parts of the pressure distributions have been omitted for the sake of clarity

FIG. 70. Variation of chordwise pressure distribution with incidence at 40 per cent semispan station. $R_{\bar{c}} = 1{\cdot}78 \times 10^6$, wire on.

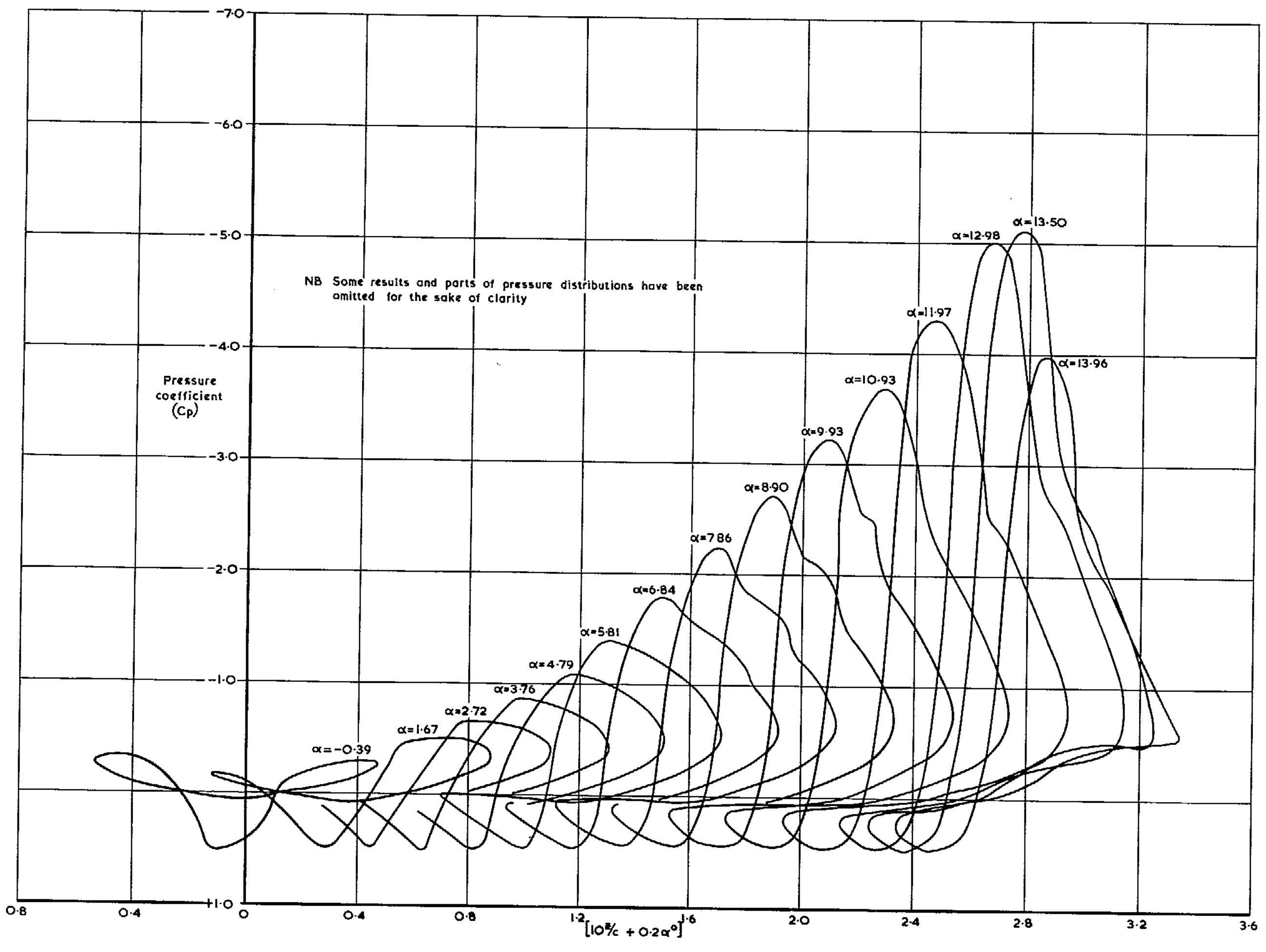

NB Some results and parts of pressure distributions have been omitted for the sake of clarity

FIG. 71. Variation of axial pressure distribution with incidence at 85 per cent semispan station. $R_{\bar{c}} = 1{\cdot}78 \times 10^6$, wire on.

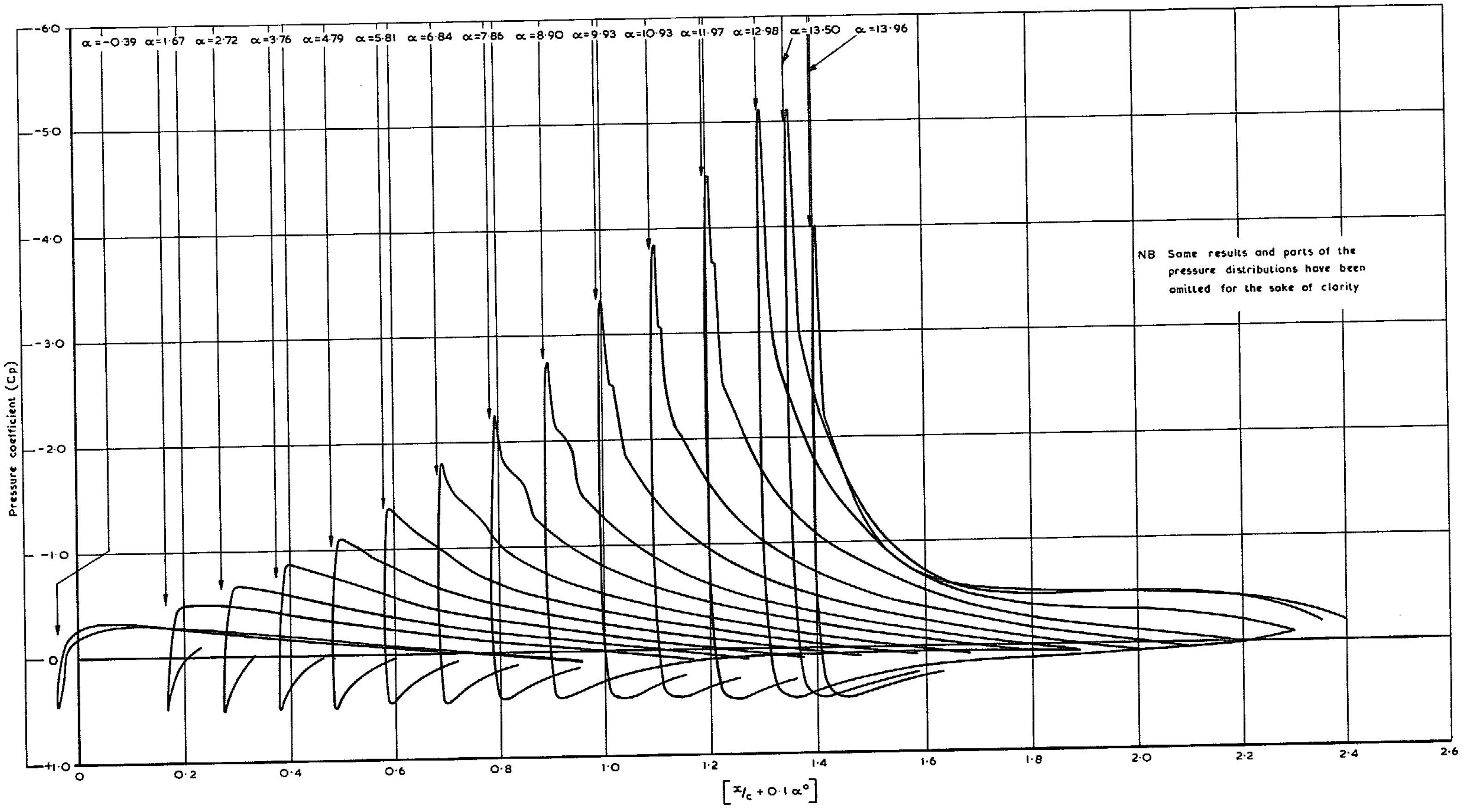

FIG. 72. Variation of chordwise pressure distribution with incidence at 85 per cent semispan station. $R_{\bar{c}} = 1{\cdot}78 \times 10^6$, wire on.

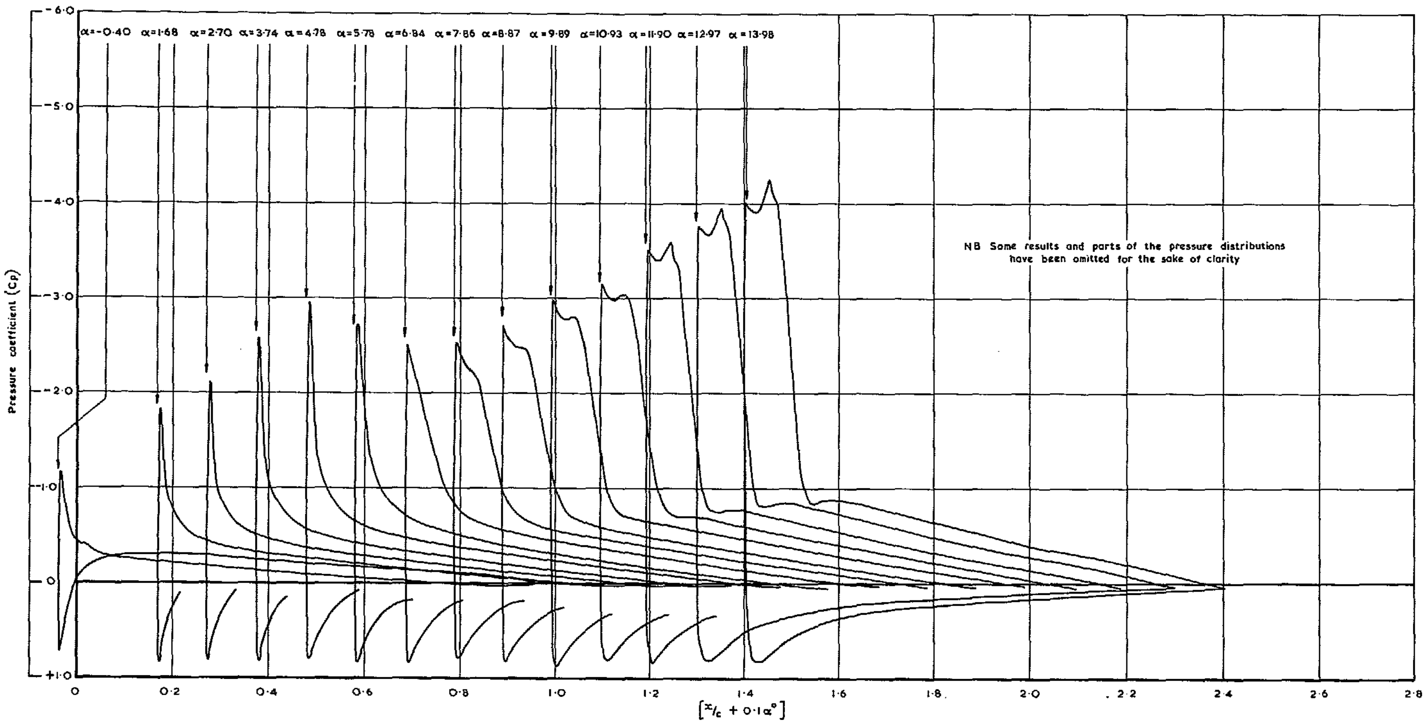

FIG. 73. Variation of chordwise pressure distribution with incidence at 3 per cent semispan station. $R_{\bar{c}} = 1{\cdot}78 \times 10^6$, wire off.

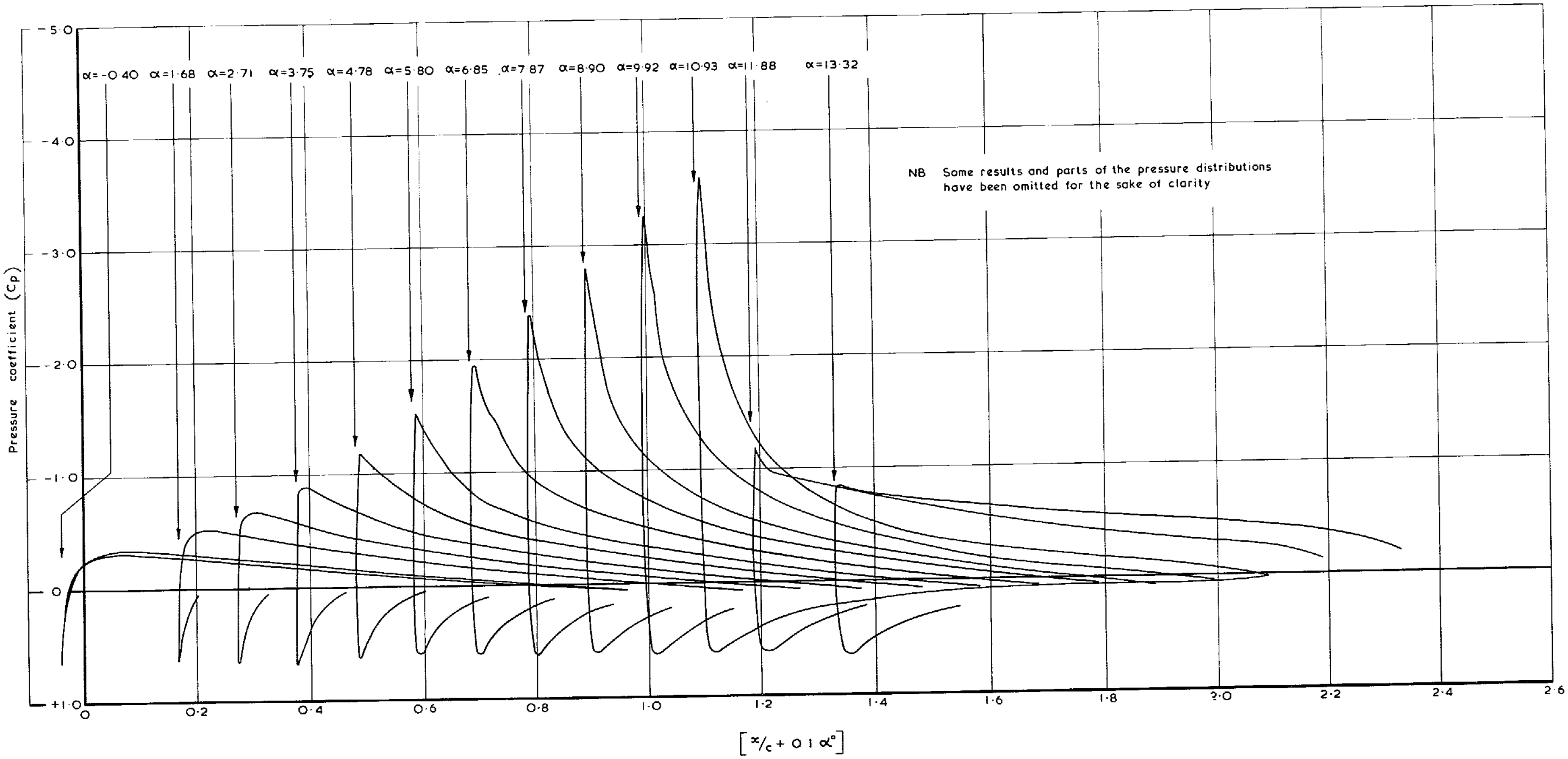

FIG. 74. Variation of chordwise pressure distribution with incidence at 40 per cent semispan station. $R_{\bar{c}} = 1{\cdot}78 \times 10^6$, wire off.

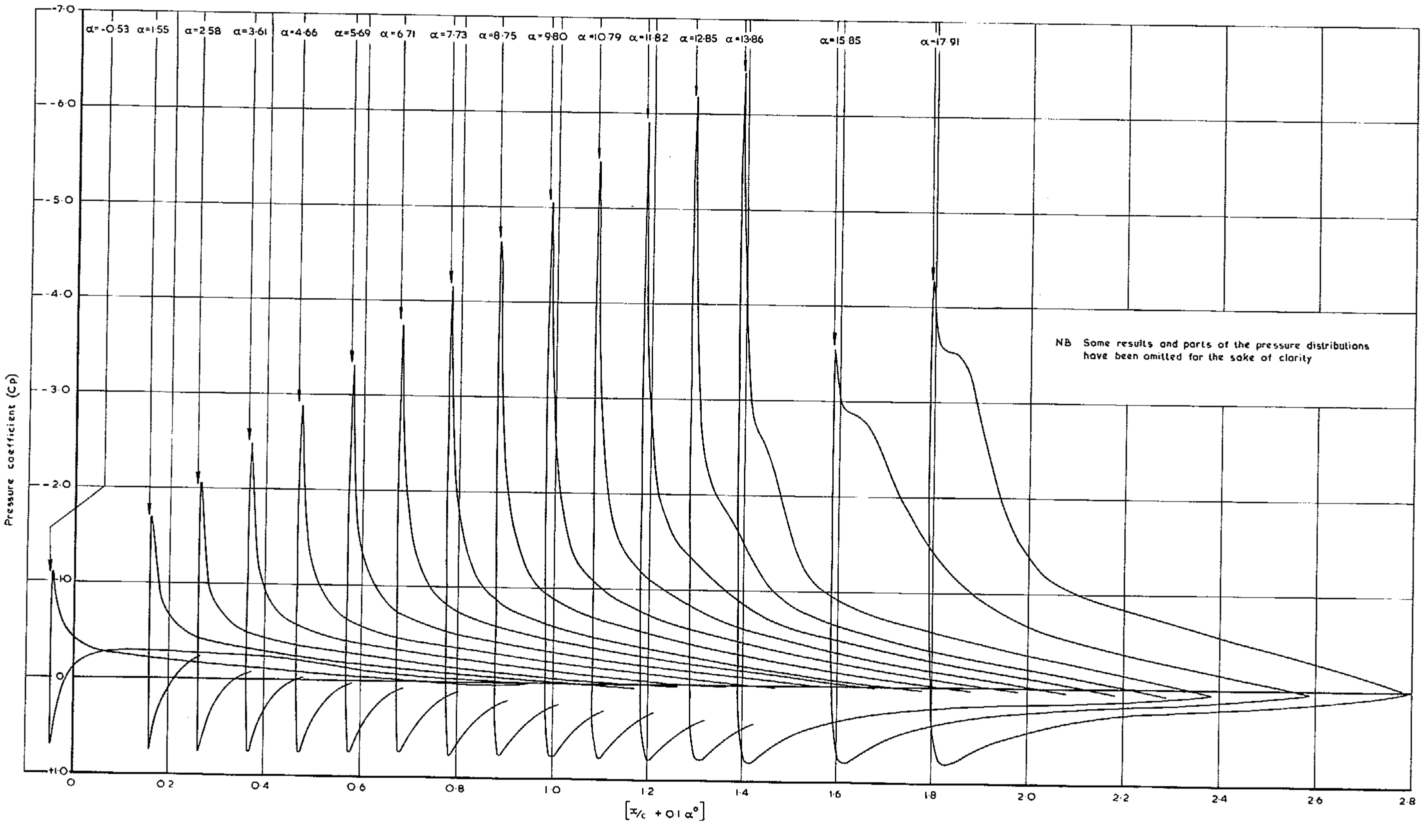

NB Some results and parts of the pressure distributions have been omitted for the sake of clarity

FIG. 75. Variation of chordwise pressure distribution with incidence at 3 per cent semispan station. $R_{\bar{c}} = 1{\cdot}02 \times 10^6$, wire on.

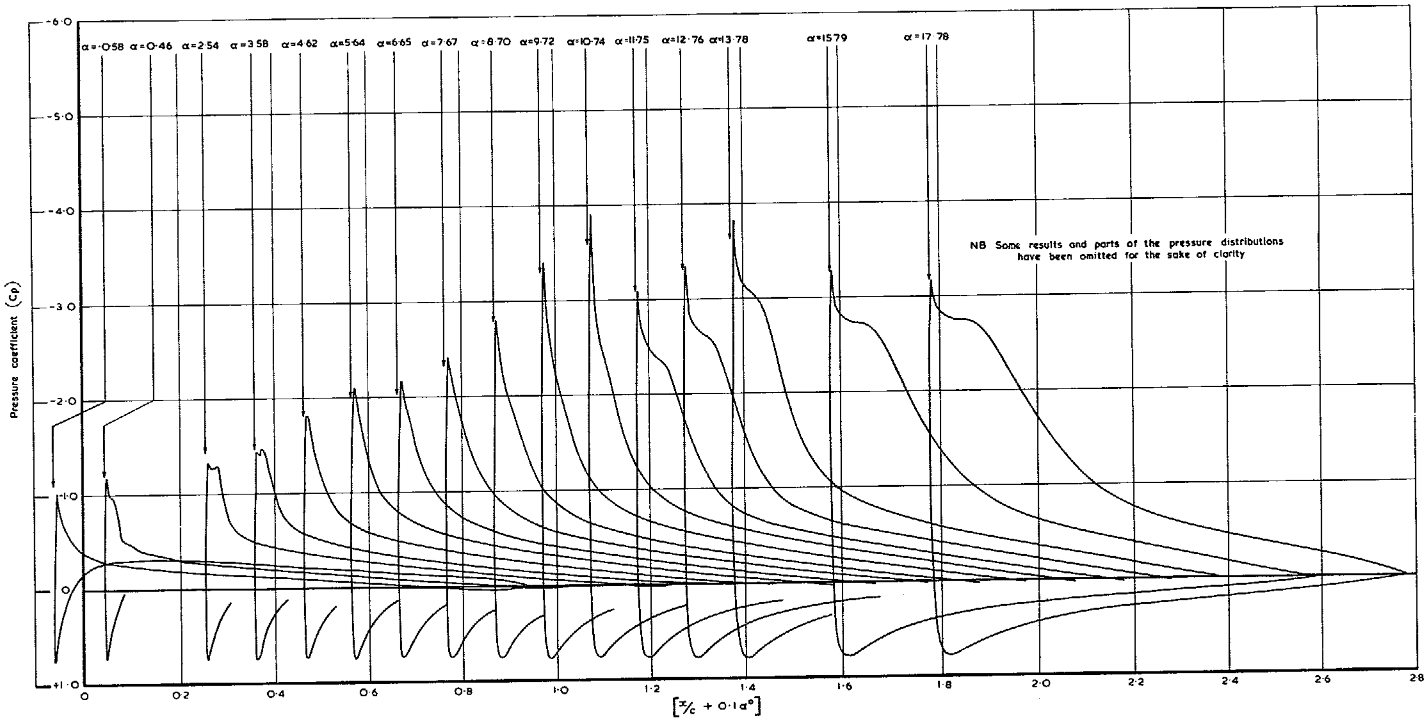

FIG. 76. Variation of chordwise pressure distribution with incidence at 3 per cent semispan station. $R_{\bar{c}} = 0{\cdot}51 \times 10^6$, wire on.

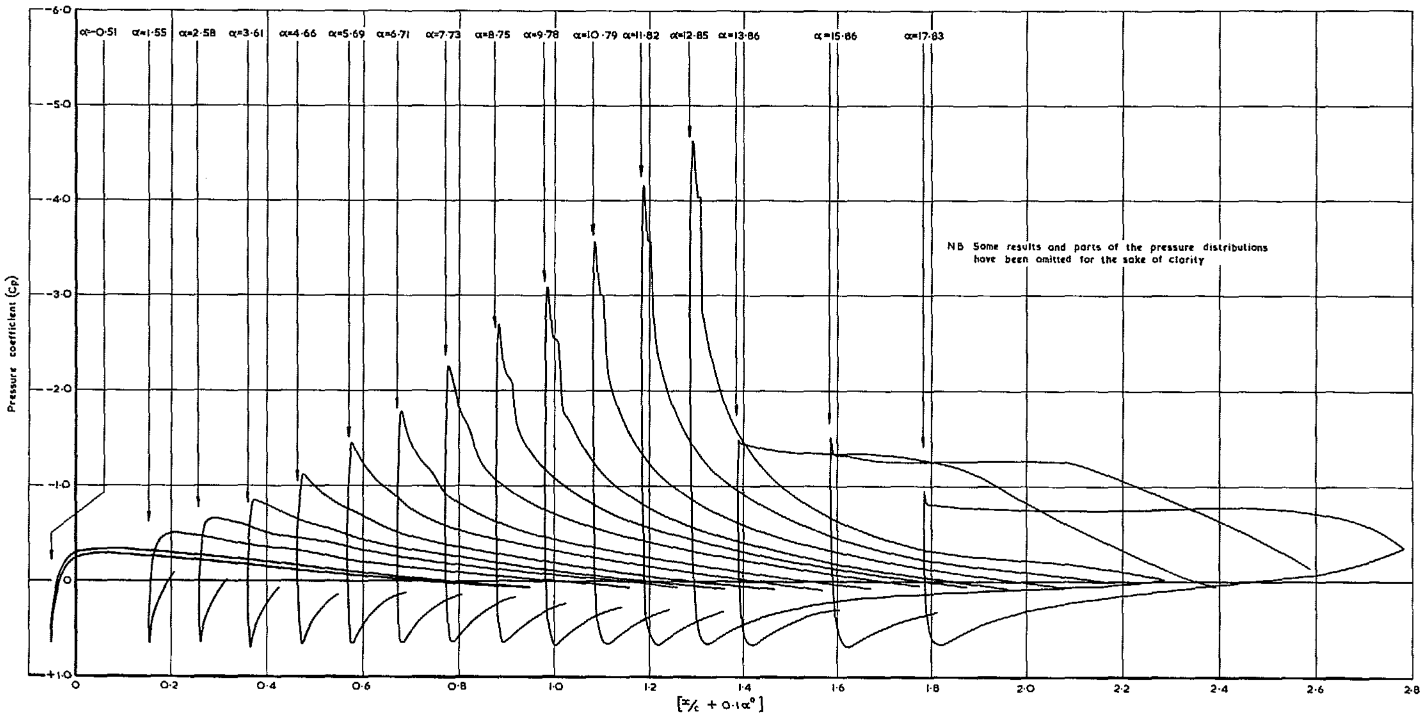

NB Some results and parts of the pressure distributions have been omitted for the sake of clarity

FIG. 77. Variation of chordwise pressure distribution with incidence at 40 per cent semispan station. $R_{\bar{c}} = 1{\cdot}02 \times 10^6$, wire on.

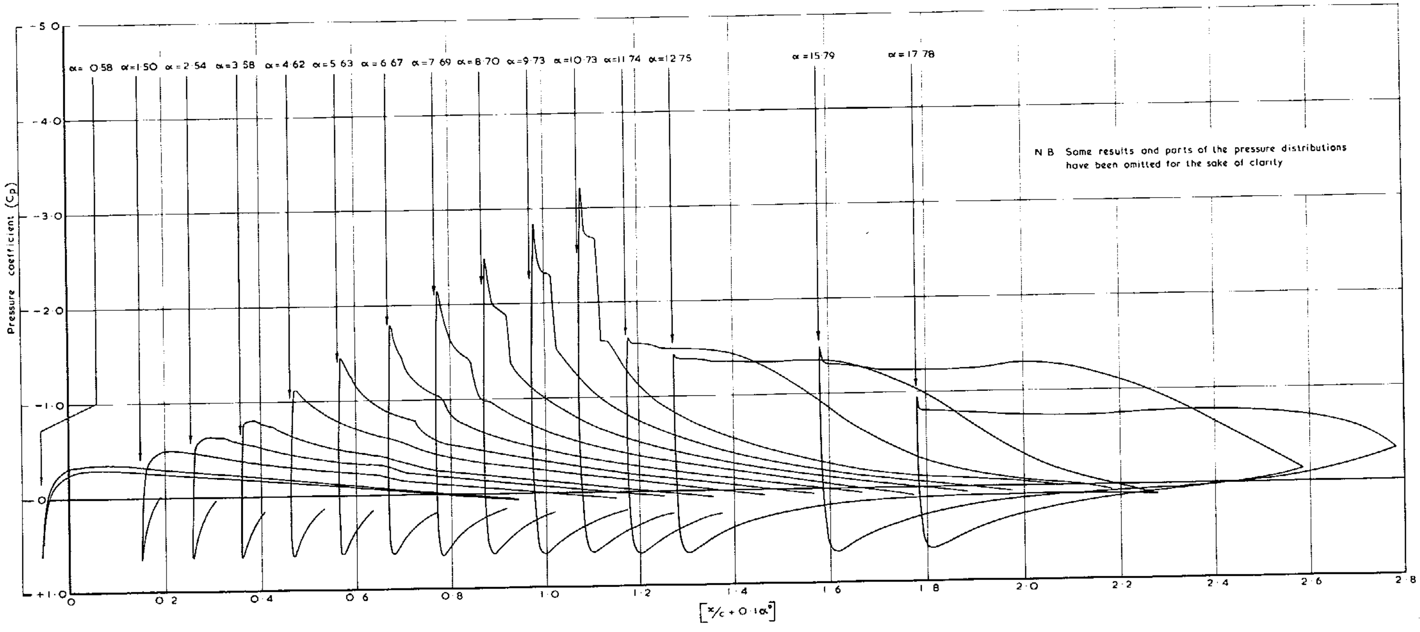

N B Some results and parts of the pressure distributions have been omitted for the sake of clarity

FIG. 78. Variation of chordwise pressure distribution with incidence at 40 per cent semispan station. $R_{\bar{c}} = 0{\cdot}51 \times 10^6$, wire on.

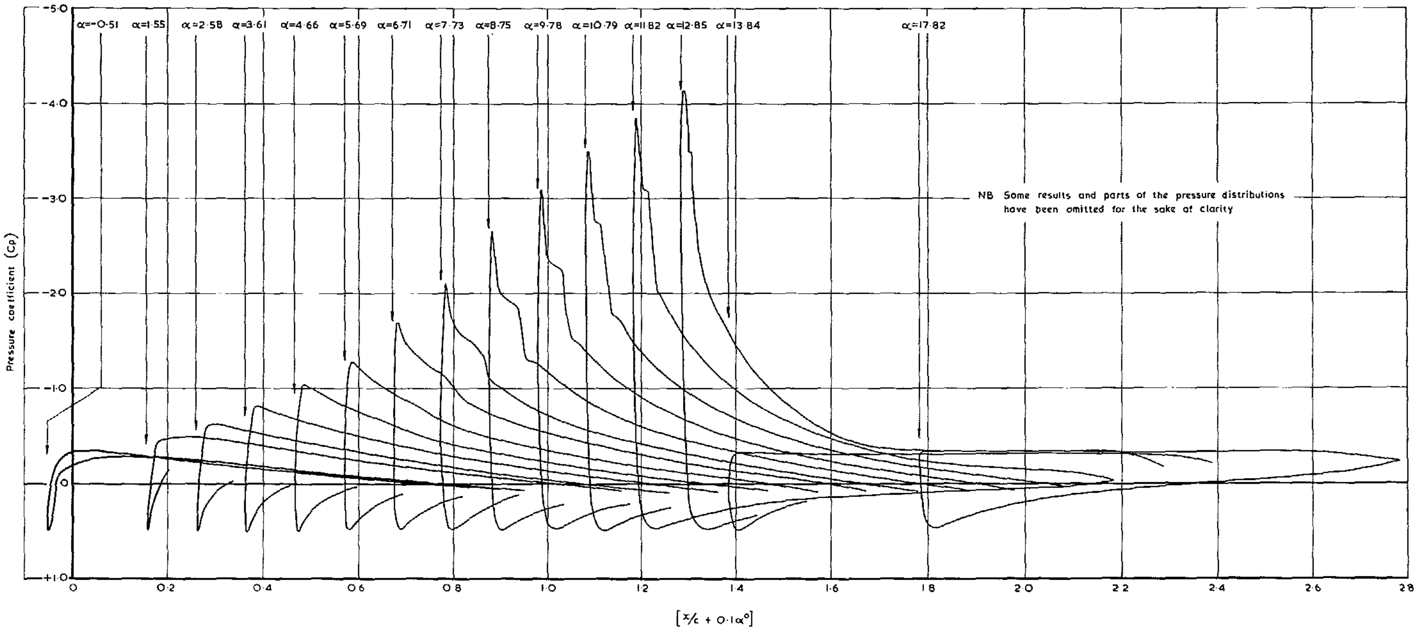

FIG. 79. Variation of chordwise pressure distribution with incidence at 85 per cent semispan station. $R_{\bar{c}} = 1{\cdot}02 \times 10^6$, wire on.

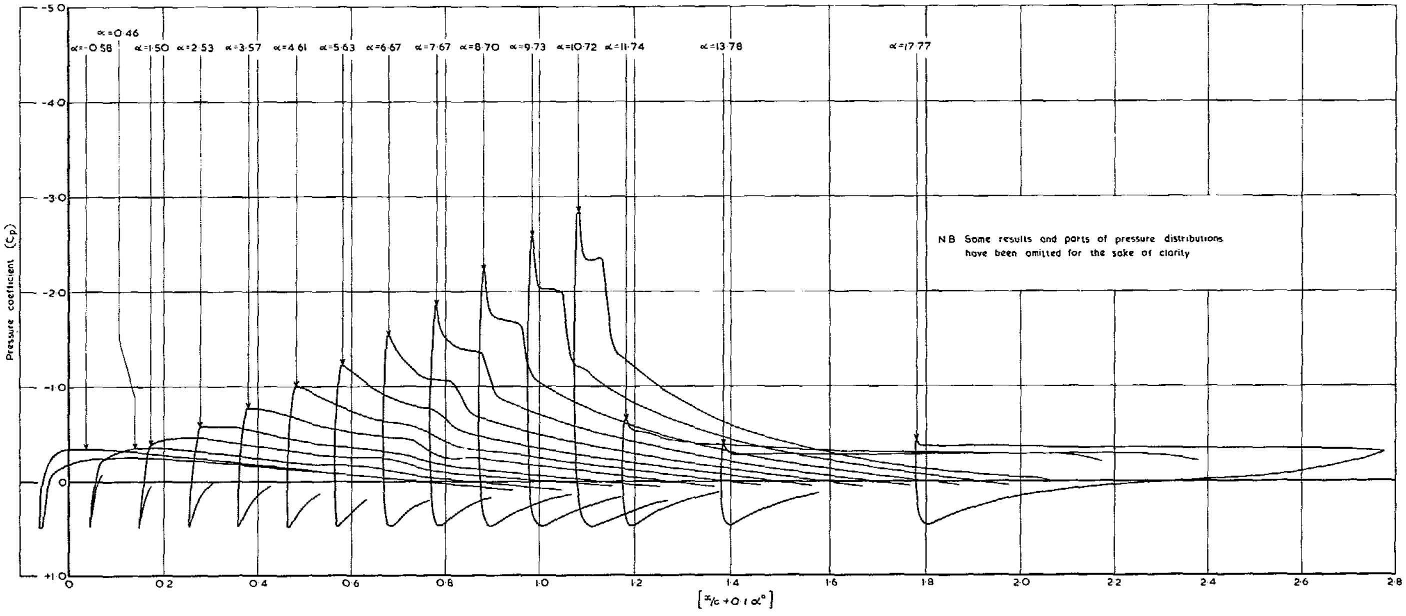

N.B. Some results and parts of pressure distributions have been omitted for the sake of clarity

FIG. 80. Variation of chordwise pressure distribution with incidence at 85 per cent semispan station. $R_{\bar{c}} = 0{\cdot}51 \times 10^6$, wire on.

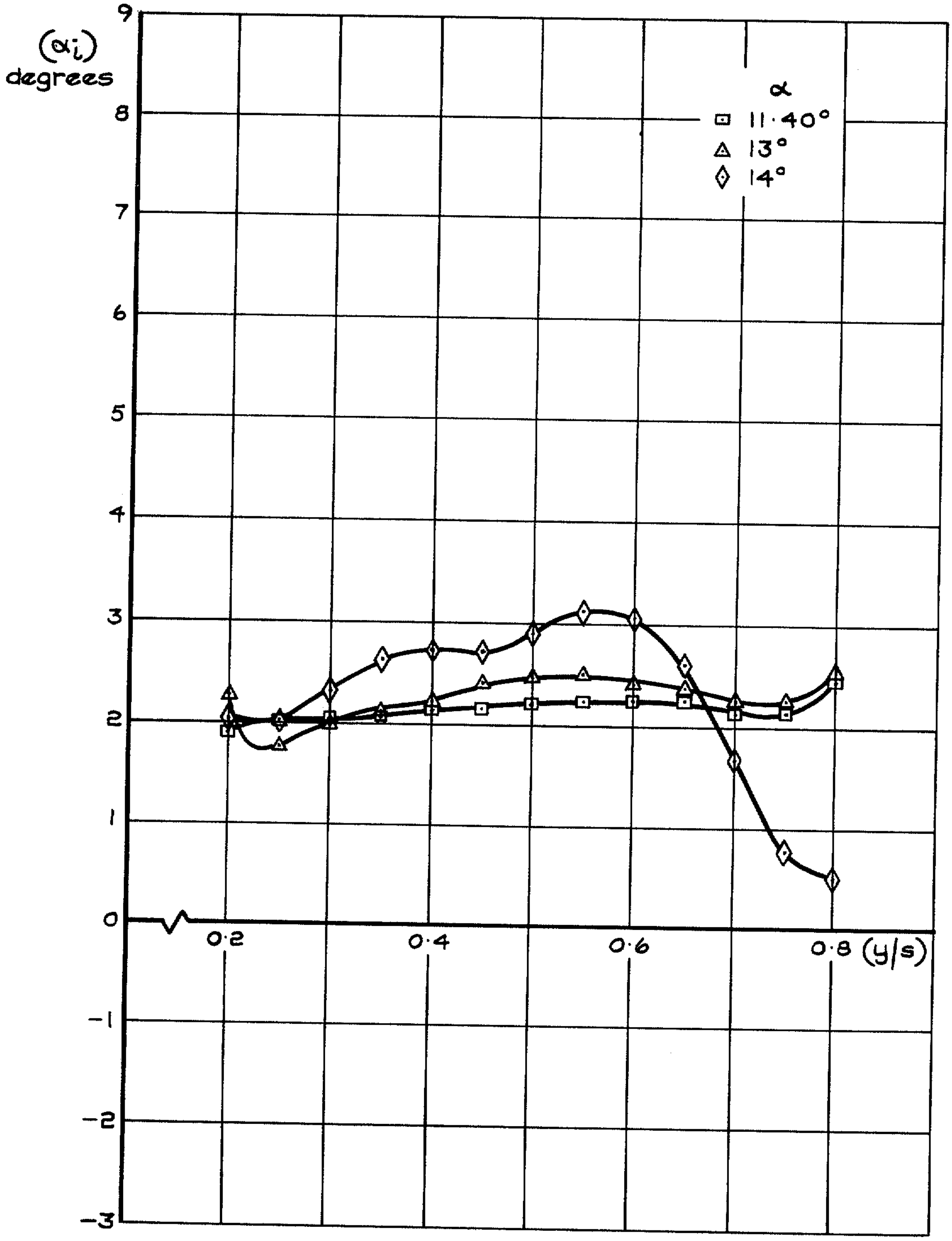

FIG. 81. Spanwise variation of downwash angle. $R_{\bar{c}} = 1{\cdot}78 \times 10^6$, wire on.

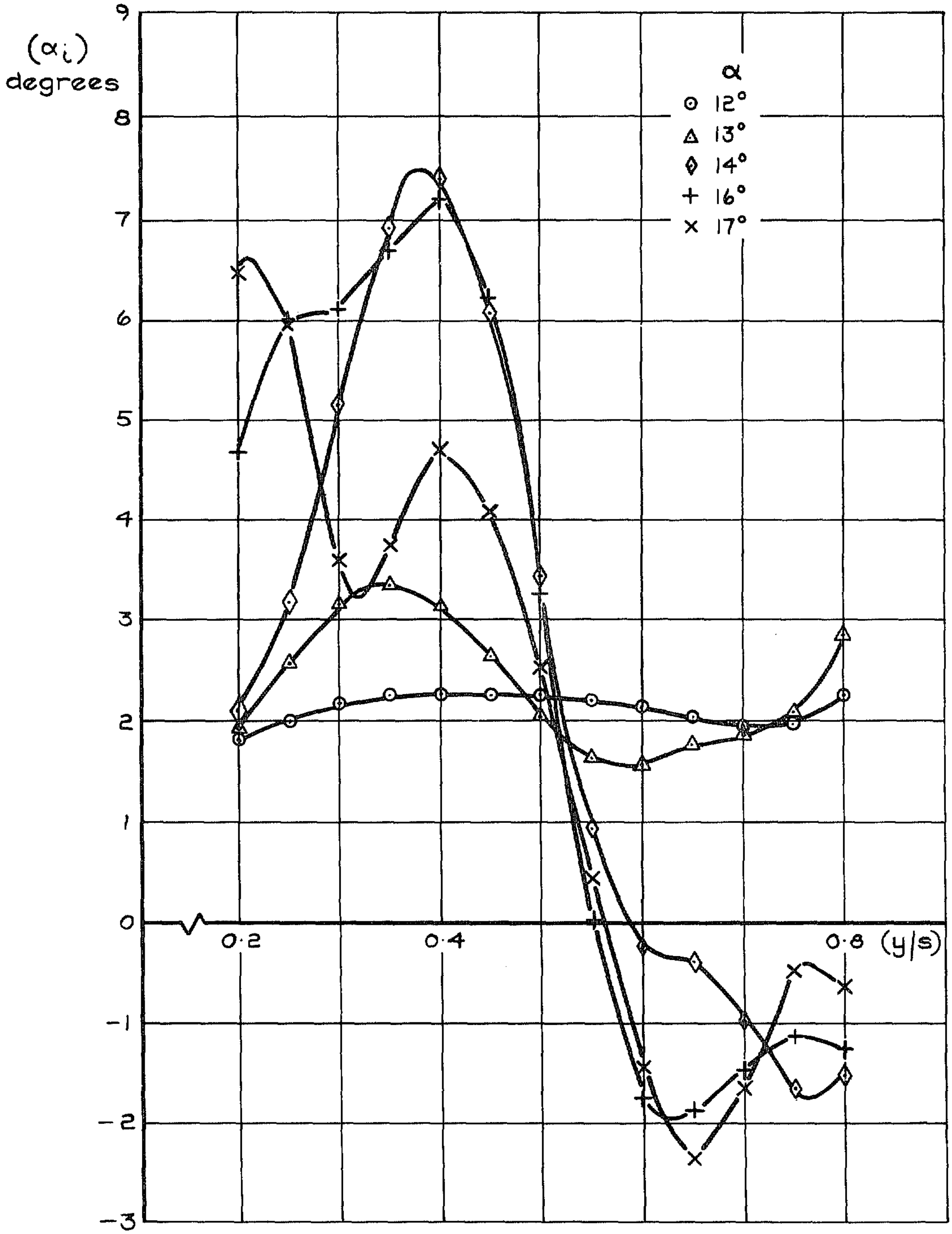

FIG. 82. Spanwise variation of downwash angle. $R_{\bar{c}} = 1{\cdot}02 \times 10^6$, wire on.

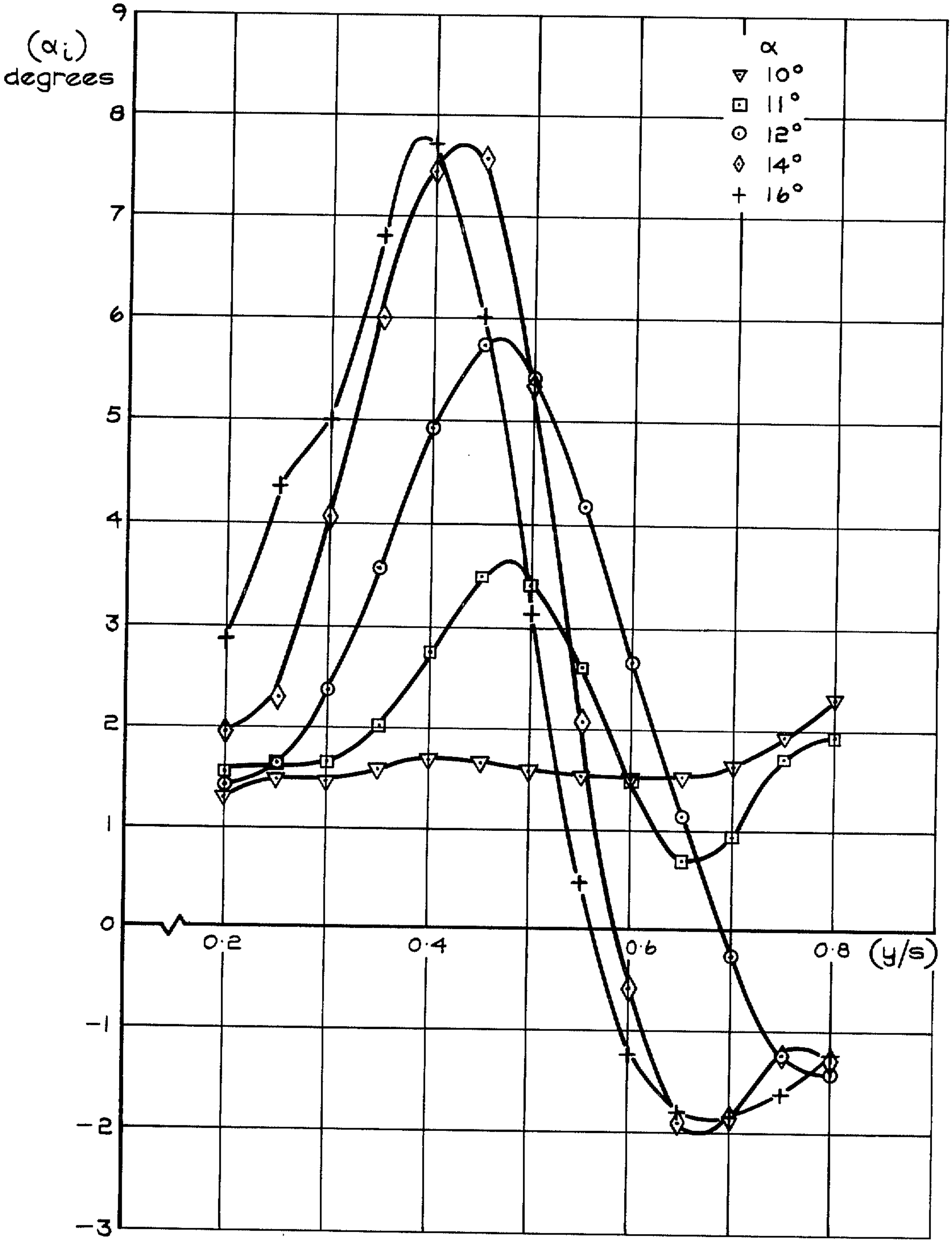

FIG. 83. Spanwise variation of downwash angle. $R_{\bar{c}} = 0{\cdot}51 \times 10^6$, wire on.

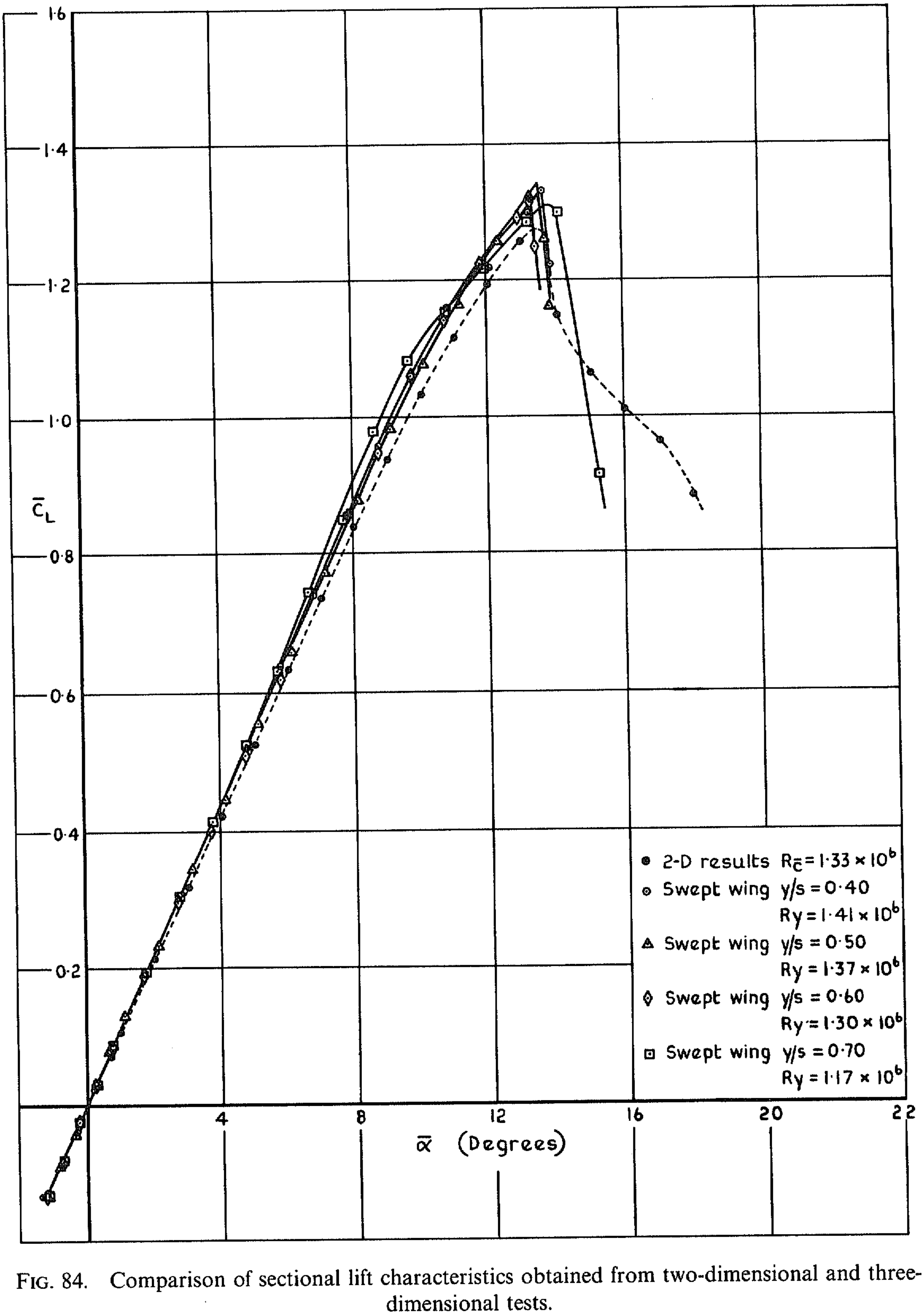

FIG. 84. Comparison of sectional lift characteristics obtained from two-dimensional and three-dimensional tests.

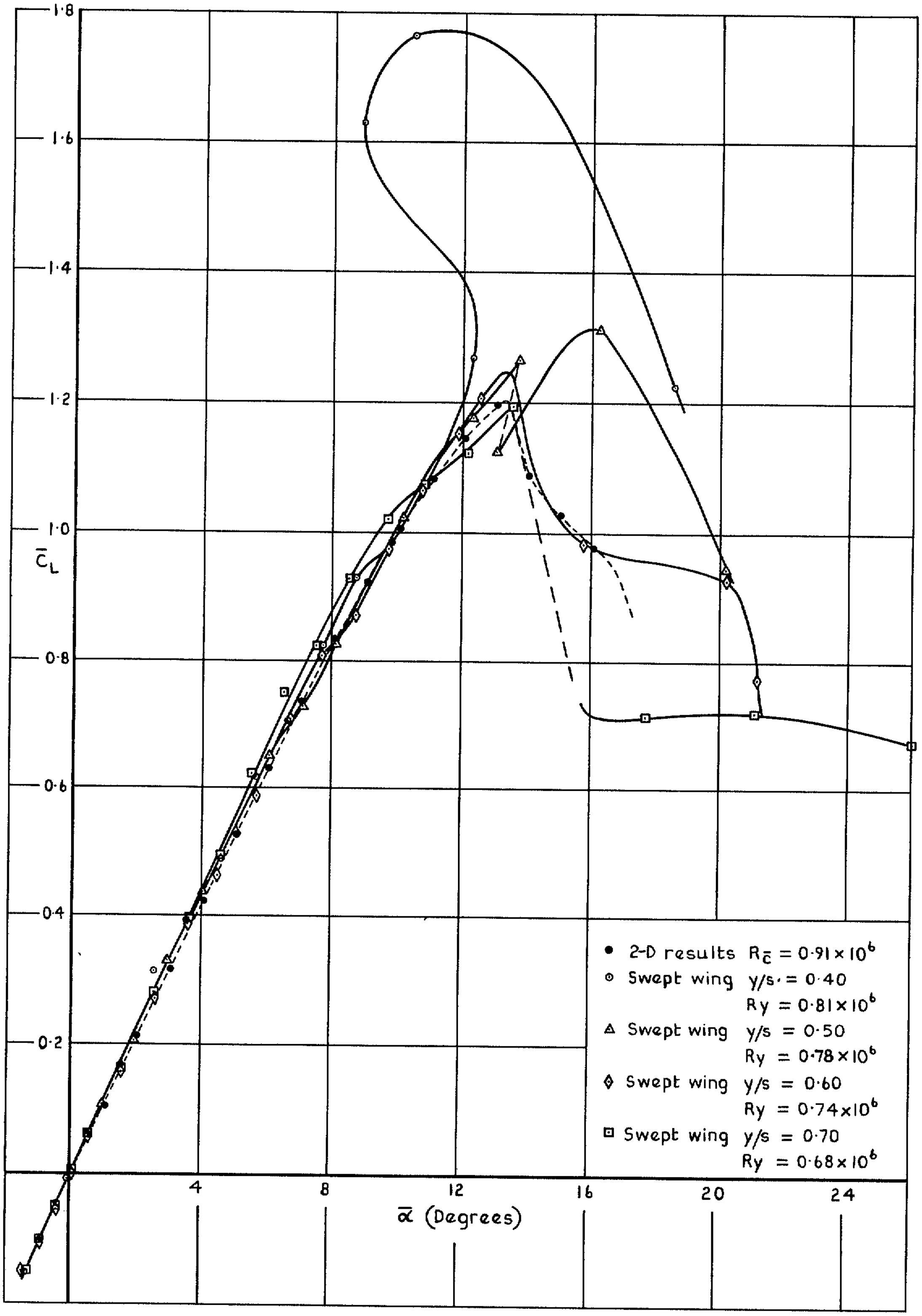

FIG. 85. Comparison of sectional lift characteristics obtained from two-dimensional and three-dimensional tests.

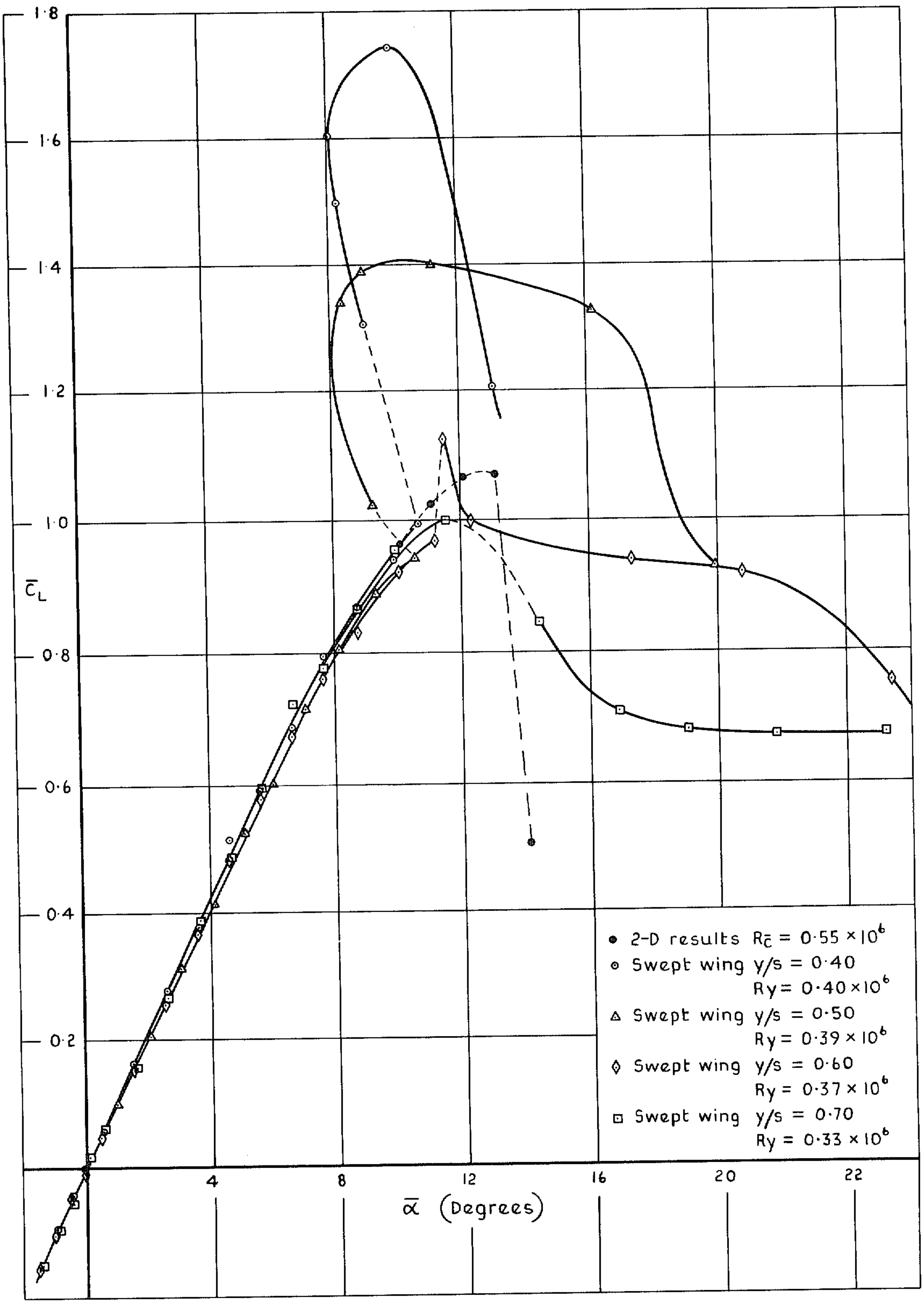

FIG. 86. Comparison of sectional lift characteristics obtained from two-dimensional and three-dimensional tests.

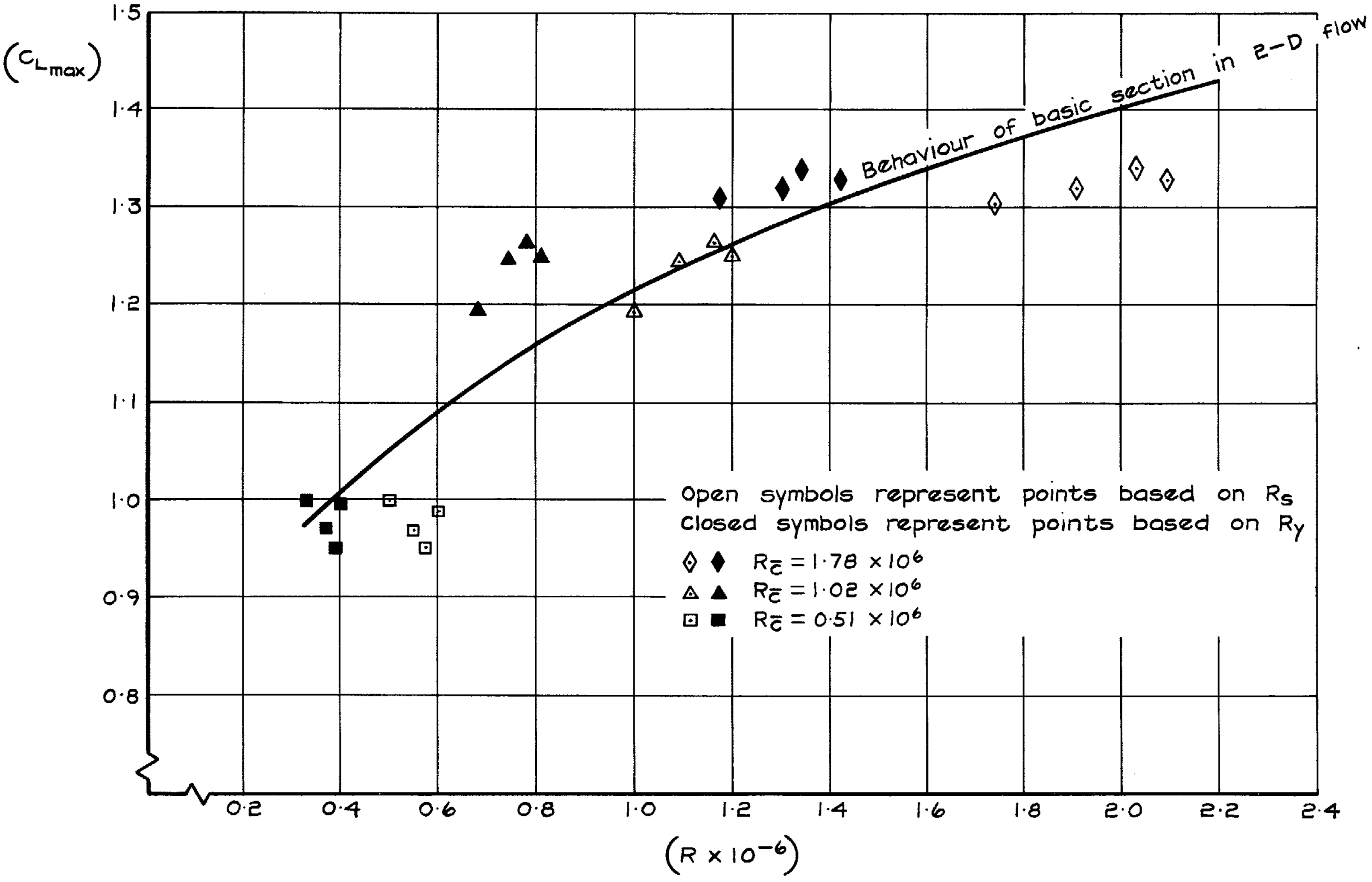

FIG. 87. Comparison between sectional $C_{L_{max}}$ in two-dimensional and three-dimensional flow.

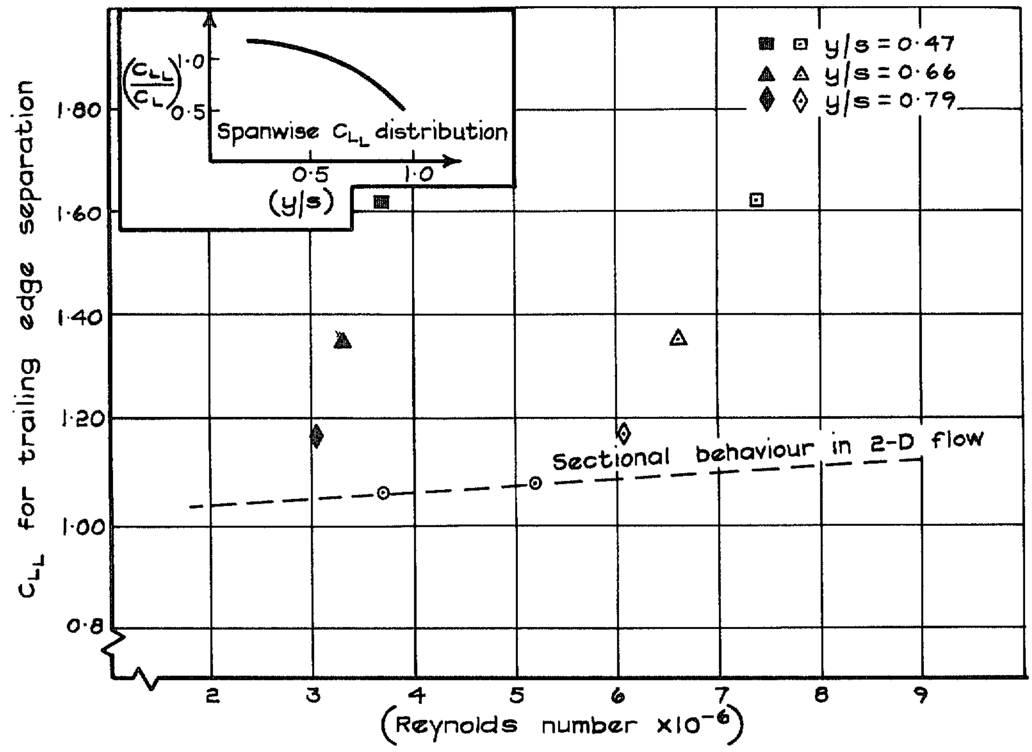

a NACA 64 A810

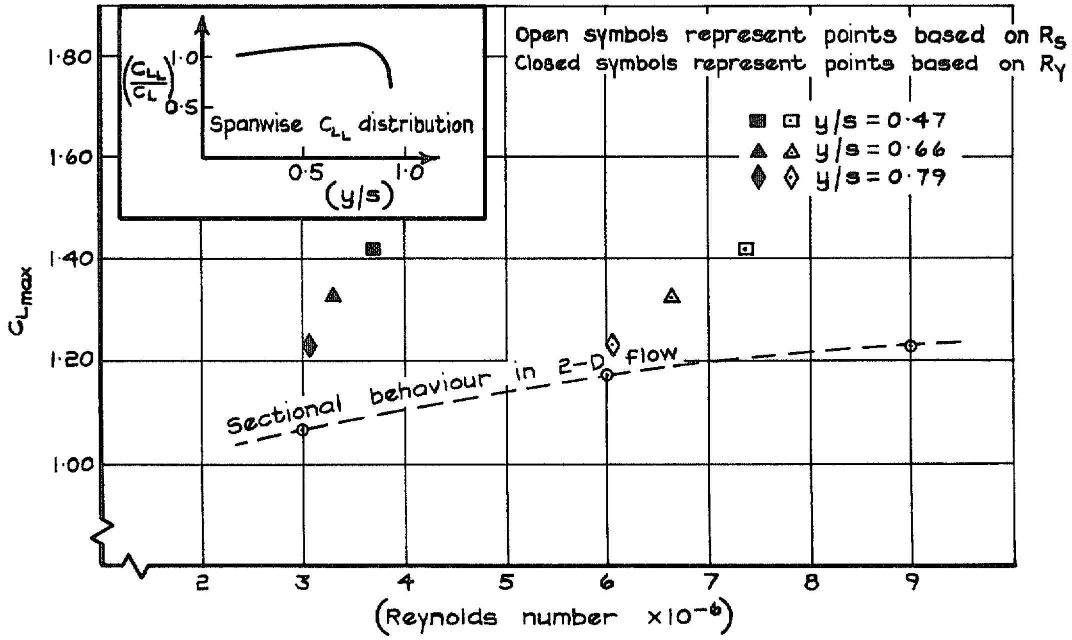

b NACA 64 A010

FIG. 88a–b. Comparison between sectional $C_{L_{max}}$ in two-dimensional and three-dimensional flow (N.A.C.A. tests).

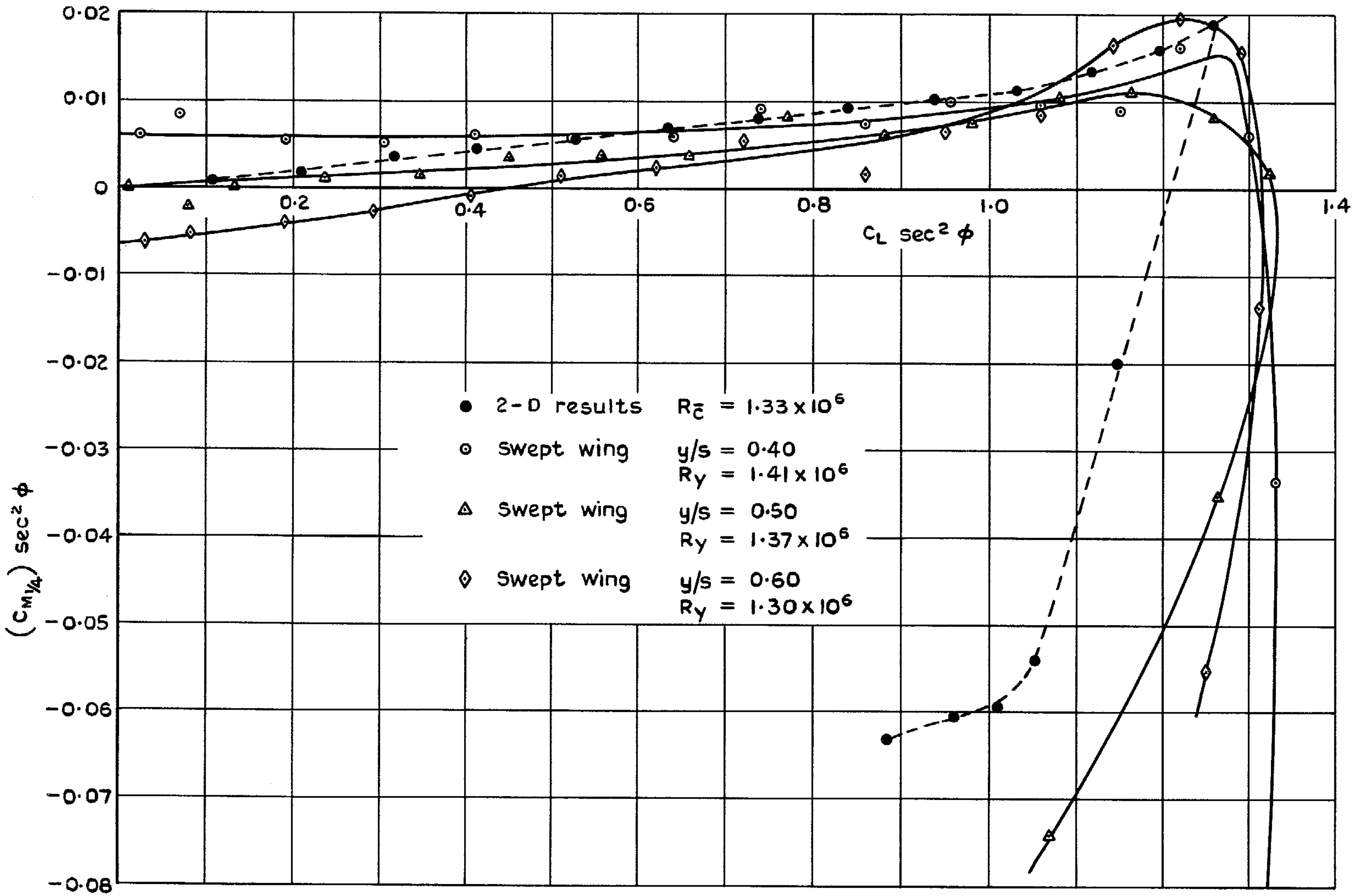

FIG. 89. Comparison between sectional pitching moments in two- and three-dimensional flow. $R_{\bar{c}} = 1{\cdot}78 \times 10^6$.

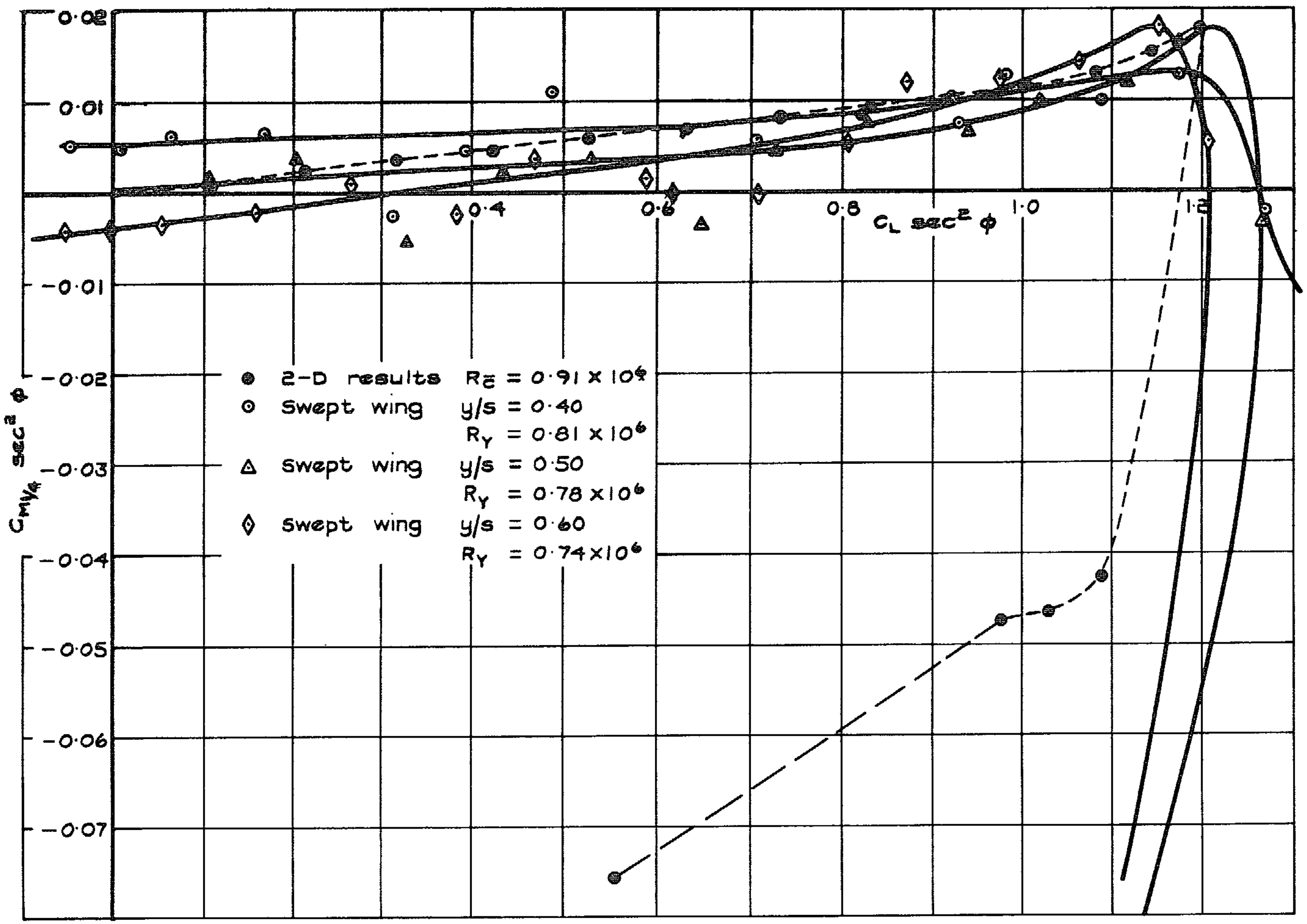

FIG. 90. Comparison between sectional pitching moments in two- and three-dimensional flow. $R_{\bar{c}} = 1{\cdot}02 \times 10^6$.

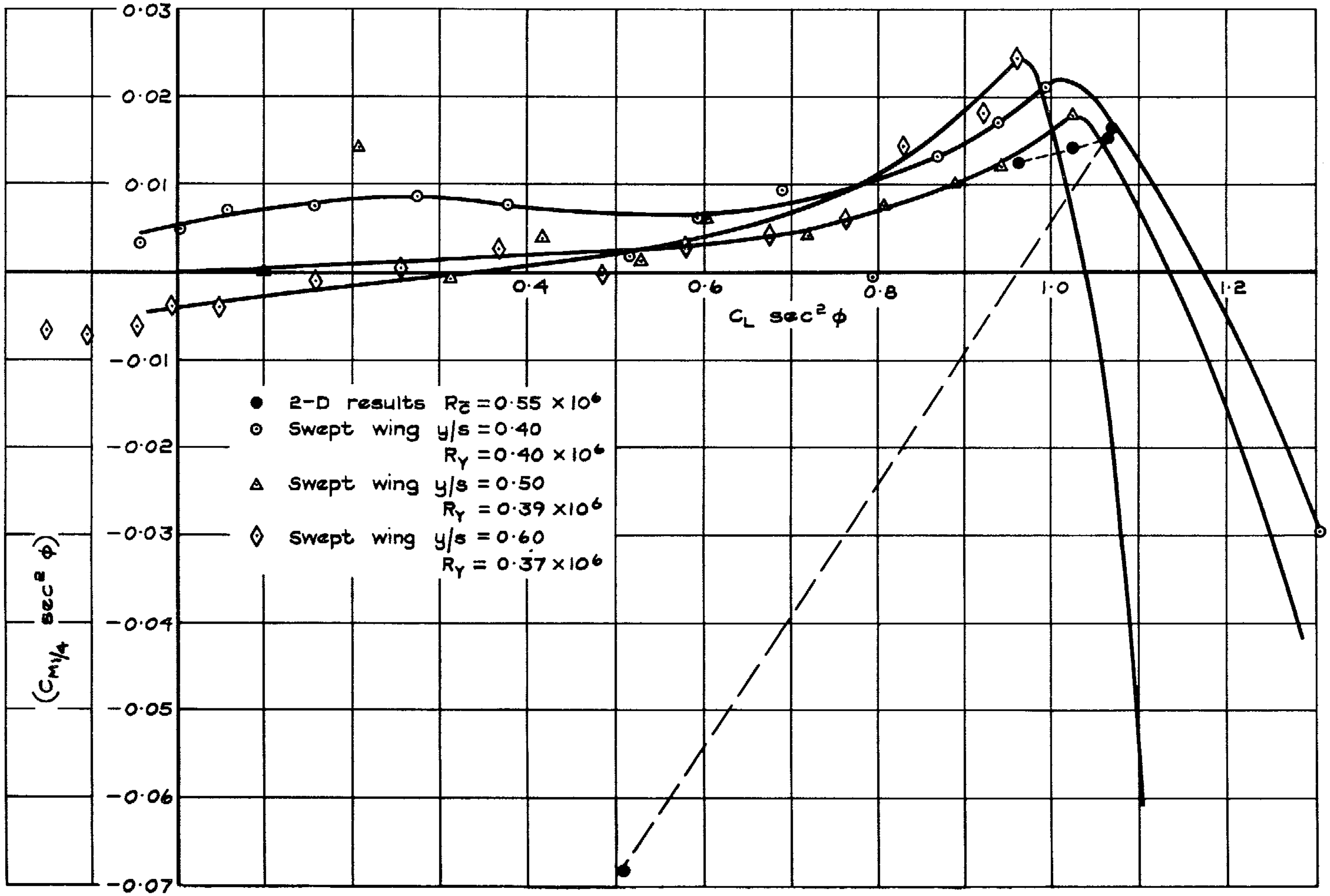

FIG. 91. Comparison between sectional pitching moments in two- and three-dimensional flow. $R_{\bar{c}} = 0·51 \times 10^6$.

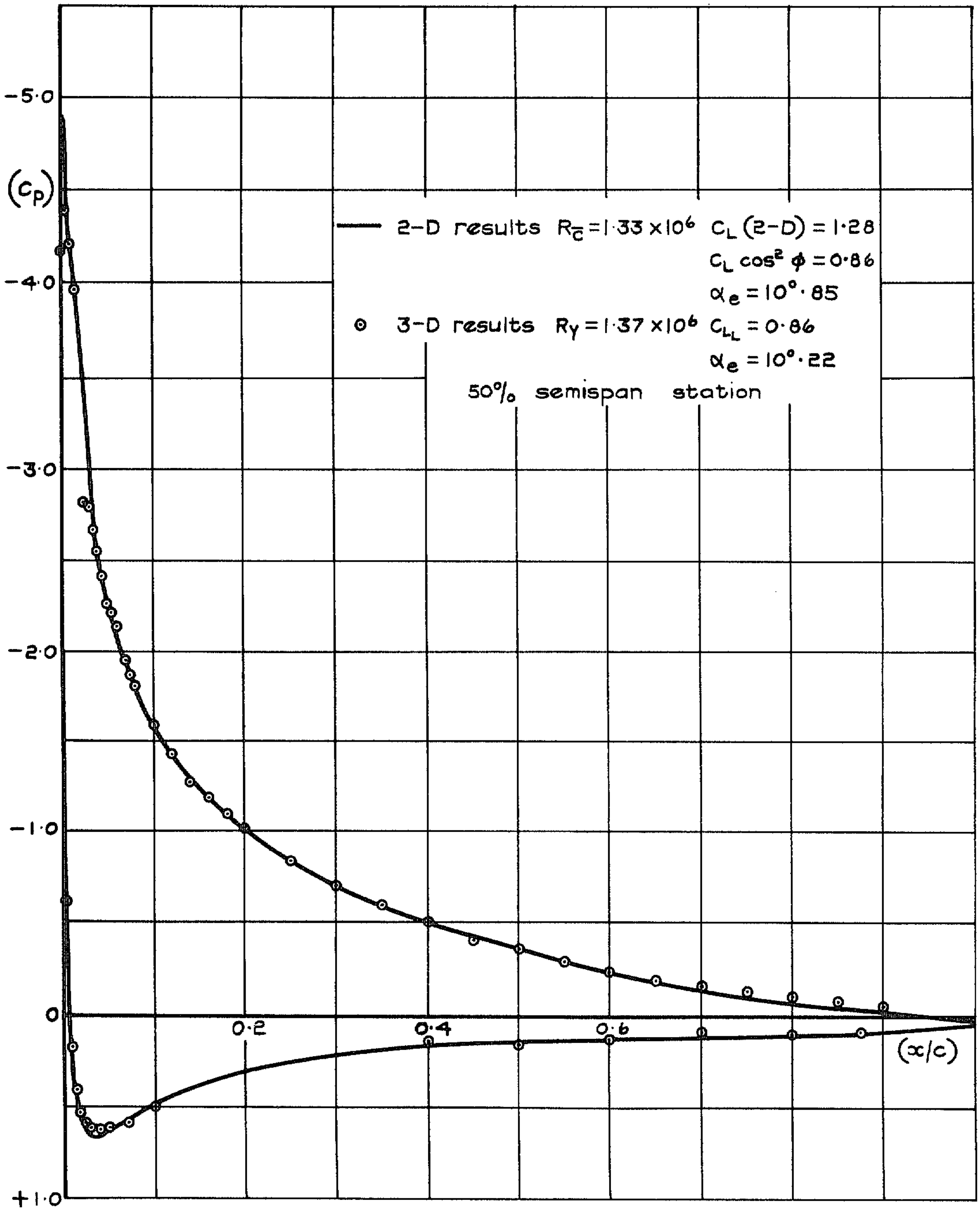

FIG. 92. Comparison between chordwise pressure distributions in two-dimensional and three-dimensional flow near the stall.

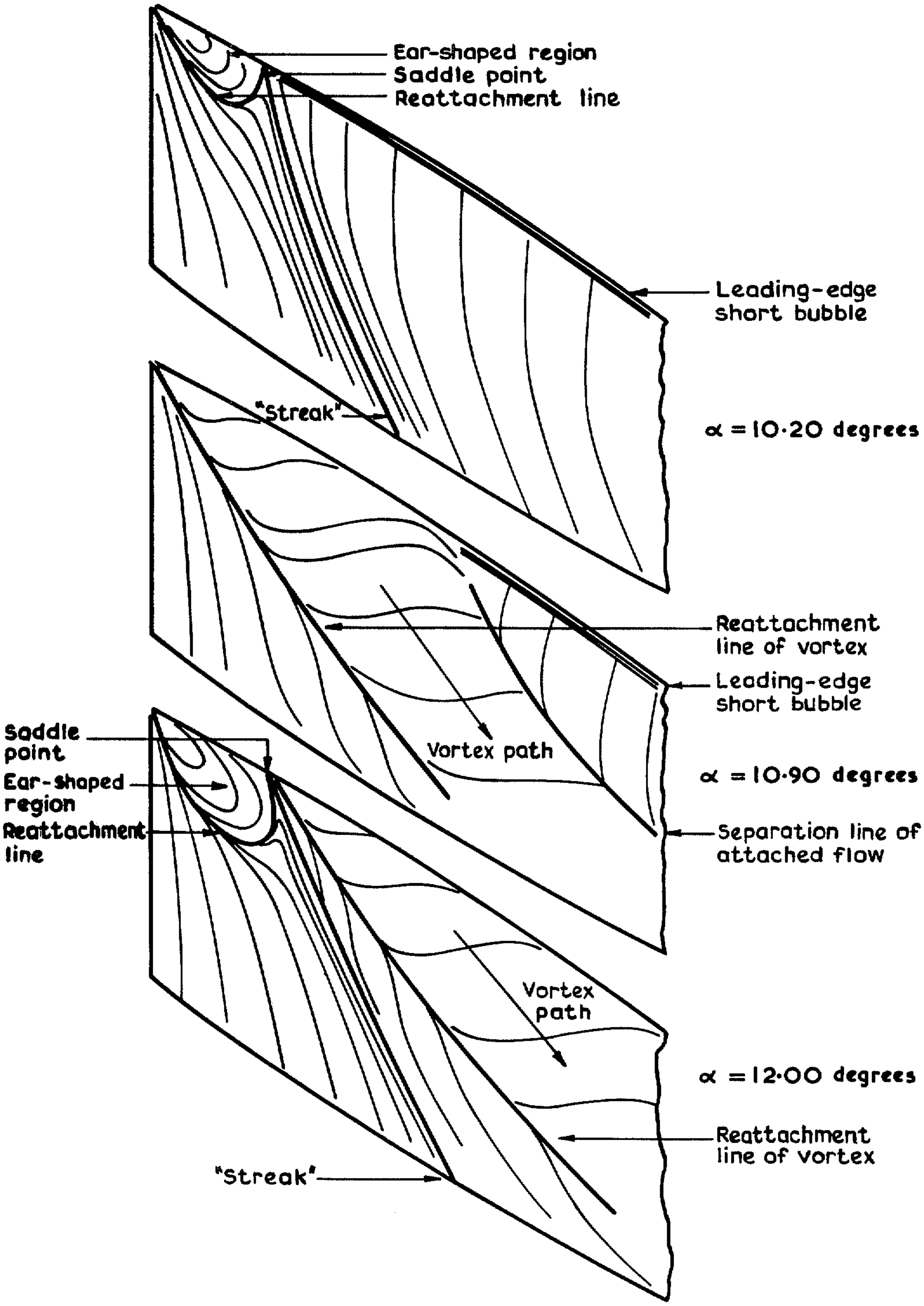

FIG. 93. Sketch interpretations of oil flow photographs on Fig. 22.

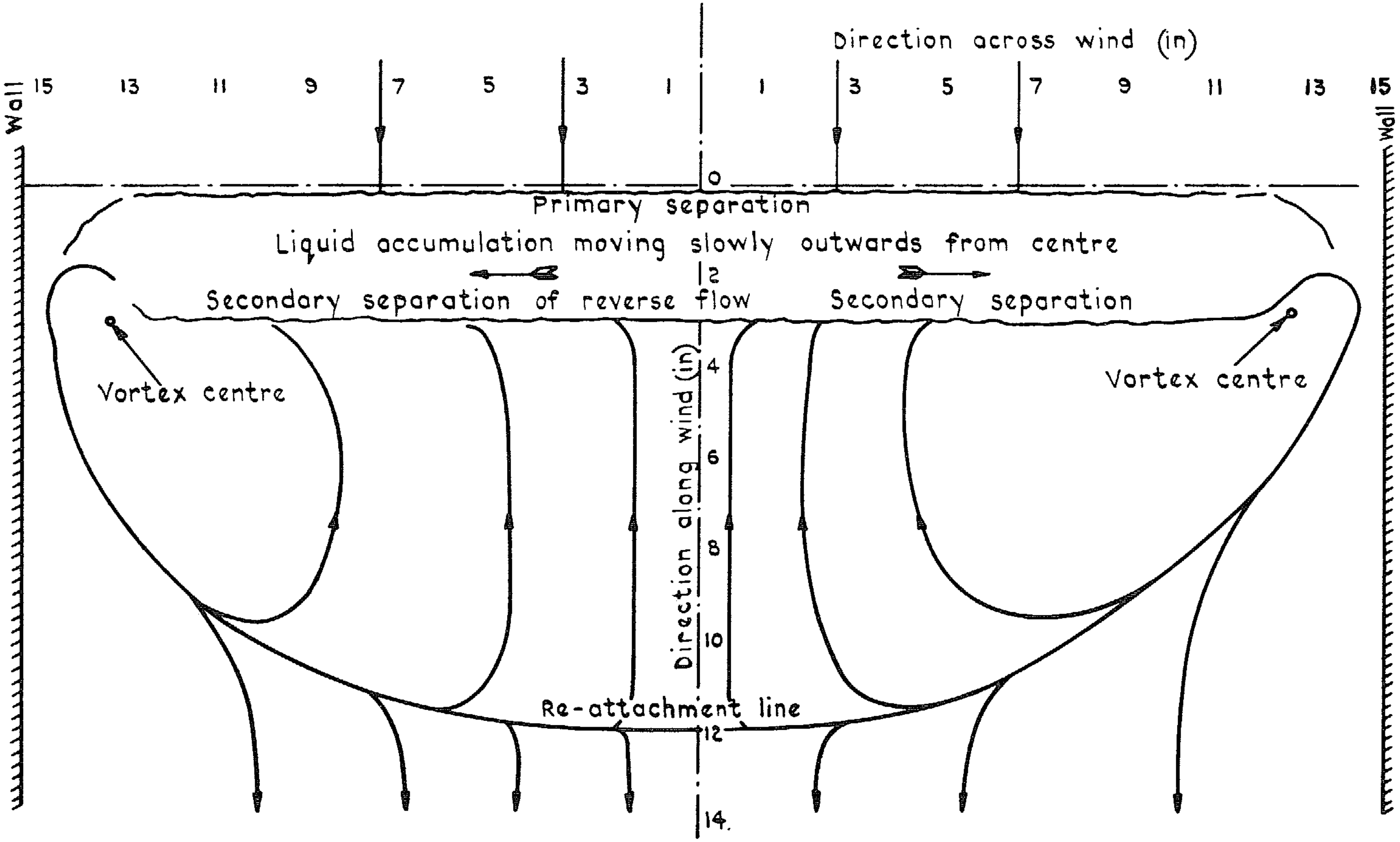

FIG. 94. Oil flow in long bubble on plate between two walls.

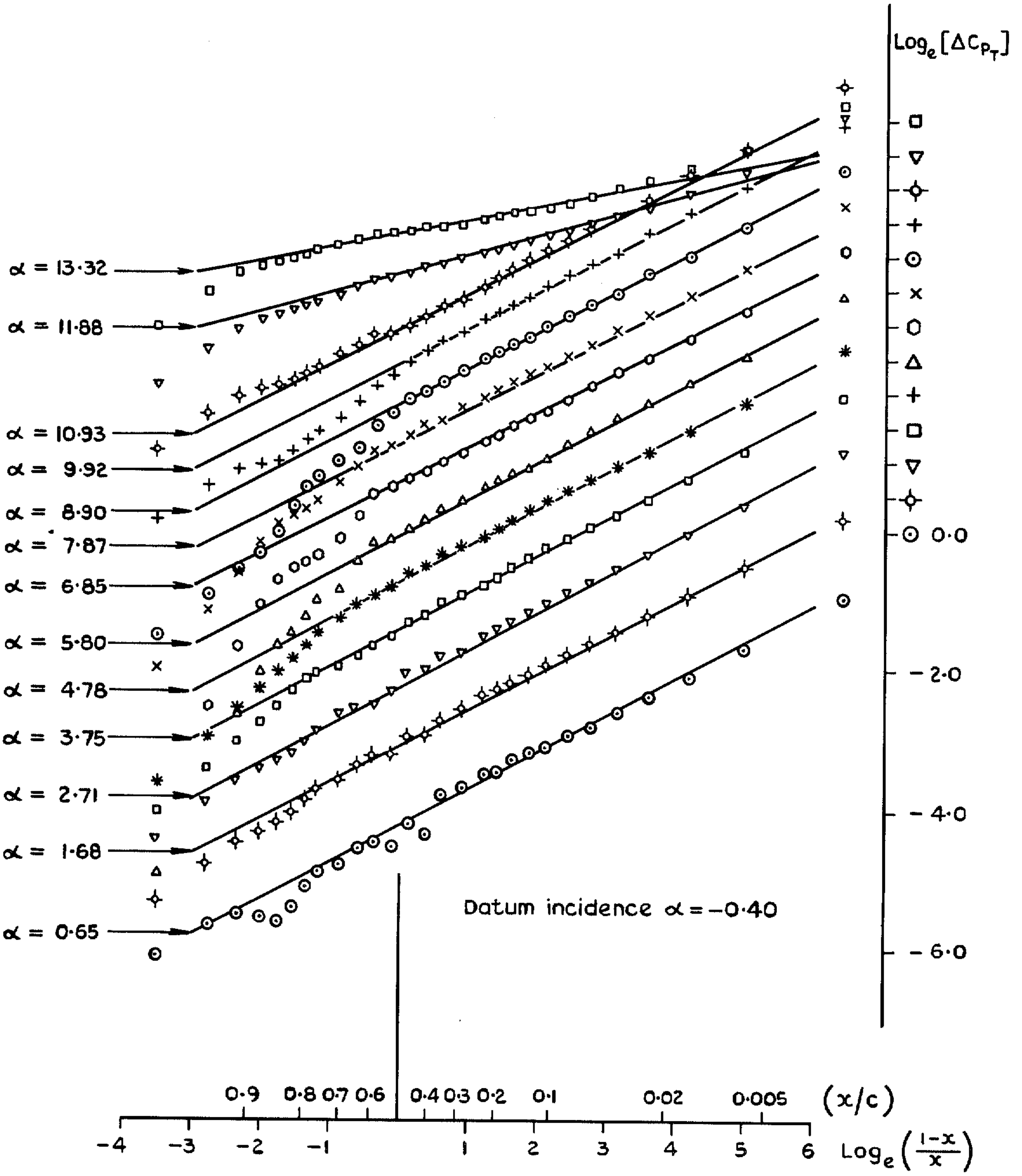

FIG. 95. Variation of the derived thin wing chordwise loading with incidence at 40 per cent semispan station. $R_{\bar{c}} = 1{\cdot}78 \times 10^6$, wire off.

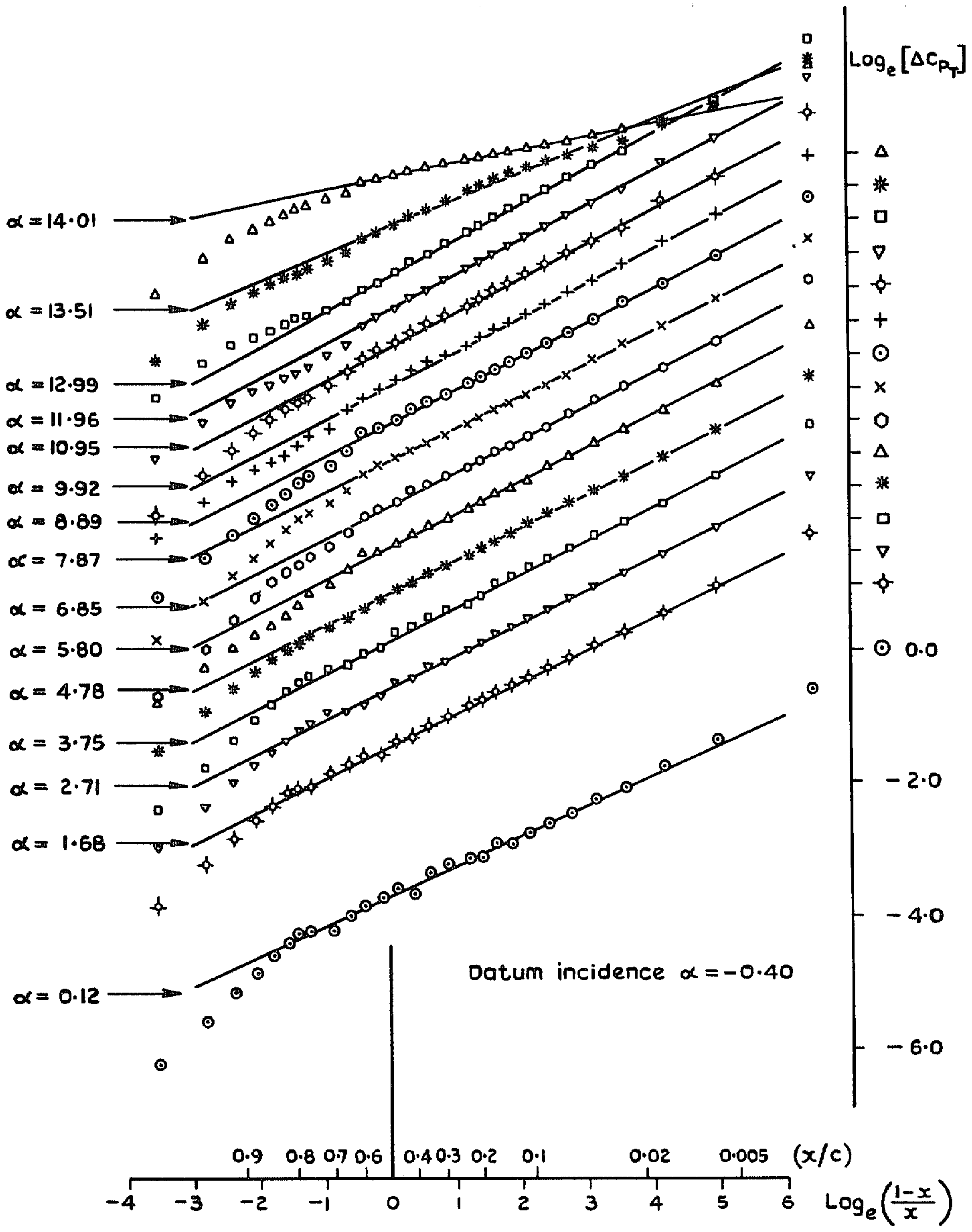

FIG. 96. Variation of the derived thin wing chordwise loading with incidence at 40 per cent semispan station. $R_{\bar{c}} = 1{\cdot}78 \times 10^6$, wire on.

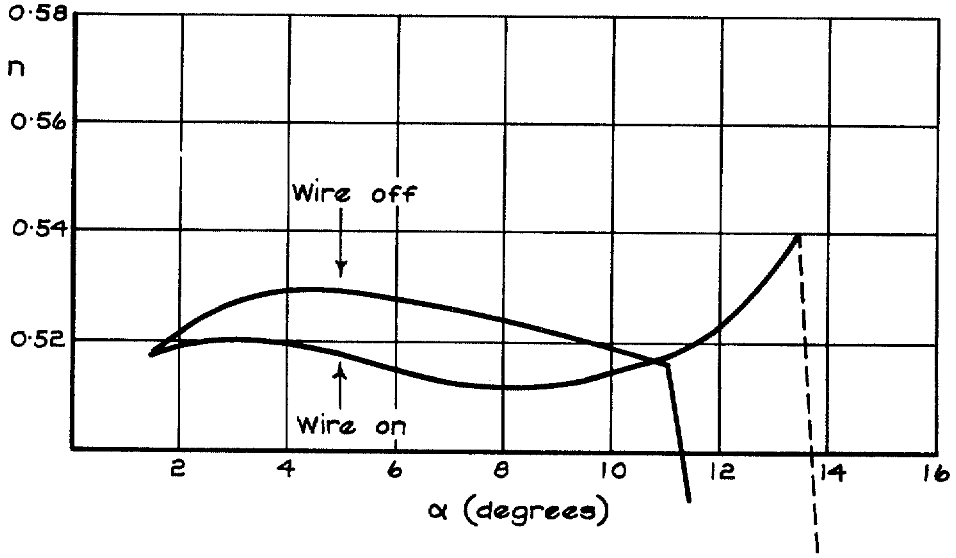

a Variation of thin wing loading parameter "n"

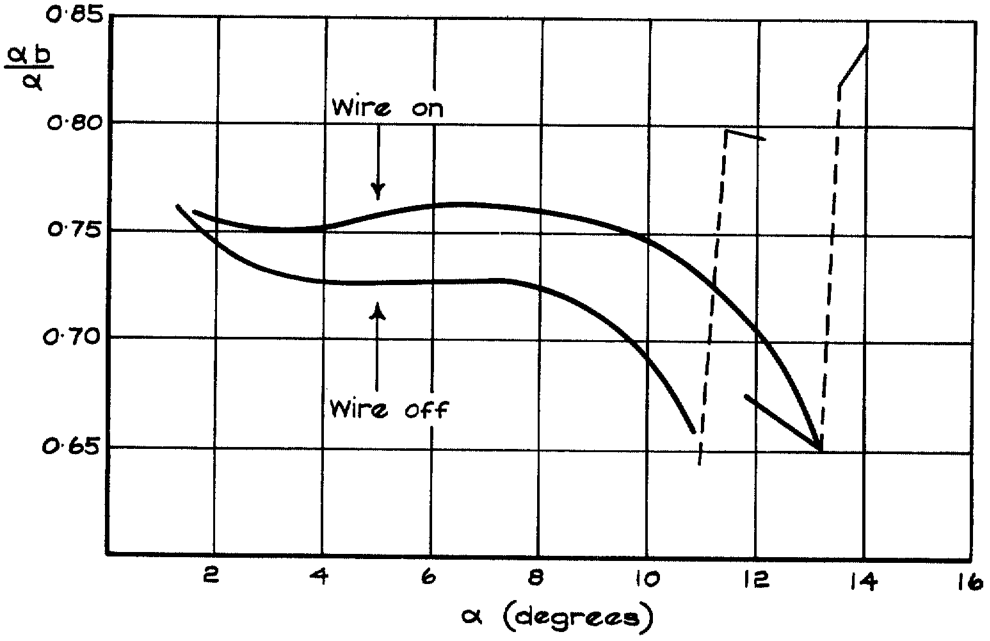

b Variation of thin wing loading parameter $\alpha b/\alpha$

FIG. 97a–b. Variation of thin wing loading parameters with incidence at 40 per cent semispan station. $R_{\bar{c}} = 1{\cdot}78 \times 10^6$, wire on and off.

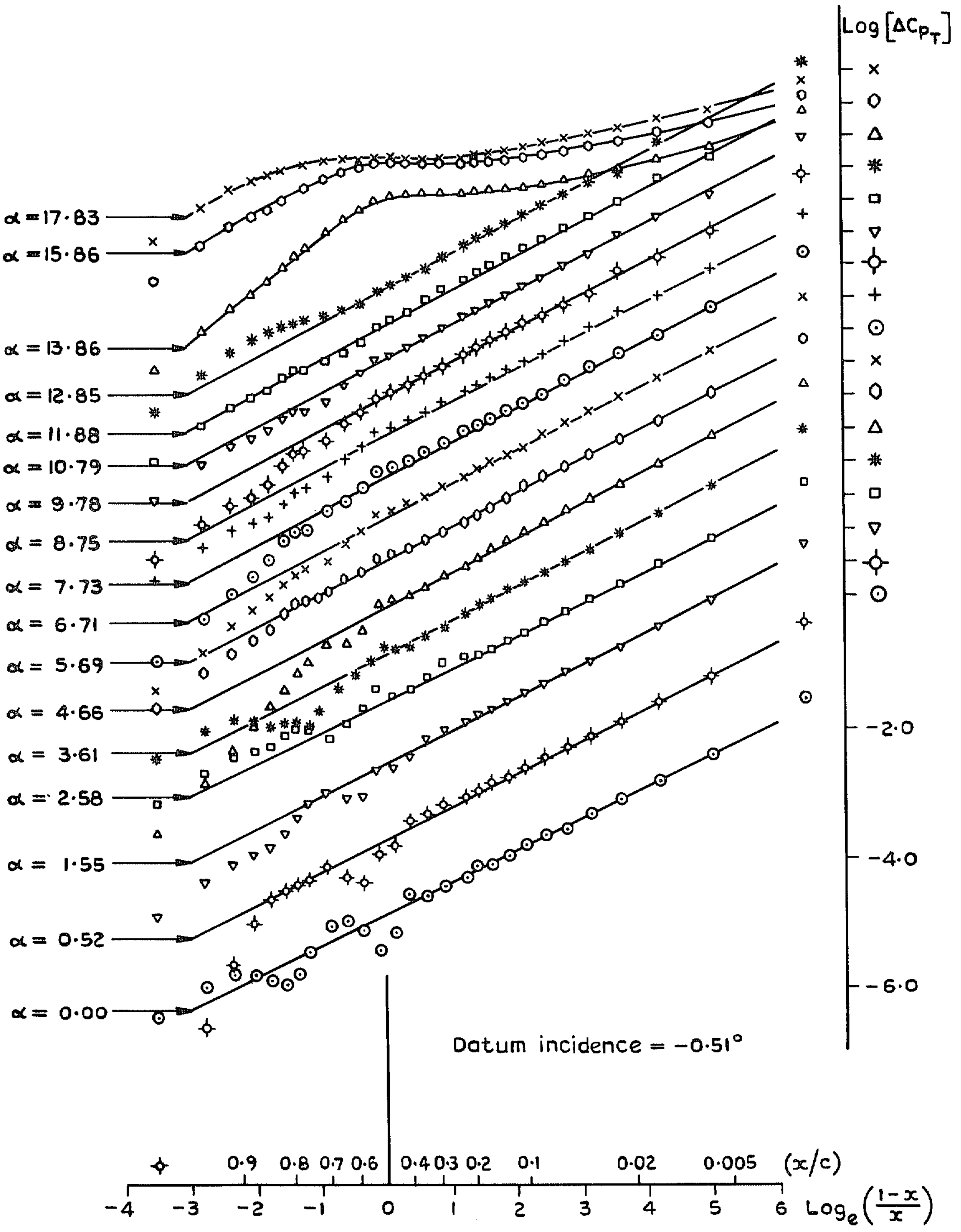

FIG. 98. Variation of the derived thin wing chordwise loading with incidence at 40 per cent semispan station. $R_{\bar{c}} = 1{\cdot}02 \times 10^6$, wire on.

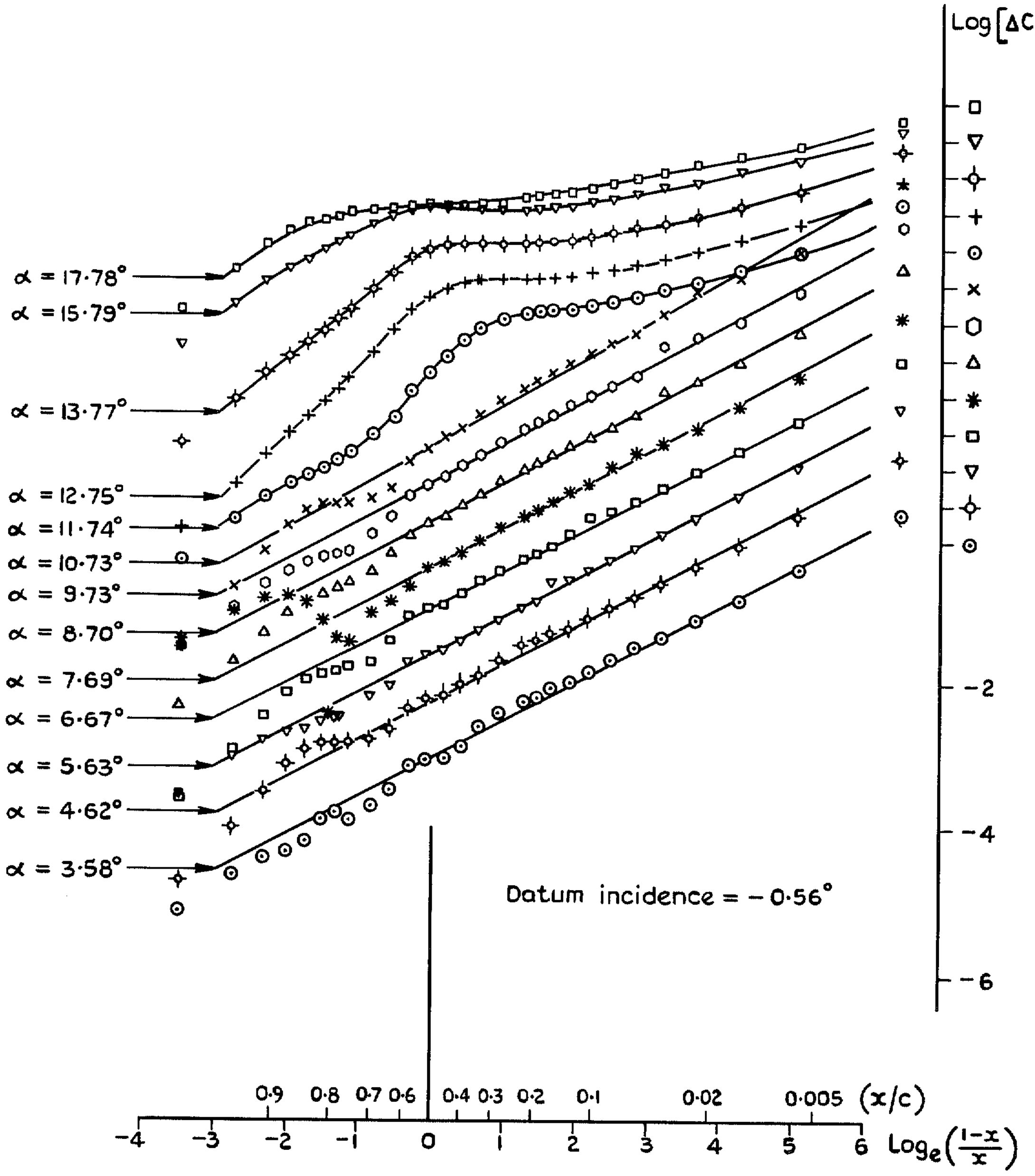

FIG. 99. Variation of the derived thin wing chordwise loading with incidence at 40 per cent semispan station. $R = 0{\cdot}51 \times 10^6$, wire on.

Printed in England for Her Majesty's Stationery Office by J. W. Arrowsmith Ltd., Bristol 3
Dd. 503426 K.5. 4/73.

HER MAJESTY'S STATIONERY OFFICE

Government Bookshops

49 High Holborn, London WC1V 6HB
13a Castle Street, Edinburgh EH2 3AR
109 St Mary Street, Cardiff CF1 1JW
Brazennose Street, Manchester M60 8AS
50 Fairfax Street, Bristol BS1 3DE
258 Broad Street, Birmingham B1 2HE
80 Chichester Street, Belfast BT1 4JY

Government publications are also available through booksellers

R. & M. No. 3721
SBN 11 470521 6*